Development of empirical potentials for amorphous silica

Dissertation

Zur Erlangung des Grades
"Doktor der Naturwissenschaften"
am Fachbereich Physik
der Johannes Gutenberg-Universität
Mainz

vorgelegt von

Antoine CARRÉ

geboren in Saint Brieuc (Frankreich)

universität mainz

Mainz, im September 2007

Die Bestimmung empirischer Potentiale für amorphes Siliziumdioxid

Ein grundlegendes Verständnis von amorphem Siliziumdioxid (SiO_2) ist von großer Bedeutung für die Geowissenschaften und die Mineralogie, als auch für Anwendungen in der Glasindustrie. Von grundlegendem Interesse ist SiO_2 auch, da es das Paradebeispiel eines Glasbildners mit einer tetraedrischen Netzwerkstruktur ist. Viele Anstrengungen sind in der Vergangenheit unternommen worden, um die mikroskopischen Eigenschaften von SiO_2 mit Hilfe von klassischen Molekulardynamik(MD)-Simulationen zu verstehen. In MD-Simulationen werden die interatomaren Wechselwirkungen mit effektiven Potentialen modelliert, ohne dabei explizit die elektronischen Freiheitsgrade zu berücksichtigen. In dieser Arbeit wird mittels einer Ab-Initio-Simulationsmethode, der sog. Car-Parrinello-Molekulardynamik (CPMD) [Phys. Rev. Lett. **55**, 2471 (1985)], ein effektives Potentialmodell für SiO_2 parametrisiert. Das resultierende neue Potential wird mit dem sog. BKS-Potential [Phys. Rev. Lett. **64**, 1955 (1990)] verglichen, das in den letzten 10 Jahren in vielen Simulationsstudien zu SiO_2 verwendet wurde.

Als erster Schritt werden CPMD-Simulationen von flüssigem SiO_2 bei 3600 K durchgeführt, um strukturelle Eigenschaften aus der CPMD mit denen resultierend aus dem BKS-Modell zu vergleichen. Das BKS-Modell führt zu einer etwas kleineren Si-O-Bindungslänge und zu einer etwas größeren Si-Si-Bindungslänge. Außerdem werden die Winkelverteilungsfunktionen nicht gut durch das BKS-Modell beschrieben. So finden wir für das BKS-Modell einen mittleren SiOSi-Winkel von 147°, während die CPMD-Simulation einen SiOSi-Winkel von 135° liefert.

Unser Ziel ist es, ein klassisches Born-Mayer/Coulomb-Paarpotential mit den CPMD-Rechnungen zu parametrisieren. Zu diesem Zweck verwenden wir die Kraftanpassungsmethode von Ercolessi und Adams [Europhys. Lett. **26**, 583 (1994)]. Die CPMD-Konfigurationen und die zugehörigen interatomaren Kräfte werden für die Fitprozedur verwendet. MD-Simulationen mit dem resultierenden Potentialmodell führen zu einer Struktur, die sich stärker als im Fall des BKS-Modells von der aus der CPMD-Simulation gewonnenen Struktur unterscheidet.

Deshalb wird ein anderes Fitkriterium auf Grundlage der Paarkorrelationsfunktionen aus der CPMD verwendet. Mit diesem Ansatz erhalten wir eine bessere Übereinstimmung mit den CPMD-Resultaten als mit dem BKS-Modell. Dies gilt in Bezug auf Paarkorrelationsfunktionen, Winkelverteilungen, Strukturfaktoren, Dichte und Druck, sowie die phononische Zustandsdichte. Bei tiefen Temperaturen sind die Selbstdiffusionskonstanten etwa ein Faktor 3 größer als die mit dem BKS-Modell berechneten, allerdings zeigen sie eine ähnliche Temperaturabhängigkeit.

Um die Transferabilität des neuen Potentials zu testen, werden auch Rechnungen an kristallinen Systemen durchgeführt. Die Gleichgewichtsgeometrie als auch die elastischen Konstanten von α-Quarz bei 0 K werden mit dem neuen Potential sehr gut beschrieben, obwohl bei seiner Parametrisierung keinerlei Informationen über kristalline Phasen eingegangen sind.

Wir haben ein neues Paarpotentialpotential für SiO_2 parametrisiert, das eine Verbesserung gegenüber bisherigen Paarpotentialmodellen darstellt. Die Fitmethodologie, die in dieser Arbeit entwickelt wurde, kann auch auf andere netzwerkbildende Systeme angewandt werden, so z.B. Mischungen von SiO_2 mit anderen Oxiden (Al_2O_3, K_2O, Na_2O, etc.).

Development of empirical potentials for amorphous silica

Amorphous silica (SiO_2) is of great importance in geoscience and mineralogy as well as a raw material in glass industry. Its structure is characterized as a disordered continuous network of SiO_4 tetrahedra. Many efforts have been undertaken to understand the microscopic properties of silica by classical molecular dynamics (MD) simulations. In this method the interatomic interactions are modeled by an effective potential that does not take explicitely into account the electronic degrees of freedom. In this work, we propose a new methodology to parameterize such a potential for silica using *ab initio* simulations, namely Car-Parrinello (CP) method [Phys. Rev. Lett. **55**, 2471 (1985)]. The new potential proposed is compared to the BKS potential [Phys. Rev. Lett. **64**, 1955 (1990)] that is considered as the benchmark potential for silica.

First, CP simulations have been performed on a liquid silica sample at 3600 K. The structural features so obtained have been compared to the ones predicted by the classical BKS potential. Regarding the bond lengths the BKS tends to underestimate the Si-O bond whereas the Si-Si bond is overestimated. The inter-tetrahedral angular distribution functions are also not well described by the BKS potential. The corresponding mean value of the $\widehat{\text{SiOSi}}$ angle is found to be $\simeq 147°$, while the CP yields to a $\widehat{\text{SiOSi}}$ angle centered around 135°.

Our aim is to fit a classical Born-Mayer/Coulomb pair potential using *ab initio* calculations. To this end, we use the force-matching method proposed by Ercolessi and Adams [Europhys. Lett. **26**, 583 (1994)]. The CP configurations and their corresponding interatomic forces have been considered for a least square fitting procedure. The classical MD simulations with the resulting potential have lead to a structure that is very different from the CP one.

Therefore, a different fitting criterion based on the CP partial pair correlation functions was applied. Using this approach the resulting potential shows a better agreement with the CP data than the BKS ones: pair correlation functions, angular distribution functions, structure factors, density of states and pressure/density were improved. At low temperature, the diffusion coefficients appear to be three times higher than those predicted by the BKS model, however showing a similar temperature dependence.

Calculations have also been carried out on crystalline samples in order to check the transferability of the potential. The equilibrium geometry as well as the elastic constants of α-quartz at 0 K are well described by our new potential although the crystalline phases have not been considered for the parameterization.

We have developed a new potential for silica which represents an improvement over the pair potentials class proposed so far. Furthermore, the fitting methodology that has been developed in this work can be applied to other network forming systems such as germania as well as mixtures of SiO_2 with other oxides (*e.g.* Al_2O_3, K_2O, Na_2O).

Contents

1 Introduction **1**

2 Simulation methods **9**
2.1 Classical simulations . . . 11
2.1.1 General considerations . . . 11
2.2 Statistical mechanics and MD simulations . . . 12
2.2.1 Algorithm . . . 13
2.2.2 Thermostats . . . 14
2.2.3 Periodic boundary conditions . . . 16
2.2.4 Interaction potential . . . 17
2.2.4.1 Short range interactions . . . 18
2.2.4.2 Long range interactions . . . 22
2.3 *Ab initio* methods . . . 29
2.3.1 The Schrödinger equation . . . 29
2.3.2 The adiabatic approximation . . . 30
2.3.3 Hilbert's space basis set . . . 32
2.3.4 Pseudopotential . . . 34
2.3.5 Solving the Schrödinger equation . . . 35
2.3.5.1 Hartree-Fock approximation . . . 35
2.3.5.2 Density Functional Theory (DFT) . . . 37
2.3.5.3 Choosing the appropriate method . . . 40
2.3.6 *Ab initio* molecular dynamics . . . 40
2.3.6.1 Born-Oppenheimer molecular dynamics . . . 40
2.3.6.2 Car-Parrinello molecular dynamics . . . 40
2.3.6.3 Choosing the appropriate method . . . 42
2.4 Characterization of the samples . . . 42
2.4.1 Structural analysis . . . 42

3 *Ab Initio* simulation **45**
3.1 Parameters calibration: Energies, forces, stresses . . . 46
3.2 Crystalline phases: Pseudo-Potential validation . . . 48
3.2.1 α-quartz . . . 49
3.2.2 β-cristobalite . . . 53
3.2.3 Electronic structure . . . 55

3.3 Liquid silica: Practical aspects . . . 56
3.3.1 Sample generation . . . 57
3.3.2 Thermostats . . . 57
3.4 Liquid silica: Comparison to classical simulation . . . 59
3.4.1 Pair correlation function . . . 59
3.4.2 Angular distribution function . . . 60
3.4.3 Mean squared displacement . . . 62
3.4.4 Pressure . . . 63
3.5 2-body potential approximation . . . 65
3.5.1 Analytical Approach . . . 65
3.5.2 Practical Considerations . . . 66

4 Force-matching procedure **73**
4.1 General fitting approach . . . 75
4.1.1 The ansatz for the potential . . . 75
4.2 Force-matching method . . . 79
4.2.0.1 Practical aspects . . . 80
4.2.0.2 Results . . . 84
4.3 Extended criterion: Stress tensor . . . 87
4.3.1 Practical Aspects . . . 87
4.3.2 Results . . . 89
4.4 Spline potential . . . 93
4.4.1 Practical aspects . . . 93
4.4.2 Results . . . 95

5 Screening potential **99**
5.1 Fitting procedure . . . 100
5.1.1 Practical considerations . . . 100
5.1.2 Results . . . 102
5.2 Liquid silica . . . 107
5.2.1 Static properties: Comparison to the BKS model . . . 109
5.2.2 Dynamic properties: Comparison to the BKS model . . . 113
5.2.3 Thermodynamical properties: Pressure . . . 119
5.3 Crystalline structure . . . 119
5.3.1 Equilibrium geometry . . . 120
5.3.2 Vibrational density of states . . . 121

6 Structural fitting procedure **123**
6.1 Fitting procedure . . . 124
6.1.1 Practical considerations . . . 124
6.1.2 Fitting . . . 129
6.2 Liquid silica . . . 132
6.2.1 Pair correlation functions . . . 132
6.2.2 Angular distribution functions . . . 133

6.2.3 Structure factors 135
6.2.4 Pressure 137
6.3 Dynamic properties 140
6.3.1 Vibrational density of states 140
6.3.2 Diffusion 141
6.4 Crystalline structure 142

Discussion and Conclusions **149**

A Stress tensor **151**
A.1 Virial theorem 151
A.1.1 Demonstration 151
A.2 General expression 154
A.2.1 General definitions 155
A.2.2 Kinetic contribution 156
A.2.3 Potential contribution 156

Chapter 1

Introduction

Silica (SiO_2) is one of the most abundant oxides on the earth's surface. About 95% of the minerals in the earth's crust are silicates, with silica being the basis oxide. Silica is also present in our everyday's life from pane windows to optic fibers and semiconductors. For its abundance and its technological interest silica has been and is still widely and intensively studied.

From a physicochemical point of view, it is interesting to study silica as it has an extremely rich phase diagram, see Fig. 1.1. Moreover silica can undergo a glass transition at a temperature T_g, which occurs when the liquid phase is cooled using a sufficiently rapid quenching rate. This temperature T_g is defined as the temperature for which the viscosity of the system is equal to 10^{13} Poise[1].

It is also worthwhile to study silica as it may be considered as a prototype for glass formers exhibiting a network structure. In the low pressure domain, all the crystalline allotropic forms as well as liquid and vitreous silica are composed of corner sharing SiO_4 tetrahedra, see Fig. (1.2). Moreover the Si-O bond is considered being half covalent and half ionic according to Pauling [114, 115] which accounts for the stiffness of the network. For these reasons there has been intense interest in studying the structural and dynamical properties of the liquid and the glass.

From a geological point of view the abundance of silica in the earth's mantle implies that its response to extreme conditions of temperature and pressure has a great importance for constructing valuable geophysical models of the earth's interior. Unfortunately investigating experimentally silica at extreme conditions is hard to achieve. Because of its high melting temperature ($\simeq$ 2000K) and of its tendency to evaporate above $T = 2143$K at ambient pressure, silica can hardly be investigated in laboratories [104, 132]. Fortunately, the general framework of thermodynamics, classical and quantum mechanics combined to the increasing power of computers allow one to carry out realistic and predictive simulations for different kinds of materials and for different length/time scales.

Quantum mechanics is the most relevant approach for understanding matter at the small length scale as it gives full access to the microscopic structural details. Nevertheless, because of the many-body problem it is not possible to solve directly the

[1] 10^{13} Poise= 10^{12} Pa.s

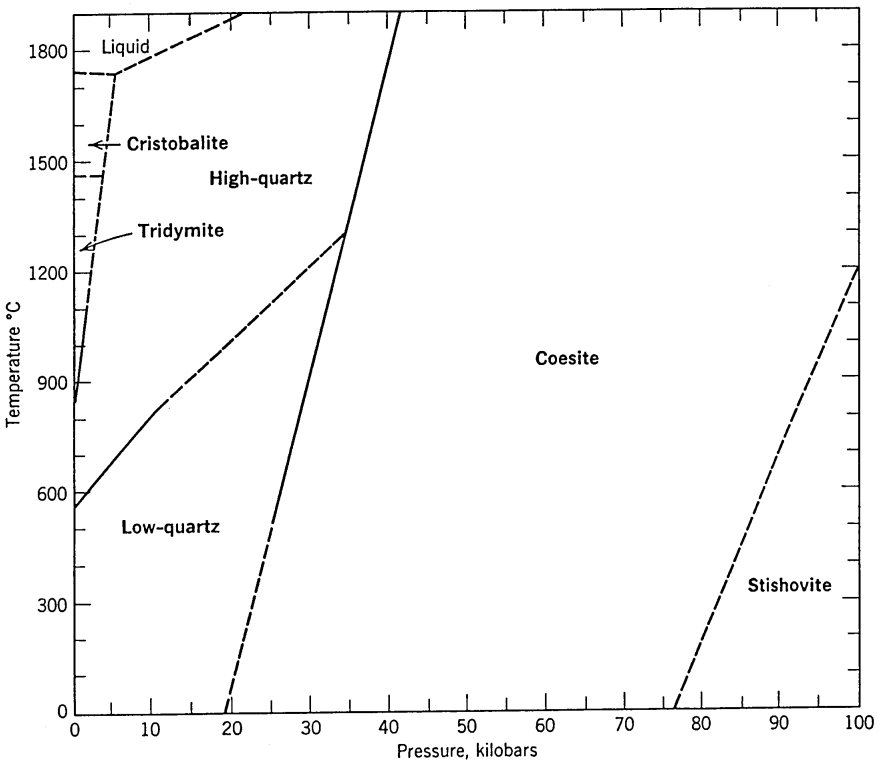

Figure 1.1: Phase diagram of silica [83].

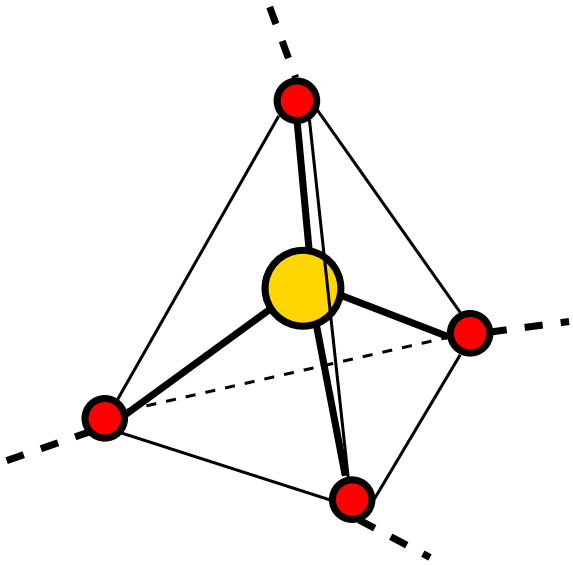

Figure 1.2: Sketch of a SiO_4 tetrahedra, the silicon atom is represented in yellow, the surrounding oxygen atoms are represented in red.

Schrödinger equation that describes the space- and time-dependence of quantum mechanical systems. Approximations as well as numerical algorithms have been proposed to circumvent the many-body problems. However even the efficient Density Functional Theory (DFT) method [72, 84] which describes the electrons of a system at the quantum level with a minimum of calculation coupled to the efficient Car-Parrinello method [25] used for describing the time evolution of the wavefunction are too complex for the studies of systems containing more than 200 atoms and for intermediate and long time scales ($t > 30$ ps [2]).

The quantum mechanics can be related to the classical one through the Ehrenfest's theorem [45]. Microscopic systems can be accurately described by means of classical mechanics, provided that the length scale of the particles considered are compatible with the typical length scale of the system (bond length, volume per particle, *etc...*). Depending on their spatial extent, called the de Broglie wavelength[3] [166] λ_T, the atoms can be described using either the quantum or the classical equations of motion. This length is the typical distance over which the precise location of a particle remains uncertain due to Heisenberg's principle. When λ_T is small compared to any relevant length scale of the system (bond length), the quantum nature of fluctuations can be ignored [29]. For silicon and oxygen atoms at 300K the de Broglie wavelengths are equal to 0.19Å and 0.25Å, respectively whereas the Si-O bond length in silica is equal to 1.6Å. According to these statements the framework of classical mechanics can be considered valid for describing SiO_2 at the atomic level. A classical mechanics approach requires the definition of a potential energy function, which describes the interactions between the particles. These potentials are also called force fields by chemists and biologists.

Constructing such potential involves two steps. Firstly an analytical form has to be assumed for the potential which depends explicitely on the degrees of freedom of the system under consideration (particle's positions, dipoles, angles, dihedral angles, *etc...*). Secondly one has to propose an actual parameterization for the functions that constitute the analytical form previously chosen. These potentials can be classified in two main classes according to the type of data retained for their parameterization. Some researchers have parameterized their potentials considering experimental data. On the contrary, some other people have fitted potentials using only *first-principle* data.

In this work we aim to propose a new and simple effective potential for describing liquid silica. The new potential should satisfy the following conditions:

- The potential should have a simple analytical form so as to allow the studies of large systems ($>$ 10000 particles) for time scales of the order of $1 - 100$ nanoseconds[4].

[2] 1 picosecond = 10^{-12} second

[3] According to the Boltzmann distribution $p = \sqrt{2\pi m k_B T}$ where T is the temperature, m is the mass of the particle, k_B is the Boltzmann constant and p is the mean momentum of the particle. The wavelength of a particle is given by the de Broglie relation $\lambda_T = \frac{h}{p}$. Consequently the wavelength of a particle can be defined as a function of the temperature $\lambda_T = \frac{h}{\sqrt{2\pi m k_B T}}$.

[4] 1 nanosecond = 10^{-9} second.

- The force-field should be parameterized using *ab initio* data following the force-matching procedure of Ercolessi and Adams [46] in order to have a good description of the microscopic interactions.

- We should provide a general methodology for deriving effective potentials from Car-Parrinello simulations. This methodology should be flexible enough to include the contribution of other species to silica into the potential. These species can be network modifiers like potassium, or sodium ions that enter generally in the composition of industrial glasses.

Before describing this methodology let us briefly recall the main advances made in this topic during the last thirty years. The first effective potential for silica has been proposed in 1976 in the pioneering work by Woodcock *et al.* [160]. This first potential is a pair potential for the liquid phase having a Born-Mayer-Huggins form:

$$V_{\mathrm{BM}}(r_{ij}) = \frac{q_i q_j}{r_{ij}} + A_{ij} \exp\left(-b_{ij} r_{ij}\right) - \frac{c_{ij}}{r_{ij}^6}, \tag{1.1}$$

where r_{ij} stands for the interatomic distance between atoms i and j, while the parameters q_i, q_j, A_{ij}, b_{ij} and c_{ij} were chosen with "little expectation of success" according to Woodcock *et al.* [160]. The silicon and oxygen charges in silica were considered to be similar to their ionic charges in contradiction with the well known semi-ionic nature of the silicon and oxygen atoms in silica [114, 115]. The typical atomic radius ($\propto b_{ij}^{-1}$) for the silicon and oxygen have been set *arbitrarily* equal to the ones of beryllium and fluorine respectively. Nevertheless this first attempt gave results which were qualitatively in good agreement with recent simulations. The parameters of this potential have been re-used for a different ansatz by Soules [136]. Interactions with some additional ions have been included in this new potential. The parameterization of this model is still debatable, as no methodological approach has been proposed for fitting the extra parameters. Thereafter this potential has also been modified by Feuston *et al.* [50] by including some angular terms [138], the parameterization was still controversial as the angular parameters were chosen to favor a perfect SiO_4 tetrahedral geometry. Later, another group [130] proposed an empirical potential suited for the study of α-quartz (see Fig. 1.3). This potential was fitted so as to reproduce as close as possible the experimental data such as structural features and dielectric and elastic properties for quartz. The fittings were now carried out using least square procedures requiring minimization algorithms. Unfortunately this potential was solely designed for the crystalline structure as the $\widehat{\mathrm{OSiO}}$ angles of the SiO_4 tetrahedra were enforced to stay close to their ideal values (109° 28"). Nevertheless, this potential gives predictive results for α-quartz. Another potential has also been proposed for perovskite ($MgSiO_3$) [100, 101] using the same fitting methodology.

Some promising steps have been made in the works of Lasaga [88] and Tsuneyuki [149]. This time the Born-Mayer parameters are fitted with a view to reproducing first-principles descriptions rather than experimental data. The quantum systems under consideration were made of single molecules of orthosilicic acid ($Si(OH)_4$) and orthosilicate ions (SiO_4^-) described using *ab initio* simulations. The structure of α-quartz

and β-cristobalite were found in fairly good agreement [88, 149] with the experimental results. The Tsuneyuki and Lasaga potentials were promising considering the nature of the system used for their fits. The Tsuneyuki potential (also called TTAM potential) has been also used by Chelikowsky and coworkers [30], who have included to the TTAM potential the potential ansatz of Lasaga and Gibbs [88] for the description of the angular dependent terms. The angular dependent terms have been modified using some new parameters. Their aim was to reproduce the experimental dependence of the $\widehat{\mathrm{OSiO}}$ angle in α-quartz with respect to the pressure. The angular parameters were very different from the one proposed by Lasaga [88], underlining the high sensitivity of the interdependency of each parameters with respect to the others.

The BKS potential [9] has partially used the fitting methodology of Lasaga and Gibbs [88] and Tsuneyuki *et al.* [149]. The goal here was to propose a potential based upon microscopic basis for the nearest-neighbor interactions. The system chosen for the fit was still a single molecule of orthosilicic acid. As the range of the interatomic forces goes beyond nearest neighbors some complementary informations have been considered in the fit using some macroscopic data that can be derived from microscopic considerations such as elastic constants. This simple potential reproduces with accuracy the structure and elastic constants of α-quartz [9, 109] and was shown to give predictive results (structure, phonons, phases transition) for the liquid phase of silica [75, 153]. Thereafter the BKS potential has been extended to other species (aluminum, phosphorus, sodium and chlorine) by using the methodology previously proposed for pure silica [85]. This extended potential was designed for the study of zeolites[5]. Later, the same group proposed empirical force-fields using a somewhat different ansatz (called BJS potential) including some dipolar terms [17, 18]. This potential was solely based on quantum considerations made on single molecules of silicic acid and pyrosilicic acid $(\mathrm{HO})_3\mathrm{SiOSi(OH)}_3$. Using this potential the stability of different crystalline phases have been checked together with the potentials proposed in Ref. [9, 79, 149]. Even if some minerals studied in their work such as Lovdarite [105] and VPI-7 [4] were not properly described by the BKS potential [9] it appears to be superior to the BJS potential.

Lately force fields with environment dependent atomic charge distributions have been developed. With the increase of the computer capabilities recent potentials became more and more complex including many body effects and requiring on the fly minimization procedure. The Polarizable Ion Model (PIM) potential proposed by Wilson and Madden [155, 156] takes into account the distortion of the electronic cloud surrounding atoms due to their environment. For this purpose eighteen additional degrees of freedom are associated to anions (oxygen atoms). These degrees of freedom are associated to five groups of variables which describe electrostatic dipoles, quadrupoles, and ionic distortions of monopolar, dipolar and quadrupolar symmetry. The time evolution of these degrees of freedom is carried out using an extended Lagrangian. In practice such a potential is not suitable for simulating big systems on long time scales. Moreover the PIM potential has not been optimally fitted, as the pair interactions have been taken from the old potential proposed by Woodcock *et al.* [160]. Demiralp *et al.*

[5]Zeolites are minerals that have a micro-porous structure

[35] also proposed a charge variable potential parameterized using empirical data relative to crystalline phases. However this potential has to be considered with attention since the results presented in Ref. [35] have not been reproduced in a later work [68].

Recently a new potential ansatz which attempts to describe all the polarizability effects that may intervene in ionic system has been proposed by Tangney *et al.* [144]. The data considered for the parameterization of this potential have been derived from *ab initio* simulation of liquid silica. The *ab initio* potential energy surface as well as the *ab initio* forces have been used as an input to the fitting procedure according to the considerations made by Ercolessi [46]. Despite some promising results [68, 92, 144] this potential is not convenient for studying glassy systems as it appears that simulations with this potential are a factor 100 slower than those with the BKS potential [67].

More complete details corresponding to the aforementioned potentials as well as some others force-fields can be found in the Refs. [9, 16, 17, 18, 30, 35, 41, 50, 51, 66, 70, 79, 85, 86, 88, 100, 101, 130, 133, 134, 136, 144, 149, 152, 155, 156, 160].

This overview of the previous works carried out on silica underlines the very high interest of the scientific community toward the physics of silica.

The present document is organized as follows: in chapter 2 the classical and quantum molecular dynamics techniques and algorithms used in the present simulations will be presented. The following chapter 3 will be concerned with the *ab initio* simulations made on liquid silica. These simulations are absolutely compulsory for fitting an empirical potential based on microscopic considerations. In preamble to this tests on α-quartz and β-cristobalite have been carried out to validate our *ab initio* approach. In chapter 4 we shall present the results of the first parameterizations done using the atomic forces issued from the first-principles simulations. These potentials are checked by classical molecular dynamics simulations and compared to the BKS potential [9]. A way of circumventing the time consuming Ewald summation systematically used for describing ionic and semi-ionic system is presented in chapter 5. Chapter 6 focuses on a new approach for fitting an effective potential which fitted observables are the pair correlation functions used for characterizing the structure of amorphous systems. This potential is compared to the widely used BKS potential [9] and to the available experimental results. The conclusion will expose the main advances we have proposed in this field as well as some perspectives.

Figure 1.3: α-quartz crystal, this mineral comprises 12.0% of the crust of the earth by volume.

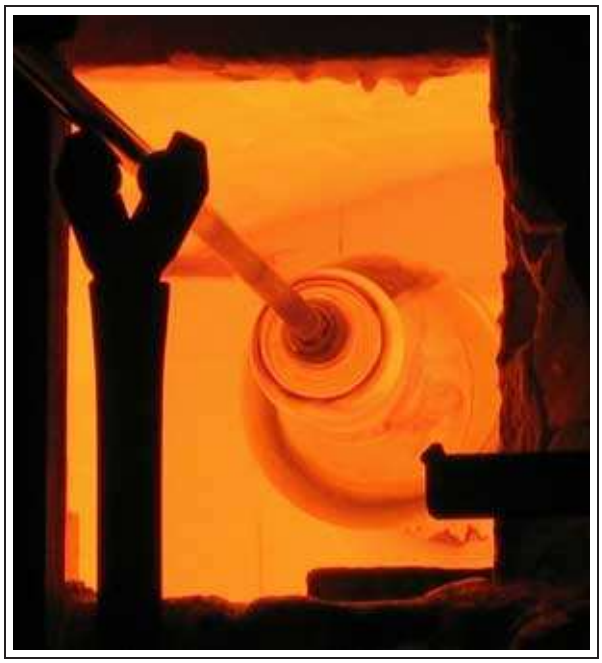

Figure 1.4: Molten silica being processed in a glass-work.

Chapter 2

Simulation methods

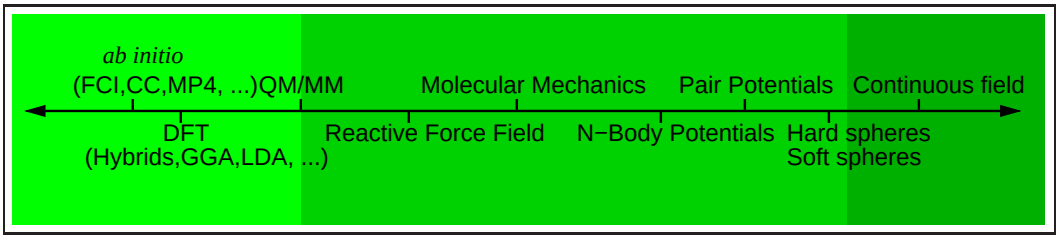

Figure 2.1: Simulation methods classified from the most complex ones (left side) suited for small system/time length to the simplest ones (right side) suited for large system/time length.

In this thesis we aim at investigating the properties of silica at the microscopic scale using computer simulations. For this purpose, lots of different approaches can be used, see Fig. 2.1. The choice of the simulation method depends on three main factors: The level of accuracy of the description, the efficiency of the algorithms compared to the number of particles under consideration, and the nature of the observables one wants to investigate. The most quantitative approaches take into account the electronic degrees of freedom using quantum mechanics descriptions. These approaches are often called first-principles or *ab initio* methods. Among this class of method one can distinguish two main currents based upon different hypothesis. On the one hand there is the Hartree-Fock theory represented by the full configuration interaction (FCI), coupled cluster (CC), *etc*, see left part of Fig. 2.1.

On the other hand, one has the Density Functional Theory (DFT) [72, 84], that can also be used with different levels of accuracy namely: Hybrid functionals, General Gradient Approximation (GGA) or Local Density Approximation (LDA). Because of the complex nature of the interactions these methods can be only used on relatively small time and length scales since they are very time consuming.

To circumvent the CPU time issue some intermediate levels of approximation have been proposed, see right part of Fig. 2.1. These methods describe the interactions between the atoms on a classical effective level, and thereby, different simplifications

can be distinguished. Chemical reactions involving transformations of molecular species can be described using reactive force fields [43, 110, 139, 140]. Bonds, angular and dihedral interactions in molecules can explicitely be reproduced by means of molecular mechanics potentials, metallic interactions using N-body potentials, and very simple systems can be quantitatively simulated using pair potentials[1].

The characteristics of materials are given within specific thermodynamical conditions, and so we also need to define the thermodynamical ensembles NVE, NVT, *etc...* as well as the state variables we want to investigate. Classes of computational algorithms for simulating the behavior of various thermodynamical systems have been developed for this purpose (Monte Carlo and Molecular Dynamics). In this chapter we will introduce the concept of Molecular Dynamics (MD).

[1]Due to their simplicity, pair potentials are often used for the description of strong glass formers.

2.1 Classical simulations

Within the framework of classical simulations, the electronic degrees of freedom are no longer explicitely taken into account. The energy and the forces of a system are now described by the means of effective interactions between atoms. These effective interactions try to reproduce at best the relevant microscopic properties (screening of ionic charges, polarization effects, directional bonding, etc ...). The nuclei are considered as point particles and the equations of motion are integrated using the principles of classical mechanics. In spite of these crude assumptions, this approach represents an excellent approximation for a wide range of materials and is routinely used for investigating relatively big systems ($N \simeq 10^3 - 10^6$ atoms) on relatively large time scales ($\tau \simeq 1$ ns- 1 μs).

2.1.1 General considerations

Equations of motion As already stated in the introduction of this chapter we want to investigate the static and dynamical features of silica. Consequently we have to compute the time dependence of given number of observables. Moreover, we want to lie at the microscopic scale, this means that for a N particles system we have to solve explicitely the $3N$ coupled 2^{nd}-order differential equations describing the time dependence of the particle's motion according to Newton's laws:

$$\frac{d\mathbf{p}_i}{dt} = \mathbf{F}_i, \quad i \in \{1, \ldots, N\} \tag{2.1}$$

where $\mathbf{F}_i$ is the total force applied on particle i, m_i is the mass of the particle i while $\mathbf{r}_i$ and $\mathbf{p}_i$ stands for the position and momentum of particle i, respectively. The velocities and forces are respectively defined by:

$$\mathbf{v}_i(t) = \frac{d\mathbf{r}_i(t)}{dt} \tag{2.2}$$

$$\mathbf{p}_i(t) = m_i \mathbf{v}_i(t) \tag{2.3}$$

$$\mathbf{F}_i(t) = -\nabla_i V(\{\mathbf{r}_j(t)\}) \tag{2.4}$$

here $V(\{\mathbf{r}_i\})$ stands for the interatomic potential.

When considering isolated systems[2] the direct integration of Eq. (2.1) leads to the conservation of the total energy $E_{\text{tot.}}$:

$$E_{\text{tot.}} = E_{\text{kin.}} + E_{\text{pot.}} \tag{2.5}$$

$$E_{\text{kin.}} = \frac{1}{2} \sum_i m_i \mathbf{v}_i^2 \tag{2.6}$$

$$E_{\text{pot.}} = V(\{\mathbf{r}_i\}) \tag{2.7}$$

in Eqs. (2.6) and (2.7), $E_{\text{kin.}}$ and $E_{\text{pot.}}$ refer to the kinetic and to the potential part of the total energy, respectively.

[2] A isolated system has no interaction with an outside system, not even energy can flow into or out of an isolated system.

2.2 Statistical mechanics and MD simulations

Ensemble The ergodic hypothesis[3] states that for an isolated system of total energy $E_{\text{tot.}} = E$, the time average of any quantity $\mathcal{A}(\{\mathbf{r}_i, \mathbf{p}_i\}_{t=0}, t)$ at time t, defined at $t = 0$ by the particles position and momentum $\{\mathbf{r}_i, \mathbf{p}_i\}_{t=0}$, is equivalent to the ensemble average of this quantity:

$$\lim_{t\to\infty} \frac{1}{t} \int_0^t dt' \mathcal{A}(\{\mathbf{r}_i, \mathbf{p}_i\}_{t=0}, t') = \frac{\int\int d\mathbf{r}_i d\mathbf{p}_i \mathcal{A}(\{\mathbf{r}_i, \mathbf{p}_i\}_{t=0}, 0)\delta\left[E - E_{\text{tot.}}(\{\mathbf{r}_i, \mathbf{p}_i\}_{t=0})\right]}{\int\int d\mathbf{r}_i d\mathbf{p}_i \delta\left[E - E_{\text{tot.}}(\{\mathbf{r}_i, \mathbf{p}_i\}_{t=0})\right]}. \tag{2.8}$$

According to this statement one can study the average behavior of a many-particle system by computing the time evolution of that system and averaging the quantity of interest over a sufficiently long time. The ensemble of configurations spanned by the integrals in the left hand of Eq. (2.8) consists of copies of the isolated system under consideration. Each identical system in the ensemble has a common fixed total energy E expressed by the Dirac function in Eq. (2.8), but different coordinates $\{\mathbf{r}_i, \mathbf{p}_i\}$ in the phase space (*i.e.* different microstates). Such an ensemble is referred as microcanonical ensemble, or NVE ensemble. The framework of molecular dynamics is particularly suited for the investigation of microcanonical ensembles. Nonetheless, some methods have been developed in order to sample different ensembles such as the canonical ensemble (NVT). These approaches are introduced in section 2.2.2.

State variable The thermodynamic state of a system can be characterized by its state variables. Some usual state variables such as the volume and the number of particles are directly accessible in molecular dynamics as the number of particles is constant and the volume is simply defined by the dimensions of the box. Some others variables need to be defined such as the instantaneous temperature or pressure.

The definition of the instantaneous temperature $T(t)$ is:

$$T(t) = \sum_{i=1}^{N} \frac{m_i \mathbf{v}_i^2(t)}{k_B N_f}, \qquad N_f = 3N - 3 \tag{2.9}$$

where k_B is the Boltzmann constant, N represents the number of particles, and N_f is the number of degrees of freedom.

An instantaneous pressure for pairwise additive interactions is given by the virial theorem:

$$P(t) = \frac{N k_B T(t)}{V} + \frac{1}{3V} \sum_{i<j} \mathbf{F}(\mathbf{r}_{ij}) \cdot \mathbf{r}_{ij}. \tag{2.10}$$

The above relation is derived in Appendix A.

[3]The ergodic hypothesis is valid for systems at equilibrium (liquids, crystals), not for vitreous phases.

2.2.1 Algorithm

The integration of the equations of motion performed at a microscopic level is called molecular dynamics simulation. As most of the time it is not possible to solve analytically the coupled equations of motion one has to use numerical algorithms called integrators. To achieve these integrations it is necessary to discretize time using a time step δt. A good integrator has to fulfill few basic conditions:

- Conciliates large time step and simple formulation for efficiency purpose;
- Preserve the mechanical constraints (conservation laws);
- Being time-reversible[4] and preserving the phase space volume according to the Liouville theorem[5].

Among these classes of well-behaved algorithms the most widespread one is the velocity Verlet algorithm. This algorithm is based on a Taylor expansion of the positions of particles with respect to time:

$$\mathbf{r}_i(t+\delta t) = \mathbf{r}_i(t) + \mathbf{v}_i(t)\delta t + \frac{\mathbf{F}_i(t)}{2m_i}\delta t^2 \tag{2.11}$$

$$\mathbf{F}_i(t+\delta t) = \mathbf{F}_i(\mathbf{r}_i(t+\delta t)) \tag{2.12}$$

$$\mathbf{v}_i(t+\delta t) = \mathbf{v}_i(t) + \frac{\mathbf{F}_i(t+\delta t) + \mathbf{F}_i(t)}{2m_i}\delta t. \tag{2.13}$$

The corresponding error for both positions and velocities is of order $\mathcal{O}(\delta t^4)$, moreover to achieve the integration of the equation of motions one needs to assume that time is discretized in interval δt. These approximations are responsible for the non-exact conservation of the total energy. In practice, during a MD simulation the total energy fluctuates around a given value. According to the results of previous simulations the relative fluctuations of the energy should be limited below the limit $\Delta E_{\text{tot.}}/E_{\text{tot.}} < 10^{-5}$, this value was shown to be convenient for a proper integration of the equation of motions [1].

The time step δt used for the integration has to be carefully chosen. It should be as large as possible to avoid any waste of computational time. But if the time step is too large energy conservation is not guaranteed. Regarding the velocity Verlet algorithm, an optimal compromise can be found according to that fluctuations of the total energy $\sigma^2_{E_{\text{tot.}}} = \langle E^2_{\text{tot.}}\rangle - \langle E_{\text{tot.}}\rangle^2$ scales like δt^2 [1], see Fig. 2.2. In the context of this work we have considered a time step of 1.6 fs which was small enough to guarantee a negligible drift of the total energy for high (T= 6100 K) and intermediate temperatures (T= 2750 K) compared to the experimental melting point of pure silica ($T_{\text{melt}} \simeq 2000$ K).

[4] As equations of motion of classical mechanics are time-reversible.

[5] The Liouville's theorem states that if the distribution of microstates is uniform in phase space initially, they will remain so at all times.

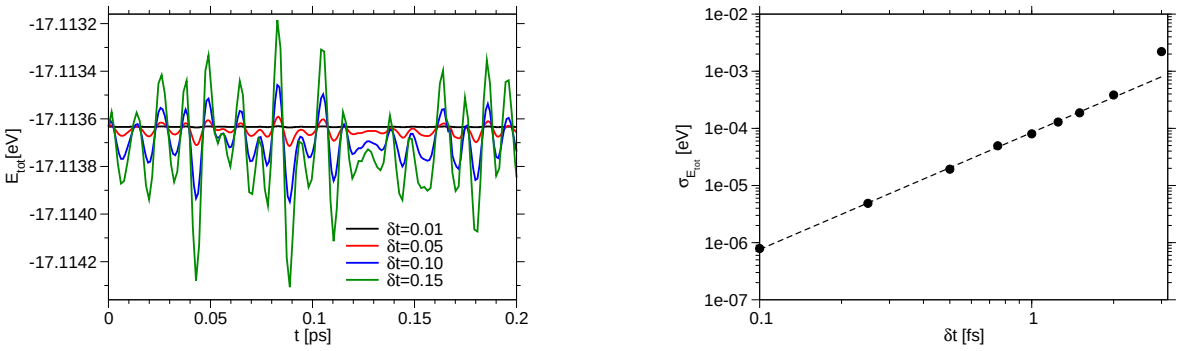

Figure 2.2: Left panel: The time dependence of the total energy represented for different time steps for a 1152 atoms sample at 6100K. Right panel: The standard deviation of the total energy $\sigma^2_{E_{\text{tot.}}} = \langle E^2_{\text{tot.}} \rangle - \langle E_{\text{tot.}} \rangle^2$ as a function of the time step δt, the averaged fluctuations scale like δt^2 for time step up to 2 fs. The dotted line correspond to the quadratic regression $\sigma_{E_{\text{tot.}}} \propto \delta t^2$

2.2.2 Thermostats

The natural ensemble in MD simulations is the microcanonical ensemble. Nevertheless, it is possible to realize simulations in other ensembles such as canonical ensemble using appropriate algorithms. From a statistical point of view, a canonical ensemble consists of copies of closed systems[6]. These systems are coupled to an external heat bath that impose its temperature T. In practice we can bring a system to the target temperature using thermostats. In this work two different kinds of thermostats have been used, the Andersen thermostat and the Nosé-Hoover thermostat.

Andersen thermostat With this method the velocities and so the momenta $\mathbf{p}_i$ of the particles are modified randomly according to a Maxwell-Boltzmann distribution law $P(\mathbf{p}_i)$:

$$P(\mathbf{p}_i) = \left(\frac{\beta}{2\pi m_i}\right)^{3/2} \exp\left[-\beta \mathbf{p}_i^2 / 2m_i\right], \quad \text{with} \quad \beta = \frac{1}{k_B T}. \tag{2.14}$$

The new momenta have to fulfill an additional constraint: The total momentum of the system has to be zero. A direct consequence of this distribution is that the translational kinetic energy per particle satisfies the equipartition theorem, $k_B T = m_i \langle \mathbf{v}_i^2 \rangle$. The strength of the coupling is determined by the frequency $w_{\text{therm.}} = 1/\Delta t$ of the connection to the "heat bath". A constant-temperature simulation now consists of the following steps:

1. Start with an initial set of positions and momenta $\{\mathbf{r}_i, \mathbf{p}_i\}_{t=t_n}$ and integrate the equations of motion for a time $t_{n+1} = t_n + \Delta t$;

2. All the particles undergo a collision with the heat bath;

[6]Closed system: Can interchange energy and mechanical work with surroundings but not matter.

3. As the total momentum $\mathbf{P}_{\text{tot.}} = \sum_i m_i \mathbf{v}_i$ is not null the N velocities $\mathbf{v}_i$ must be shifted:
$$\mathbf{v}_i := \mathbf{v}_i - \frac{\mathbf{P}_{\text{tot.}}}{N m_i} \tag{2.15}$$

4. The N velocities are rescaled to the target temperature according to equation (2.9):
$$\mathbf{v}_i := \alpha \mathbf{v}_i, \quad \text{with,} \quad \alpha = \sqrt{\frac{k_B T N}{\sum_i m_i \mathbf{v}_i^2}}. \tag{2.16}$$

Nosé-Hoover thermostat The approach of Nosé [112] is based on the use of an extended Lagrangian. In this method an extra coordinate ν is introduced. This coordinate can be interpreted as a scaling factor of the time step (in the following, the real time of the simulation is denoted by t' and the virtual time variable by t). According to this definition the real and virtual momenta and coordinates are given by:

$$\mathbf{r}_i' = \mathbf{r}_i \tag{2.17}$$
$$\mathbf{p}_i' = \mathbf{p}_i/\nu \tag{2.18}$$
$$\nu' = \nu \tag{2.19}$$
$$t' = t/\nu. \tag{2.20}$$

In order to tune the overall kinetic energy, and consequently the temperature, of the system on-the-fly, the coordinate ν has to be coupled into the equations of motion. The Lagrangian of the extended system proposed by Nosé is:

$$\mathcal{L}_{\text{Nosé}} = \sum_i \frac{1}{2} m_i \nu^2 \dot{\mathbf{r}}_i^2 - V(\{\mathbf{r}_i\}) + \frac{1}{2} Q \dot{\nu}^2 - \frac{s}{\beta} \ln \nu \tag{2.21}$$

where Q is an effective "mass" associated to ν, and s corresponds to the number of degree of freedom of the system considered. The corresponding Hamiltonian is [112]:

$$\mathcal{H}_{\text{Nosé}} = \sum_i \frac{\mathbf{p}_i^2}{2 m_i \nu^2} + V(\{\mathbf{r}_i\}) + \frac{p_\nu^2}{2Q} + \frac{s}{\beta} \ln \nu \tag{2.22}$$

The system described by this equation is microcanonical and its partition function can be written:

$$\Omega(E) = \int \Pi_{i=1}^N \mathbf{dp}_i \mathbf{dr}_i dp_\nu d\nu \delta \left[\mathcal{H}_{\text{Nosé}}(\{\mathbf{r}_i, \mathbf{p}_i\}, p_\nu, \nu) - E\right] \tag{2.23}$$
$$= C \int \Pi_{i=1}^N \mathbf{dp}_i' \mathbf{dr}_i \exp\left[-\frac{3N+1}{s} \beta \mathcal{H}(\{\mathbf{r}_i, \mathbf{p}_i'\})\right] \tag{2.24}$$

where C is a normalization constant, in the above equations, we have used the "real" momentum $\mathbf{p}_i' = \mathbf{p}_i/\nu$ and introduced $\mathcal{H}$, the Hamiltonian of the real system:

$$\mathcal{H}(\{\mathbf{r}_i, \mathbf{p}_i'\}) = \sum_i \frac{\mathbf{p}_i'^2}{2 m_i} + V(\{\mathbf{r}_i\}). \tag{2.25}$$

The corresponding Nosé equations of motion are given by:

$$\frac{d\mathbf{r}'_i}{dt'} = \frac{\mathbf{p}'_i}{m_i} \tag{2.26}$$

$$\frac{d\mathbf{p}'_i}{dt'} = -\frac{\partial V}{\partial \mathbf{r}'_i} - p'_\nu \nu' \mathbf{p}'_i / Q \tag{2.27}$$

$$\frac{1}{\nu'}\frac{d\nu'}{dt'} = p'_\nu \nu' / Q \tag{2.28}$$

$$\frac{d\left(\nu' p'_\nu / Q\right)}{dt'} = \left(\sum_i \frac{\mathbf{p}'^2_i}{m_i} - s k_B T\right) / Q \tag{2.29}$$

According to an original idea proposed by Hoover [73] the above equations can be expressed in a more convenient way by introducing the following notations: $\xi = \ln \nu$ and $p_\xi = \nu p_\nu$. Moreover, if one sets $s = 3N$, the equations of motion (2.26-2.29) using the real variables (here the primed notations have been left out) become:

$$\frac{d\mathbf{r}_i}{dt} = \frac{\mathbf{p}_i}{m_i} \tag{2.30}$$

$$\frac{d\mathbf{p}_i}{dt} = -\frac{\partial V}{\partial \mathbf{r}_i} - p_\xi \mathbf{p}_i / Q \tag{2.31}$$

$$\frac{dp_\xi}{dt} = \sum_i \frac{\mathbf{p}_i^2}{m_i} - 3N k_B T \tag{2.32}$$

$$\frac{d\xi}{dt} = p_\xi / Q. \tag{2.33}$$

If the instantaneous temperature of the system is above/below the temperature T imposed by the thermostat, the momentum p_ξ increases/decreases, see Eq. (2.32). The momentum p_ξ is connected to the time evolution of momenta $\mathbf{p}_i$ by means of a friction term $p_\xi \mathbf{p}_i / Q$, see Eq. (2.31). If the instantaneous temperature is far from the target temperature the momentum p_ξ will regulate the magnitude of the friction terms, thus, the temperature of the system is controlled. The frequency of the thermostat should be chosen as some characteristic frequency of the system ω, for which one wishes to insure a maximal coupling between particles and thermostat [97]. To achieve this, the mass of the thermostat should be set according to the relation: $Q \sim 3N k_B T / \omega^2$.

2.2.3 Periodic boundary conditions

It is obvious that one can only study a system having a limited number of particles using computer simulations. The particles are contained in a finite cell having a specific geometry. Most of the properties of a homogeneous macroscopic system are considered to be independent of the interfaces. For example if one considers the energy of a macroscopic system, the neglect of the surface energy is in fact an good approximation as the corresponding error made by neglecting the surface energy is insignificant. The ratio of the surface energy to bulk energy is proportional to $N^{-1/3}$, which is negligible

for a macroscopic system made of $N \simeq 10^{24}$. On the contrary in MD simulations one can simulate systems made of $N < 10^7$ atoms, the influence of the surface is still significant for these scales, consequently computer simulations have to deal with finite size effects [7]. In order to simulate bulk phases it may be crucial to choose periodic boundary conditions (PBC) that mimic the presence of an infinite bulk surrounding our N-particle system, *i.e.* the original system is surrounded by its replicas according to the initial cell geometry, see Fig. 2.3. If a particle leaves the central cell for the left one, it will be immediately replaced by an atom coming from the right cell, thus the system does not feel any wall or vacuum area. Moreover this method preserve the conservation of the total energy and so the total momentum. Nevertheless special care have to be taken, since for example, the total energy of the system is not rotationally invariant[8] as shown in Fig. 2.3. The use of PBC has a direct consequence on the properties investigated. In practice particles may interact with their own replicas, in such case one has to carefully assess the relevance of the properties of the system investigated. For example the normal modes having wavelengths greater or equal to the cell size are meaningless, this feature is described in more details in section (3.2.1).

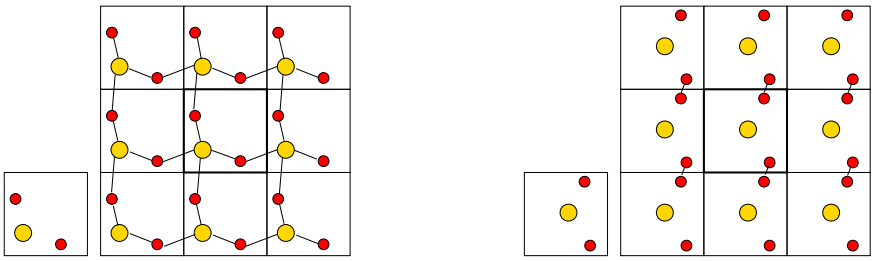

Figure 2.3: Left panel: The original pattern and the replicated system revealing a tetrahedral network, silicon (yellow) atoms surrounded by oxygens (red) atoms. Right panel: Similar pattern compared to the left panel rotated and duplicated, here the tetrahedral network is totally broken pointing out the rotational dependence of the energy.

2.2.4 Interaction potential

Interaction potentials are the keystone of any molecular dynamics simulation as by their means one can probe the phase space through the resolution of the equations of motion. According to this point of view they hold all the structural and thermodynamical informations of a system.

Formally, one can decompose the potential energy into different contributions:

$$V = \sum_i V_1(\mathbf{r}_i) + \frac{1}{2!}\sum_{i,j\neq i} V_2(\{\mathbf{r}_{ij}\}) + \frac{1}{3!}\sum_{i,j\neq i,k\neq i,j} V_3(\{\mathbf{r}_{ij},\mathbf{r}_{ik}\}) + \dots \tag{2.34}$$

[7] To a system having N particles within a box of volume V with a corresponding density $\rho = N/V$ one can associate a typical length $L \propto N^{1/3}$ as $N = \rho V$ and $V \propto L^3$, the Surface/Volume ratio scales like $N^{-1/3}$. For a cubic system made of 10^6 atoms this ratio is equal to 6%.

[8] The angular momentum is not constant

The first contribution corresponds to the self energy of the system which is assumed to be zero by convention. Higher order interactions ($V_n, n > 3$) are hardly tractable and the computational time required for the computation of the energy and forces can be prohibitive[9]. For this reason, in the next section, we will mainly expose technical and practical details related to pair interactions.

2.2.4.1 Short range interactions

A short range term is usually defined as one in which the spatial interaction falls off faster than r^{-d}, where d is the dimensionality of the system [1]. For ionic compounds the most common choice is the Buckingham/Born-Mayer potential [22]:

$$V_{\mathrm{BM}}(r_{ij}) = A_{ij} \exp\left(-b_{ij} r_{ij}\right) - \frac{c_{ij}}{r_{ij}^6} \tag{2.35}$$

where r_{ij} stands for the interatomic distance between two particles i and j, and A_{ij}, b_{ij}, c_{ij} are the parameters of the potential. When using such potential, only the closest j-particles surrounding the particle i are required for an accurate computation of the energy and forces applied on i. The influence of the other particles can be dropped out providing only very slight changes in the physical description of the system[10]. In practice, one has to define a cutoff distance r_{cut} which is consistent with the energy conservation and computation efficiency constraints. Interatomic distances beyond this limit are not considered.

Sometimes, the cutoff radius r_{cut} may be larger than the simulation cell, in such case atoms replicas have to be taken into account, see Fig. 2.4. In particular, this is a crucial issue for crystalline structures properties, where the energy is expressed as a sum over the lattice vectors $(\mathbf{a}, \mathbf{b}, \mathbf{c})$. The total energy of the system is expressed:

$$V = \sum_{\ell,m,n} {\sum_{i,j}}' \frac{1}{2!} V_2^{\mathrm{trunc}}(\mathbf{r}_{ij} + \ell\mathbf{a} + m\mathbf{b} + n\mathbf{c}), \tag{2.36}$$

where the primed sum indicates that, for $l = m = n = 0$, the $i = j$ terms are omitted.

On the contrary, for cutoff distances lower than the lattice parameters, the atoms do not interact with their own images (see Fig. 2.5), and the previous sum can be restricted to the nearest images of particles. In practice computing the nearest distances of particles surrounding a given atom r_{ij}^{NI} can be implemented in a very simple way using the following definition:

$$\mathbf{r}_{ij}^{\mathrm{NI}} = \mathbf{r}_{ij} - \mathbf{h}\left[\mathbf{h}^{-1}\mathbf{r}_{ij}\right]_{\mathrm{NINT}}, \tag{2.37}$$

where $[\ldots]_{\mathrm{NINT}}$ denotes the nearest integer values and the matrix $\mathbf{h}$ is defined by the lattice vector ($\mathbf{h} = ((\mathbf{a})(\mathbf{b})(\mathbf{c}))$). Then the coordinates will be always within the box centered at the origin of the coordinates system.

[9] The computational time τ needed for a n-order contribution for N particles scales like the binomial coefficient $\binom{n}{N}$, for $n = 4 \Rightarrow \tau \propto N^4$

[10] The truncation may lead to systematic shifts in the pressure.

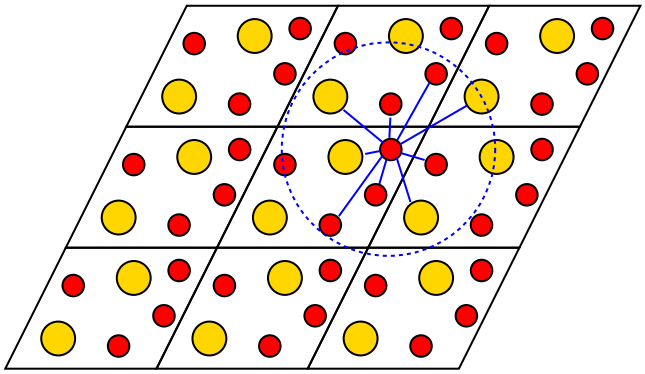

Figure 2.4: The cutoff distance is beyond the cell dimensions $r_{\text{cut}} > L_{\text{box}}/2$, the atoms interact with atoms belonging to cell replicas.

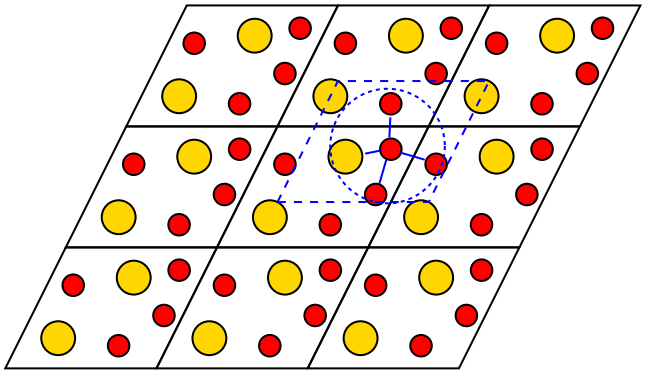

Figure 2.5: The interactions are truncated for $r_{\text{cut}} < L_{\text{box}}/2$, the red atoms interact with the nearest ions images belonging to the sphere.

Smoothing the potential The natural way to truncate a potential consists in using a spherical cut-off radius. A brute force truncation will lead to discontinuities in the energy and forces unless the potential smoothly tends to zero at that distance by design. To avoid discontinuity in the energy due to the potential truncation at r_{cut} a constant shift can be added so that the energy at the cutoff boundary becomes zero, see Eq. (2.38). The continuity of the forces is also determining for the stability of the dynamics as forces are involved at each step of the velocity Verlet algorithm, see Eqs. (2.11-2.13). This issue can be solved using a smoothing function $G_{r_{\text{cut}}}(r)$ that goes to zero at r_{cut}:

$$V_2^{\text{shifted}}(r_{ij}) = V_2(r_{ij}) - V_2(r_{\text{cut}}) \tag{2.38}$$

$$V_2^{\text{trunc}}(r_{ij}) = \begin{cases} V_2^{\text{shifted}}(r_{ij}) G_{r_{\text{cut}}}(r_{ij}) & : \quad r_{ij} \leq r_{\text{cut}} \\ 0 & : \quad r_{ij} > r_{\text{cut}} \end{cases} \tag{2.39}$$

$$G_{r_{\text{cut}}}(r_{ij}) = \exp\left(-\frac{\gamma^2}{(r_{ij} - r_{\text{cut}})^2}\right). \tag{2.40}$$

For our simulations we have retained the smoothing function given by Eq. (2.40). Here, the factor γ in the exponent can be seen as length scale over which the potential function is smoothened. The function, Eq. (2.40), makes the potential and its derivatives continuous.

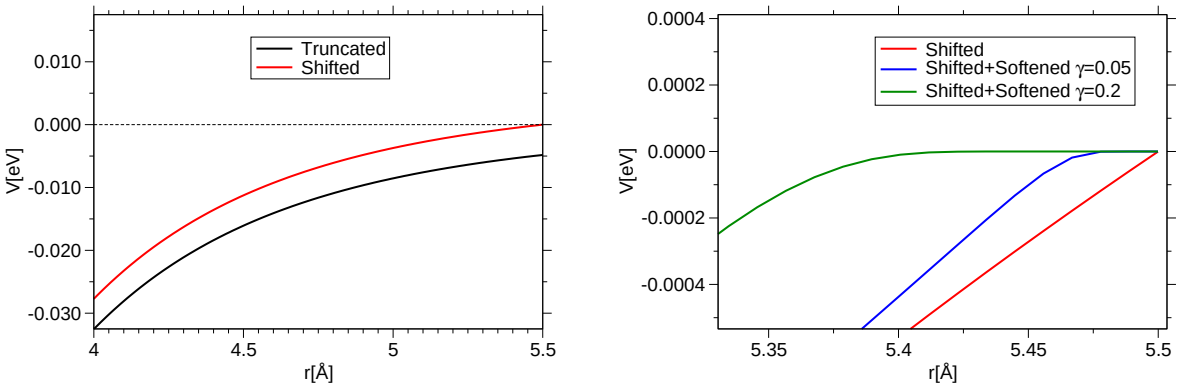

Figure 2.6: Left panel: Shifted potential for the Si-O short ranged part of the Born-Mayer potential using the BKS parameterization [9]. Right panel: Shifted and softened potential for the Si-O short range part of the BKS [9] potential.

Saving CPU time The calculation of the forces is the most time consuming stage during a MD simulation, see Eq. (2.12). It can be worthwhile to use a "Verlet list" so as to minimize the overall computational time required for simulation. As stated in the previous paragraph the short range contributions of interatomic potentials are truncated beyond a chosen distance r_{cut}. For a "large" system, *i.e.* a system with a typical cell dimension L_{box} that satisfies the inequality[11] $r_{\text{cut}} < L_{\text{box}}/2$, some pairs of atoms $\{ij\}$ separated by a distance $r_{\text{cut}} < r_{ij} < L_{\text{box}}/2$ do not interact. According to this statement it is possible to enhance the speed of the calculation of the forces. Listing all the pairs of atom that belong to the range below r_{cut} is an expensive process which scales like $\mathcal{O}(N^2)$. In practice, one can avoid using such time consuming procedure at each time step by listing all pairs of atoms $\{ij\}$ fulfilling the constraint $r_{ij} < r_{\text{v}}$, where $r_{\text{v}} > r_{\text{cut}}$. An illustrative example of such list (or "Verlet list") is given in Fig. 2.7, where we have represented the particles surrounding a given particle i, the particles within the sphere defined by r_{cut} interact with particle i, but only particles belonging to the sphere of radius r_{v} have been considered for the calculation of the interatomic distances.

This list must be updated when a particle belonging to the list has moved by more than $|r_{\text{v}} - r_{\text{cut}}|/2$ [12]. A more simple method consists in updating the list after a

[11] This constraint is imposed by the periodic boundary conditions.

[12] If the positions of two particles i and j, defined at $t = 0$ by $\mathbf{r}_i$ and $\mathbf{r}_j$ respectively, have been changed by $|r_{\text{v}} - r_{\text{cut}}|/2$ at $t = \Delta t$ then the interatomic distance at $t = \Delta t$ $r_{ij}(t = \Delta t)$ is limited as follows: $r_{ij}(t = 0) - |r_{\text{v}} - r_{\text{cut}}| \leq r_{ij}(t = \Delta t) \leq r_{ij}(t = 0) + |r_{\text{v}} - r_{\text{cut}}|$

given number of steps, the refreshing rate depending both on the thickness of the layer $|r_v - r_{cut}|$ and on the temperature investigated.

On one hand, the cutoff r_v of the "Verlet list" should not be too large otherwise one takes into account lots of non interacting pairs of atoms, on the other hand using a very small value of $|r_v - r_{cut}|$ implies frequent updates of the list. By using a Verlet list one can significantly reduce the overall computational time required for molecular dynamics simulations, as the main part of the calculations scale like $\mathcal{O}(N)$.

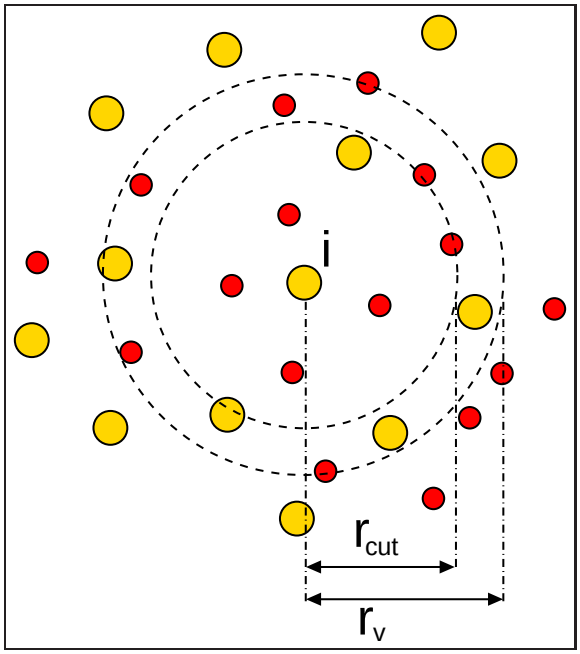

Figure 2.7: The Verlet list: A particle i interacts with those particles within the cutoff radius r_{cut}. The Verlet list contains all the particles within a sphere of radius r_v.

Very short range interactions The dispersion terms $\propto r^{-6}$ and the attractive Coulomb interactions diverge for low distances. Consequently, force fields using such terms tend to have an infinitely negative potential energy. The BKS potential [9] is an illustrative example: In Fig. 2.8 we have represented in dashed line the potential energy corresponding to the O-O and Si-O interactions. If nothing is done to prevent such shortcomings, the particles of the system may fuze together permanently. In order to circumvent this issue, Horbach and Kob [75] have truncated the BKS below $R_{cut} = 1.43847$ Å for the O-O term and below 1.19412 Å for the Si-O term, these numerical values correspond to the local maxima of the BKS for the O-O and Si-O pairs respectively. Below these cutoffs the missing part of the potential has been replaced by quadratic terms. The parameters of the repulsive wall are defined so as to ensure the continuity of the interatomic potential and its derivative at R_{cut}. In practice, these spurious quadratic parts do not play any significant role as the corresponding bond lengths are rather unlikely even for high temperatures ($T \geq 6100$K).

Another way to solve the diverging short range issue consists in adding repulsive terms to the potential [60]:

$$V_2^{\text{rep}}(r_{ij}) = 4\varepsilon_{ij}\left(\frac{\sigma_{ij}}{r_{ij}}\right)^{24}. \tag{2.41}$$

The power law dependence ensure a strong decrease of the repulsive potential for distances beyond σ_{ij}. As this method does not require any linking between the potential and the repulsive terms, it has been widely used in the simulations described in chapter 6. An illustrative example of the addition of a repulsive potential to the BKS is represented by the dashed lines in Fig. 2.8.

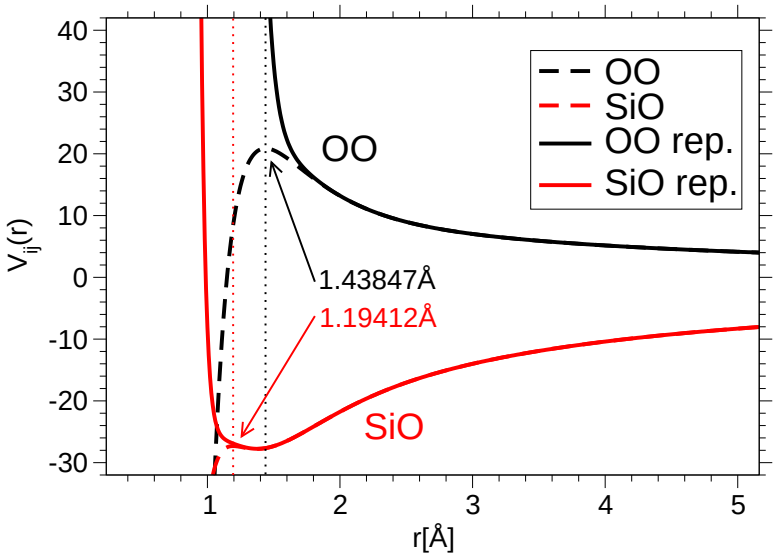

Figure 2.8: Attractive diverging behavior for the BKS O-O and Si-O interactions (dashed line) curbed by the means of additional terms added to the potential (solid line). The local maximum of the pair potentials are represented using vertical lines located at $R_{\text{cut}} = 1.19412$Å and $R_{\text{cut}} = 1.43847$Å.

2.2.4.2 Long range interactions

When considering an ionic or iono-covalent system, the Coulomb interaction is by far the dominant term and can represent typically, up to 90% of the total energy. The interactions between two particles i and j with charges q_i and q_j separated by a distance r_{ij} are described by Coulomb's law:

$$V_{ij}^{\text{Coul.}}(r_{ij}) = \frac{q_i q_j}{4\pi\varepsilon_0 r_{ij}}. \tag{2.42}$$

Thus, the total electrostatic energy ($V^{\text{Coul.}}$) of a system consisting of point charges is:

$$V^{\text{Coul.}} = \sum_i \sum_{j\neq i} V_{ij}^{\text{Coul.}}(r_{ij}). \tag{2.43}$$

The computation of this energy requires special attention as the interaction between ions decays like $1/r_{ij}$ whereas the number of interacting ions increases with the surface area of a sphere of radius $4\pi r^2$. Hence, the energy density of interactions increases with distance, rather than decaying, therefore it is necessary to take into account long range interactions for the calculation of the Coulomb energy. The Coulomb energy for periodic systems is only a conditionally convergent series[13]. Many approaches have been developed to increase the speed of convergence of the Coulomb energy, one can mention the solution proposed by Evjen [48], or the particle mesh method proposed by Hockney and Eastwood [71]. However, by far the most widely employed method is the one proposed by Ewald [49]. The slow converging series involving the interactions of point charges can be formally splitted in two fast converging contributions. In practice the point charges surrounding an atom i are lessened by subtracting Gaussian charge distributions, see Fig. 2.9. These screened interactions (V^{Real}) can be computed efficiently in the real space, see Fig. 2.10. Thereafter, the missing terms accounting for the interactions between the point charge centered on the atom i and the compensating screening charges ($V^{\text{Rec.}}$) are transformed by means of a Fourier transform and computed efficiently in the reciprocal space, see Fig. 2.11. The underlying physical considerations accounting for this formal decomposition are now exposed in the rest of this section.

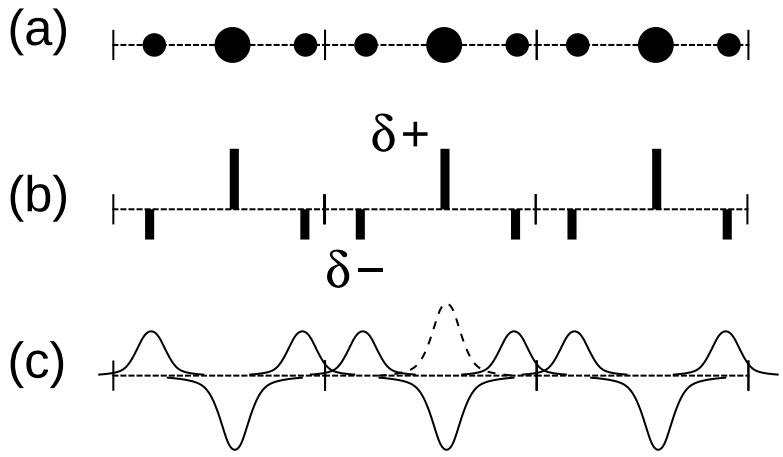

Figure 2.9: (a) A one-dimensional particle configuration connected to its periodic replicas. (b) The point charge distributions related to the above configuration. (c) A simplified representation of a periodic Gaussian distribution of charges $\rho^{\text{PBC}}(\mathbf{r})$ in continuous line, the self term $\rho_i^{\text{Self}}(\mathbf{r})$ is represented by the dashed curves.

General consideration In a real physical system the overall charge of an ion results from the counterbalancing contributions of the negative charge of electrons and the

[13]A series or integral is said to converge absolutely if the sum or integral of the absolute values of the summand or integrand is finite. A conditionally convergent series or integral is one that converges but does not converge absolutely.

positive charges of protons. In this section we assume that the charge distribution of a given ion i is a point charge, although, electrons move along on atomic orbitals according to the principles of quantum mechanics. As a consequence, these ionic charges can not rigorously be considered as being point charges, and they should have a spatial distribution $z(\mathbf{r})$. The electrostatic energy of Eq. (2.43) can be rewritten in this context:

$$V^{\text{Coul.}} = \frac{1}{2}\sum_{i=1}^{n}\int q_i z(\mathbf{r}_i - \mathbf{r})\phi_i(\mathbf{r})d\mathbf{r} \tag{2.44}$$

where $\phi_i(\mathbf{r})$ has been derived from the charge density $\rho_i(\mathbf{r})$ using the Poisson's equation:

$$-\nabla^2\phi_i(\mathbf{r}) = 4\pi\rho_i(\mathbf{r}), \tag{2.45}$$

where $\rho_i(\mathbf{r})$ is the contribution of particle i to the overall charge distribution. In a periodic system, with a geometry defined through the lattice vectors $\{\mathbf{a}, \mathbf{b}, \mathbf{c}\}$, the charge density surrounding a given atom i is given by:

$$\rho_i(\mathbf{r}) = \sum_{\ell,m,n}\sum_{j}{}' q_j z(\mathbf{r}_j - \mathbf{r} + \ell\mathbf{a} + m\mathbf{b} + n\mathbf{c}) \tag{2.46}$$

where the prime sum $\sum'$ excludes all the $j = i$ terms for $l = m = n = 0$. The charge density $\rho_i(\mathbf{r})$ can be splitted in two contributions $\rho^{\text{PBC}}(\mathbf{r})$ and $\rho_i^{\text{Self}}(\mathbf{r})$:

$$\rho_i(\mathbf{r}) = \sum_{\ell,m,n}\sum_{j} q_j z(\mathbf{r}_j - \mathbf{r} + \ell\mathbf{a} + m\mathbf{b} + n\mathbf{c}) - q_i z(\mathbf{r}_i - \mathbf{r}) \tag{2.47}$$

$$= \rho^{\text{PBC}}(\mathbf{r}) + \rho_i^{\text{Self}}(\mathbf{r}) \tag{2.48}$$

$$\rho^{\text{PBC}}(\mathbf{r}) = \sum_{\ell,m,n}\sum_{j} q_j z(\mathbf{r}_j - \mathbf{r} + \ell\mathbf{a} + m\mathbf{b} + n\mathbf{c}) \tag{2.49}$$

$$\rho_i^{\text{Self}}(\mathbf{r}) = q_i z(\mathbf{r}_i - \mathbf{r}) \tag{2.50}$$

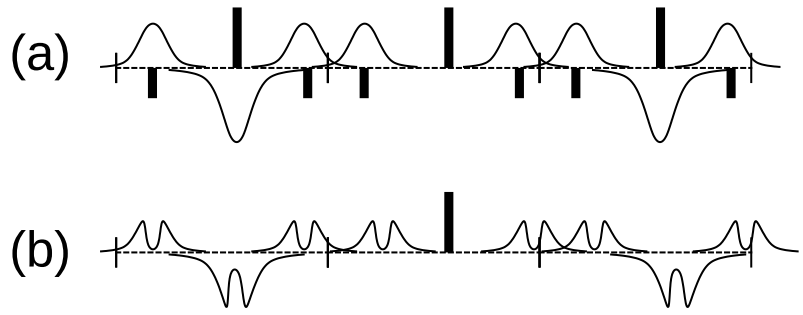

Figure 2.10: (a) Point charge and their screening Gaussian distributions superimposed. (b) The point charges (black stick) are screened by the Gaussian charge distributions (continuous curve).

Reciprocal space sum In this section we want to evaluate the interaction of a point charge with the surrounding Gaussian screening distribution. These interactions are represented in Fig. 2.11. To achieve this calculation we take advantage of the periodicity of the system to transform the electrostatic Gaussian distribution by means of Fourier transforms. The electric potential corresponding to this charge distribution can be computed straightforwardly in the reciprocal space using the Poisson equation.

In Eq. (2.48), the charge density has been splitted into two terms. The first one $\rho^{\mathrm{PBC}}(\mathbf{r})$ corresponds to the total charges distributions, and this term is invariant by translation[14]. The second term, $\rho_i^{\mathrm{Self}}(\mathbf{r})$ accounts for the self-charge of atom i. If one assumes a Gaussian charge distribution centered on each atom, the periodic part of the density, see Eqs. (2.48), can then be expressed in the real space in a simple form:

$$\rho^{\mathrm{PBC}}(\mathbf{r}) = \sum_{\ell,m,n} \sum_{j} q_j (\alpha/\pi)^{\frac{3}{2}} \exp\left[-\alpha |\mathbf{r} - (\mathbf{r}_j + \ell\mathbf{a} + m\mathbf{b} + n\mathbf{c})\,|^2\right]. \tag{2.51}$$

In the Fourier/reciprocal space this density is expressed as:

$$\rho^{\mathrm{PBC}}(\mathbf{k}) = \sum_{j} q_j \exp\left(-i\mathbf{k}\cdot\mathbf{r}_j\right) \exp\left(-\mathbf{k}^2/4\alpha\right). \tag{2.52}$$

The parameter α determines the magnitude of the screening charge, see Fig. 2.12.

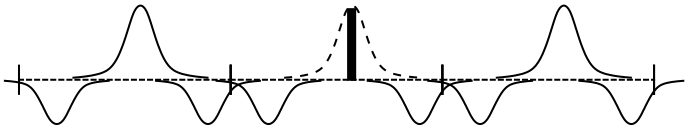

Figure 2.11: Sketch of the interactions in the reciprocal space, the sum of all the interactions between the point charge (black stick) and the periodic Gaussian charges distribution (continuous and dashed) account for the reciprocal energy term V^{PBC}. The self interaction term V^{Self} represents the spurious interaction of the point charge with its own Gaussian distribution (dashed). The Coulomb energy in the reciprocal space expressed as $V^{\mathrm{Rec.}} = V^{\mathrm{PBC}} - V^{\mathrm{Self}}$ is represented by the interaction with all the continuous distributions.

Solving the Poisson equation, see (2.45), in the reciprocal space and proceeding to a backward Fourier transformation[15] leads to the electrostatic potential ϕ^{PBC} [53]:

$$\begin{aligned} \phi^{\mathrm{PBC}}(\mathbf{r}) &= \sum_{\mathbf{k}\neq 0} \sum_{j} \frac{4\pi q_j}{k^2} \exp\left[i\mathbf{k}\cdot(\mathbf{r}-\mathbf{r}_j)\right] \exp\left(-\mathbf{k}^2/4\alpha\right) && (2.53) \\ &= \phi_i^{\mathrm{Rec.}}(\mathbf{r}) + \phi^{\mathrm{Self}}(\mathbf{r}) && (2.54) \end{aligned}$$

where $\phi^{\mathrm{Rec.}}(\mathbf{r})$ and $\phi^{\mathrm{Self}}(\mathbf{r})$ correspond to the electrostatic potentials related to the charge distributions $\rho^{\mathrm{Rec.}}(\mathbf{r})$ and $\rho^{\mathrm{Self}}(\mathbf{r})$ defined in Eqs. (2.47) and (2.50), respectively.

[14] $\rho^{\mathrm{PBC}}(\mathbf{r}) = \rho^{\mathrm{PBC}}(\mathbf{r}+\mathbf{T})$ where $\mathbf{T}$ is a vector of the Bravais lattice.

[15] The Fourier transform is a linear operator that maps functions to other functions: Considering a function $f(\mathbf{r})$, the corresponding Fourier transform $\tilde{f}(\mathbf{k})$ is given $\tilde{f}(\mathbf{k}) = \int d\mathbf{r} f(\mathbf{r}) \exp(-i\mathbf{k}\cdot\mathbf{r})$.

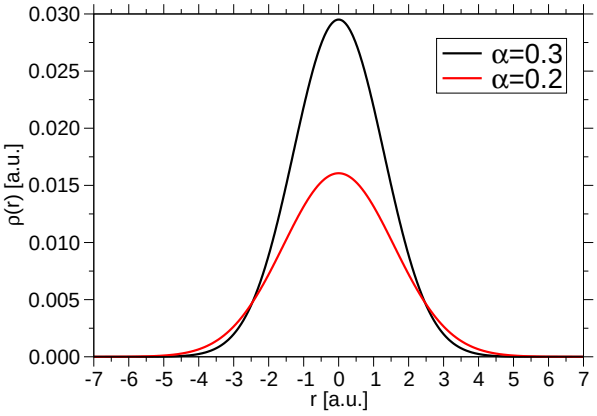

Figure 2.12: Representation of the Gaussian charge density $\rho(\mathbf{r}) = \left(\frac{\alpha}{\pi}\right)^{\frac{3}{2}} \exp\left(-\alpha \mathbf{r}^2\right)$, introduced in Eq. (2.51).

The energy of a point charge V^{PBC} in the periodic potential $\phi^{\mathrm{PBC}}(\mathbf{r})$ can be derived using Eqs. (2.44) and (2.53) and by considering a point charge distribution $z(\mathbf{r}) = \delta(\mathbf{r} - \mathbf{r}_i)$ in Eq. (2.44):

$$
\begin{aligned}
V^{\mathrm{PBC}}(\{\mathbf{r}_i\}) &= \sum_{i=1}^{n} \int q_i \delta(\mathbf{r}_i - \mathbf{r}) \phi^{\mathrm{PBC}}(\mathbf{r}) d\mathbf{r} && (2.55)\\
&= \sum_{i=1}^{n} q_i \phi^{\mathrm{PBC}}(\mathbf{r}_i) && (2.56)\\
&= \underbrace{\sum_{i=1}^{n} q_i \phi^{\mathrm{Rec.}}(\mathbf{r}_i)}_{V^{\mathrm{Rec.}}(\{\mathbf{r}_i\})} + \underbrace{\sum_{i=1}^{n} q_i \phi^{\mathrm{Self}}(\mathbf{r}_i)}_{V^{\mathrm{Self}}(\{\mathbf{r}_i\})} && (2.57)
\end{aligned}
$$

This value needs to be corrected as we have considered the interaction of the point charge with its own electrostatic field $\phi_i^{\mathrm{Self}}(\mathbf{r})$, see Fig. 2.11. It can be straightforwardly shown that this term is equal to:

$$
\begin{aligned}
V^{\mathrm{Self}}(\{\mathbf{r}_i\}) &= \sum_i \int q_i \delta(r) \overbrace{\frac{q_i \mathrm{erf}\left(\sqrt{\alpha} r\right)}{r}}^{\phi_i^{\mathrm{Self}}(r)} dr && (2.58)\\
&= (\alpha/\pi)^{\frac{1}{2}} \sum_i q_i^2 && (2.59)
\end{aligned}
$$

where $\mathrm{erf}(x)$ is the error function is defined $\mathrm{erf}(x) \equiv \int_0^x \exp\left(-u^2\right) du$, and the complementary error function, defined as $\mathrm{erfc}(x) \equiv 1 - \mathrm{erf}(x)$.

Hence, the interaction energy in the reciprocal space is given by:

$$
V^{\mathrm{Rec.}}(\{\mathbf{r}_i\}) = V^{\mathrm{PBC}}(\{\mathbf{r}_i\}) - V^{\mathrm{Self}}(\{\mathbf{r}_i\}) \qquad (2.60)
$$

$$
\begin{aligned}
&= \frac{1}{2}\sum_{\mathbf{k}\neq 0}\sum_{i,j}\frac{4\pi q_i q_j}{\Omega k^2}\exp\left[i\mathbf{k}\cdot(\mathbf{r}_i-\mathbf{r}_j)\right]\exp\left(-k^2/4\alpha\right) \\
&\quad -(\alpha/\pi)^{\frac{1}{2}}\sum_i q_i^2. \qquad (2.61)
\end{aligned}
$$

where Ω represents the volume of the simulation cell.

Real space sum The energy of an atom in the real space is given by the calculation of the interactions of the point charges of the atom considered with the screening Gaussian distributions charges of its surrounding neighbors. These distributions are represented in Fig. 2.10. The electrostatic field ϕ_i^{Real} can be derived using the expression of both Coulomb field ($\frac{q_i}{r}$) and the electric field corresponding to a Gaussian charge distribution given by Eq. (2.58):

$$
\begin{aligned}
\phi_i^{\text{Real}}(r) &= \frac{q_i}{r}-\frac{q_i\text{erf}\left(\sqrt{\alpha}r\right)}{r} \\
&= \frac{q_i\text{erfc}\left(\sqrt{\alpha}r\right)}{r}. \qquad (2.62)
\end{aligned}
$$

Replacing the above results in Eq. (2.44) leads to the following expression for the real part of the Coulomb energy:

$$
V^{\text{Real}} = \frac{1}{2}\sum_{i\neq j} q_i q_j \frac{\text{erfc}(\sqrt{\alpha}r_{ij})}{r_{ij}} \qquad (2.63)
$$

Practical aspects The total electrostatic interactions of a point charges system expressed using the Ewald summation is given by summing the contributions of the terms (2.61) and (2.63):

$$
\begin{aligned}
V^{\text{Coul.}} &= \frac{1}{2}\sum_{i\neq j} q_i q_j \frac{\text{erfc}(\sqrt{\alpha}r_{ij})}{r_{ij}} - (\alpha/\pi)^{\frac{1}{2}}\sum_i q_i^2 \\
&\quad +\frac{1}{2}\sum_{\mathbf{k}\neq 0}\sum_{i,j}\frac{4\pi q_i q_j}{\Omega k^2}\exp\left[i\mathbf{k}\cdot(\mathbf{r}_i-\mathbf{r}_j)\right]\exp\left(-k^2/4\alpha\right) \qquad (2.64)
\end{aligned}
$$

This splitting of the Coulomb potential in a sum of two fast converging contributions enhances the calculation speed of the electrostatic energy. The screening parameter α tunes the spatial extent of the screening Gaussian distribution and has to be defined consistently with the cutoff radii of the real and reciprocal contributions. Large values of α correspond to significant screening in the real space, the reciprocal term represents the main contribution to the Coulomb energy. On the contrary, when using a small value of α the Coulomb energy is mainly represented by the real space term, see Fig. 2.12.

All these parameters can be defined so as to ensure a good balancing of the error and a good balancing of the the computation time in both real and reciprocal space

for a given specified accuracy A> $|E^{\text{Coul.}} - E^{\text{Coul.}}_{\text{Ewald}}|$ [121], [78]:

$$r_{\text{cut}} = \left(\frac{-\ln(A)}{\alpha}\right)^{\frac{1}{2}}, \quad \text{and} \quad k_{max} = 2\alpha^{\frac{1}{2}}\left(-\ln(A)\right)^{\frac{1}{2}}. \tag{2.65}$$

A short glimpse underlining the influence of the different parameters α, and k_{max} is given in Fig. 2.13.

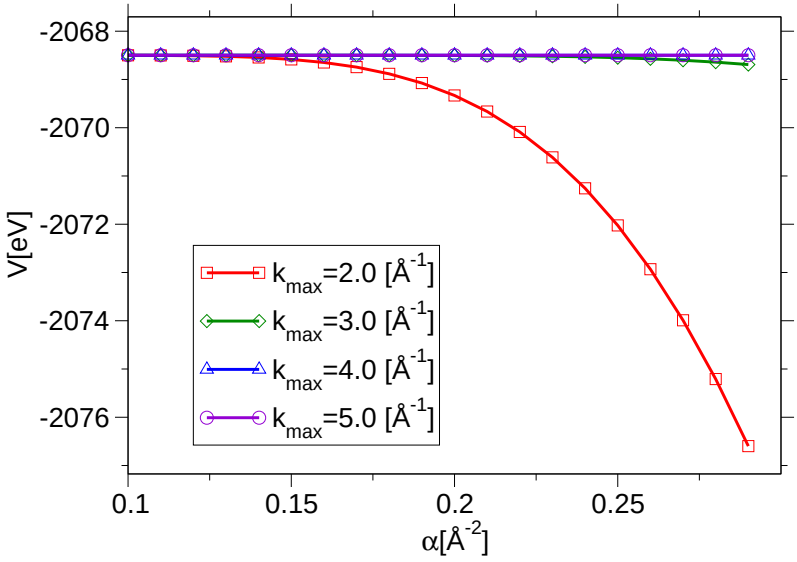

Figure 2.13: Convergence of the electrostatic energy as a function of the Gaussian parameter α represented for different values of the cut off radius in the reciprocal space (k_{max}). The system under consideration is made of 114 atoms, contained in a cubic box ($L_{\text{box}} = 11.98$Å), the cut off distance in the real space is fixed to 10Å. For an accuracy $A = 10^{-10}$, the optimal parameters are $\alpha = 0.230$ and $k_{\text{max}} = 4.605\text{Å}^{-1}$ accounting for 1568 wave-vectors.

2.3 Ab initio methods

In physics a calculation is said to be from first principles if it starts directly at the level of fundamental laws of physics and does not make assumptions such as model and fitting parameters. This is also known as *ab initio*. For example, calculation or simulation of molecular electronics systems by directly solving the complex Schrödinger equation is considered as an *ab initio* calculation. Some of the basic concepts of quantum mechanics, simplifying hypotheses and numerical approaches for solving the Schrödinger equation will now be exposed in this section. These elements are compulsory for the understanding of the relevant criteria used to choose the appropriate approach for studying the system one wants to investigate. Hence we will mainly present the methods used of calculation for the structure of poly-electronic systems such as the Hartree-Fock (HF) methods and Density Functional Theory approach (DFT).

2.3.1 The Schrödinger equation

Quantum mechanics is a more fundamental theory than Newtonian mechanics in the sense that it provides accurate and precise descriptions for many phenomena that the "classical" Newtonian theory simply cannot explain on the atomic and subatomic level. A brief presentation of the first principles is given in this section. According to the postulates of quantum mechanics a state (or wave function) of a microscopic system is defined by a unit ray[16] in a complex Hilbert space. Formally, each vector (or quantum state) in the ray can be decomposed in a sum of basis vectors of the Hilbert space. The natural basis adapted to our system calculation will be presented in section (2.3.3).

The time evolution of the state vector $|\psi\rangle$ of a poly-electronic system is given by the time dependent Schrödinger equation:

$$i\hbar\frac{d}{dt}|\psi\left(\{\mathbf{r}_i\},\{\mathbf{R}_i\},t\right)\rangle = \mathcal{H}(t)|\psi\left(\{\mathbf{r}_i\},\{\mathbf{R}_i\},t\right)\rangle, \tag{2.66}$$

where, the electronic and ionic positions are denoted by $\{\mathbf{r}_i\}$ and $\{\mathbf{R}_i\}$, respectively. The reduced Planck constant is denoted by $\hbar$ and $\mathcal{H}$ is the quantum Hamiltonian. In many situations, the energy operator $\mathcal{H}$ does not depend on time. Then it can be shown that the time-dependent Schrödinger equation simplifies to the time-independent Schrödinger equation:

$$\mathcal{H}|\psi\left(\{\mathbf{r}_i\},\{\mathbf{R}_i\}\right)\rangle = E\psi\left(\{\mathbf{r}_i\},\{\mathbf{R}_i\}\right)\rangle. \tag{2.67}$$

The Hamiltonian of the many-electrons systems contains both kinetic and Coulombic contributions:

$$\mathcal{H} = \sum_{i=1}^{n}\frac{-\nabla_i^2}{2m_i} + \sum_{I=1}^{N}\frac{-\nabla_I^2}{2M_I} + \sum_{i=1}^{n}\sum_{j=1;j<i}\frac{z_i z_j e^2}{r_{ij}} + \sum_{i=1}^{n}\sum_{I=1}^{N}\frac{z_i Z_I e^2}{|\mathbf{r}_i-\mathbf{R}_I|} + \sum_{I=1}^{n}\sum_{J=1;J<I}^{N}\frac{Z_I Z_J e^2}{R_{IJ}}. \tag{2.68}$$

[16] A ray is a one-dimensional subspace, two vectors belong to the same ray and so, represent the same state if they differ only by a phase factor.

In this expression the charge and mass of electrons are denoted by z_i, and m_i respectively, whereas the charges and mass of ions are denoted by Z_i, and M_i respectively. Regarding the kinetic energy, the correspondence between the quantum Hamiltonian and the classical one is made straightforward assuming the following definition for the quantum impulsion operator:

$$P_i = -i\hbar\nabla_i \qquad \text{and so} \qquad E_{\text{kin.}} = \sum_i \frac{\langle P_i^2 \rangle}{2m_i} = \langle \psi(\{\mathbf{r}_i\})| \sum_i \frac{-\nabla_i^2}{2m_i} |\psi(\{\mathbf{r}_i\})\rangle. \quad (2.69)$$

In Eq. (2.68) the electronic degrees of freedom $\{\mathbf{r}_i\}$ and the ionic ones $\{\mathbf{R}_i\}$ are coupled. The adiabatic[17] approximation commonly used to decouple these variables for a conservative system is presented in section (2.3.2). The time integration of Eq. (2.68) is tackled in section (2.3.6).

In this work we have also performed simulations for crystalline phases. In practice, an ideal crystal can be described by assuming that a wave function must be periodic on a certain Bravais lattice, and for this purpose, one has to define a specific set of boundary conditions (so-called Born-Von Karman boundary conditions). For such systems, the wavefunctions of independent particles can be classified using the Bloch theorem:

$$\psi_{\mathbf{k}}(\mathbf{r}) = \exp(i\mathbf{k}\cdot\mathbf{r}) u_{\mathbf{k}}(\mathbf{r}), \quad (2.70)$$

where $\psi_{\mathbf{k}}(\mathbf{r})$ is an eigenfunction (or Bloch function) identified by its crystal momentum $\mathbf{k}$ and $u_{\mathbf{k}}(\mathbf{r})$ is a function which has to satisfy the translational invariance property of the crystal ($u_{\mathbf{k}}(\mathbf{r}) = u_{\mathbf{k}}(\mathbf{r} + \ell\mathbf{a} + m\mathbf{b} + n\mathbf{c})$). Using these notations, the Hamiltonian of independent particles of the system can then be rewritten:

$$\mathcal{H}(\mathbf{k}) u_{i,\mathbf{k}}(\mathbf{r}) = \left[\frac{-(\nabla + i\mathbf{k})^2}{2m} + \sum_{I=1}^{N} \frac{z Z_I e^2}{|\mathbf{r} - \mathbf{R}_I|} \right] u_{i,\mathbf{k}}(\mathbf{r}) = \varepsilon_{i,\mathbf{k}} u_{i,\mathbf{k}}(\mathbf{r}) \quad (2.71)$$

where $\varepsilon_{i,\mathbf{k}}$ corresponds to the ith-eigenvalue of the Hamiltonian at given $\mathbf{k}$. These eigenvalues are usually represented with respect to their $\mathbf{k}$-variable in the so called band diagram [82], each band corresponds to a given state i. It is worthwhile to note that any intrinsic properties f_i of a crystal have to be calculated by averaging the $\mathbf{k}$-dependent property $f_{i,\mathbf{k}}$ over the all crystal momenta[18]. In practice, many calculation can be carried out at a zero crystal momentum ($\mathbf{k} = 0$), so called Γ point according to the Bouckaret, Smoluchowski and Wigner notation.

2.3.2 The adiabatic approximation

Introduction This approximation was originally proposed by M. Born and J. R. Oppenheimer in 1927 [21] to simplify the many-body problem due to the ion-electron coupling in quantum mechanics. It consists of two steps: In the first step the nuclear

[17] In quantum mechanics an adiabatic process is an infinitely slow change in the Hamiltonian of a system. Adiabatic processes are important idealizations of "sufficiently slow" processes.

[18] $f_i = \frac{1}{\Omega_{\text{BZ}}} \int_{\Omega_{\text{BZ}}} d\mathbf{k} f_{i,\mathbf{k}}$, where Ω_{BZ} is the volume of the first Brillouin zone.

kinetic and Coulomb energy are neglected, that is, the corresponding operators are subtracted from the total molecular Hamiltonian. In the remaining electronic Hamiltonian ($\mathcal{H}_{\text{elec.}}$) the nuclear positions enter as parameters. The electron-nucleus interactions are not removed and the electrons still "feel" the Coulomb potential of the nuclei clamped down at certain positions in space[19]. The electronic Schrödinger equation:

$$\mathcal{H}_{\text{elec.}}|\psi(\{\mathbf{r}_i\})\rangle_{\{\mathbf{R}_i\}} = E_{\text{elec.},\{\mathbf{R}_i\}}|\psi(\{\mathbf{r}_i\})\rangle_{\{\mathbf{R}_i\}} \tag{2.72}$$

is solved for a fixed nuclear geometry. The electronic energy eigenvalue $E_{\text{elec.},\{\mathbf{R}_i\}}$ depends on the chosen positions $\{\mathbf{R}_i\}$ of the nuclei. Varying these positions $\{\mathbf{R}_i\}$ in small steps and repeating the resolution of the electronic Schrödinger equation, one obtains $E_{\text{elec.},\{\mathbf{R}_i\}}$ as a function of $\{\mathbf{R}_i\}$. This is the potential energy surface (PES): $E_{\text{elec.}}(\{\mathbf{R}_i\})$. In the second step of the Born-Oppenheimer approximation the nuclear kinetic and Coulomb energy are reintroduced and the Schrödinger equation for the nuclear motion is solved.

Decoupling the ionic and electronic wavefunction The physical object of interest in this theory is the ionic and electronic wavefunction Θ. This wavefunction depends on the microscopic positions of the particles constituting the system, namely the nuclear positions $(\mathbf{R}_1, \mathbf{R}_2, \ldots, \mathbf{R}_N)$ and the electronic positions $(\mathbf{r}_1, \mathbf{r}_2, \ldots, \mathbf{r}_n)$.

$$\Theta(\mathbf{r}_1, \mathbf{r}_2, \ldots, \mathbf{r}_n, \mathbf{R}_1, \mathbf{R}_2, \ldots, \mathbf{R}_N) \tag{2.73}$$

Starting from the Schrödinger equation with a time-independent Hamiltonian ($\mathcal{H}$) one should in principle solve the following equation:

$$\mathcal{H}\Theta(\mathbf{r}_1, \ldots, \mathbf{r}_n, \mathbf{R}_1, \ldots, \mathbf{R}_N) = E\Theta(\mathbf{r}_1, \ldots, \mathbf{r}_n, \mathbf{R}_1, \ldots, \mathbf{R}_N) \tag{2.74}$$

with $\mathcal{H}$ defined as follow:

$$\mathcal{H} = \sum_{i=1}^{n} \frac{-\nabla_i^2}{2m_i} + \sum_{I=1}^{N} \frac{-\nabla_I^2}{2M_I} + \sum_{i=1}^{n} \sum_{j=1;j<i} \frac{z_i z_j e^2}{r_{ij}} + \sum_{i=1}^{n} \sum_{I=1}^{N} \frac{z_i Z_I e^2}{|\mathbf{r}_i - \mathbf{R}_I|} + \sum_{I=1}^{n} \sum_{J=1;J<I}^{N} \frac{Z_I Z_J e^2}{R_{IJ}}. \tag{2.75}$$

An exact resolution to the Schrödinger's equation of a system of electrons and nucleus is not affordable because of the many-body problem. As a consequence one has to make appropriate approximations and hypotheses so as to simplify this equation. A very valuable approximation is the Born-Oppenheimer (BO) approximation which asserts that electronic and nuclear motions can be decoupled. This assumption is reliable considering the difference in the mass ratio between nucleus and electron, $m_p/m_e \simeq 1836$[20]. Assuming that the momenta of electrons and nuclei are similar, one can assert

[19]This first step of the BO approximation is therefore often referred to as the clamped nuclei approximation.

[20]The proton mass is $m_p = 1.67262171(29)^{-27}$ kg, the electron mass is $m_e = 9.1093826(16)^{-31}$ kg, the ratio $m_p/m_e \simeq 1836$

that the heavy nuclei move more slowly than the light electrons. This approximation leads to the following factorization [98]:

$$\Theta(\mathbf{r}_1,\ldots,\mathbf{r}_n,\mathbf{R}_1,\ldots,\mathbf{R}_N) = \psi_{\mathbf{R}_1,\ldots,\mathbf{R}_n}(\mathbf{r}_1,\ldots,\mathbf{r}_n)\times\Omega(\mathbf{R}_1,\ldots,\mathbf{R}_N). \tag{2.76}$$

The function ψ depends explicitly on the electronic positions $\{\mathbf{r}_1,\ldots,\mathbf{r}_n\}$ and parametrically on the nuclear positions $\{\mathbf{R}_1,\ldots,\mathbf{R}_N\}$ as it must be consistent with the electronic Hamiltonian that contains R_i dependent terms. The ionic wavefunction is defined by $\Omega(\mathbf{R}_1,\ldots,\mathbf{R}_n)$. Thus, the Hamiltonian $\mathcal{H}$ of Eq. (2.75) can be decomposed in two parts, one depending on the electronic positions as well as on the ionic and electronic momenta $\mathcal{H}_{\text{elec.}}$; the other depending solely on the ionic positions and momentum $\mathcal{H}_{\text{nucl.}}$:

$$\mathcal{H} = \underbrace{\sum_{i=1}^{n}\frac{-\nabla_i^2}{2m_i} + \sum_{i=1}^{n}\sum_{j=1;j<i}\frac{z_i z_j e^2}{r_{ij}} + \sum_{i=1}^{n}\sum_{I=1}^{n}\frac{z_i Z_J e^2}{|\mathbf{r}_i-\mathbf{R}_J|}}_{\mathcal{H}_{\text{elec.}}} + \underbrace{\sum_{I=1}^{N}\frac{-\nabla_I^2}{2M_I} + \sum_{I=1}^{n}\sum_{J=1;J<I}\frac{Z_I Z_J e^2}{R_{IJ}}}_{\mathcal{H}_{\text{nucl.}}}. \tag{2.77}$$

Using this assumption one can solve the time independent Schrödinger equation in two steps, by first solving the electronic equation (2.78) thereafter solving the Eq. (2.79) using the solutions of (2.78):

$$\langle\psi^\dagger|\mathcal{H}_{\text{elec.}}|\psi\rangle = E_{\text{elec.}}(\mathbf{R}_1,\ldots,\mathbf{R}_n) \tag{2.78}$$

$$\langle\Theta^\dagger|\mathcal{H}|\Theta\rangle = \langle\Omega^\dagger|E_{\text{elec}}(\mathbf{R}_1,\ldots,\mathbf{R}_n)|\Omega\rangle + \langle\Theta^\dagger|\mathcal{H}_{\text{nucl.}}|\Theta\rangle \tag{2.79}$$

$$= \langle\Omega^\dagger|\langle\psi^\dagger|\mathcal{H}_{\text{elec.}}|\psi\rangle|\Omega\rangle + \langle\Theta^\dagger|\mathcal{H}_{\text{nucl.}}|\Theta\rangle \tag{2.80}$$

The total Hamiltonian can be diagonalized by first solving the Schrödinger equation using the electronic Hamiltonian and considering frozen ionic positions, see Eq. (2.78). Then the ionic wavefunction is obtained by solving the Schrödinger equation using the electronic wavefunction see Eq. (2.79-2.80). Generally this approximation is considered excellent for non degenerated electronic states. Otherwise, if there exist a small gap[21] in the electronic excitation spectrum smaller than typical energies of nuclear motion, then the nuclear motion may couple with some the electronic states.

2.3.3 Hilbert's space basis set

The first postulate of quantum mechanics states that the wavefunction describing a state is built upon a basis of the Hilbert space. An appropriate choice of the basis set depends on the nature of the system. In this work we are considering a periodic system[22] that matches with the use of plane waves:

$$f_{\mathbf{k}}(\mathbf{r}) = \frac{1}{\sqrt{\Omega}}\exp\left(i\mathbf{k}\cdot\mathbf{r}\right). \tag{2.81}$$

[21] The electronic gap or band gap generally refers to the energy difference between the top of the valence band/highest unoccupied orbital and the bottom of the conduction band/lowest occupied orbital.

[22] Using the Born-von Karman periodic boundary conditions

In theory a wavefunction should be described by means of a complete basis of vectors[23]. In practice it is not possible to handle such kind of basis set, the wavefunction is described using a finite number of plane waves. According to the quantum definition of the momentum operator, see Eq. (2.69), the number of plane waves can be defined using an energy cutoff E_{cut} as the kinetic energy of plane waves is equal to $E_{\mathbf{k}} = \hbar^2 k^2 / 2m_e$, All the plane waves with an energy $E_{\mathbf{k}} < E_{\text{cut}}$ are taken into account for the calculation of the wavefunction.

Thus a wavefunction $\psi(\mathbf{r})$ can be represented as a linear combination of these basis functions:

$$\psi(\mathbf{r}) = \sum_{\mathbf{k}} c_{i\mathbf{k}} f_{\mathbf{k}}(\mathbf{r}) \tag{2.82}$$

Using Fourier transform, these functions can also be defined as a set of values on a equally spaced grid in real space, see Fig. 2.14.

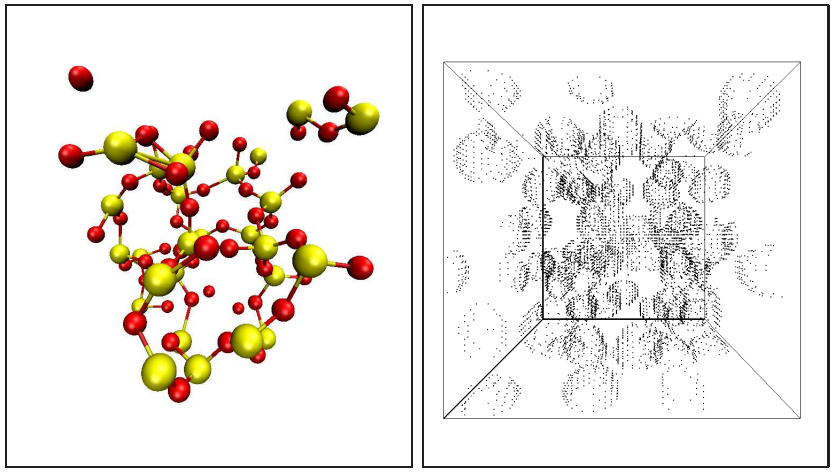

Figure 2.14: Left panel: Atomic configuration of a 78 atom sample. Right panel: Representation of the corresponding electronic density using grid points of space.

Contrary to the Gaussian basis set[24] mainly used for the calculation of molecules in vacuum, plane waves are non centered functions as they do not depend on the position of the nucleus. Thus, wavefunctions build using plane waves do not carry any extra additional dependence on the nuclei positions by construction. As a consequence one get rids of the spurious Pulay terms [119, 120] which parasite the calculation of the interatomic forces. These terms account for the explicit dependence of the electronic cloud with respect to the ions positions. The electronic wavefunction is coupled to the ionic positions through the Schrödinger equation, but the basis set used for building the wavefunction should not depend on the ionic positions.

Nevertheless, unlocalized basis may bring some shortcomings, for example, refined descriptions of complex oscillatory behavior of the wavefunction may require lots of

[23] In such case the basis set is infinite.

[24] These orbitals centered on an atom at a given position $\mathbf{R}$ have the following analytical form $\phi(\mathbf{r} - \mathbf{R}) = (2\alpha/\pi)^{3/4} e^{-\alpha|\mathbf{r}-\mathbf{R}|^2}$

plane waves. To get around of this problem one can make a clever use of pseudopotentials to avoid the complex nodal structure of core states. The pseudopotential are described in section (2.3.4). Another aspect which may be pointed out in this context concerns the heterogeneous systems (simple molecules in a box for example) made with large vacuum regions may also demand lots of plane waves even for a restricted amount of electrons.

2.3.4 Pseudopotential

The electrons of an atom can be classified in two groups: The core electrons and the valence electrons. By definition core states are localized close to the nuclei, whereas the valence states belong to the outer shell[25] of the electronic structures. When investigating real systems of elements heavier than He, one is faced with the problem of the tightly bound core states ($|\psi_{\text{core}}\rangle$) which affect the shape of the wavefunction of valence state ($|\psi_{\text{val.}}\rangle$) close to the nucleus. According to the principles of quantum mechanics the eigenstates of any given Hamiltonian are orthogonal, and as a consequence, the overlapping integral between the valence and the core states $\langle\psi_{\text{core}}|\psi_{\text{val.}}\rangle$, is equal to zero. This orthogonality constraint accounts for the rapid oscillatory behavior of the valence wave function close to the nucleus. This region of space characterized by rapid oscillations of the wave function can be defined by a core radius R_c. The rapid variations of the wavefunction close to the nucleus have two consequences. First the kinetic energy of electrons is rather high in the vicinity of the ions, see Eq. (2.69). Some relativistic effects connected to this high kinetic energy level have to be taken into account, and this is also true for the core electrons. These relativistic effects can be described using the Dirac equation[38, 39]. Unfortunately solving this equation or even the simplified relativistic Hamiltonian (fine structure Hamiltonian) for all the electrons is not affordable because of computer resource limitation.

What is more, the complex oscillatory behavior of the valence states can only be accurately described by means of several basis functions at the expense of the computational efficiency, see section (2.3.3). Some approximations have been proposed to simplify the Hamiltonian resolution, considering the core states as chemically inert which means that they are not perturbated by the electronic structure of other atoms, and well-separated from the valence states. By doing so, the influence of the core electrons can be mimicked by adding terms (the so called pseudopotentials or PP) to the Hamiltonian. The eigenvalues and eigenfunctions of this extended Hamiltonian are called pseudo-valence eigenvalues and pseudo-valence wavefunctions. In this work we have considered the norm-conserving pseudopotentials according to the criteria proposed by Hamman and coworkers [61].

[25] Orbitals with the same value of the principal quantum number n are said to comprise a "shell"

2.3.5 Solving the Schrödinger equation

2.3.5.1 Hartree-Fock approximation

Theory This method is a mean field method based upon a first idea of D. R. Hartree and then improved by V. Fock in the 1930's [52]. Their aim was to factorize the electronic wavefunction into 1-variable orthonormal independent contributions (called spin orbitals or also molecular orbitals, χ_i) to overcome the many-body problem due to electron interactions. However this cannot be done in a trivial way due to the intrinsic nature of electrons. The antisymmetry or Pauli exclusion principle implies that electrons (which are fermions) are strongly correlated, as they are not allowed to share the same quantum state. To fulfill this principle, a many-electron wavefunction has to be antisymmetric with respect to the interchange of two electrons (both space coordinates and spin) with the spin orbitals χ. This can be formally expressed by the following property of the wavefunction, according to the notation of Eq. (2.66):

$$\psi(\mathbf{r}_1,\ldots,\mathbf{r}_i,\ldots,\mathbf{r}_j,\ldots,\mathbf{r}_n,\mathbf{R}_1,\ldots,\mathbf{R}_N) = -\psi(\mathbf{r}_1,\ldots,\mathbf{r}_j,\ldots,\mathbf{r}_i,\ldots,\mathbf{r}_n,\mathbf{R}_1,\ldots,\mathbf{R}_N). \tag{2.83}$$

The wavefunction $\psi(\mathbf{r}_1,\ldots,\mathbf{r}_n)$ solution of the electronic Hamiltonian is decomposed in an antisymmetric combination of molecular orbitals by means of a Slater determinant:

$$\psi(\mathbf{r}_1,\ldots,\mathbf{r}_n) = \frac{1}{\sqrt{n!}} \begin{vmatrix} \chi_i(\mathbf{r}_1) & \chi_j(\mathbf{r}_1) & \cdots & \chi_k(\mathbf{r}_1) \\ \chi_i(\mathbf{r}_2) & \chi_j(\mathbf{r}_2) & \cdots & \chi_k(\mathbf{r}_2) \\ \vdots & \vdots & \ddots & \vdots \\ \chi_i(\mathbf{r}_n) & \chi_j(\mathbf{r}_n) & \cdots & \chi_k(\mathbf{r}_n) \end{vmatrix}. \tag{2.84}$$

The electronic Hamiltonian of Eq. (2.77) can formally be decomposed into two contributions:

$$\mathcal{H}_{\text{elec}} = \sum_{i=1}^{n} \frac{-\nabla_i^2}{2m} + \sum_{i=1}^{n}\sum_{J=1}^{N} \frac{z_i Z_J e^2}{|\mathbf{r}_i - \mathbf{R}_J|} + \sum_{i=1}^{n}\sum_{j=1;j<i} \frac{z_i z_j e^2}{r_{ij}} \tag{2.85}$$

$$\mathcal{H}_{\text{elec}} = \theta_1(\{\mathbf{r}_i\}) + \theta_2(\{\mathbf{r}_i\}) \tag{2.86}$$

$$h(\mathbf{r}) = -\frac{\nabla^2}{2m} + \sum_{I=1}^{N} \frac{z Z_J e^2}{|\mathbf{r} - \mathbf{R}_J|} \tag{2.87}$$

$$\theta_1(\{\mathbf{r}_i\}) = \sum_{i=1}^{N} h(\mathbf{r}_i) \tag{2.88}$$

$$\theta_2(\{\mathbf{r}_i\}) = \sum_{j=1;j<i} \frac{z_i z_j e^2}{r_{ij}} \tag{2.89}$$

The first term θ_1 represents the sum of one-electron contribution $h(r)$ of the kinetic energy and Coulomb interactions with the nuclei. The term θ_2 accounts for the Coulomb interactions between electrons. Using the orthonormality constraint of the molecular orbitals $\langle\chi_i|\chi_j\rangle = \delta_{ij}$ and the antisymmetric properties of the wavefunction one can

simplify the Eq. (2.78). The total electronic energy of the system can then be expressed as:

$$E(\{\chi_a\}) = \langle\psi|\mathcal{H}_{\text{elec}}|\psi\rangle = \sum_a^n [\chi_a|h|\chi_a] + \frac{1}{2}\sum_a^n\sum_b^n [\chi_a\chi_a|\chi_b\chi_b] - [\chi_a\chi_b|\chi_b\chi_a] \quad (2.90)$$

with

$$[\chi_a|h|\chi_b] = \int d\mathbf{r}_1 \chi_a^*(\mathbf{r}_1) h(\mathbf{r}_1)\chi_b(\mathbf{r}_1) \quad (2.91)$$

$$[\chi_a\chi_b|\chi_c\chi_d] = \int d\mathbf{r}_1 d\mathbf{r}_2 \chi_a^*(\mathbf{r}_1)\chi_b^*(\mathbf{r}_1) r_{12}^{-1}\chi_c(\mathbf{r}_2)\chi_d(\mathbf{r}_2). \quad (2.92)$$

Then, it is convenient to introduce the following operators:

- The Coulomb operator $\mathcal{J}_b$ that represents the average Coulomb interaction between two electrons (ignoring the Pauli exclusion principle):

$$\mathcal{J}_b(\mathbf{r}_1)\chi_a(\mathbf{r}_1) = \left\{\int d\mathbf{r}_2 \chi_b^*(\mathbf{r}_2) r_{12}^{-1}\chi_b(\mathbf{r}_2)\right\}\chi_a(\mathbf{r}_1) \quad (2.93)$$

- The exchange operator $\mathcal{K}_b$:

$$\mathcal{K}_b(\mathbf{r}_1)\chi_a(\mathbf{r}_1) = \left\{\int d\mathbf{r}_2 \chi_b^*(\mathbf{r}_2) r_{12}^{-1}\chi_a(\mathbf{r}_2)\right\}\chi_b(\mathbf{r}_1) \quad (2.94)$$

  which balances the overestimated contribution of the Coulomb operator.

In fact, because of the Pauli exclusion principle, electrons having the same spin orientation are not allowed to occupy simultaneously the same positions. It is possible to support this argument by defining the probability $P(\mathbf{r}_i, \mathbf{r}_j)$ of finding simultaneously electron i at $d\mathbf{r}_i$ and electron j at $d\mathbf{r}_j$:

$$P(\mathbf{r}_i, \mathbf{r}_j)d\mathbf{r}_i d\mathbf{r}_j = \int \dots \int d\mathbf{r}_1 \dots d\mathbf{r}_n |\psi(\mathbf{r}_1, \dots, \mathbf{r}_i, \dots, \mathbf{r}_j, \dots, \mathbf{r}_n)|^2 d\mathbf{r}_i d\mathbf{r}_j, \quad (2.95)$$

Imposing $\mathbf{r}_i = \mathbf{r}_j$ in Eq. (2.83) yields:

$$\psi(\mathbf{r}_1, \dots, \mathbf{r}_i, \dots, \mathbf{r}_i, \dots, \mathbf{r}_n) = 0, \quad (2.96)$$

and thus, $P(\mathbf{r}_i, \mathbf{r}_j)d\mathbf{r}_i d\mathbf{r}_j = 0$, the region around an electron in which no other electron with parallel spin can go is called a Fermi hole. Because of these Fermi holes, the electrostatic energy of electrons is overestimated as the Coulomb operator does not make any distinction between correlated and uncorrelated pairs of electrons.

According to the variational principle one knows that the energy of a ground state of a quantum system E_0 is the lower bound of any energies given by approximate wavefunctions for this system. To derive the Hartree-Fock equations the electronic energy E must be minimized with respect to the spin orbitals. In addition to this we suppose that spin orbitals are orthonormal. This condition must be taken into account

by the minimization procedure. The Lagrange multipliers method is devoted to this task leading to the following set of equations:

$$\delta\mathcal{L} = \delta E - \sum_{a}^{n}\sum_{b}^{n} \varepsilon_{ba}\delta[\chi_a|\chi_b] = 0 \tag{2.97}$$

$$\sum_{a}^{n}\sum_{b}^{n} \varepsilon_{ba}\delta[\chi_a|\chi_b] = \sum_{a}^{n}\sum_{b}^{n} \varepsilon_{ba}[\delta\chi_a|\chi_b] + \text{c.c.} \tag{2.98}$$

$$\delta E = \sum_{a}^{n}[\delta\chi_a|h|\chi_a] + \frac{1}{2}\sum_{a}^{n}\sum_{b}^{n}[\delta\chi_a\chi_a|\chi_b\chi_b] - [\delta\chi_a\chi_b|\chi_b\chi_a] + \text{c.c.} \tag{2.99}$$

where c.c. stands for the conjugate values of the left terms, and the variables ε_{ba} are the Lagrange multipliers.

Following the operator formalism introduced above the Hartree-Fock equation is now given by:

$$\delta\mathcal{L} = \sum_{a}^{n}\int \mathbf{r}_1\delta\chi_a^*(\mathbf{r}_1)\left\{h(\mathbf{r}_1)\chi_a(\mathbf{r}_1) + \sum_b\left(\mathcal{J}_b(\mathbf{r}_1) - \mathcal{K}_b(\mathbf{r}_1)\right)\chi_a(\mathbf{r}_1) - \sum_{b}^{n}\varepsilon_{ab}\chi_b(\mathbf{r}_1)\right\} = 0 \tag{2.100}$$

which leads to the set of Hartree-Fock equations:

$$f(\mathbf{r}_1)|\chi_a\rangle = \left[h(\mathbf{r}_1) + \sum_b\left(\mathcal{J}_b(\mathbf{r}_1) - \mathcal{K}_b(\mathbf{r}_1)\right)\right]|\chi_a\rangle = \sum_{b}^{n}\varepsilon_{ab}|\chi_b\rangle \tag{2.101}$$

Solving the Hartree-Fock equation The Fock operator f can be interpreted as an average potential experienced by the ith electron due to the presence of the other electrons. This average potential depends on the others spin orbitals. Therefore the Hartree-Fock equations are non-linear and self-consistent. Consequently they must be solved iteratively. This procedure is called the Self Consistent Field (SCF) method. For further details see [143].

2.3.5.2 Density Functional Theory (DFT)

This approach has been introduced in the early 60's by the theorem exposed by P. Hohenberg and W. Kohn[72]. Their aim was to get rid of the many-body wavefunction, that depends on $3 \times n$ electronic spatial coordinates, and replace it by the more simple electronic density that simply depends on three spatial coordinates, see Eq. (2.102). The main features of this method will now be outlined.

Theory The physical object of importance in this theory is the electronic density, the density $\rho(\mathbf{r})$ of any given system of particles is directly derived from the many-body wavefunction corresponding to this quantum system:

$$\rho(\mathbf{r}) = \int \dots \int d\mathbf{r}_2 \dots d\mathbf{r}_n \psi^*(\mathbf{r}, \mathbf{r}_2, \dots, \mathbf{r}_n)\psi(\mathbf{r}, \mathbf{r}_2, \dots, \mathbf{r}_n). \tag{2.102}$$

The keystones of this theory can be summarized as follows:

- All properties of the electronic ground state and hence of a molecular system at ground state can be completely determined by the ground state density ρ_0;
- The energy of systems having the same type and number of particles in any given external potential can be given using a universal functional. The density that minimize the functional is the exact ground state.

These are existence theorems but no functional and so no solutions can be directly derived from these statements. In order to proceed two assumptions have been proposed by Kohn and Sham in 1964 [84]:

- The exact ground state density $\rho_0(r)$ can be represented by the ground state density of an auxiliary system (described by an auxiliary Hamiltonian) of non-interacting particles, see Eq. (2.103). This hypothesis is known as the "*non-interacting-V-representability*":

  $$E_{\text{KS}}[\rho_0(\mathbf{r})] = E[\rho_0(\mathbf{r})]. \tag{2.103}$$

  This property does not hold for excited states $\rho(r)$:

  $$E_{\text{KS}}[\rho(\mathbf{r})] \neq E[\rho(\mathbf{r})]. \tag{2.104}$$

- The auxiliary Hamiltonian is given by the sum of the usual kinetic operator and an auxiliary potential $V_{\text{eff}}(\mathbf{r})$.

The goal is to propose a relevant starting formulation for the functional. Using the previous formalism from the Hartree-Fock theory one can easily express the electronic density in term of orbitals $\phi_i(\mathbf{r})$:

$$\rho(\mathbf{r}) = \sum_i^n f_i |\phi_i(\mathbf{r})|^2. \tag{2.105}$$

where the f_is represent the integer occupation number of the orbitals.

Following the Kohn-Sham ansatz, almost all the operators of the Hamiltonian can be formally expressed in terms of density-dependent terms:

- $T_s[\rho(\mathbf{r})]$ represents the kinetic contribution to the energy;
- $V_{\text{ext}}(\mathbf{r})$ stands for the nucleus-electron interaction potential;

- $E_{\text{Hartree}}[\rho(\mathbf{r})]$ stands for the classical electron-electron interactions;
- $E_{\text{xc}}[\rho(\mathbf{r})]$ accounts for the exchange correlation contribution due to the Pauli exclusion principle which correlates electrons, as stated by Eqs. (2.83) and (2.96).

Using the above notations, the auxiliary Hamiltonian can be explicitely expressed as:

$$\begin{aligned} E_{\text{KS}}[\rho(\mathbf{r})] &= \underbrace{\frac{1}{2}\sum_{i}^{n} f_i |\nabla\phi_i(\mathbf{r})|^2}_{T_s[\rho(\mathbf{r})]} + \int d\mathbf{r}\rho(\mathbf{r}) \underbrace{\sum_I \frac{Z_I e}{|\mathbf{R}_I - \mathbf{r}|}}_{V_{\text{ext}}(\mathbf{r})} + \\ &\underbrace{\frac{1}{2}\int d\mathbf{r}_1 d\mathbf{r}_2 \frac{\rho(\mathbf{r}_1)\rho(\mathbf{r}_2)}{|\mathbf{r}_1 - \mathbf{r}_2|}}_{E_{\text{Hartree}}[\rho(\mathbf{r})]} + \sum_{I,J} \frac{Z_I Z_J e^2}{R_{IJ}} + E_{\text{xc}}[\rho(\mathbf{r})]. \end{aligned} \tag{2.106}$$

The constrained minimization of this functional (2.106) with respect to the one electron orbitals by means of the Lagrange multipliers method leads to the Kohn-Sham equations:

$$\frac{1}{f_i}\frac{\partial E_{\text{KS}}[\rho(\mathbf{r})]}{\partial\phi_i(\mathbf{r})} = \underbrace{\left[-\frac{1}{2}\nabla^2 + V_{\text{ext}}(\mathbf{r}) + \frac{\delta E_{\text{Hartree}}}{\delta\rho(\mathbf{r})} + \frac{\delta E_{\text{xc}}}{\delta\rho(\mathbf{r})}\right]}_{\mathcal{H}_{\text{KS}}} \phi_i(\mathbf{r}) = \varepsilon_i\phi_i(\mathbf{r}) \tag{2.107}$$

which can be reformulated by the following Schrödinger equation:

$$(\mathcal{H}_{\text{KS}} - \varepsilon_i)\phi_i(\mathbf{r}) = 0 \tag{2.108}$$

where $\mathcal{H}_{\text{KS}}$ is the effective Hamiltonian and ε_i are its corresponding eigenvalues. The functional derivative of the exchange correlation energy is called the exchange correlation potential:

$$V_{\text{xc}}[\rho(\mathbf{r})] = \frac{\delta E_{\text{xc}}}{\delta\rho(\mathbf{r})} \tag{2.109}$$

The exact expression for the exchange correlation functional is unknown and some additional hypotheses have to be considered. The simplest approximation relies on the assumption that the exchange-correlation energy density at each point corresponds to the one of the homogeneous electron gas. However, even for such a simple model system the expression of the correlation energy has to be calculated numerically with Monte Carlo methods. This approximation is called the Local Density Approximation (LDA), see (2.110). Some more advanced approximations, the so-called Generalized Gradient Approximations or GGA, are based on more complex operators making use of the density gradient of mth order, see (2.111).

$$E_{\text{xc}}^{\text{LDA}}[\rho(\mathbf{r})] = \int d\mathbf{r}\rho(\mathbf{r})\varepsilon_{\text{xc}}^{\text{LDA}}\left(\rho(\mathbf{r})\right) \tag{2.110}$$

$$E_{\text{xc}}^{\text{GGA}}[\rho(\mathbf{r})] = \int d\mathbf{r}\rho(\mathbf{r})\varepsilon_{\text{xc}}^{\text{GGA}}\left(\rho(\mathbf{r}); \nabla^n\rho(\mathbf{r})\right). \tag{2.111}$$

2.3.5.3 Choosing the appropriate method

As discussed in the previous subsection, the Hartree-Fock approach requires the diagonalization of the matrix associated to the Fock operator. This is a calculation of order M^3, where M stands for the number of elements of the basis set (number of plane waves or number of Gaussians). Furthermore, the 4-index matrix elements needed to compute the Fock matrix scales like a M^4 process. This makes the Hartree-Fock method useful for single molecules made with a rather small number of electrons by means of Gaussian basis set. In this work we aim at performing MD simulations of relatively large systems (100 atoms) on relatively long time scale (up to 10 ps). Thus the more computationally tractable DFT method has been favored for this task.

2.3.6 Ab initio molecular dynamics

As already mentioned earlier, the direct resolution of the time dependent Schrödinger equations is not affordable due to both mathematical (many-body problems) and numerical problems (CPU time). Several approaches (Ehrenfest, Born-Oppenheimer, Car-Parrinello molecular dynamics) have been developed in order to circumvent these difficulties.

2.3.6.1 Born-Oppenheimer molecular dynamics

The complicated time-dependent equations of motion linking the ionic wavefunction and the electronic wavefunction is simplified assuming that ions are classical particles, and that electronic wavefunctions depend implicitly on time [90]. The electronic and the ionic degrees of freedom are coupled through the adiabatic approximation, see section (2.3.2), and for this reason this method is called the Born-Oppenheimer molecular dynamics method (BOMD). The equations of motions of the BOMD are:

$$M_I \ddot{\mathbf{R}} = -\nabla_I \left(\min_{\psi_0} \{ \langle \psi_0 | \mathcal{H}_\mathrm{e} | \psi_0 \rangle \} \right) \quad (2.112)$$

$$E_0 | \psi_0 \rangle = \mathcal{H}_e | \psi_0 \rangle \quad (2.113)$$

Here, the time-dependence of the electronic degrees of freedom follows from the parametrical dependence of the electronic wavefunction with respect to the nuclear positions. This approach is time consuming as the minimum of energy of the electronic system has to be reached self consistently for each time step.

2.3.6.2 Car-Parrinello molecular dynamics

The aim of this method is to avoid any systematic energy minimizations of the electronic wavefunction. To achieve this goal the wavefunction is coupled more explicitely to the time variable by introducing a fictitious dynamics of the electrons. This coupling is considered fictitious as it is not grounded on any physical assumption. The Car-Parrinello (CP) molecular dynamics (CPMD) should be regarded as an on-the-fly optimization scheme [53, 99]. This method relies on the use of an extended Lagrangian

considering the wavefunction as a function of its one-particle orbitals ϕ_i. The functional derivatives with respect to the one-particle orbitals can then be interpreted as classical fields that drive the wavefunction to its minimum [99]. As ions and electrons evolve altogether it is not possible to converge to the electronic ground state corresponding to the instantaneous ionic configuration at each time step. This means that the instantaneous wavefunction and so the associated forces do not correspond to the BO forces. Some orthonormality constraints are also included in the extended Lagrangian through a set of Lagrange multipliers (Λ_{ij}). A fictitious kinetic term with a fictitious mass (μ) is added to the Lagrangian [25, 99, 151]:

$$\begin{aligned}\mathcal{L} &= \mu \sum_i \int d\mathbf{r} \langle \dot{\phi}_i(\mathbf{r}) | \dot{\phi}_i(\mathbf{r}) \rangle + \frac{1}{2} \sum_I M_I \dot{\mathbf{R}}_I^2 - E\left[\{\phi_i\}, \{\mathbf{R}_I\}\right] \\ &+ \sum_{i,j} \Lambda_{ij} \left(\int d\mathbf{r} \phi_i^*(\mathbf{r}) \phi_j(\mathbf{r}) - \delta_{ij} \right).\end{aligned} \tag{2.114}$$

The corresponding Euler-Lagrange equations of motion derived from Eq. (2.114) are:

$$\mu \ddot{\phi}_i(\mathbf{r}, t) = -\frac{\delta E}{\delta \phi_i^*(\mathbf{r}, t)} + \sum_j \Lambda_{ij} \phi_j(\mathbf{r}, t), \tag{2.115}$$

$$M_I \ddot{\mathbf{R}} = -\nabla_I E\left[\{\phi_i\}, \mathbf{R}\right]. \tag{2.116}$$

The conserved quantity associated to this Lagrangian is:

$$E_{\text{tot.}} = \sum_i \frac{1}{2} \mu_i \left\langle \dot{\phi}_i | \dot{\phi}_i \right\rangle + \sum_I \frac{1}{2} M_I \dot{\mathbf{R}}_I^2 + \langle \psi_0 | \mathcal{H}_e | \psi_0 \rangle. \tag{2.117}$$

Following the adiabatic approximation and according to the variational principle, the wavefunction has to be close to its ground state during a molecular dynamics simulation. The electronic degrees of freedom must evolve adiabatically. As a consequence the fictitious mass μ controlling the inertia of the orbitals has to be checked to ensure a proper decoupling of the electrons with respect to the nuclei. Two competing criteria have to be taken into account. The fictitious mass has to be chosen such that the lowest electronic eigenfrequency is above the highest phonon frequency[26]. On the contrary setting μ to very low values to ensure a proper decoupling of the ionic and electronic degrees of freedom can be realized at the expense of the computational time efficiency as the maximum length of the molecular dynamics time step $\delta t^{\max}$ is proportional to [113]:

$$\delta t^{\max} = \left(\frac{\mu}{E_{\text{cut}}} \right)^{1/2}, \tag{2.118}$$

here E_{cut} represents the cutoff used for defining the plane waves basis set, see section (2.3.3).

During a well-conditioned CP run the electronic wavefunction should be always close to the BO surface (*i.e.* the minimum energy ground state). Due to the addition

[26] These electronic vibration mode scale with $\mu^{-1/2}$

of electronic terms in the Lagrangian the total ionic momentum is not equal to zero at each time step. However this does not disturb the physical time evolution due to the smallness and boundness of the observed differences and the intrinsic averaging effect of small-amplitude high-frequency oscillations within a few molecular dynamics time steps. The accuracy of the simulation can be monitored through the fictitious kinetic energy associated to the electronic wavefunction ($\propto 1/2 \sum_i \mu_i \dot{\phi}_i^2$). To remain close to the Born-Oppenheimer surface the electronic temperature has to remain close to zero.

The standard CP works for systems with a gap. The typical minimum frequency of the electronic mode $w_e^{\min}$ is connected to the band gap[27] E_{gap} through:

$$w_e^{\min} \propto \left(\frac{E_{\text{gap}}}{\mu} \right)^{1/2} . \tag{2.119}$$

When considering metallic or metal-like systems for example, the electronic gap is very small or even vanishes ($E_{\text{gap}} \to 0$), in such systems zero-frequency electronic modes $w_e^{\min} = 0$ overlap with the phonon spectrum, the adiabaticity[28] does not hold anymore. The energy flow (and so the corresponding temperature drift) from ions to electrons can be counterbalanced by thermostats [137], this method is especially useful for systems having a small electronic gap E_{gap}.

2.3.6.3 Choosing the appropriate method

In this work we have used the Car-Parrinello approach for two main reasons. First the CP approach only needs a single orthogonalization process at each time step which is by far more tractable than the full systematic diagonalizations required by the BO molecular dynamics. Moreover the energy conservation is accurately fulfilled which makes the CP method applicable to the microcanonical ensemble. On the contrary the BO molecular dynamics leads to some systematic drift, the total energy is hardly conserved with this method, in practice it has to be coupled with ionic thermostats [99].

2.4 Characterization of the samples

The molecular dynamics trajectories we obtained by means of the aforementioned approaches have been characterized using standard observables. The definition of these observable and their physical fundaments are described in this section.

2.4.1 Structural analysis

Pair distribution function The number of atomic pairs $dn_{\alpha\beta}$ given for two definite species α and β (α,$\beta \in \{\text{Si,O}\}$) separated by a distance ranging in between r and $r+dr$

[27] The electronic gap E_{gap} refers to the energy difference between the top of the valence band and the bottom of the conduction band, where electrons are able to jump from one band to another.

[28] Refer to section (2.3.2) for the definition of quantum adiabaticity.

can be formally given as a function of the pair correlation function (PDF) $g_{\alpha\beta}(r)$ by:

$$dn_{\alpha\beta} = \frac{\mathcal{N}_{\alpha\beta}}{V} g_{\alpha\beta}(r) 4\pi r^2 dr \qquad \text{with} \qquad \mathcal{N}_{\alpha\beta} = \begin{cases} N_\alpha (N_\alpha - 1) & \text{if } \alpha = \beta \\ N_\alpha N_\beta & \text{if } \alpha \neq \beta \end{cases} \tag{2.120}$$

where N_α and N_β represent the number of atoms α and β. The function $g_{\alpha\beta}(r)$ can also be defined using the local (particle) density $\rho_{\alpha\beta}(r)$ as follows:

$$\rho_{\alpha\beta}(\mathbf{r}) = \sum_{i=1}^{N_\alpha} \sum_{j=1, j\neq i}^{N_\beta} \delta(\mathbf{r} - \mathbf{r}_i + \mathbf{r}_j), \qquad \alpha, \beta = \{\text{Si, O}\}. \tag{2.121}$$

Using the above function (2.121) one can define the pair distribution function $g_{\alpha\beta}(r)$ (also named pair correlation function) of Eq. (2.120) as:

$$g_{\alpha\beta}(r) = \frac{V}{\mathcal{N}_{\alpha\beta}} \left\langle \rho_{\alpha\beta}(\mathbf{r}) \right\rangle . \tag{2.122}$$

In the above equation $\langle \cdot \rangle$ stands for the ensemble average. By construction $g_{\alpha\beta}(r) = 1$ for an ideal gas. For a non ideal system any deviation of $g_{\alpha\beta}(r)$ from unity reflects correlations between the particles due to the intermolecular interactions [53]. The pair distribution function describes the density of interatomic distances in a material. The PDF presents some characteristic oscillations for short and intermediate distances. The first maximum represents the average distance between an atom of type α and its first neighbors of type β, the second peak corresponds to the second neighbors shell, etc ... For large distances these oscillations vanish to converge slowly to 1, and this accounts for the equiprobability of spatial atomic distributions.

Structure factor Scattering experiments give direct access to informations in the reciprocal space. To establish a connection between experiment and simulation it can be worthwhile to calculate the partial structure factors which are given via the Fourier transform of the corresponding pair correlation function:

$$S_{\alpha\beta}(\mathbf{k}) = 1 + \frac{\mathcal{N}_{\alpha\beta}}{V} \int \exp\left[-i\mathbf{k}\cdot\mathbf{r}\right] g_{\alpha\beta}(\mathbf{r}) d\mathbf{r} \quad \text{with} \quad \alpha, \beta \in \{\text{Si,O}\} \tag{2.123}$$

The structure factor can be expressed as a sum using the definition of Eq. (2.121) in Eq. (2.123):

$$S_{\alpha\beta}(\mathbf{k}) = \frac{1}{N} \left\langle \sum_{i=1}^{N_\alpha} \sum_{j=1}^{N_\beta} \exp\left[i\mathbf{k}\cdot\mathbf{r}_{ij}\right] \right\rangle \tag{2.124}$$

To compare our results for the structure factors to the experimental results extracted from the neutron diffraction for real silica we have also calculated the neutron scattering function $S_n(|\mathbf{k}|)$[29]:

$$S_n(|\mathbf{k}|) = \frac{1}{N_{\text{Si}} b_{\text{Si}}^2 + N_{\text{O}} b_{\text{O}}^2} \sum_{i=1}^{N} \sum_{j=1}^{N} b_i b_j \left\langle \exp\left[i\mathbf{k}\cdot\mathbf{r}_{ij}\right] \right\rangle \tag{2.125}$$

[29] In the expression of $S_n(|\mathbf{k}|)$ we use the norm of $\mathbf{k}$ as we assume the system is isotropic, this assumption is valid for a liquid or an amorphous system.

where the b_i are the neutron scattering lengths, for further details see [63]. Sears [131] has reported for b_{Si} and b_{O} the values 0.4149^{-12} cm and 0.5803^{-12} cm, respectively.

Angle distribution functions In order to further characterize the local structure of a given material one can use the angular distribution functions. The angles are defined between a particle j and two particles belonging to the neighborhood of j. The particles neighboring the particle j have a distance compatible with the first peak of the PDF. These distributions are especially suited for investigating the geometry of networks. Silica is a strong glass former made of interconnected tetrahedral patterns, see Fig. 2.15. The probability distributions of the $\widehat{\mathrm{OSiO}}$ and $\widehat{\mathrm{SiOSi}}$ angles give information about the intra-tetrahedral and inter-tetrahedral geometry, respectively (see Fig. 2.15). The probability $P_{\widehat{\alpha\beta\gamma}}(\theta)$ of having an angle θ between atoms of type α, β and γ is given by:

$$P_{\widehat{\alpha\beta\gamma}}(\theta) = \frac{1}{\mathcal{N}} \left\langle \sum_{i=1}^{N_\alpha} \sum_{j=1}^{N_\beta} \sum_{k>i}^{N_\gamma} \delta(\theta_{ijk} - \theta)\Theta(r_{\alpha\beta} - r_{ij})\Theta(r_{\beta\gamma} - r_{jk}) \right\rangle \tag{2.126}$$

where $\Theta(x)$ stands for the Heaviside function which screens out the irrelevant bond lengths. The maximum bond lengths ($r_{\alpha\beta}$, $r_{\beta\gamma}$) are defined through the first minima of the Si-O partial pair correlation function[30]. The constant $\mathcal{N}$ is a normalization constant.

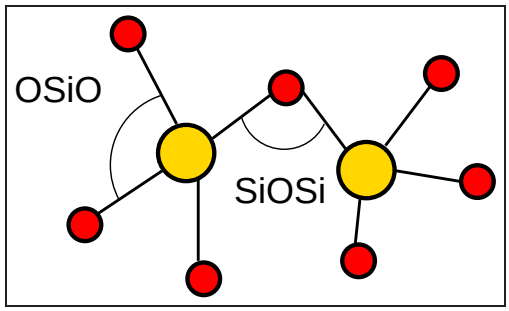

Figure 2.15: Sketch of the specific angles defined in a silica network.

[30] $\simeq 2.35$Å.

Chapter 3

Ab Initio simulation

In this thesis we aim at describing with accuracy the interactions between atoms in silica. These interactions can be described with details at the atomic level by means of *ab initio* simulations. In the previous chapter we have introduced the main principles of quantum mechanics along with the hypothesis/approximations and numerical methods commonly assumed to solve the many-body problem arising from the electron-electron interactions. Choosing the appropriate approximation can be motivated by physical assumptions, but most of the time setting up the appropriate parameters can be seen as an art. In this chapter we will expose the different parameters chosen for silica and the methodological approach followed to generate liquid silica models by means of *ab initio* simulations.

3.1 Parameters calibration: Energies, forces, stresses

CPMD All the *ab initio* calculations carried out in this work have been made using `CPMD 3.9.2`[1] [25, 33, 99]. The CPMD code is a parallelized plane wave/pseudopotential implementation of Density Functional Theory, particularly designed for *ab initio* molecular dynamics.

Functional The choice of the right exchange functional correlation, already described in section (2.3.5.2), is of great importance. In the past silica polymorphs have been extensively investigated using DFT. D. R. Hamann [62] has compared features issued from both LDA and GGA functional approximations for the high pressure phase transition in between α-quartz and stishovite. In this study it was demonstrated that GGA yields correct relative energies and reasonably good prediction of the transition pressure. However, the structural parameters are less accurate than those predicted by LDA calculations. Moreover, local density approximation has been extensively used in previous work on silica phases, especially for its amorphous and liquid form, and has been reported to give reliable results when compared to experiments [10, 11, 12, 127, 128]. In this work we have used the LDA form proposed by Goedecker *et al.* [55].

Pseudopotential Pseudopotentials are of great importance in *ab initio* simulations as they mimic the influence of the core states on the valence wavefunctions. By using these potentials one gets rid of numerically handling the core states which are not any longer explicitely considered. The pseudopotential formulations proposed by Bachelet-Haman-Schlüter [6] and Troullier-Martins [148] have been respectively used for the silicon and oxygen atoms according to the methodology proposed in previous works [10].

Energy Cutoff As mentioned in section (2.3.3), the energy cutoff parameter determines the accuracy of the wavefunctions and all its related features such as energy/forces/stress tensor. This cutoff dependence has been checked on an amorphous system of 114 atoms, see Figs. 3.1, 3.2 and 3.3. Covalent interactions in silicates are mostly controlled by the oxygen electrons, for an accurate description of the densely charged parts of the electronic density, namely the two oxygen lone pairs and the four bindings sp^3 orbitals of silicon, one should consider an energy cutoff higher than 70 Ry, see Fig. 3.1. For these values, see Figs. 3.1 and 3.2, the energy and the forces are reasonably converged. The stress tensor, see appendix (A), is more problematic, even if this quantity can be considered as a first order energetic feature like forces. In practice we know that the convergence of the stress tensor is hard to achieve, in classical simulations using the BKS potential the stress tensor was found to be sensitive to the short range cutting distance [153]. In quantum simulations a proper convergence of the stress tensor is also difficult to achieve with a 70 Ry cutoff[2] as illustrated by Fig.

[1] `http://www.cpmd.org/`

[2] The stress tensor is calculated by summing many atomic and non-local contributions. The overall error cumulated while summing all the individual contribution may account for the imprecision of the

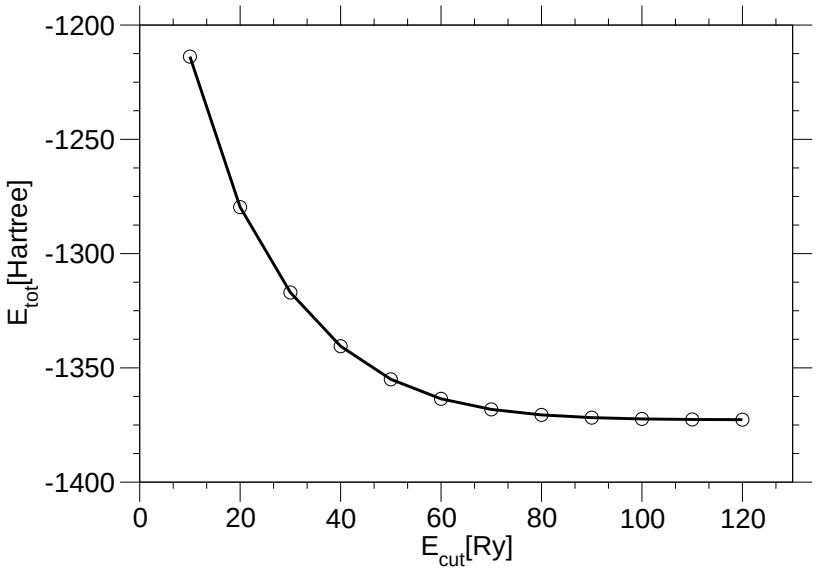

Figure 3.1: The total electronic energy (in Hartree unit, 1 Ha= 2 Ry) as function of the energy cutoff.

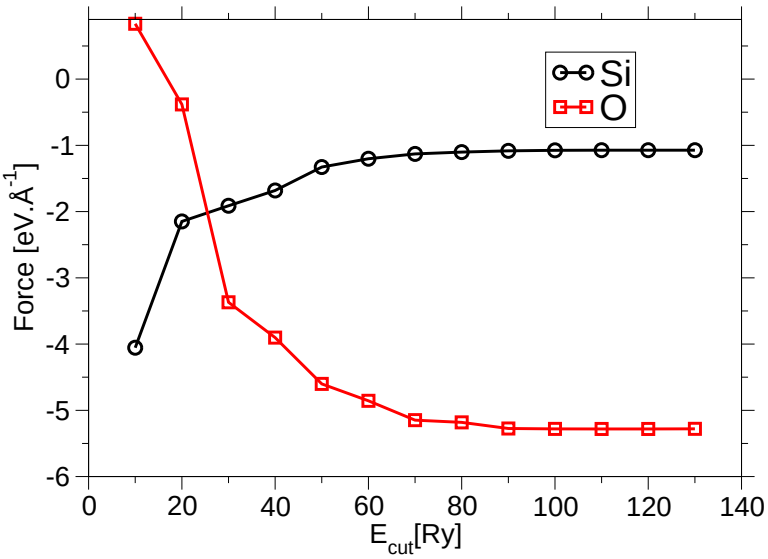

Figure 3.2: The x-component of the force for a silicon atom and for an oxygen atom represented as a function of the energy cutoff for a sample of liquid silica made of 114 atoms..

3.3. We opted for a 130 Ry cutoff[3] for the calculation of the forces that are destined

stress tensor when using a 70 Ry cutoff.

[3]For a cubic box made of 114 atoms with $L_{box} \simeq 12$ Å, a 70 Ry cutoff accounts for 459329 plane waves, while using a 130 Ry cutoff requires 1162083 plane waves, the energy cutoff $E_{\rm cut}$ is defined as the squared value of the reciprocal vector. The scaling factor between the two numbers of planewaves

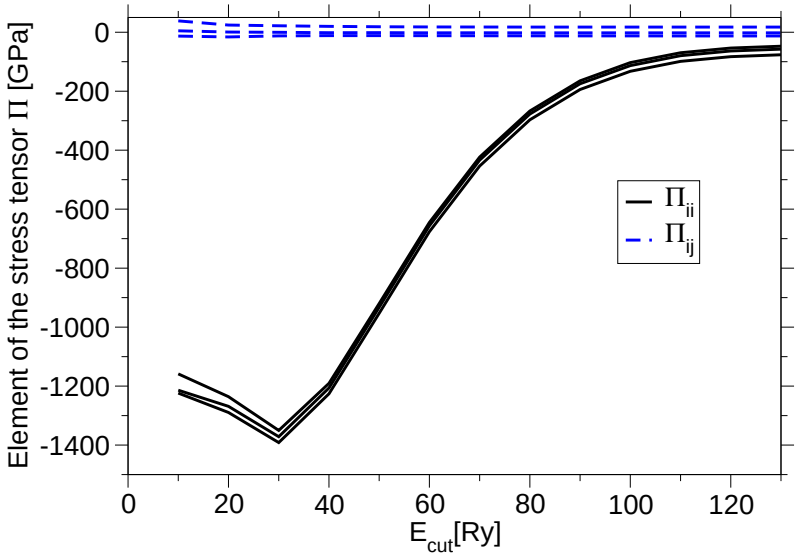

Figure 3.3: Diagonal (ii) and off-diagonal (ij) components of the stress tensor Π represented with respect to the energy cutoff. The internal pressure P is given by $P = \Pi_{11}+\Pi_{22}+\Pi_{33}$.
.

to be used in the fitting procedure in chapter (4). The 130 Ry cutoff has been chosen consistently with the results of our calculations presented on Fig. 3.3 and to the values reported in the literature [145]. A 70 Ry cutoff has been used for the CP molecular dynamics runs.

3.2 Crystalline phases: Pseudo-Potential validation

Introduction Investigating crystalline phases by means of first-principles approaches can be viewed as an evidential test for checking the validity of the simulation parameters. Crystals show translational invariance properties which are compatible with the periodic boundary conditions used in simulation. According to Bloch's theorem, see section (2.3.1), accurate simulations can be carried out on such system even with a restrained number of atoms by averaging over k-points. Due to the symmetric properties of crystals only few parameters (lattice constants and asymmetric parameters) are needed to define their overall structure. Moreover, these parameters can be experimentally determined with a great accuracy [154, 103, 161]. For this reason the comparison of the predicted structure to the experimental one can be envisaged as an enlightening test for the simulation parameters (functional, pseudopotentials and cutoff). These tests have partially been carried out by M. Benoit and coworkers [10] but the precise influence of the stress tensor on the lattice parameters calculation has not been tackled. In this section we clarify this issue.

is $(130/70)^{3/2} = 2.828 = 1162083/459329$.

3.2.1 α-quartz

The α-quartz, see Fig. 3.4 is the stable crystalline phase of silica. Its stability domain goes from 0 K to 846 K at 1 bar, above 846 K α-quartz undergoes a phase transition to β-quartz. As α-quartz is very stable for low temperatures there is no need to take into account the effects of the thermal expansion to accurately reproduce the cell parameters, a simple optimization procedure is sufficient in this case. Moreover, due to this high stability at standard conditions of pressure and temperature, α-quartz has been widely investigated by experiments. Moreover, quartz can be considered as being a low-symmetrical polymorph of silica (fewer internal constraints than β-cristobalite for example), which means that several parameters are required to define properly the structure. For all these reasons α-quartz can be regarded as a relevant crystalline phase for testing the chosen pseudopotentials.

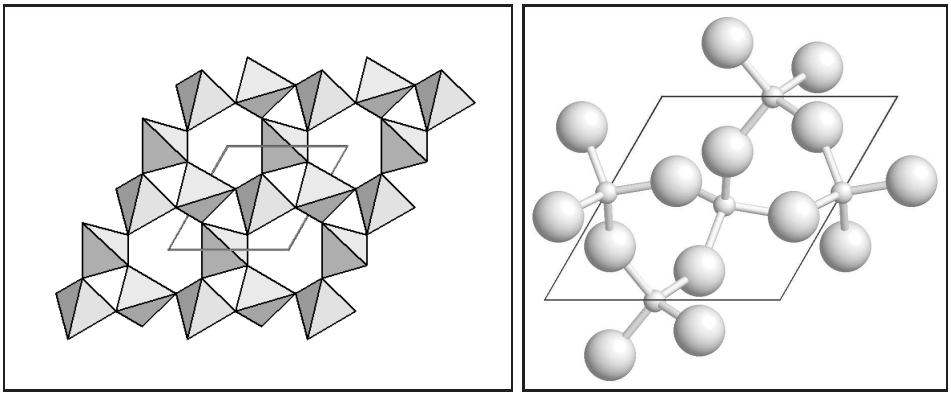

Figure 3.4: Left panel: α-quartz network of interconnected tetrahedra in the conventional setting. Right panel: The atomic structure of α-quartz according to the space group $P3_121$, the silicon atoms are represented by small spheres, while oxygen atoms are represented by big spheres.

Geometry optimization With a view to checking whether the *ab initio* methodology we have set up is able to predict the equilibrium structure of α-quartz, we have performed two kinds of geometric optimizations. In the first case the atomic positions are relaxed at constant cell parameters. In the second case, both atomic positions and cell parameters are optimized. As stated in appendix A the forces applied on the cell are proportional to the stress tensor, thus while optimizing the cell parameters we can checked if the internal pressure of the system were reliably described, see Eq. (A.63). The simulations have been carried out using $2 \times 2 \times 2$ trigonal unit cell corresponding to a 72 atom sample.

As reported by Xu [165] and Chelikowsky [31] the energy band diagram of α-quartz for valence states is relatively flat and thus one can consider that calculations can be limited to the Γ point only as energetic features do not depend on the crystal momentum, see section (2.3.1). The results are presented in Table 3.1. The structure

is in very good agreement with the experimental one and comparable with the ones given in literature using the same kind of methodology [94, 62]. It is worthwhile to note that for the frozen cell case the internal pressure is badly reproduced ($\simeq -3$ GPa). This negative pressure accounts for the volume contraction observed during the full lattice optimization.

Parameters	Experiment	fixed cell	error[%]	relaxed cell	error[%]
a[Å]	4.9124	-	-	4.850	1.27
c[Å]	5.4038	-	-	5.350	0.99
α[°]	90.	-	-	90.1	0.11
β[°]	90.	-	-	89.9	0.11
γ[°]	120.	-	-	120.1	0.08
V[Å^{-3}]	112.933	-	-	108.850	3.68
u	0.4701	0.471	0.19	0.464	1.29
x	0.4139	0.414	0.24	0.411	0.70
y	0.2674	0.265	0.89	0.283	5.83
z	0.2144	0.212	1.12	0.212	1.12

Table 3.1: Cell parameters for α-quartz crystal. The results corresponding to the *ab initio* simulations have been carried out at 0K on a 72 atoms sample using $E_{\text{cut}} = 130$ Ry.

Phonon density of states A phonon is a quantized mode of vibration occurring in a rigid lattice. The study of phonons is an important part of solid state physics, because phonons play a major role in many of the physical properties of solids, including the thermal and electrical conductivities of materials. At low temperature these vibrations can be treated within the harmonic approximation. The distribution of vibrational states (VDOS) over frequency $g(\nu)$ gives the number of vibrational states having a frequency in the range ν and $\nu + d\nu$.

Within the harmonic approximation the potential energy of the system V can be written as a function of $\mathbf{u}_i$ which corresponds to the displacement of the atoms i from its equilibrium positions $\mathbf{r}_i^0$:

$$\mathbf{u}_i^0 = \mathbf{r}_i - \mathbf{r}_i^0 \tag{3.1}$$

Using the above notation the potential energy V of the system can be expressed:

$$V(\{\mathbf{r}\}) \simeq V(\{\mathbf{r}^0\}) + \sum_{i,\alpha} \left(\frac{\partial V(\{\mathbf{r}\})}{\partial r_{i,\alpha}} \right)_{\{\mathbf{r}^0\}} u_{i,\alpha} + \sum_{i,\alpha;j,\beta} \left(\frac{\partial^2 V(\{\mathbf{r}\})}{\partial r_{i,\alpha} \partial r_{j,\beta}} \right)_{\{\mathbf{r}^0\}} u_{i,\alpha} u_{j,\beta}, \tag{3.2}$$

here $u_{i,\alpha}$ represents the Cartesian coordinates of the displacement $\mathbf{u}_i$ with $\alpha \in \{x, y, z\}$.

The coupled equations of motion of the system are:

$$m_i \frac{\partial^2 \mathbf{r}_i}{\partial t^2} \quad = \quad \mathbf{F}_i(\mathbf{r}) = -\frac{\partial E(\{\mathbf{r}\})}{\partial \mathbf{r}_i} \tag{3.3}$$

$$m_i \frac{\partial^2 u_{i,\alpha}}{\partial t^2} = -\sum_{j,\beta} C_{i,\alpha;j,\beta} u_{j,\beta}, \tag{3.4}$$

where

$$C_{i,\alpha;j,\beta} = \left(\frac{\partial^2 V(\{\mathbf{r}\})}{\partial r_{i,\alpha} \partial r_{j,\beta}} \right)_{\{\mathbf{r}^0\}}. \tag{3.5}$$

Using the above equation one can define the dynamical matrix:

$$D_{i,\alpha;j,\beta} = \frac{1}{\sqrt{m_i m_j}} C_{i,\alpha;j,\beta}. \tag{3.6}$$

The system of equations described in Eq. 3.4 can be solved in the harmonic approximation where the vibrational modes at frequency w are described by displacements:

$$\mathbf{u}_i(t) = \mathbf{u}_i \exp(\imath w_\nu t). \tag{3.7}$$

so that Eq. 3.4 becomes for each i:

$$-w_\nu^2 m_i u_{i,\alpha} = -\sum_{j,\beta} C_{i,\alpha;j,\beta} u_{j,\beta} \tag{3.8}$$

The full solution for all vibrational states is the set of independent oscillators, each with vibrational frequency w_ν determined by the classical equation:

$$\det \left| \frac{1}{\sqrt{m_i m_j}} C_{i,\alpha;j,\beta} u_{j,\beta} - w_\nu^2 \right| = 0 \tag{3.9}$$

The associated set of vectors corresponding to a given eigenfrequency give the normalized direction for the displacement of each atoms at w_ν.

In this work the VDOS of α-quartz has been calculated and processed using the correction function derived by Taraskin and Elliot [146] with a view to comparing it to the neutron scattering experiments carried out by Strauch [141], see Fig. 3.5.

This correction function connects the vibrational density of states given by simulation (named "true" vibrational density of states according to the nomenclature of Ref. [146]) with the one measured in inelastic neutron experiments. Experimentally, the VDOS is extracted from an analysis of the dynamical structure factor[4] which is only roughly proportional to the true VDOS. However the inelastic neutron scattering VDOS $g_{\text{ins}}(\nu)$ can be connected to the true VDOS $g(\nu)$ using the correction function $C(\nu)$ as follows:

$$g_{\text{ins}}(\nu) = C(\nu) g(\nu) \tag{3.10}$$

where $C(\nu)$ is given by:

$$C(\nu) \simeq 1 + \frac{m_{\text{Si}} + 2m_{\text{O}}}{b_{\text{Si}}^2 + 2b_{\text{O}}^2} [\rho_{\text{Si}}(\nu) - \rho_{\text{Si}}^{(0)}] \left(\frac{b_{\text{Si}}^2}{m_{\text{Si}}} - \frac{b_{\text{O}}^2}{m_{\text{O}}} \right) \tag{3.11}$$

[4] $S(\mathbf{Q},\omega) = \frac{1}{2\pi\hbar N \langle b^2 \rangle} \int_\infty^\infty \sum_{i,i'} \overline{b_i b_{i'}} \left\langle e^{\imath \mathbf{Q}.\mathbf{R}_i(0)} e^{\imath \mathbf{Q}.\mathbf{R}_{i'}(t)} \right\rangle e^{\imath\omega t} dt$

$$\rho_{\mathrm{Si}}(\nu_j) = \sum_{i\in\mathrm{Si}} |\mathbf{e}_i^j|^2 / \sum_{\ell} |\mathbf{e}_\ell^j|^2 \tag{3.12}$$

$$\rho_{\mathrm{Si}}^{(0)} = \frac{N_{\mathrm{Si}} m_{\mathrm{Si}}}{N_{\mathrm{Si}} m_{\mathrm{Si}} + N_{\mathrm{O}} m_{\mathrm{O}}}. \tag{3.13}$$

In the above equations m_i represents the mass of the atom i, b_i is the scattering cross section, N_i is the number of atoms of species i, $N = N_{\mathrm{Si}} + N_{\mathrm{O}}$ stands for the total number of atoms considered. The vector $\mathbf{e}_i^j$ corresponds to the displacement of the particle i at frequency ν_j.

The experimental spectrum of α-quartz presented in Fig. 3.5 has been built by summing of the contributions of the different dispersion branches given in Ref. [141]. The density has then been smoothed using a Gaussian broadening of width $2\sigma = 1.05$ THz. It is worthwhile to note that neutron scattering experiments may lack of precision in the low frequency range, below 8 THz, as the Brillouin zone has not been homogeneously sampled [141]. We note that the calculated high-frequency double peak position is in very good agreement with experimental data. This was not the case for a similar calculation using the DFT LDA reported by Roma *et al.* [123] on a $2 \times 2 \times 1$ supercell (36 atoms) when the positions and the widths of this high frequency band do not agree with experimental data. In the intermediate frequency range (10 to 30 THz), the peak heights and frequencies are qualitatively well reproduced.

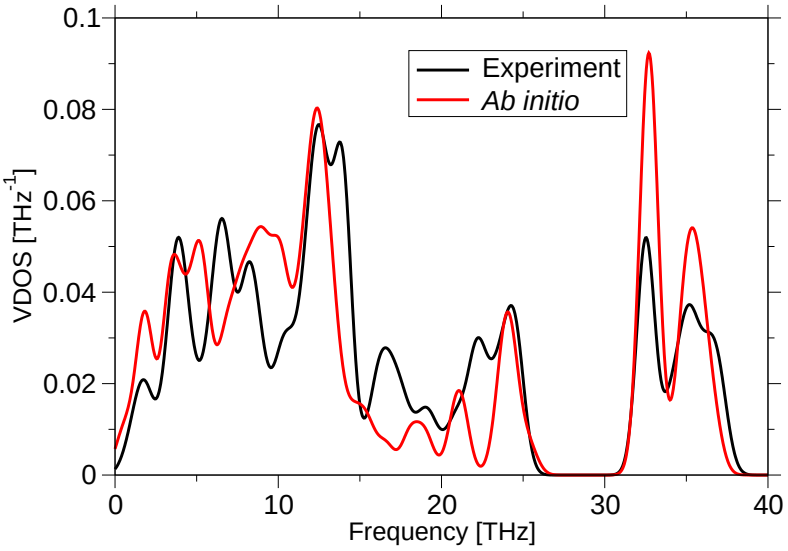

Figure 3.5: Vibrational density of states of α-quartz. The experimental data at 20K from [141], and present *ab initio* data at 0K.

Molecular dynamics Car-Parrinello molecular dynamics simulations have been carried out on the crystalline sample at 300 K using the experimental lattice parameters. The temperature investigated is low ($T_{\mathrm{melt}} \simeq 1500$ K), the ions move with small amplitude around their equilibrium positions. Moreover the electronic gap, see section

(2.3.6.2), in α-quartz is well-defined see Fig. 3.9, as a consequence there is no need to use the ionic and electronic thermostats, see section (2.3.6.2). The normalized differential correlation function $T_n(r)$ has been computed and compared to the experimental data provided by Tucker and coworkers [150]. The TCF can be defined using the partial pair correlation function $g_{ij}(r)$:

$$T_n(r) = \frac{\sum_{i,j\in\{\mathrm{Si,O}\}} c_i b_i c_j b_j (g_{ij}(r) - 1)}{\sum_{i\in\{\mathrm{Si,O}\}} (c_i b_i)^2} + 1, \tag{3.14}$$

where $c_i = N_i/N$ (N_i corresponds to the number of atoms i considered, whereas N stands for the total number of atoms), b_i is the neutron scattering cross section of atom i. Apart from the first peak height, all the peaks are well localized and well reproduced (see Fig. 3.6). The first peak is connected to the Si-O bond at 1.60 Å. The second peak accounts for the O-O distances the small pre-peak a 3.05 Å corresponds to the Si-Si pair.

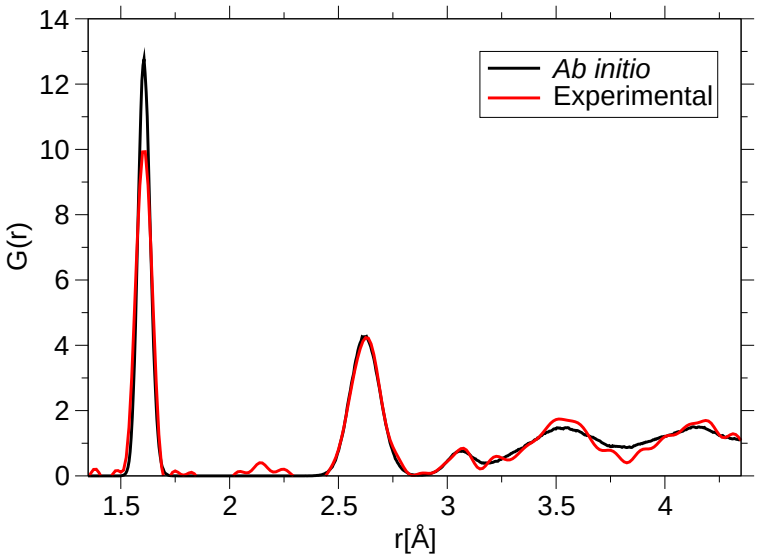

Figure 3.6: In black, the *ab initio* pair correlation function as defined in Eq. (3.14). The overall length of the simulation is equal to 11.5 ps, the average temperature is equal to 308K. In red the experimental $G(r)$, the small peaks at 2.15Å and the pre-peaks surrounding the Si-O peaks at 1.6Å can be considered as noise.

3.2.2 β-cristobalite

The β-cristobalite is the stable crystalline phase of silica for high temperature. Its stability domain ranges from 1743K to 2000K at 1 bar. Above 2000K the crystal melts. Although the structures of most SiO_2 polymorphs are well known, the determination of structure of β-cristobalite has been controversial, with at least five different structural forms proposed up to now [8, 111, 116, 162, 163]. Many studies on cristobalite refer

to its hypothetical "ideal" form as proposed by Wyckoff [164], this structure is represented in Fig. 3.7. In this section we will refer to the structure proposed by Wright and Leadbetter [161], this crystal is different from the one proposed by Wyckoff, the structure can be visualized as resulting from rotations of about $\pm 20°$ of each SiO_4 tetrahedron of the ideal structure, see Fig. 3.8.

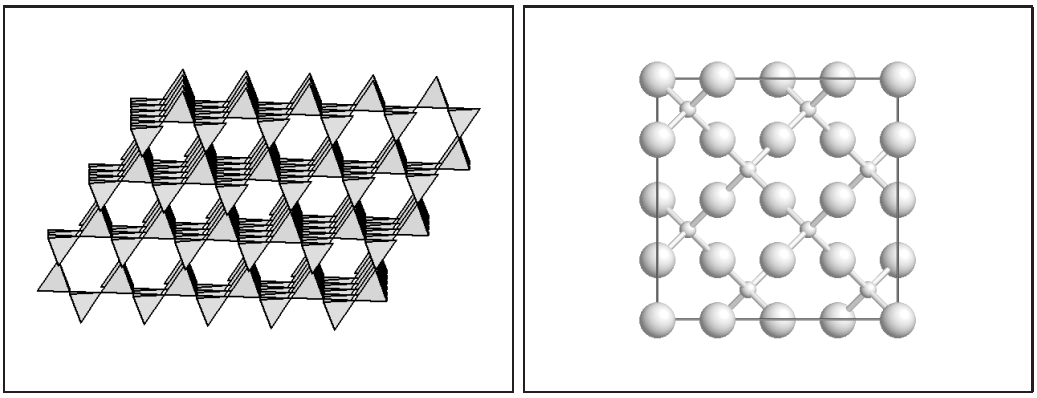

Figure 3.7: Left panel: β-cristobalite network of interconnected tetrahedra. Right panel: The atomic structure of β-cristobalite, the silicon atoms are represented by small spheres, oxygen atoms are represented by big spheres.

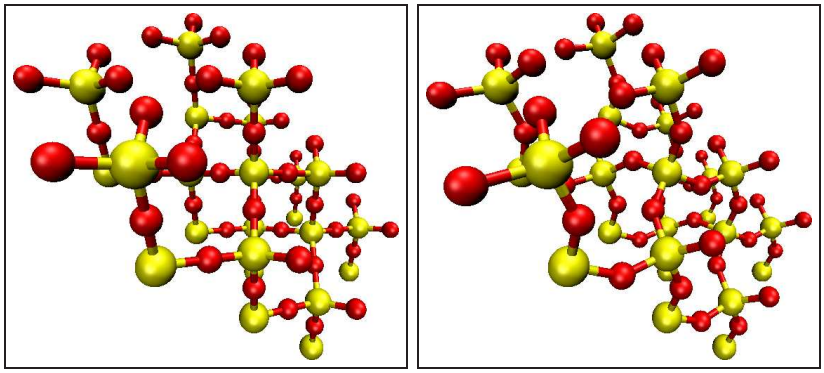

Figure 3.8: Left panel: Ideal β-cristobalite structure. Right panel: The β-cristobalite structure proposed by Wright and Leadbetter [161], the SiO_4 tetrahedron of the ideal structure are rotated.

Geometry optimization Like the α-quartz case, two kinds of optimization have been achieved. The system under consideration here was made of $3 \times 2 \times 2$ tetragonal body-centered unit cells. The corresponding results are compiled in Table 3.2. It was not possible to proceed to constrained optimizations according to the point group symmetry properties[5]. As a consequence all the atomic positions were affected by

[5]The `CPMD` code is mainly devoted to *ab initio* molecular dynamics, not especially suited for the crystalline optimization.

the optimization process. Nonetheless only slight changes were observed ($< 5\%$), and the resulting structure is in good agreement with the one given by Liu and coworkers [93]. These results have to be considered with care as the optimization process used in this case does not take into account thermal effects which can have some influence on the structure, for example thermal expansion accounting for an increase of the cell parameters and cell volume.

Parameters	Experiment	fixed cell	error[%]	relaxed cell	error[%]
a[Å]	5.0424	-	-	5.0263	0.31
$c = \sqrt{2}a$[Å]	7.131	-	-	7.1083	0.31
$\alpha[^\circ]$	120.	-	-	120.7	0.58
$\beta[^\circ]$	120.	-	-	120.7	0.58
$\gamma[^\circ]$	90.	-	-	89.12	0.98
V[Å^{-3}]	90.652	-	-	88.67	2.19
x	0.09	0.086	4.44	0.086	4.44

Table 3.2: Cell parameters for β-cristobalite crystal. The results corresponding to the *ab initio* data have been carried out at 0K on a 72 atoms sample using a 130 Ry cutoff.

3.2.3 Electronic structure

The electronic structure can be characterized by means of the electronic density of states (EDOS). The EDOS $g(E)$ quantifies the number of allowed quantum energy levels per unit volume of the system, within the energy range E to $E + dE$. To achieve the calculation of the EDOS the wavefunction of the system has been quenched to the Born-Oppenheimer surface and the Kohn-Sham orbitals and their corresponding eigenvalues have been calculated. Crystals as α-quartz and β-cristobalite are made of regular tetrahedra, the Si-O bond lengths and both $\widehat{\text{OSiO}}$ and $\widehat{\text{SiOSi}}$ angles are well-defined. This allows a straight interpretation of the electronic density of states as the crystalline symmetry enhances the degeneracy of the electronic states accounting for the characteristic peaks in the density of states. The peaks near -20.0 eV correspond to the oxygen $2s$ states, the ones included in the range going from -10.0 eV to -5 eV correspond to Si sp^3 hybridized orbitals bonded to O $2p$ orbitals, see Fig. 3.10, and the states above -5.0 eV and below 0 eV correspond to the oxygen $2p$ non-bonding orbitals [14], the band gap given by our calculations is equal to 5.8 eV . This result is smaller than the experimental one of 9 eV reported for α-quartz [59, 69] [6]. Such a discrepancy was expected as LDA calculations are well known for underestimating the experimental band gap, nevertheless this result is compatible with precedent calculations carried out on such systems [14, 127], and are also consistent with previous experimental results reported by V. P. Zakaznova-Herzog *et al.* [167].

[6]The band gap for pure silicon at 300K is $E_g = 1.11$ eV, for germanium $E_g = 0.67$ eV, both are indirect transitions [82].

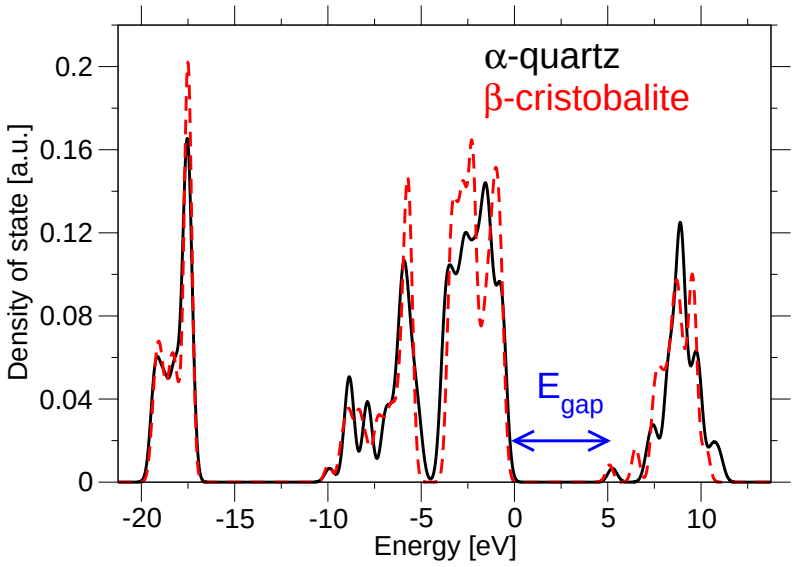

Figure 3.9: Electronic density of states of α-quartz and β-cristobalite ($E_{gap} \simeq 5.8$ eV). The Fermi levels (the energy of the highest occupied quantum state) have been conventionally set to 0, the spectrum has been smoothed used a Gaussian broadening of width $2\sigma = 0.40$ eV.

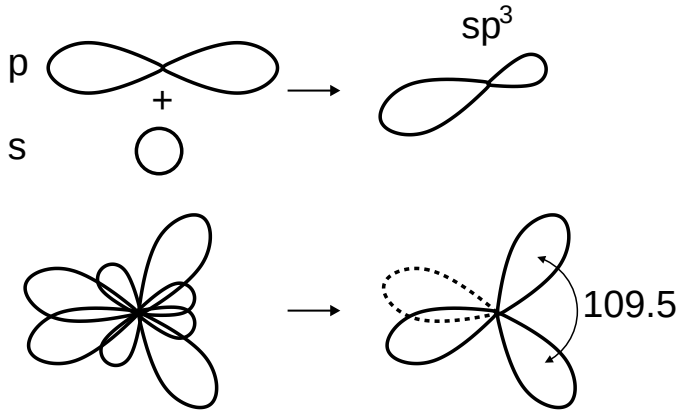

Figure 3.10: Linear combination of s and p orbitals corresponding to sp^3 orbitals .

3.3 Liquid silica: Practical aspects

Introduction The structure of silica at low pressure is characterized by a continuous network of SiO_4 tetrahedra connected by their vertices. For this reason amorphous and liquid forms of silicon dioxide are often considered as a prototypical example of a network-forming disordered material. The strength of the bonding makes defects in silica such as three or five-coordinated silicon atoms rather unlikely [13]. Unfortunately, structural rearrangement and thus relaxation need bond breakings. Therefore creating and sampling realistic glasses requires rare reordering events and is a challenging task

through first-principle methods.

3.3.1 Sample generation

The natural procedure to generate a liquid configuration using molecular dynamics consists in melting a crystal. Quenching and thermalizing silica samples in this manner by first-principles methods is computationally very expensive. Therefore, in this work, we follow the methodology proposed by Benoit *et al.* [10]. First liquid samples are equilibrated by means of classical molecular dynamics and then the resulting configuration was used as starting point for the CPMD runs. The liquid phase is thus accessible at lower CPU time cost, since part of the equilibration are carried out within the framework of classical molecular dynamics. The classical sample considered was made of 216 atoms using the BKS potential [9]. A β-cristobalite sample has been molten at a very high temperature (7000K) and then cooled down to 3600K. From this sample we extracted and thereafter equilibrated a subset of 114 atoms contained in a 11.98 Å box corresponding to a density of 2.2 g.cm^{-3}. The corresponding final atomic configuration and velocities were considered as input data for the CPMD run. The first 3.5 ps of the CP dynamics has not been taken into account for the calculations of the different observables, the CPMD simulation last for 16 ps. The time step considered for the simulations was 0.0725 fs and the fictitious electronic mass for the CP dynamics was set to $\mu = 600$ a.u.

3.3.2 Thermostats

Ionic thermalization The ionic temperature has been kept close to 3600 K using Nosé-Hoover chains thermostats [73, 112], see section (2.2.2). This approach consists in adding chains of interconnected dissipative terms to some degrees of freedom of the system. It is preferable to use chains of Nosé-Hoover thermostats instead of a single Nosé-Hoover term to ensure a homogeneous sampling of the phase space [96]. In this case chains made of four thermostats have been used. Each chain was coupled to each nuclear degree of freedom of the system ("massive thermostating approach"). This procedure shortened considerably the equilibration period [117]. Furthermore, these terms require a fictitious mass parameter Q calibrated in order to synchronize the thermostating chain to a typical phonon frequency of the nuclear system [97]. The characteristic peaks ($\sim 32 - 35$ THz) in the high frequency domain shown in Fig. 3.5 have been used as a reference for setting the mass parameters.

Electronic thermalization The electronic density of states has been computed using our 114 atom samples and compared to the density of α-quartz (see Fig. 3.11). In the molten silica sample the band gap is significantly reduced in this case. Problems may arise because of the small gap that may lead to zero-frequency electronic modes which might overlap with the phonon spectrum[7] (see section (2.3.6.2)). To tone down

[7] $w_{\text{ion}}^{\min} \ll w_{\text{elec.}}^{\min}$, with $w_{\text{elect.}}^{\min} \propto \left(\frac{E_{\text{gap}}}{\mu}\right)^{1/2}$

the electronic temperature and so to ensure adiabaticity, Nosé-Hoover thermostating chains have been coupled to the orbital degrees of freedom [99]. Preceding attempts done without electronic thermostats lead to systematic drifts as shown in Fig. 3.12.

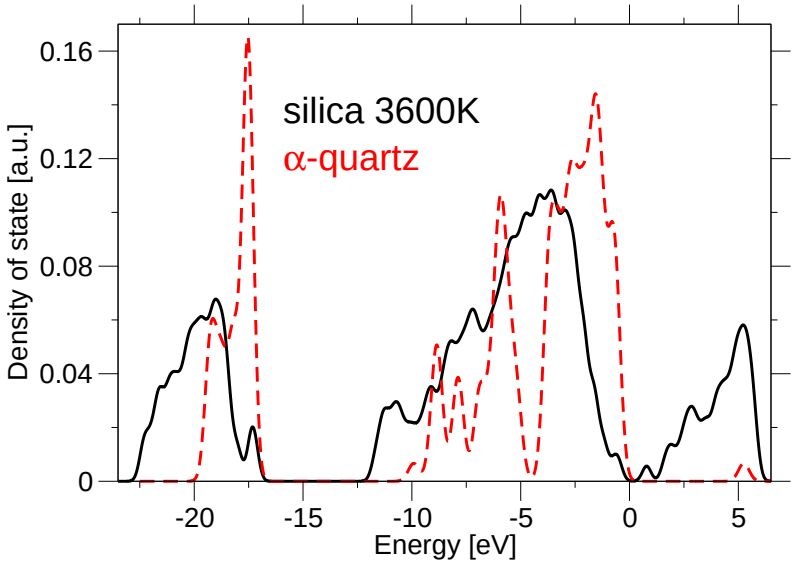

Figure 3.11: Electronic density of states of SiO_2 at 3600K ($E_{gap} \simeq 1.29$ eV), the spectra have been smoothed using a Gaussian broadening $2\sigma = 0.40$ eV.

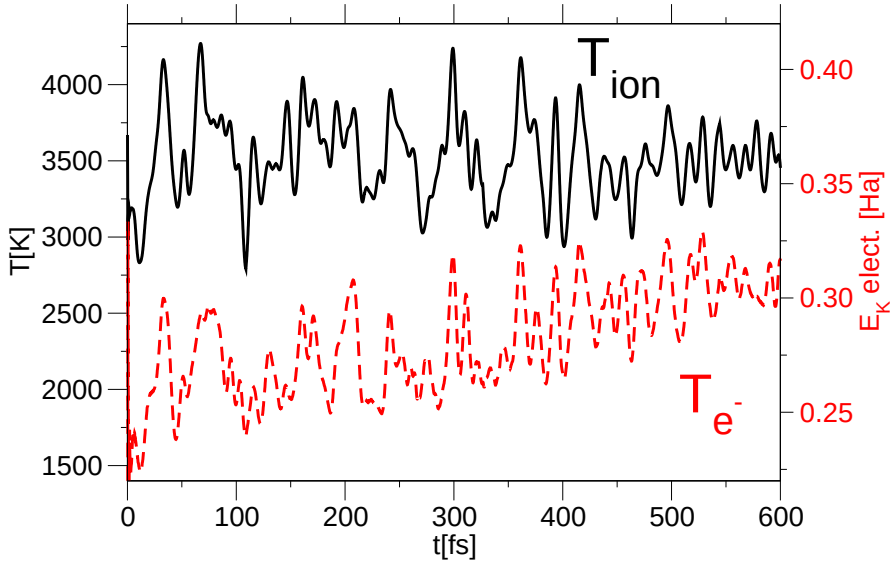

Figure 3.12: Ionic temperature (solid) and electronic (dashed) kinetic energy represented as a function of time. The ions are thermalized by means of Nosé-Hoover chain thermostats, the electronics orbitals are not connected to any thermostat.

3.4 Liquid silica: Comparison to classical simulation

In this section we present the results of our Car-Parrinello simulations. Systematic comparisons have been made with classical molecular dynamics carried out using the BKS potential. The classical simulations have been done with a system of 1152 atoms, the density set to 2.2 g/cm^3 in agreement with the *ab initio* simulations.

3.4.1 Pair correlation function

The *ab initio* simulations have been carried out at high temperature (3600 K). Very few experiments have been made on molten silica samples as accurate diffraction measurements on high temperature liquids imply many technical difficulties, especially on liquid silica which evaporates quickly above 2410 K [104]. For these reasons a comparison between theory and experiments is difficult to achieve. Recently, Mei and coworkers [104] have investigated the structure of liquid SiO_2 (2100°C) at 1 atm. by means of x-ray diffraction.

Experimentally, the average Si-O bond increases upon heating the glass from 1.597 Å at 25°C to 1.626 Å in the temperature range 1870 K $< T <$ 2370 K [104]. These results are consistent with the CPMD simulation within the NVT ensemble where the average distance is found equal to 1.625 Å. Previous simulation made on liquid silica by means of *ab initio* simulations predict an equilibrium distance of 1.67 Å for the Si-O bond [128].

The average coordination number $Z_{\alpha\beta}(r)$ representing the average number of atom β surrounding an atom α as a function of the distance $r_{\alpha\beta}$ has also been calculated, see Fig. 3.14. For a distance $r_{\alpha\beta} = 2.36$ Å corresponding to the first minimum of $g_{\mathrm{SiO}}(r)$ the average coordination numbers for the Si-O and O-Si are equal to 4 and 2 respectively. The silicon atoms are surrounded by four oxygens whereas the oxygens are surrounded by two silicon atoms, which support the assumption that a strong tetrahedral network exists even at high temperatures. As no few many experimental data referring to the liquid state were available, the structure of our system has also been compared to the one corresponding to the experimental vitreous phase, see Table 3.3. The results given by simulations are in very good agreement with the experiments.

The *ab initio* simulations have also been compared to the MD simulations with the BKS potential. The partial pair correlation function corresponding to both classical and first-principles simulations is shown in Fig. 3.13. It appears that the BKS potential systematically overestimates the maxima of the peaks. Indeed, the sample configurations as given by the BKS potential are more structured than the ones given by CPMD. This can be seen as a remaining effect of the nature of the system (crystal) chosen for the fitting of the BKS. As can be seen in Table 3.3 the positions of the first peaks of the partial pair correlation function for the O-O and Si-O pair are quite well reproduced, whereas the Si-Si peak is predicted at 3.123 Å for the BKS whereas the CPMD simulations describe the first Si-Si peak at 3.097 Å.

Peaks positions [Å]		Experiments			Theory	
		Mozzi [108]	Grimley [57]	Mei [104]	CPMD	BKS
SiO	first	1.62	1.608	1.626	1.625	1.601
	second	4.15	-	-	4.031	4.0495
OO	first	2.65	2.626	-	2.647	2.616
	second	4.95	-	-	4.991	4.977
SiSi	first	3.12	3.077	-	3.097	3.123
	second	5.18	-	-	5.098	5.151

Table 3.3: Localization of the first and second nearest-neighbor peaks in the radial distribution function $g(r)$.

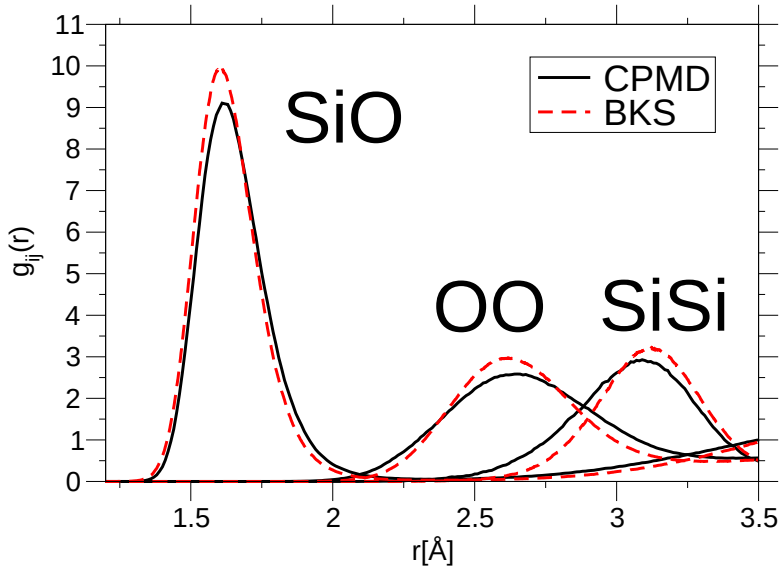

Figure 3.13: The different partial pair distribution functions. The solid line correspond to the *ab initio* simulations. In dashed lines the classical results as given by the BKS potential.

3.4.2 Angular distribution function

The angular distribution function characterizes the geometry of the tetrahedral network. The plots representing the intra-tetrahedral angle $\widehat{\text{OSiO}}$ and the inter-tetrahedral angle $\widehat{\text{SiOSi}}$ are shown in Fig. 3.16. The average inter-tetrahedral angle, as predicted by `CPMD`, is found to be equal to 105°[8], the experimental results [104] support a 107°±2° value. The value of the $\widehat{\text{SiOSi}}$ angle is linked to the nature of the tetrahedral network. Tetrahedra are connected together to form rings, examples of rings are given in Figs. 3.15: A ring can be defined as a closed loop of covalent bonds formed in the structure. A network dominated by 6-membered rings is consistent with an average angle

[8]Close to the value suited for the perfect tetrahedral system 109°.

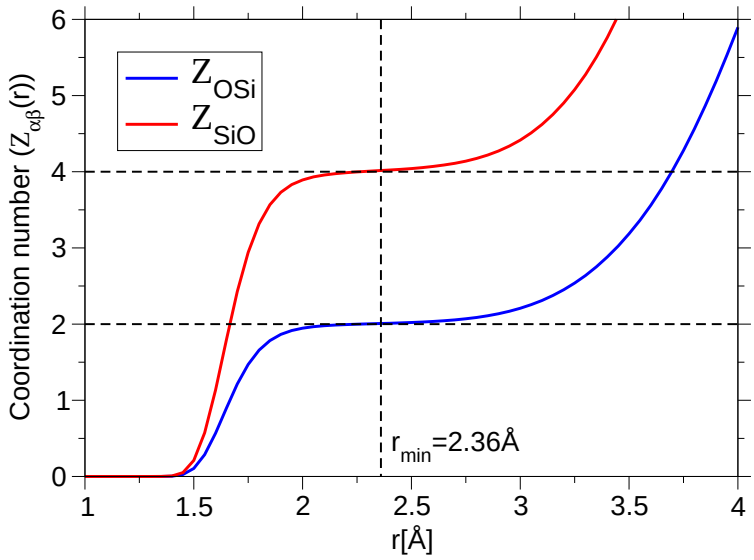

Figure 3.14: Coordination number $Z_{\alpha\beta}(r)$ representing the average number of β species surrounding an α atom as a function of the distance $r_{\alpha\beta}$.

of $\simeq 147°$. On the other hand an increase of the ratio of 3-membered rings supports a decreasing of the $\widehat{\text{SiOSi}}$ angle. As shown by Raman experiments [102], at high temperature the 3-membered rings topology is more significantly represented. These results are in qualitative agreement with the theory where the average $\widehat{\text{SiOSi}}$ value is localized at 136°, whereas the experimental value is estimated at 138° [104].

The classical simulations give an overall good description of the intra-tetrahedral angle. Nevertheless, the classical inter-tetrahedral angle is not in good agreement with the *ab initio* results where the average angle is found equal to 147°, comparable to the experimental values for low temperatures.

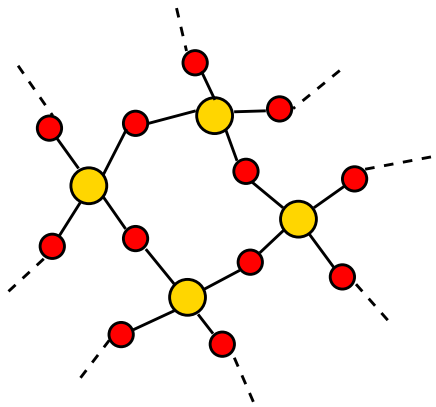

Figure 3.15: Sketch of a ring of size $n = 4$ in a silica network.

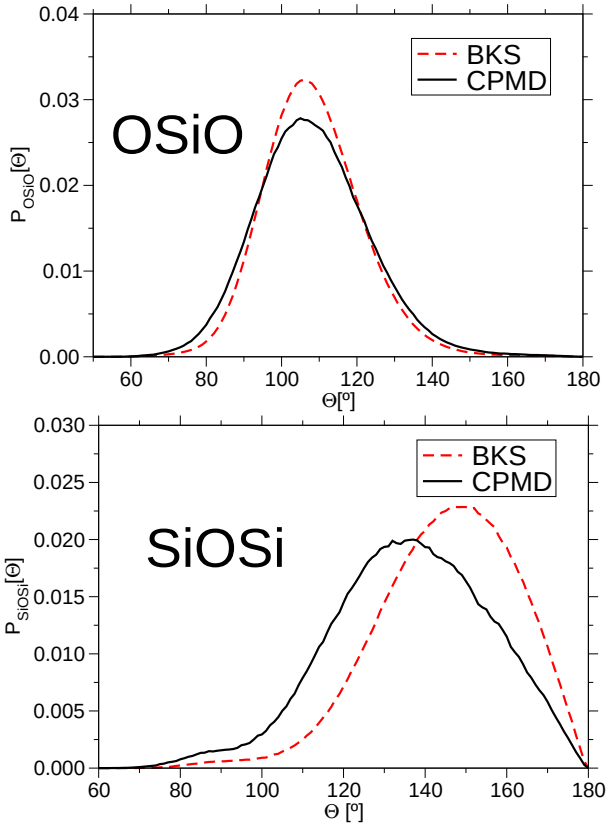

Figure 3.16: Angular distribution function corresponding to the classical and first-principle simulations. The first SiO neighbor shell as been defined using a 2.35Å cutoff.

3.4.3 Mean squared displacement

One of the simplest quantities to study the dynamics of a fluid system on a microscopic level is the mean squared displacement (MSD) $\langle r^2(t)\rangle$ of a tagged particle (of type α):

$$\left\langle r_\alpha^2(t)\right\rangle = \frac{1}{N_\alpha}\sum_{l=1}^{N_\alpha}\left\langle |\mathbf{r}_l(t)-\mathbf{r}_l(0)|^2\right\rangle \tag{3.15}$$

According to the Einstein relation the MSD is proportional to the self-diffusion constant (D_α) for the long time scale:

$$\lim_{t\to\infty}\frac{\langle r_\alpha^2(t)\rangle}{t} = 6D_\alpha \tag{3.16}$$

The MSD computed for our classical and *ab initio* simulations are shown in Figs. 3.17 and 3.18. Here, it is not possible to directly compare the two kinds of simulation as the *ab initio* dynamics features is affected by the thermostats connected to the ions. The effects of thermostats in the CPMD simulations may account for the absence of the small bumps that are yet described in the BKS MSD for intermediate time

scales (at 240 fs), see Figs. 3.17 and 3.18. These small bumps correspond to the so-called boson peak which is a vibrational feature at low frequencies [1-2 THz] whose precise origin is currently still a matter of debate [75]. As we have not reached the diffusive regime we are not able to proceed to a proper extraction of the self-diffusion constant. Nevertheless the dynamics in CPMD simulations using Nosé-Hoover chains of thermostats seems to be more diffusive than the classical dynamics given by the BKS potential.

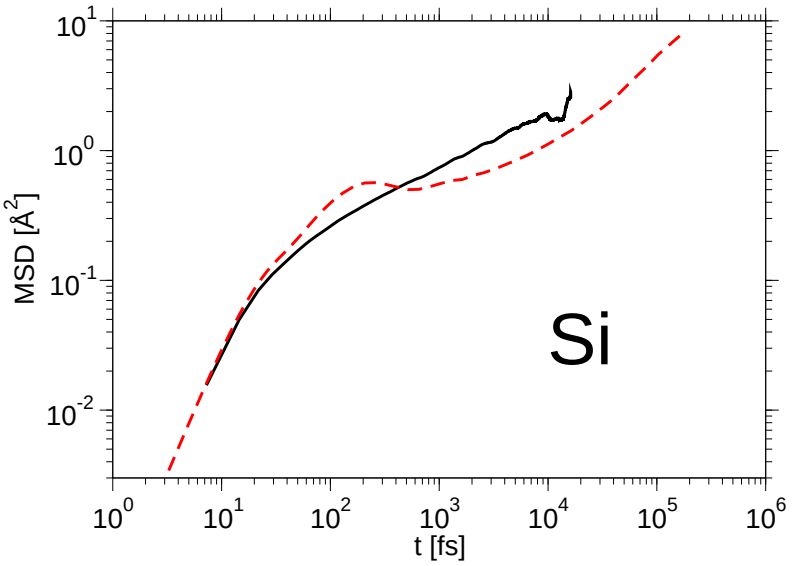

Figure 3.17: Time dependence of the silicon mean squared displacement corresponding to the CPMD simulations (solid lines) and to the BKS simulations (dashed lines).

3.4.4 Pressure

The pressure gives informations relative to the mechanical stability of the system. The pressure is connected to the stress tensor Π by the following relation:

$$P = \frac{1}{3}\mathrm{Tr}\,(\Pi) + \frac{Nk_BT}{V}. \tag{3.17}$$

Further details concerning the stress tensor are given in Appendix A. As already stated in the previous section (3.1) and illustrated in Fig. 3.3, the stress tensor requires a large plane wave cutoff ($\geq$ 130 Ry). Because of a prohibitive computational time cost *ab initio* molecular dynamics simulations were not accessible. Nevertheless, for the few equally spaced configurations extracted for the purpose of the force fitting we have computed the pressure using a 130 Ry cutoff. Due to the poor ensemble averaging[9] one can hardly assert whether or not the value of the pressure is fully converged. The

[9]Only 100 configurations have been used for this calculation

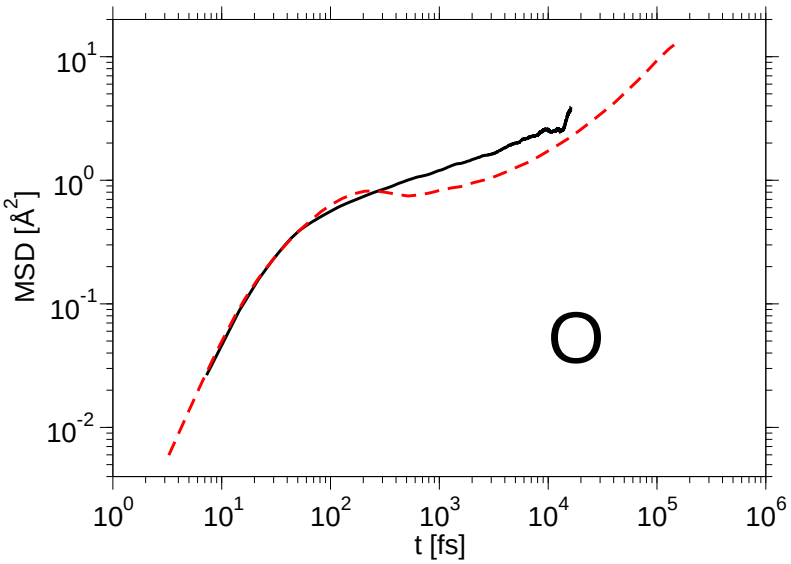

Figure 3.18: Time dependence of the oxygen mean squared displacement corresponding to the CPMD simulations (solid lines) and to the BKS simulations (dashed lines).

estimated average value of pressure is -6.9 ± 1.6 GPa[10]. On the one hand, our system exhibits a strong negative pressure at 3600 K for a 2.2 g/cm^3 density, which means that it tends to increase its density. One the other hand experimental data [7] shows that the density of SiO_2 decreases for temperature above 1820K (1.929 g.cm^{-3} at 2322K). These results show that even if our estimation of the pressure is qualitative, this value is in strong disagreement with experiment. This bad agreement can be understood from the hardness of silica, the bulk modulus K[11] reported in the literature at 1773K is $K = 17.57$ GPa [91], qualitatively an isotropic variation of the volume of 10% leads to a change in the pressure of $\simeq 1.75$ GPa ($0.1K = 1.75$). It is also worthwhile to mention that during the optimization of the crystalline structure, small changes of the cell parameters were leading to significant changes of the stress tensor, for example a change of the volume of 5% of α-quartz cell leads to a change of the internal pressure of 10.2 GPa. Consequently, due to the sensitiveness of the stress tensor with respect to the cell parameters one can easily understand that even slight changes in the density may lead to wrong values of the internal pressure.

[10]The kinetic contribution to the pressure is not dominant. It can be derived form the ideal gas equation, $\langle P_{kin} \rangle = \rho RT/M_{SiO_2}$: With $\rho = 2200$ kg.m^{-3}, $M_{SiO_2} = 60.0843$ g.mole^{-1}, the kinetic pressure is found equal to 1.09 GPa.

[11]The bulk modulus is defined $K = -V(\partial P/\partial V)_T = 1/\chi_T$ where χ_T is the isothermal compressibility.

3.5 2-body potential approximation

Introduction Even if bondings in silica can be accurately described by means of *ab initio* calculation through many-body interactions, it can be worthwhile to ask whether the classical pair interactions approach works according to the encouraging results given by the BKS potential. In this section we have tried to investigate the nature of the effective bonding as described by first-principles methods.

3.5.1 Analytical Approach

Formally, the interaction potential and all its connected features such as forces and stresses can be decomposed in a sum of 1-,2-,..., N-body interactions for a system made of N atoms, see Eq. (2.34). Following the encouraging results shown by the BKS potential our working hypothesis consist in considering the *ab initio* interactions dominated by two-body terms.

Two-body potential For any system described by two-body interactions it is possible to rebuild the pair potential by means of the total effective forces applied on the atoms. By definition the total force applied on an atom i is given by:

$$\mathbf{F}_i = \sum_{j \neq i} -\frac{\partial V_2(\{r_{ij}\})}{\partial r_{ij}} \mathbf{e}_{ij} \qquad \text{with} \qquad \mathbf{e}_{ij} = \frac{\mathbf{r}_{ij}}{r_{ij}} \tag{3.18}$$

Hence, by deriving the scalar product of the force by the unitary interatomic vector $\mathbf{e}_{ij}$, one can retrieve the value of the second derivative of the potential:

$$\left(\frac{\partial \left(\mathbf{F}_i \cdot \mathbf{e}_{ij} \right)}{\partial r_{ij}} \right)_{\mathbf{r}_i} = -\frac{\partial^2 V_2(\{r_{ij}\})}{\partial r_{ij}^2}, \qquad \text{where:} \quad \mathbf{e}_{ij} \cdot \mathbf{e}_{kl} \neq 0. \tag{3.19}$$

From Eq (3.19) it is straightforward to calculate the potential by successive integrations.

N-body potential For a system characterized by N-body interactions the preceding approach is a more delicate issue. The example of a system presenting only three-body interactions is quite instructive. In this case, the dependence of the interatomic force $\mathbf{F}_{ij}$ applied an atom i by an atom j with respect to the interatomic distances r_{ij} is not null and cannot be assigned to any two-body interactions, see Eq. (3.19) and Fig. 3.19. Indeed, a formal decomposition of the different contributions is not feasible. Furthermore, special care has to be taken when extracting the effective two-body interactions part of a N-body interacting system. Contrary to the idealized two-body case, the surrounding environment[12] may play a role. This two-body potential assumption will not give much more informations concerning the exact shape of an underlying effective two-body potential. It could be seen as a mean of quantifying the effective nature of the interactions (qualitative potential energy shape, minimum of the Si-O attractive energy term, effective range, *etc...*).

[12]Here we take into account all the atoms and we exclude the i and j atoms.

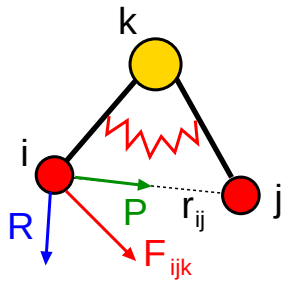

Figure 3.19: Interactions between particles i, j and k are described only by a three-body potential that describes repulsion between bond pairs. Assuming that the bond lengths are constant (rigid bond) the partial force applied on atom i $\mathbf{F}_{ijk} = \mathbf{P} + \mathbf{R}$ (in red) is perpendicular to the interatomic vector $\mathbf{r}_{ik}$. The pair term $\mathbf{P}$ depends on the interatomic distance r_{ij} although no pair potentials are used for the description of the potential energy.

3.5.2 Practical Considerations

In practice, one considers a given pair of atom $\{ij\}$ and then by slightly perturbating the interatomic distance r_{ij} one can evaluate the numerical values of the effective pair potential. In the following part of the text, this method will be called "perturbative approach/method". For this purpose, one has considered a small backward/forward displacements $\varepsilon/2$ of an atom j along the interatomic direction $\mathbf{e}_{ij}$ (see Fig. 3.20). The distance between the two atoms i and j is slightly perturbed by a quantity ε. Then, the corresponding forces are calculated by:

$$\mathbf{F}_i^{\pm} = \mathbf{F}_i\left(\{\mathbf{R}_1, \ldots, \mathbf{R}_j \pm \varepsilon \times \mathbf{e}_{ij}, \ldots, \mathbf{R}_N\}\right) \tag{3.20}$$

Here the quantity of interest is the centered differences between the initial forces and the perturbed ones (see Fig. 3.20):

$$\Delta\mathbf{F}_i^{\pm} := \mathbf{F}_i - \mathbf{F}_i^{\pm} \tag{3.21}$$

using the interatomic vector $\mathbf{e}_{ij}$ the quantity $\Delta\mathbf{F}_i^{\pm}$ can be formally decomposed in two contributions $\mathbf{R}$ and $\mathbf{P}$:

$$\Delta\mathbf{F}_i^{\pm} = \left(\Delta\mathbf{F}_i^{\pm} \cdot \mathbf{e}_{ij}\right)\mathbf{e}_{ij} + \Delta\mathbf{F}_i^{\pm} - \left(\Delta\mathbf{F}_i^{\pm} \cdot \mathbf{e}_{ij}\right)\mathbf{e}_{ij} \tag{3.22}$$

$$\mathbf{P} := \left(\Delta\mathbf{F}_i^{\pm} \cdot \mathbf{e}_{ij}\right)\mathbf{e}_{ij} \tag{3.23}$$

$$\mathbf{R} := \Delta\mathbf{F}_i^{\pm} - \left(\Delta\mathbf{F}_i^{\pm} \cdot \mathbf{e}_{ij}\right)\mathbf{e}_{ij} = \Delta\mathbf{F}_i^{\pm} - \mathbf{P} \tag{3.24}$$

where $\mathbf{P}$ refers to the pair term contribution and $\mathbf{R}$ refers to the residual contributions due to the high-order interactions:

$$\frac{\Delta\mathbf{F}_i^{\pm}}{\Delta R_{ij}} = \frac{\Delta\mathbf{F}_i^{\pm}}{\epsilon} \overset{\epsilon\to 0}{\longrightarrow} \frac{\partial\mathbf{F}_i}{\partial r_{ij}}. \tag{3.25}$$

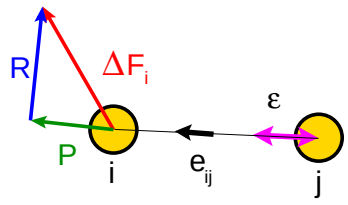

Figure 3.20: Representation of the force differences applied on a given atom i after a small perturbation of the position of atom j. The perturbation ε has to be collinear to the interatomic axe.

In the previous section we have outlined the importance of the surrounding environment when using N-body potential. As the effective force may depend on the environment, force perturbation and calculation have been carried out on carefully chosen configurations computed along the *ab initio* molecular dynamics simulation presented in section (3.3). The typical configurations considered have to contain the appropriate pairs of atoms corresponding to distances for which the second derivative of the potential has to be computed. This criterion ensures that the distance one investigates occurred "naturally" during the simulation, thus one does not need to proceed to any artificial and *arbitrary* displacements of ions.

To ensure a good convergence of the results, perturbations are computed on two independent samples made of 78 atoms and averaged. As the method is time consuming (372 *ab initio* wavefunctions have to be optimized for the force calculation) previous tests have been done on a model system using the BKS potential. The numerical results stemming from these simulations were in good agreement with the analytical ones. The ε step used for the numerical computation of the derivatives has been set to 0.1 Å. The distances considered for retrieving the effective pair interaction were hold in the intervals $[1.9-5.0]$ Å (124 calculations[13]), $[1.4-5.0]$ Å (114 calculations), $[2.4-5.0]$ Å (104 calculations) for the O-O, Si-O, and Si-Si pairs, respectively.

Results The collinearity ratio defined by $|\mathbf{P}|/|\Delta\mathbf{F}_i^{\pm}|$, according to the notation introduced in Eqs. (3.22) and (3.23), gives an information concerning the prominence of the pair interactions in the overall force due to the displaced atom j on the reference atom i considered, see previous section. The three collinearity ratios corresponding to the O-O, Si-O and Si-Si terms are represented on Figs. 3.21. Firstly, it appears that the force pair term $\mathbf{P}$ contributes mainly to the interactions, and this statement is especially true for the Si-Si interaction. In the network of silica, the oxygen atoms bridge two adjacent silicon atoms, and the corresponding $\widehat{\text{SiOSi}}$ angle is mainly defined by the orientation of the oxygen $2p$ atomic orbitals. Bending this $\widehat{\text{SiOSi}}$ angle should be energetically penalizing as the two electronic clouds centered close to the oxygen atoms can hardly overlap due to Pauli's principle (two electrons repulsion) and due to their

[13]The total number of calculation for a given pair of species if given by number of interval $10 * (5.0 - 1.9) = 31$ multiplied by two because of the backward/forward displacements and multiplied by two as two different configurations at each distance have been considered.

dipolar interactions. However we can see from Fig.3.21 that the expected three-body effects of the bridging oxygens between two silicon atoms are negligible.

On the other hand, the O-O interactions seem to be more affected by the N-body interactions. The many-body perturbations (contributions of 3-, 4-, ... body interactions) are more significant for distances greater than 3 Å. This distance corresponds to the sphere containing the first oxygen neighbors. The three-body effects linked to directional covalent bonds are more significant for the $\widehat{\text{OSiO}}$ angle than compared to the $\widehat{\text{SiOSi}}$ one. Even if the electronic cloud between oxygen and silicon is mainly localized on the oxygen atom, its distortion has a weaker influence than the repulsion occurring between Si-O sp^3 orbitals and dipolar moment. The smaller $\widehat{\text{OSiO}}$ angle and the relative compactedness of oxygens (oxygens that are unwilling to overlap) surrounding silicon atoms may explain these observations. The forces computed using the perturbative approach are plotted in Fig. 3.23. In this figure one can see that the O-O interactions are weaker than the Si-Si ones. Consequently, the relative collinearity ratio associated to the O-O interactions is more sensitive to statistical errors and may not properly describe the bonding[14].

The effective forces given by the perturbative method are given in Fig. 3.23. As expected the interaction between pair of atoms for the same species are repulsive, the O-O term is less repulsive than the Si-Si one. The Si-O term is repulsive for the very short distances and shows a minimum at 1.9 Å (the equilibrium position for the Si-O term is at 1.6 Å).

The direct comparison with the classical forces, see Fig. 3.23, shows that the BKS interactions are stronger than the ones computed using this perturbative approach. A possible explanation can be found by recalling how the BKS parameters were fitted [9]. The procedure proposed by van Beest *et al.* [9] mainly focus on a limited set of features corresponding to α-quartz, indeed, such symmetrical structures does not disclose a wide variety of bond distances and angles. For example, in a perfect crystal the pair distribution function is represented by a discrete distribution of the distances[15], whereas for a liquid/glass the pair distribution function is continuous.

Nevertheless the position of the minimum of the Si-O interaction given by the BKS potential is in good agreement to the one given using the perturbative approach, see Fig. 3.23. This results is somehow surprising as for an effective pair potential, the position of such minimum results from the complex interplay between all the contributions of different pairs potential.

The perturbative approach demonstrated that the forces in silica calculated by means of *ab initio* method can mainly be described by pair terms, see Figs. 3.21. Moreover this effective potential energy shape calculated using CPMD is consistent with the one given by BKS potential. Considering these results we have proposed in

[14]In Eq. (3.25) the derivative of the potential is calculated using the ratio $\Delta\mathbf{F}_i^{\pm}/\Delta R_{ij}$. If the potential is weak for a distance R_{ij}, then $\Delta\mathbf{F}_i^{\pm} \simeq \mathbf{0} \simeq \Delta R_{ij}$, the calculation of the ratio $\Delta\mathbf{F}_i^{\pm}/\Delta R_{ij}$ can not be precisely determined.

[15]The BKS potential parameters have been optimized for some well-defined distances quantified by the integer numbers (ℓ, m, n) using the following relation: $r_{\mathrm{ij}}(\ell, m, n) = |\mathbf{r}_{\mathrm{i}} - \mathbf{r}_{\mathrm{j}} + \ell\mathbf{a} + m\mathbf{b} + n\mathbf{c}|$ where $\mathbf{a}$, $\mathbf{b}$ and $\mathbf{c}$ stands for the cell vectors of α-quartz.

the next chapter to reoptimize the BKS potential ansatz in order to reproduce at best the forces given by the *ab initio* approach.

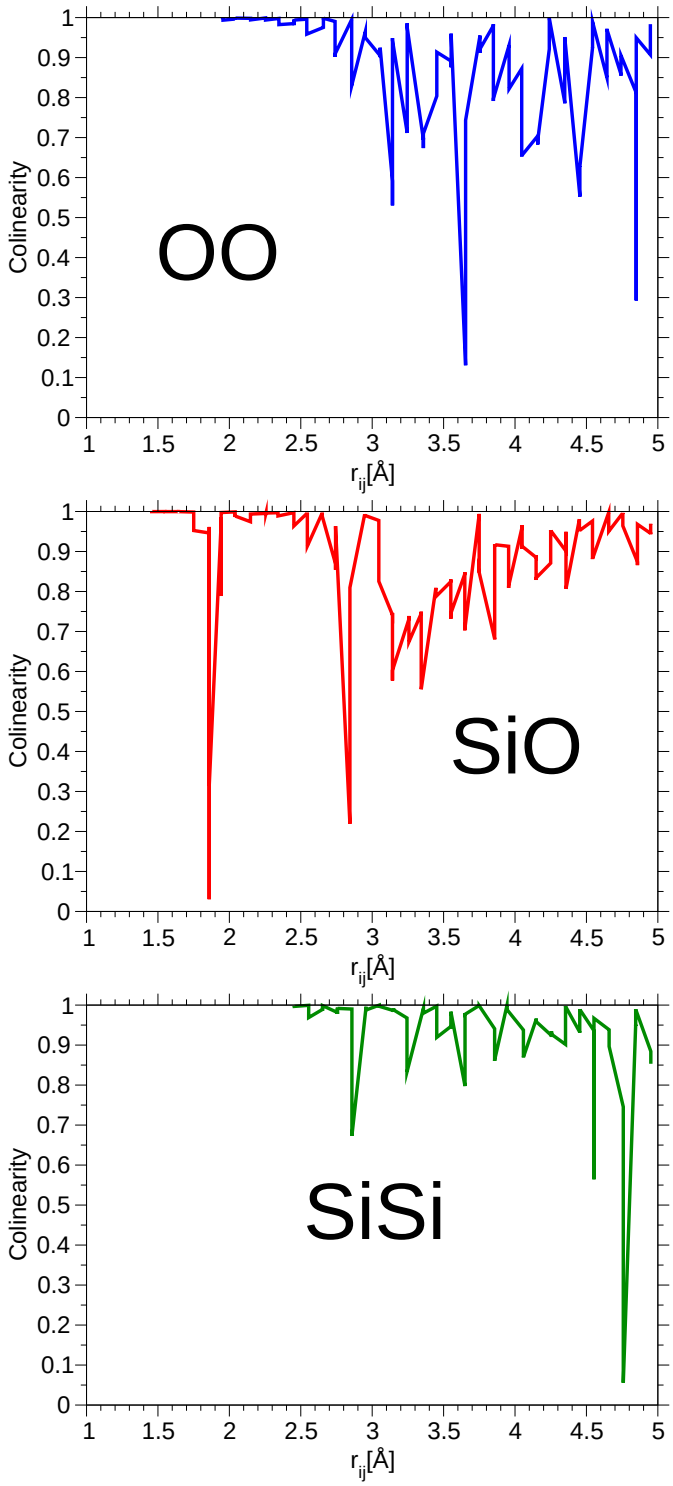

Figure 3.21: The $|\mathbf{P}|/|\Delta\mathbf{F}|$ ratio quantifying the nature of the forces (two-body, n-body) is represented on this three plots.

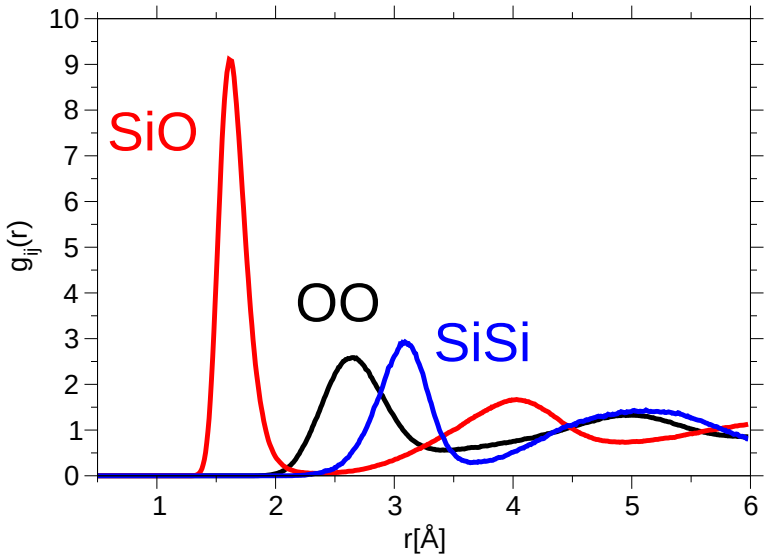

Figure 3.22: Partial pair correlation function for a 144 atomic system at 3600K simulated using CPMD.

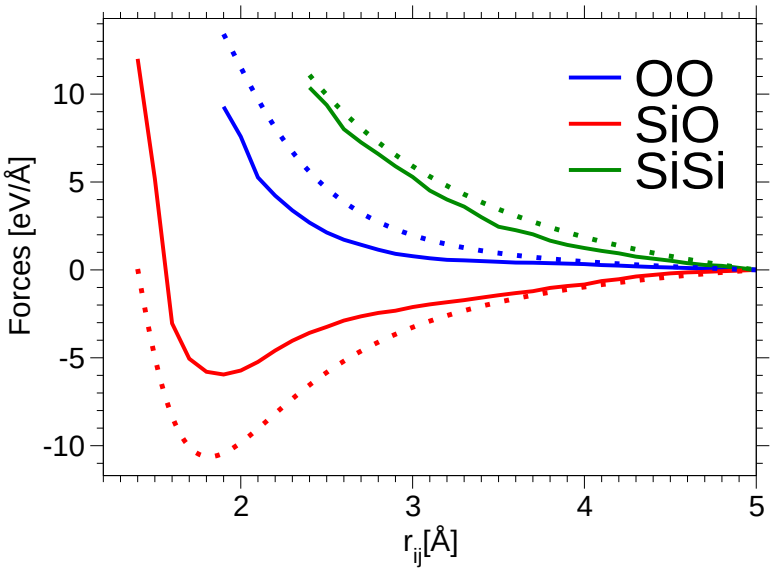

Figure 3.23: The effective forces computed through the perturbative approach using first-principle description (solid lines), the system was made of 78 atoms contained in a 10.558 Å box, for a SiO_2 sample at 3600K. The corresponding BKS forces are represented in dotted lines.

Chapter 4

Force-matching procedure

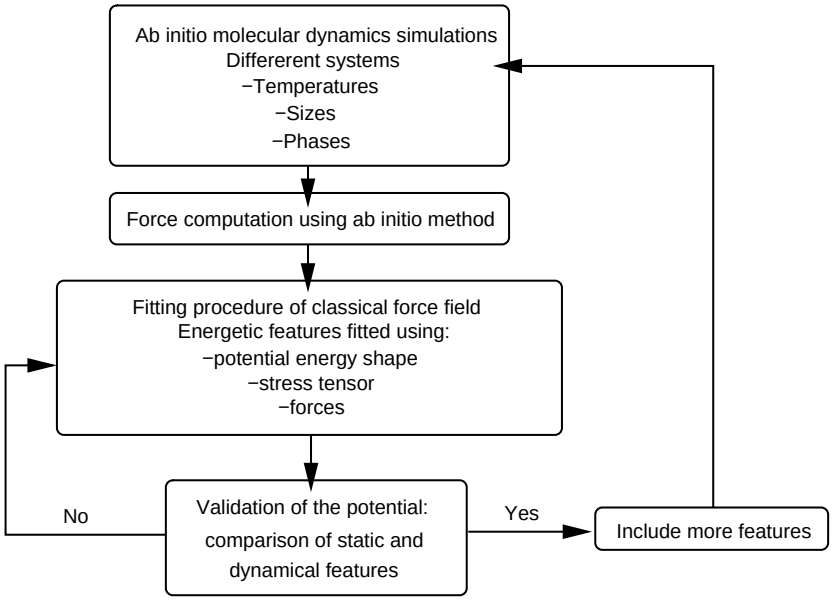

Figure 4.1: Schematic representation of the force matching procedure.

First-principles simulations are not computationally tractable for systems containing more than $\simeq 10^2$ atoms and for time scale larger than $\simeq 10^1$ ps. Simulations of big systems for long time scales can only be achieved using classical potential. A variety of approaches have been proposed over the years to build these potentials. At one extreme, some groups chose to fit the potential (that is to parameterize the functions which appear in its analytical form) using available experimental data. At the other extreme, other groups try to start from a first-principles description of the material and use their simulation results to fit a classical potential. Of course, the latter approach is the most satisfactory as any experimental result reproduced by means of first-principle fitted potential can be interpreted as the results of microscopic contributions whereas the former fitting method is more likely to reproduce artificially experimental results. Moreover first-principles molecular dynamics codes allow to generate

large quantities of useful and reliable data, such as forces acting on atoms in a variety of different geometries and coordinations under lots of different conditions (different densities, temperatures, pressures, *etc*). In this work we have used the force-matching procedure proposed by Ercolessi [46] so as to define a classical potential based upon first-principle considerations. This procedure was found to be convenient for fitting potentials using *ab initio* data for amorphous phases for which no elastic constants or lattice parameters can be defined. This approach consists of a numerical optimization procedure which tries to match as closely as possible the *ab initio*-derived forces to the ones derived from a classical potential. The results given by the classical potential so obtained have to be checked and for this purpose simulations must be realized to see whether the classical results are consistent with the *ab initio* one. The overall procedure that we have followed is given in Fig. 4.1.

4.1 General fitting approach

Introduction Potential fittings should not be considered as a science, but as an "art", as we do not know *a priori* which kind of ansatz are appropriate for the description of our system and which features are relevant for the fitting of the analytical form assumed for our potential. One can imagine using (or even mixing) different contributions such as stress tensors, energies, forces, angular distributions, structure factors etc... in order to improve the description of the system. In this section we introduce the general methods, criteria and algorithms we have set up in order to find the optimal set of parameters suited for the potential energy ansatz we assumed.

4.1.1 The ansatz for the potential

Motivation The Born-Mayer potential including Coulombic interactions, see also section (2.2.4.1), has been retained in this work as its formulation is relatively simple (pairwise interactions):

$$V = \sum_{i<j} V(r_{ij}) = \sum_{i<j} \left[\frac{q_i q_j}{r_{ij}} + A_{ij} \exp\left(-b_{ij} r_{ij}\right) - \frac{c_{ij}}{r_{ij}^6} \right], \tag{4.1}$$

where r_{ij} stands for the interatomic distance between atoms i and atoms j, while $\{A_{ij}, b_{ij}, c_{ij}, q_i\}$ are the parameters of the potential. This potential form[1] has the advantage that it has a pairwise form which is quick and easy to evaluate, so that large system sizes and long times may be simulated with relative ease. Furthermore this kind of potential parameterized using the BKS parameters [9] has already given some encouraging results [9, 75, 153]. For example the short- and medium-range structure of the glass are quite well reproduced [75, 153], as well as the characteristic double peak structure of the vibrational density of state in the vitreous phase [12]. Furthermore, the crystalline properties of α-quartz (elastic constants and cell parameters) and the α to β quartz phase transition are also properly described [109]. Moreover it is also convenient to choose the Born-Mayer potential combined together with Coulomb interactions as many groups have already studied silica using this ansatz [75, 80, 153]. From a practical point of view, a reparameterization of a potential implies minor changes in the simulation programs compared to the amount of work needed to code routines for complex potential that makes use of self-consistent many body interactions [144].

The Born-Mayer potential The Born-Mayer potential [22] is one of the most widespread potentials for simulating ionic systems. This rigid ion model is mostly suited for the description of pure ionic systems such as sodium chloride. But many features typical for a iono-covalent system are left out, such as the three-body interactions due to directional sp^3 bondings and repulsion between lone pairs of electrons and bonded electrons. This potential assumes that ions are rigid in the sense that they

[1] The Born-Mayer potential is defined by two terms: $V_2^{\mathrm{BM}}(r_{ij}) = A_{ij} \exp(-b_{ij} r_{ij}) - c_{ij}/r^6$. The repulsive term $A_{ij} \exp(-b_{ij} r_{ij})$ is also called Buckingham potential.

cannot become aspherically distorted and they cannot change their size/charge in the condensed phase according to their environment.

Interactions in pure ionic system can be divided into two main contributions:

- Coulomb interactions as the dominant interaction in ionic systems;
- Covalent interaction, due to the Pauli exclusion principle the overlapping of the electronic clouds of ions is energetically penalized.

These two contributions have been explicitely taken into account in the definition of the analytical expression of the potential, see Eq. (4.1). The terms $1/r$ and $1/r^6$ originally account for the Coulomb interaction [82] and the exponential term originally accounts for the repulsive interactions between ions due to the Pauli principle. In practice the exact physical contributions of each term can hardly been disentangled as the fitting procedure cannot split the *ab initio* forces into different physical contributions. The numerical parametrization of the Born-Mayer potential is an effective parametrization, we are not allowed to interpret the physical meaning of each parameters separately.

Least squares criterion A fitted potential is considered to be succesful if, by considering it, one generates statical and dynamical features that are as close as possible to the original ones used for defining its parameters. As a consequence, finding a proper set of parameters comes to minimizing the discrepancies between the original and the predicted data. In order to define the magnitude of these discrepencies we need to define a suited estimator. The estimator used for the fits has to fulfill some basic constraints. Firstly its goal is to quantify the discrepancy between the original data and the data given by the fitted model. Secondly the estimator has to be flexible enough to take into account some numerical fluctuations. Most of the time, the original data are not free of numerical noise, even for a perfect model some differences will remain. Additionnally, its formulation has to be simple so as to facilitate the use of efficient numerical minimization algorithms.

The original data we may use for fitting our potential ansatz have occured with a certain likelihood. For example some theoretical data are calculated within a given accuracy (structure factors computed using *ab initio* molecular dynamics or experimental values for the phase transition temperature [87]) and hence we have to take into account the measurement errors (called noise) in the definition of the estimator by means of the standard deviations σ_i.

For fitting N observables $\mathbf{y}_i$ $\{i \in 1, \ldots, N\}$ that depends on some degree of freedom $\mathbf{x}_i$ to a model function/functional $f(\mathbf{x}_i; a_1, \ldots, a_M)$ depending on M adjustable parameters[2] a_j, $\{j \in 1, \ldots, M\}$. We have used an *arbitrary* criterion the so-called Chi-Square (χ^2) defined as:

$$\chi^2(a_1, \ldots, a_M) = \left[\sum_{i=1}^{N} \frac{\left(\mathbf{y}_i - f(\mathbf{x}_i; a_1, \ldots, a_M)\right)^2}{\sigma_i^2} \right]. \tag{4.2}$$

[2] $\mathbf{y}_i$ and $\mathbf{x}_i$ may not have the same dimension, in simulation the stress tensor has 6 components whose values depends on the atomic positions (for a system made of N atoms this represents $3N$ variables).

The value of χ^2 is always greater or equal to 0, $\chi^2 = 0$ would correspond to an "ideal" model function/functional. If the observable $\mathbf{y}_i$ is described with a good accuracy the corresponding standard deviation σ_i is small and so $1/\sigma_i$ is large, on the contrary is the observable $\mathbf{y}_i$ is poorly described $1/\sigma_i$ is small. In the above definition the standard deviation acts like a weighting factor that favors the accurate data over the inaccurate ones.

Minimization methods *Ab initio* calculations are carried out using N-body interactions computed by means of a self-consistent algorithm. According to this statement one can easily understand that parameters used for a simple two-body potential description may hardly reproduce the *ab initio* data. To tackle these issues, robust and very general algorithms are required to find the minima in the parameter space [118]. These algorithms rely on a simple Taylor expansion of χ^2 around a given set of parameter $\mathbf{a}^{(0)} = \{a_1^{(0)}, a_2^{(0)}, \dots a_M^{(0)}\}$ that we are now explaining:

$$\chi^2(\mathbf{a}) = \chi^2(\mathbf{a}^{(0)}) + (\mathbf{a} - \mathbf{a}^{(0)}) \cdot \nabla\chi^2(\mathbf{a}^{(0)}) + \frac{1}{2}(\mathbf{a} - \mathbf{a}^{(0)})^\dagger \cdot \mathbb{D} \cdot (\mathbf{a} - \mathbf{a}^{(0)}) + \mathcal{O}((\mathbf{a}^{(0)})^3) \quad (4.3)$$

where the matrix $\mathbb{D}$ is also named the Hessian matrix of the function χ^2 defined as:

$$(\mathbb{D})_{ij} = \frac{\partial^2\chi^2(\mathbf{a})}{\partial a_i^{(0)} \partial a_j^{(0)}}. \quad (4.4)$$

Two kinds of situation can be encountered during the optimization process:

- The parameters $\mathbf{a}$ are far from any minimum and therefore the $\chi^2(\mathbf{a})$ can be found using the iterative steepest descent algorithm (the set of parameter $\mathbf{a}$ at iteration l is labeled $\mathbf{a}^{(l)}$) based upon the first term of its Taylor expansion. The gradient $-\nabla\chi^2(\mathbf{a}^{(n)})$ indicates the direction from a point $\mathbf{a}^{(n)}$ to reach the minimum of the function χ^2. This gradient is called the steepest descent direction [98]. At step $n+1$ the improved set of parameters $\mathbf{a}^{(n+1)}$ is given by the gradient (scaled with an adjustable step length const. or an adjustable vector) according to the following equation:
$$\mathbf{a}^{(n+1)} = \mathbf{a}^{(n)} - \text{const.}\nabla\chi^2(\mathbf{a}^{(\mathrm{n})}). \quad (4.5)$$

- Close to the minimum, the gradient is negligible and it cannot be used anymore. To gain accuracy and efficiency second order methods based on the Hessian ($\mathbb{D}$) are necessary:
$$\mathbf{a}^{(n+1)} = \mathbf{a}^{(n)} + \mathbb{D}^{-1}[-\nabla\chi^2(\mathbf{a}^{(n)})] \quad (4.6)$$

Starting from its definition of χ^2, see Eq. (4.2) the gradient components of χ^2 can be expressed as:

$$\frac{\partial\chi^2}{\partial a_k} = -2\sum_{i=1}^{N} \frac{[\mathbf{y}_i - f(\mathbf{x}_i; a)]}{\sigma_i^2} \frac{\partial f(\mathbf{x}_i; \mathbf{a})}{\partial a_k}. \quad (4.7)$$

The Hessian components can be defined as:

$$\frac{\partial \chi^2(\mathbf{a})}{\partial a_k \partial a_l} = 2\sum_{i=1}^{N} \frac{1}{\sigma_i^2}\left[\frac{\partial f(\mathbf{x}_i;\mathbf{a})}{\partial a_k}\frac{\partial f(\mathbf{x}_i;\mathbf{a})}{\partial a_l} - [\mathbf{y}_i - f(\mathbf{x}_i;\mathbf{a})]\frac{\partial^2 f(\mathbf{x}_i;\mathbf{a})}{\partial a_k \partial a_l}\right]. \tag{4.8}$$

For practical purpose the second term in the expression of the Hessian are considered to be negligible when one is close to the minimum as $[y_i - f(x_i;\mathbf{a})] \simeq 0$:

$$\frac{\partial \chi^2(\mathbf{a})}{\partial a_k \partial a_l} \simeq 2\sum_{i=1}^{N} \frac{1}{\sigma_i^2}\left[\frac{\partial f(\mathbf{x}_i;\mathbf{a})}{\partial a_k}\frac{\partial f(\mathbf{x}_i;\mathbf{a})}{\partial a_l}\right] \tag{4.9}$$

These two minimization algorithm can be artfully mixed together according to the proposition of Levenberg and Marquardt [118]. The Levenberg and Marquardt algorithm is presented in the following section.

Levenberg-Marquardt minimization: Marquardt following a first idea of Levenberg proposed to mix together the two aforementioned methods allowing the whole procedure to switch from the gradient technique to the Hessian one as the minimum is approached. For this purpose one can introduce the following notations based on the Eqs. (4.6), (4.7) and (4.8):

$$\beta_k := -\frac{1}{2}\frac{\partial \chi^2}{\partial a_k}, \quad \alpha_{kl} := \frac{1}{2}\frac{\partial^2 \chi^2}{\partial a_k \partial a_l}, \quad \text{and} \quad \Delta a_l = a_l^{(n+1)} - a_l^{(n)} \tag{4.10}$$

Using the above definition of β_k and α_{kl}, the Eqs (4.5), and (4.6) can be rewritten as:

$$\sum_{l=1}^{M} \alpha_{kl}\Delta a_l = \beta_k \quad \text{and} \quad \Delta a_l = \text{const.}\beta_\text{l} \tag{4.11}$$

respectively. Thus the parallel between the two approaches becomes now prominent. The steepest descent method requires the use of a typical step length for updating the vector parameter (Δa_l in Eq. (4.11)). The components for the rescaling vector may not have the same magnitude as the parameters of the model do not play equivalent role. It is possible to propose relevant starting values of the rescaling vector from the diagonal terms of the Hessian matrix:

$$\Delta a_l = \frac{1}{\lambda \alpha_{ll}}\beta_l \quad \text{or} \quad \Delta a_l \lambda \alpha_{ll} = \beta_l \tag{4.12}$$

where λ stands for an arbitrary rescaling term. The idea of Levenberg and Marquardt[118] consists in mixing the steepest descent and the second order method using the Hessian by changing the parameter λ. The numerical algorithm consists in solving iteratively the following set of linear equations:

$$\sum_{i=1}^{M} \alpha_{ij}(1 + \lambda\delta_{ij})\Delta a_j = \beta_i, \qquad \text{with} \qquad \alpha'_{ij} = \alpha_{ij}(1 + \lambda\delta_{ij}) \tag{4.13}$$

For $\lambda \gg 1$ the redefined Hessian (α'_{ij}) is diagonal dominant, leading to the gradient approach, whereas for $\lambda \ll 1$, the Hessian approach is used.

4.2 Force-matching method

Introduction The very first potential proposed for silica [160] was based on naive considerations that complex *ab initio* methods could not be afforded. The usual procedure at that time consisted in fixing directly as many parameters as possible using very simple chemical and/or physical considerations. For example, Coulomb charges were set to the ionic ones even for iono-covalent compounds [160]. The remaining parameters were fitted so as to reproduce some experimental data. Crystalline phases have been mainly used for this purpose, and features such as elastic constants, dielectric constants, bulk modulus, asymmetric parameters were equally used for the parameterization of the remaining parameters [9].

This method has many limitations: Firstly, because of their simple analytical forms classical potentials fitted using data relative to a given phase can hardly be transferable[3] to another phase. For example a potential fitted on crystalline phases might not be accurate for molten silica. Moreover lots of experimental results used for the fits of these potential are macroscopic features. A potential fitted using macroscopic data may artificially reproduce these features as the local informations have not been taken into account. On the contrary an "ideal" effective potential should be able to mimic at best the local interactions (interatomic forces) and consequently it should be able to mimic also macroscopic features.

The "force-matching" method of Ercolessi and Adams [46] has been proposed so as to circumvent these shortcomings. This method is a numerical optimization procedure which tries to match as closely as possible to the *ab initio* data (forces, stress tensor, elastic constant, *etc...*) using a classical potential. It has been applied first to aluminum systems [46] and thereafter has been widely used for other compounds and for different kind of potentials: Spline potentials [77], many-body polarizable potentials [144], etc ...

Merit function To evaluate the accuracy of the fit one needs to define the χ^2 function (also named "merit function"), we have first considered the *ab initio* forces:

$$\chi^2 = \frac{1}{3N} \left\langle \sum_{i=1}^{N} \sum_{\alpha \in (x,y,z)} \left[\frac{\mathbf{F}_{i,\alpha}^{\mathrm{CP}} - \mathbf{F}_{i,\alpha}^{\mathrm{Class.}}}{\sigma_i} \right]^2 \right\rangle \tag{4.14}$$

where:

- $\mathbf{F}_{i,\alpha}^{\mathrm{CP}}$ refers to the spatial components of the *ab initio* forces for a given atom i;
- $\mathbf{F}_{i,\alpha}^{\mathrm{Class.}}$ refers to the spatial components of the classical forces for a given atom i;
- σ_i stands for the standard deviation of the *ab initio* force distribution for a given atom i;
- N is the number of atoms of a given atomic sample;

[3] The ability of a potential to work properly in different environments is called *transferability*.

- $\langle\cdot\rangle$ denotes the averaging over different samples.

The standard deviations do not depend on the configuration sample as all the samples are supposed to be equivalent for the fit. Nevertheless these coefficients depend on the atoms as the forces have not the same statistical distribution for silicons or for oxygens, see Fig. 4.2. The definition of σ_i is:

$$\sigma_i = \sqrt{\langle \mathbf{F}_i^{\mathrm{CP}\,2} \rangle - \langle \mathbf{F}_i^{\mathrm{CP}} \rangle^2}. \tag{4.15}$$

The σ_i can be approximated by the following expression:

$$\sigma_i \simeq \sqrt{\langle \mathbf{F}_i^{\mathrm{CP}\quad 2} \rangle} \simeq |\langle \mathbf{F}_i^{\mathrm{CP}} \rangle| \quad \text{as} \quad \langle \mathbf{F}_i^{\mathrm{CP}} \rangle \simeq 0. \tag{4.16}$$

Consequently, Eq. (4.14) becomes:

$$\chi^2 \simeq \frac{1}{3N} \left\langle \sum_{i=1}^{N} \sum_{\alpha \in (x,y,z)} \left[\frac{\mathbf{F}_{i,\alpha}^{\mathrm{CP}} - \mathbf{F}_{i,\alpha}^{\mathrm{Class.}}}{|\langle \mathbf{F}_i^{\mathrm{CP}} \rangle|} \right]^2 \right\rangle. \tag{4.17}$$

The relative error[4] of the forces can then be introduced:

$$\delta_i^{\mathrm{Force}} = \frac{|\mathbf{F}_i^{\mathrm{CP}} - \mathbf{F}_i^{\mathrm{Class.}}|}{|\langle \mathbf{F}_i^{\mathrm{CP}} \rangle|} \tag{4.18}$$

the χ^2 can then be considered as the squared value of the relative error associated to the forces averaged over the positions of the particles:

$$\chi^2 \simeq \frac{1}{3N} \left\langle \sum_{i=1}^{N} \delta_i^{\mathrm{Force}\,2} \right\rangle. \tag{4.19}$$

4.2.0.1 Practical aspects

The Forces For a two-body potential the components of forces $\mathbf{F}_i^{\mathrm{Class.}}$ applied on an atom i can be defined:

$$\mathbf{F}_i^{\mathrm{Class.}} = \sum_{k \neq i} \mathbf{F}_{ij}^{\mathrm{Class.}} \quad \text{with} \quad F_{x,i}^{\mathrm{Class.}} = -\sum_{j \neq i} \frac{\partial V(r_{ij})}{\partial r_{ij}} . \frac{x_i - x_j}{r_{ij}} \tag{4.20}$$

$$F_{x,i}^{\mathrm{Class.}} = \sum_{j \neq i} F_{ij}^{\mathrm{Class.}} . \frac{x_i - x_j}{r_{ij}}. \tag{4.21}$$

Here r_{ij} stands for the interatomic distance between atoms i and j, $F_{ij}^{\mathrm{Class.}}$ is the classical interatomic forces applied on atom i by atom j, and x is one the Cartesian coordinates of the atom i. The minimization procedure is based upon the calculation

[4] In numerical analysis, the relative error in some data is the discrepancy between an exact value and some approximation to it.

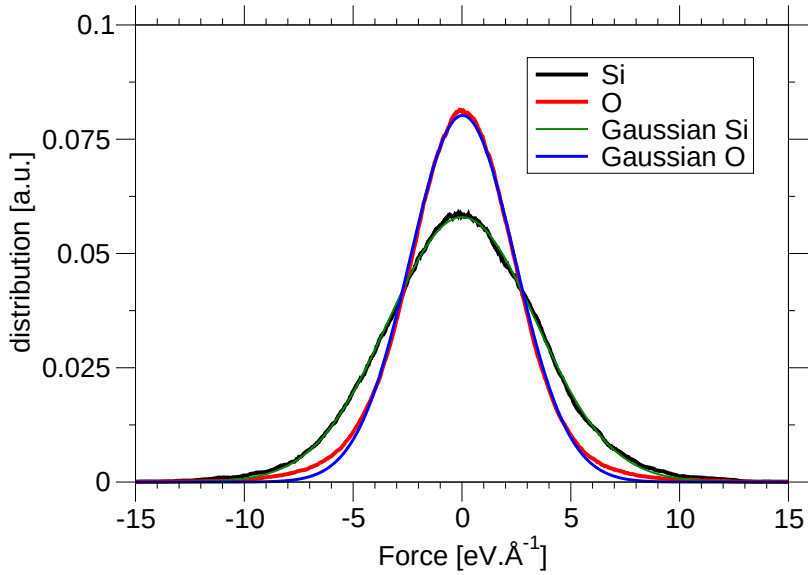

Figure 4.2: Distribution of *ab initio* forces for a 114 atoms system at 3600K. The black and red curves represent the raw data for silicon and oxygen, the green and blue curves represent the corresponding approximated Gaussian distribution.

of the gradient of the forces with respect to the Born-Mayer potential parameters, see section (4.1.1). These components can be derived using (4.20):

$$\frac{\partial \mathbf{F}_{ij}^{\text{Class.}}}{\partial q_i} = \begin{cases} -\frac{2q_i}{r_{ij}^2}.\frac{\mathbf{r}_{ij}}{r_{ij}}, & \text{if } q_i = q_j \\ \frac{2q_j}{r_{ij}^2}.\frac{\mathbf{r}_{ij}}{r_{ij}}, & \text{if } q_j = -2q_i \end{cases} \tag{4.22}$$

$$\frac{\partial \mathbf{F}_{ij}^{\text{Class.}}}{\partial A_{ij}} = b_{ij}\exp(-b_{ij}r_{ij}).\frac{\mathbf{r}_{ij}}{r_{ij}} \tag{4.23}$$

$$\frac{\partial \mathbf{F}_{ij}^{\text{Class.}}}{\partial b_{ij}} = A_{ij}\exp(-b_{ij}r_{ij})(1-b_{ij}r_{ij}).\frac{\mathbf{r}_{ij}}{r_{ij}} \tag{4.24}$$

$$\frac{\partial \mathbf{F}_{ij}^{\text{Class.}}}{\partial c_{ij}} = -\frac{6}{r_{ij}^7}\frac{\mathbf{r}_{ij}}{r_{ij}} \tag{4.25}$$

where the constant α_{ij} depends on the species under consideration. If i refers to a silicon atom and j refers to an oxygen atom then $\alpha_{ij} = -1/2$. On the contrary if i is an oxygen atom and j is a silicon atom $\alpha_{ij} = -2$. Due to the charge neutrality ($\sum_i q_i = 0$) the derivative of the Coulomb terms is simple to handle despite the complicated Ewald summation term.

Atomic configurations The original data used for the fitting have been taken from the *ab initio* simulations discussed in chapter (3). The first 3.5 ps of the CPMD corresponding to the ballistic regime ($\langle r^2(t)\rangle \propto t^2$) have not been used, see also Figs. 3.17 and 3.18. We have used the part of the dynamics corresponding to the plateaux and

beyond to be sure that the configuration samples were properly relaxed. One hundred configurations have been taken from the *ab inition* molecular dynamics trajectory. These configurations were separated from each others by a constant time interval of 160 fs.

Fitting parameters In our quantum simulations the wavefunctions are developed on plane waves basis (*i.e.* Fourier decomposition of an infinite periodic system, see also section (2.3.3)), the atoms are interacting with the others and also with their periodic images (the Fourier decomposition of the wavefunction supposes that the system is infinitely periodic). Due to the periodic boundary positions the only exploitable interatomic distances are the ones below $L_{\text{box}}/2$.

In our case this length $L_{\text{box}}/2 = 5.99$Å as we have 38 SiO_2 molecules. This correlation length is very small and might affect the fitting. In order to check whether the system size has an influence of on the fitted potential some *ab initio* simulations have also been carried out on a smaller system made of 78 atoms (*i.e.* $L_{\text{box}}/2 = 5.28$ Å for 26 SiO_2 molecules). Fitting have been made both for the 78 atoms system and for the 114 atoms system. In Fig. 4.3, the differences between the two obtained potentials are shown. The χ^2 and the parameters of the two resulting potentials are tabulated in Table 4.1. Some changes occur in the parameters with respect to the system size, the magnitudes of these changes is linked to the typical distances (first maxima of the $g(r)$) between atomic pairs. The Si-O terms are less affected than the O-O terms or the Si-Si terms. It can be easily understood that the geometry of the system affects the accuracy of the fitting. In silica, the SiO_4 tetrahedra are linked by their vertices, so all the closest silicon atoms surrounding a given silicon atom are linked by bridging oxygens. As a consequence the Si-Si terms of the potential are partially blurred by non trivial three-body interactions ($\widehat{\text{SiOSi}}$ energy terms). Nevertheless, the whole χ^2 is not changed significantly, and as one can see in Fig. 4.3 the curves representing the two different potentials do not show any significant changes.

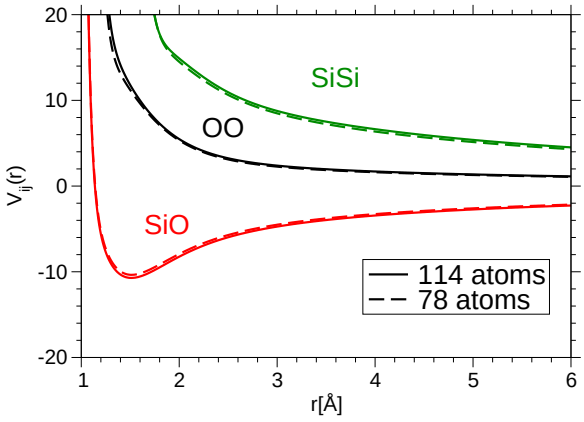

Figure 4.3: Influence of the system size on the force fitted potential.

Usually classical potentials used for ionic system are described by the addition of

Parameters		78 atoms	114 atoms
χ^2		0.180509	0.173765
q_{Si}	[C]	1.340998	1.374323
A_{OO}	[eV]	761.216893	666.333770
b_{OO}	[Å^{-1}]	2.761536	2.748299
c_{OO}	[eV Å^6]	60.514256	41.663842
A_{SiO}	[eV]	26892.664010	26486.505961
b_{SiO}	[Å^{-1}]	5.197433	5.184248
c_{SiO}	[eV Å^6]	145.701309	145.456110
A_{SiSi}	[eV]	2773.666970	3976.776182
b_{SiSi}	[Å^{-1}]	2.728367	2.794342
c_{SiSi}	[eV Å^6]	671.387028	882.596651

Table 4.1: Parameter sets extracted from two different *ab initio* trajectories.

long and short range terms, which in our case are the Coulomb term and Born-Mayer term respectively. For the short range term, no explicit values can be proposed *a priori*, and the atoms may interact with their periodic images. These particles-particles replica interactions play a significant role in crystalline structure calculations for example.

To check whether the interactions with the periodic replicas of the atoms play a role some fitting have been made using different cutoffs for the Born-Mayer potential larger than $L_{\text{box}}/2$ (see Figs. 4.5 and 4.4). As it can be seen in Fig. 4.4 the cutoff does not seem to have a major influence on χ^2. This can be easily understood as the parameters only vary from their average value by less than 20%, see Fig. 4.5. Note that even if the Coulomb interactions are computed using the Ewald summation, which take explicitely into account the interactions with the periodic replicas, the silicon charge vary slightly with respect to the cutoff. This effect is due to the complicated interplay between the long and short rang contributions of the potential. To be on the safe side all the fittings presented in the following section have been made using a $r_{\text{cut}} = 10$Å cutoff.

In this work two different potential ansatz have been considered. First, following the considerations of van Beest *et al.* [9, 85] no short range term has been assigned to the silicon-silicon part of the potential. Practically this allows a reduction of 10% of the computational time. These potentials without any short range Si-Si terms are named in the following part of the text "constrained" potentials. These constrained potentials ansatz have led to good results for the BKS potential [19, 68, 75, 153]. Secondly, if the Si-Si short ranged interactions are considered the corresponding potentials are named in the following part of the text "unconstrained" potentials.

In order to check the influence of the *ab initio* parameters on the final results two kind of pseudopotentials have been tested for the computation of the original forces. The first calculations have been made using the pseudopotentials described in Ref [10] (labeled NCPP for Norm Conserving Pseudopotential in the following) using a cutoff $E_{\text{cut}} = 130$ Ry. These pseudopotentials are designed for an accurate description of

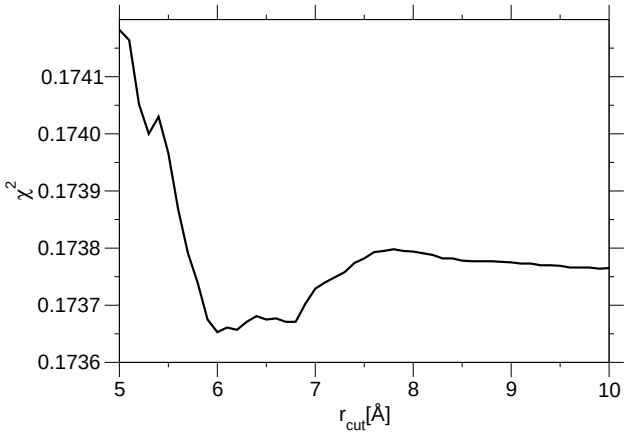

Figure 4.4: Influence of the short range cutting distance on the χ^2, for 100 configurations extracted from an *ab initio* molecular dynamics runs at 3600K.

the inner atomic orbitals. Consequently these PP must be developed on a large plane waves basis set in order to describe their rough shape, see also section (2.3.4).

Another series of simulations have been made using the ultrasoft pseudopotentials proposed by the group of D. Vanderbilt (VDB PP) that have shown some abilities in reproducing the right crystalline parameters for a wide variety of crystalline phases [94]. These pseudopotentials are smooth and so they require small energy cutoff by design, in the present case a cutoff of $E_{\text{cut}} = 40$ Ry has been used following the reference [94].

4.2.0.2 Results

Fitting Results To ensure a good exploration of the parameter space, different starting parameters have been used as input. The final results are quite insensitive to the initial parameters. It turns out that one minimum of the χ^2 is clearly localized by the Levenberg-Marquardt algorithm. The fitting results for the different ansatz made on a 114 atoms liquid system are summarized in Table 4.3.

After a whole fitting process the final χ^2 associated to an unconstrained set of parameters is equal to 0.17 while for the constrained case it is equal to 0.18. Surprisingly the accuracy of the fit is comparable even if three degrees of freedom have been constrained. However the parameters are quite different and lead to different potential energy curves, see Fig. 4.6. In addition to this, it appears that the different pseudopotentials used for the computation of the forces do not lead to very different results, even if the parameters are slightly different and the corresponding potential energy curves are quite similar (see Fig. 4.7).

For an appropriate comparison, the χ^2 associated to the BKS potential has also been calculated, a value of 1.21 has been found this means that the description of the forces have been improved by a factor 7. Following the considerations leading to Eq. (4.16) of the relative error in the description of the forces using the BKS is equal to 110% whereas the force fitted potential gives a relative error of 42%.

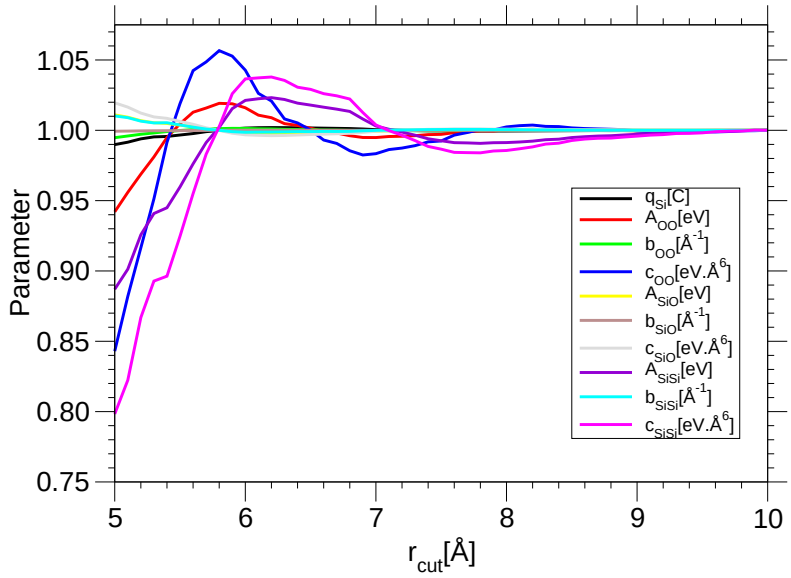

Figure 4.5: Influence of the short range cutting distance on the parameters, for 100 configurations taken from an *ab initio* molecular dynamic at 3600K. All the parameters have been rescaled using their corresponding values calculated for a 10Å cutoff.

These preliminary results seems to indicate that the BKS potential appears to be inaccurate for the force computation of liquid silica. Even if the structure and the elastic constants are well reproduced, the forces are not accurate. This fact may underline a lack of transferability of the BKS potential that is mostly suited to crystalline phases by construction. These results indicate that the underlying microscopic interactions (pair interactions) summed for calculating the elastic constants[5] are not properly described. These shortcomings illustrate the limitation of the empirical fitting approach used for the BKS.

Molecular Dynamics Simulation The classical-forces derived from the force fitted potentials are now very close to the *ab initio* forces. Nevertheless, simulations have to be carried out to check whether the force fitted potential gives results similar to the *ab initio* ones. Firstly one has to check the static features such as the angular distribution functions, the pair correlation functions, or the pressure. To achieve this, some classical molecular dynamics have been made in the NVT ensemble (the temperature was kept constant by means of a stochastic collision algorithm, see section 2.2.2). The sample were made of 1152 atoms in a 25.904 Å cubic box corresponding to a density of 2.2 g/cm^3, and the temperature was set equal to 3600 K. For these classical simulations the short range part of the potential has been cutoff at 5.5 Å following the methodology proposed by K. Vollmayr *et al.* [153]. Even if this cutoff is not the one used in the fitting routine it has been shown that it has no significant effects on the structure

[5]The elastic constants (C_{ij}) represent the second derivatives of the energy density with respect to strain (ε_i) defined in Appendix A, $C_{ij} = \frac{1}{V}\left(\frac{\partial^2 V}{\partial\epsilon_i \partial\epsilon_j}\right)$.

Parameters		BKS	N. C. P.P. [10]		VDB P.P. [94]	
			const.	unconst.	constr.	unconst.
χ^2		1.21	0.18	0.17	0.18	0.17
q_{Si}	[C]	2.4	1.51	1.37	1.52	1.406121
A_{OO}	[eV]	1388.77300	566.034828	666.333770	600.322980	695.838375
b_{OO}	[Å^{-1}]	2.76	2.742411	2.748299	2.771985	2.776613
c_{OO}	[eV Å^6]	175.00	22.175162	41.663842	25.665206	43.614650
A_{SiO}	[eV]	18003.7572	24068.698306	26486.505961	22524.405722	24657.035366
b_{SiO}	[Å^{-1}]	4.87318	5.178984	5.184248	5.211330	5.216538
c_{SiO}	[eV Å^6]	133.5381	128.571683	145.456110	111.922618	126.274364
A_{SiSi}	[eV]	-	-	3976.776182	-	4521.106337
b_{SiSi}	[Å^{-1}]	-	-	2.794342	-	2.819346
c_{SiSi}	[eV Å^6]	-	-	882.596651	-	965.488324

Table 4.2: Different sets of parameters given by the fitting procedure.

[64]. The potential collapse of particles which may be induced by the $1/r^6$ terms of the classical potential for small distances has been controlled by means of a repulsive Lennard-Jones potential, see section (2.2.4.1). The simulation length has been set to 10 ps. According to the previous results of J. Horbach and W. Kob [75] for the BKS potential, this time is long enough to reach the diffusive regime at $T = 3600$ K.

Results The pair distribution function are shown in Figs. 4.8 and 4.9. Apart from the location of the first peak for the Si-O pair, the others peak positions and the peak height are in strong disagreement with the *ab initio* results. The plots representing the pair correlation functions given by the VDB set of parameters have not been represented here as they show the same quantitative features.

The angular distributions have also been computed, and the corresponding results for the for $\widehat{\mathrm{OSiO}}$ and $\widehat{\mathrm{SiOSi}}$ angle are in strong disagreement with the *ab initio* results, see Figs. 4.10, 4.11. A close inspection of the configurations reveals lots of edge sharing tetrahedra (or two-membered rings), see Fig. 4.12, which account for the bump presents at 90° for the $\widehat{\mathrm{SiOSi}}$ angle distribution function. These two-membered rings lead to a shortening of the Si-Si distances, and thus explains the wide Si-Si peaks for the pair correlation function.

A reliable pair potential has to fulfill several basic requirements. Firstly it has to give reasonable description of the structure. Secondly, once the structure has been properly described one can check the dynamical properties of the model. There is no need to check whether the dynamical features are well reproduced if the static features are not. For example, it is necessary to describe properly the structure of the vitreous state (static properties) so as to compute the corresponding vibrational density of states (dynamical properties). The static properties given by the potentials we fit using the *ab initio* forces are in strong disagreement with the original data and consequently no further investigation have been done within this simple force-matching scheme.

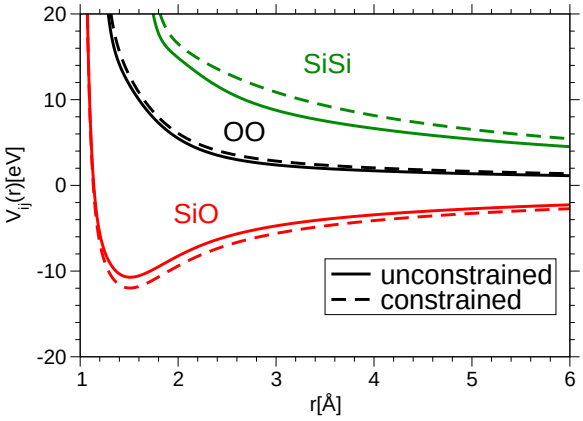

Figure 4.6: Potential energy curves for the constrained and unconstrained set of parameters set using the NCPP pseudo-potentials.

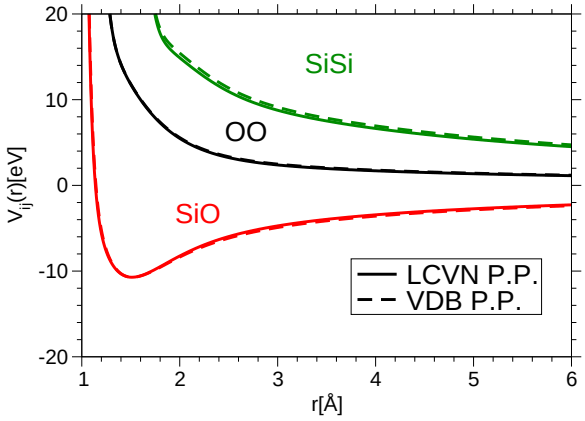

Figure 4.7: Potential energy curves for the unconstrained sets of parameters set using the NCPP and the VDB pseudo potentials.

4.3 Extended criterion: Stress tensor

Introduction As we have seen in the previous section classical potentials derived for silica using a simple force matching procedure using only the *ab initio* forces do not lead to satisfactory results. In addition to their bad structural predictions such force-fields were also giving a negative pressure ($\simeq -1$ GPa). The pressure is usually computed using the stress tensor whose components are defined by the sum of the interatomic forces multiplied by the associated interatomic distances. As a consequence, the stress tensor is quite sensitive to the medium and long range forces, and thus, this feature could help refining the description of the potential. Moreover, a system with a negative internal pressure is not stable as it tends to cavitate. According to the work of P. Tangney [129, 145], including the stress tensor in the fitting criterion can help refining the pressure and so improving the stability of the system.

4.3.1 Practical Aspects

Extended χ^2 Because of its different microscopic definition, the stress tensor cannot simply be added to the initial merit function, see Eq. (4.14). We have proposed a new definition of χ^2_Θ, based in Eq. (4.14) which includes the stress tensor components in our fitting procedure:

$$\chi^2_\Theta = \Theta\chi^2_{\text{Force}} + (1-\Theta)\chi^2_{\text{Stress}} \tag{4.26}$$

$$\chi^2_{\text{Force}} = \frac{1}{3N}\left\langle \sum_{i=1}^{N}\sum_{\alpha\in(x,y,z)}\left[\frac{\mathbf{F}^{\text{CP}}_{i,\alpha} - \mathbf{F}^{\text{Class.}}_{i,\alpha}}{\sigma_i}\right]^2\right\rangle \tag{4.27}$$

$$\chi^2_{\text{Stress}} = \frac{1}{9}\left\langle \sum_{u,v=1}^{3}\frac{\left[\Pi^{\text{CP}}_{uv} - \Pi^{\text{Class.}}_{uv}\right]^2}{\sigma_{uv}}\right\rangle \tag{4.28}$$

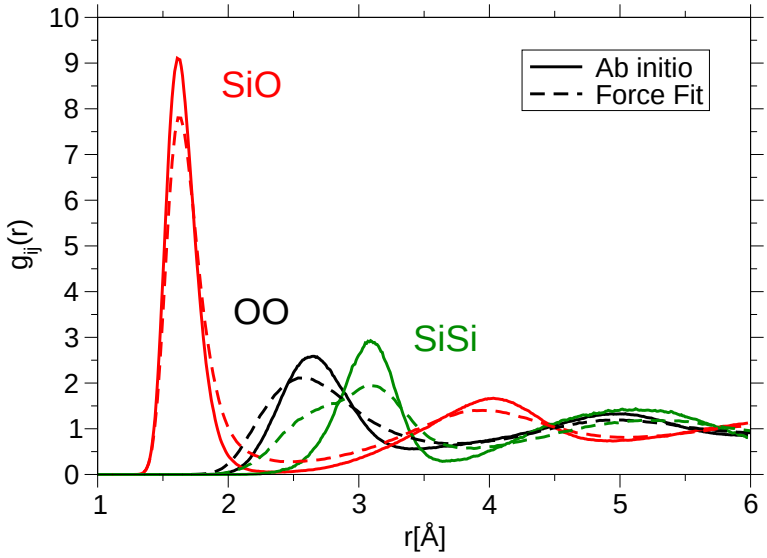

Figure 4.8: Comparison of the partial pair correlations function. Bold lines correspond to *ab initio* calculations and dashed lines to simulations with the constrained potential (see text).

where:

Θ balances the contribution of the forces and the stress tensor components in the definition of the extended χ^2_Θ, $\Theta \in [0,1]$;

Π_{uv} denotes the stress tensor elements, Π^{CP}_{uv} corresponds to the *ab initio* stress tensor and $\Pi^{\mathrm{Class.}}_{uv}$ corresponds to the classical one;

σ_{uv} is the standard deviation of the *ab initio* stress tensor[6].

The physical considerations leading to the analytical definition of the stress tensor for the short and long range terms can be found in appendix A. To fit the stress tensor one needs to compute its derivatives with respect to the potential parameters. For the short range part of the potential these derivatives are found to be given by:

$$\Pi_{\alpha,\beta} = -\frac{1}{\Omega}\frac{\partial V}{\partial \varepsilon_{\alpha,\beta}} = -\frac{1}{\Omega}\sum_{i<j}\frac{\partial V(r_{ij})}{\partial r_{ij}}\frac{r_{ij,\alpha}r_{ij,\beta}}{r_{ij}} \tag{4.29}$$

$$\frac{\partial \Pi_{\alpha,\beta}}{\partial A_{ij}} = -\frac{1}{\Omega}\frac{\partial^2 V}{\partial A_{ij}\partial \varepsilon_{\alpha,\beta}} = -\frac{1}{\Omega}\sum_{i<j} -b_{ij}\exp\left(-b_{ij}r_{ij}\right)\frac{r_{ij,\alpha}r_{ij,\beta}}{r_{ij}} \tag{4.30}$$

$$\frac{\partial \Pi_{\alpha,\beta}}{\partial b_{ij}} = -\frac{1}{\Omega}\frac{\partial^2 V}{\partial b_{ij}\partial \varepsilon_{\alpha,\beta}} = -\frac{1}{\Omega}\sum_{i<j} A_{ij}\exp\left(-b_{ij}r_{ij}\right)\left(b_{ij}-A_{ij}\right)\frac{r_{ij,\alpha}r_{ij,\beta}}{r_{ij}} \tag{4.31}$$

[6] $\sigma_{11} = 2.0866060$ GPa, $\sigma_{12} = 1.7711912$ GPa, $\sigma_{13} = 1.4110304$ GPa, $\sigma_{22} = 2.3733704$ GPa, $\sigma_{23} = 1.3618785$ GPa, $\sigma_{33} = 2.2730932$ GPa.

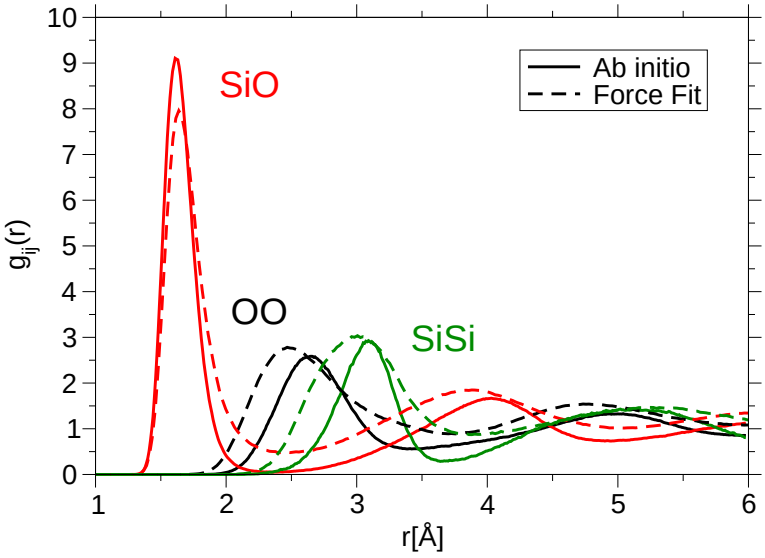

Figure 4.9: Comparison of the partial pair correlations function. Bold lines correspond to *ab initio* calculations and dashed lines to simulations with the unconstrained potential (see text).

$$\frac{\partial \Pi_{\alpha,\beta}}{\partial c_{ij}} = -\frac{1}{\Omega}\frac{\partial^2 V}{\partial b_{ij}\partial \varepsilon_{\alpha,\beta}} = -\frac{1}{\Omega}\sum_{i<j}\frac{6}{r_{ij}^7}\frac{r_{ij,\alpha}r_{ij,\beta}}{r_{ij}}. \tag{4.32}$$

Here Ω stands for the volume of the cell considered. For the long range term, a simple expression is obtained due to the neutrality constraint linking the silicon charges and the oxygen charges:

$$\frac{\partial \Pi_{\alpha\beta}}{q_i} = -\frac{1}{\Omega}\frac{\partial^2 V}{\partial q_i \partial \varepsilon_{\alpha\beta}} \tag{4.33}$$

$$= \frac{1}{2q_i}\Pi_{\alpha\beta}. \tag{4.34}$$

As no value for the balancing factor Θ can be proposed *a priori*, five sets of fittings have been carried out by setting its value to 0.005, 0.25, 0.50, 0.75, 0.995 and 1. A constrained potential (frozen Si-Si parameters) and an unconstrained one have been considered here.

4.3.2 Results

Fitting results During the optimization process some numerical instabilities have been observed for the unconstrained potential. Indeed, the A_{SiSi} and b_{SiSi} parameters were diverging and for this reason we will only discuss the fitting results obtained for the constrained potential.

As can be seen in Fig. 4.14 even slight perturbations ($\Theta = 0.995$) of the χ^2_Θ lead to significant improvements of the stress tensor. This implies that one can improve the

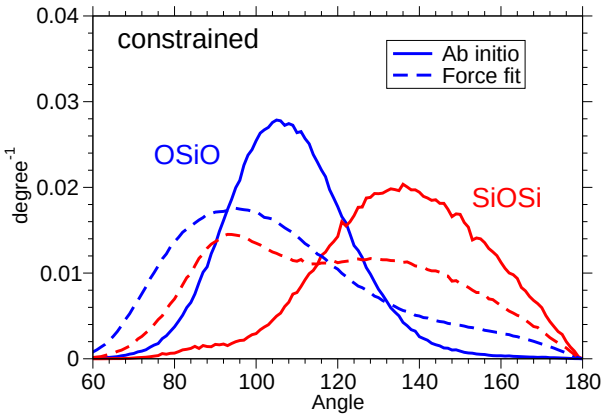

Figure 4.10: Comparison of the angular distribution function. Bold lines correspond to *ab initio* calculations and dashed lines to simulations with the constrained potential (see text).

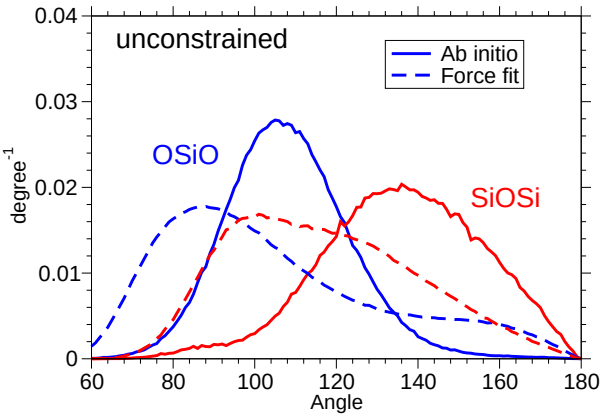

Figure 4.11: Comparison of the angular distribution function. Bold lines correspond to *ab initio* calculations and dashed lines to simulations with the unconstrained potential (see text).

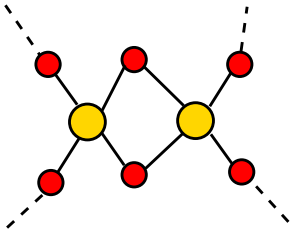

Figure 4.12: Edge sharing tetrahedra.

tensorial features without loosing accuracy on the forces and this for a wide range of values for Θ ($\in [0.25-0.75]$). This has to be correlated to the stability of the parameters in this range as can be seen in Fig. 4.13. The overall χ^2 ($\chi^2 = \chi^2_{\text{Force}} + \chi^2_{\text{Stress}}$) of the system is optimal around $\Theta = 0.50$ (see Figs. 4.14 and 4.15) consequently optimizations of the parameters have been carried out for this value. A comparison of these parameters with the force fitted ones ($\Theta = 1$) is given in Table 4.3. The stress Chi-Square corresponding to the force-fitted parameters $\chi^2_{\text{Stress}}{}^{\Theta=1} = 2.54$ has been significantly lowered by the fitting procedure using the stress weighted criterion, by a factor 25. ($\chi^2_{\text{Stress}}{}^{\Theta=0.5} = 0.10$), the accuracy of the description of the forces is unspoilt. The ionic charges as well as the Si-O parameters are somewhat changed ($q_{\text{Si}}^{\Theta=1} = 1.505$, $q_{\text{Si}}^{\Theta=0.5} = 1.447$, $A_{\text{SiO}}^{\Theta=1} = 24063.405609$, $A_{\text{SiO}}^{\Theta=0.5} = 25228.921758$), in contrast to this the O-O parameters have been significantly modified. Classical simulations in the NVT ensemble have been made using the new potential (see Fig. 4.16). Unfortunately these results are comparable to the previous one given using a pure force fitting approach.

As previously mentioned, see section (3.4.4), the pressure in the CP simulations is in strong disagreement with the experimental results. To circumvent this problem

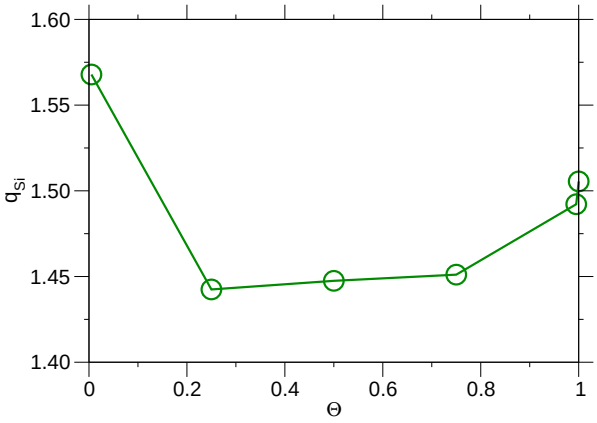

Figure 4.13: Variation of the silicon Coulomb charge as a function of the balancing parameter Θ.

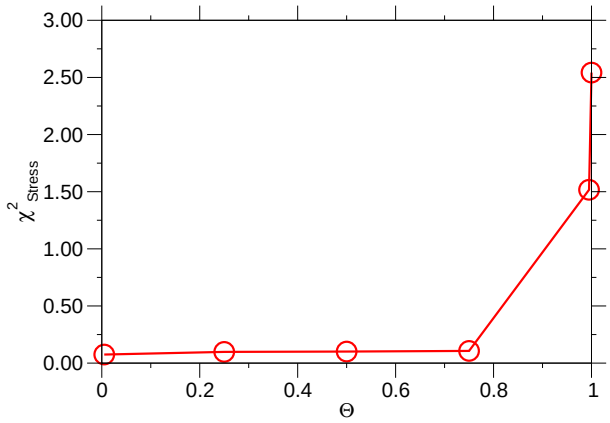

Figure 4.14: Variation of χ^2_{Stress} as a function of the balancing parameter Θ.

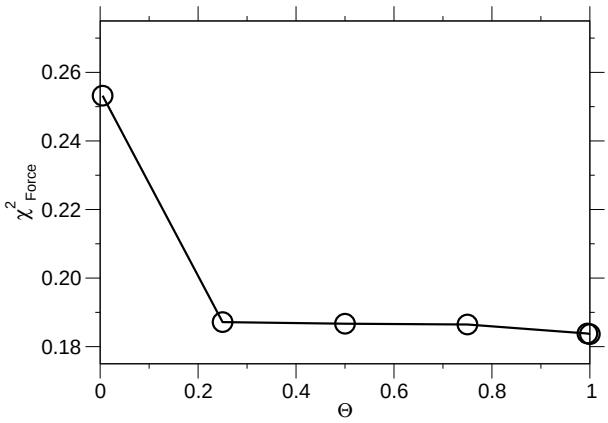

Figure 4.15: Variation of χ^2_{Force} as a function of the balancing parameter Θ.

and to improve the structural features, another series of fitting have been made using the *ab initio* data relative to the forces mixed with an arbitrary null stress tensor. A potential enforced to simulate a null stress tensor may avoid an overall falling down of the tetrahedral network. The corresponding numerical results are given in Table 4.3. Generally, for a simple classical potential, forces and stress tensors are connected to the first derivatives of the potential. As a consequence, a potential that reproduces accurately the forces may also describe properly the stress tensor. This assumption is consistent with the accuracy of the fit for the $\Theta = 0.5$ potential as both the χ^2_{Stress} and the χ^2_{Force} have been significantly improved, see Figs. (4.15), (4.14). On the contrary, by setting artificially the stress tensor to zero we break the consistency between the stress tensor and the forces. As a consequence it is difficult to improve simultaneously the χ^2_{Stress} and the χ^2_{Force} as the physical connection between the *ab initio* forces and the associated stress tensor does not hold anymore. This explanation accounts for the

Parameters		BKS		$\Theta = 1$		$\Theta = 0.5$	
		a.i. Stress	0 Stress	*a.i.* Stress	0 Stress	*a.i.* Stress	0 Stress
χ^2_{Stress}		0.96	8.57	2.54	0.92	0.10	0.81
χ^2_{Force}		1.21		0.18		0.18	0.18
q_{Si}	[C]	2.4		1.505497		1.44749	1.489117
A_{OO}	[eV]	1388.7730		565.908889		1358.848936	422.540596
b_{OO}	[Å^{-1}]	2.76		2.741589		2.903263	2.668126
c_{OO}	[eV Å^6]	175.		22.340312		141.887703	2.546299
A_{SiO}	[eV]	18003.7572		24063.405609		25228.921758	23643.106335
b_{SiO}	[Å^{-1}]	4.87318		5.178611		5.178662	5.187982
c_{SiO}	[eV Å^6]	133.5381		128.598107		137.227850	124.729092

Table 4.3: BKS original set of parameters compared to the ones obtained using definition (4.26) for the χ^2 and for two values of Θ. The abbreviation *a.i.* means that the *ab initio* observables have been taken into consideration for the fit.

value of 0.81 of the χ^2_{Stress} we obtained after fitting the null stress tensor for $\Theta = 0.5$, whereas we obtained a value of 0.10 when using the *ab initio* stress tensor for the fit. This underlines the lack of physical insight assumed when using a fictitious stress tensor. Moreover these new parameters are similar to the ones given for $\Theta = 1$, which is consistent with the inaccurate results obtained during a molecular dynamics simulations using the force-field fitted with a null stress tensor, see Fig. 4.17.

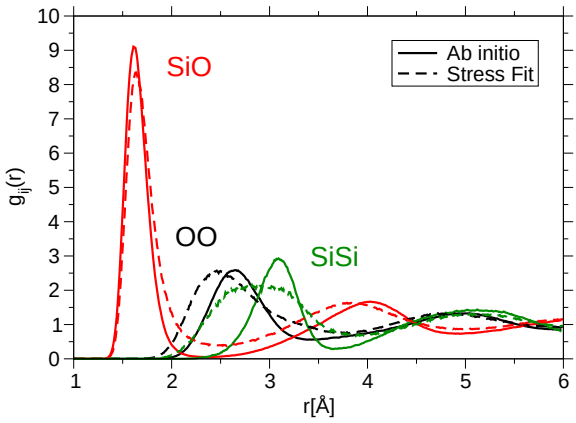

Figure 4.16: Pair correlation function issued from the *ab initio* force/stress data.

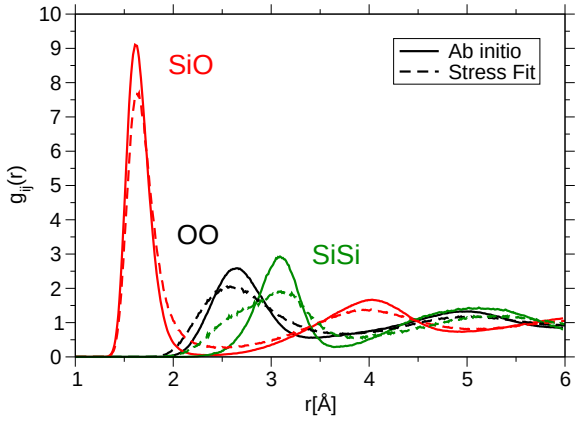

Figure 4.17: Pair correlation function issued from the potential fitted using both *ab initio* forces mixed with a null stress tensor.

It is worthwhile to note that the stress tensor given by the BKS potential is closer to the *ab initio* results than to the assumed null stress tensor. This can be easily interpreted as the BKS is mainly devoted to the description of the more dense crys-

talline phases [7]. The equilibrium density of silica as given by the BKS potential (2.3 g.cm^{-3}) was found to be somewhat superior to the experimental one (2.2 g.cm^{-3}), see Ref. [75]. Consequently, a silica system having a density of 2.2 g.cm^{-3} is characterized by a negative pressure (components of the stress tensor must be negative) when described by the BKS potential. This statement accounts for the smaller value of the χ^2_{Stress} obtained when using the stress tensor given by the *ab initio* (whose components are also negative) calculations rather than the null stress tensor. However, even if the BKS potential tends to underestimate the pressure of the system, it leads to quantitative good structural results. In contrast to this, the fitted potential given for $\Theta = 1$ better reproduces the null stress tensor than the BKS although it gives totally wrong structural features.

4.4 Spline potential

In the preceding section we have not been able to propose any satisfactory sets of parameters. These unsuccessful attempts could be explained by the intrinsic limitations imposed by the analytical form retained for the potential. To check this hypothesis we have developed a more general fitting approach, based on the hypothesis that the potential has not a Born-Mayer functional form anymore. Hence we have opted for a more flexible formulation based on cubic splines. This method has already been proposed for different materials by F. Ercolessi [46] and S. Izvekov [77].

4.4.1 Practical aspects

A spline function $f(x)$ is defined on a grid of variables (x_0, y_0),(x_1, y_1),...,(x_n, y_n) [118]. The spline function is a sum of piecewise cubic polynomial functions $S_i(x)$ which interpolate the gap between adjacent points (x_i, y_i) and (x_{i+1}, y_{i+1}), see Fig. 4.18:

$$f(x) = \sum_{i=0}^{n} S_i(x) \tag{4.35}$$

where $S_i(x)$ functions has the following definition:

$$S_i(x) = \begin{cases} 0, & \text{if} \quad x \in]-\infty, x_i[\cup]x_{i+1}, +\infty[\\ a_i(x-x_i)^3 + b_i(x-x_i)^2 + c_i(x-x_i) + d_i, & \text{if} \quad x \in [x_i, x_{i+1}] \end{cases}$$

The spline coefficients can be defined through the following constraints:

$$\begin{aligned} S_i(x_i) &= y_i, & S_i(x_{i+1}) &= y_{i+1}, \\ S_i'(x_i) &= c_i, & S_i'(x_{i+1}) &= c_{i+1}. \end{aligned}$$

[7] $\rho_{\alpha-\text{quartz}} = 2.6495$ g.cm^{-3}.

The condition of second-order continuity $S''_{i-1}(x_i) = S''_i(x_i)$ can be formulated using the matrix formalism:

$$\underbrace{\begin{bmatrix} f_1 & h_1^{-1} & 0 & \cdots & 0 & 0 \\ h_1^{-1} & f_2 & h_2^{-1} & \cdots & 0 & 0 \\ 0 & h_2^{-1} & f_3 & \cdots & 0 & 0 \\ \vdots & \vdots & \vdots & \ddots & \vdots & \vdots \\ 0 & 0 & 0 & \cdots & f_{n-2} & h_{n-2}^{-1} \\ 0 & 0 & 0 & \cdots & h_{n-2}^{-1} & f_{n-1} \end{bmatrix}}_{\mathbf{TD}} \underbrace{\begin{bmatrix} c_1 \\ c_2 \\ c_3 \\ \vdots \\ c_{n-2} \\ c_{n-1} \end{bmatrix}}_{\mathbf{C}} = \underbrace{\begin{bmatrix} g_1 - c_0 h_0^{-1} \\ g_2 \\ g_3 \\ \vdots \\ g_{n-2} \\ g_{n-1} - c_n h_{n-1}^{-1} \end{bmatrix}}_{\mathbf{G}} \tag{4.36}$$

where h_i, f_i and g_i are defined as:

$$h_i = x_{i+1} - x_i \tag{4.37}$$

$$f_i = 2(h_{i-1}^{-1} - h_i^{-1}) \tag{4.38}$$

$$g_i = \frac{3}{h_{i-1}^2}(y_i - y_{i-1}) + \frac{3}{h_i^2}(y_{i+1} - y_i)\,. \tag{4.39}$$

The resolution of the tridiagonal system leads to the coefficients c_i. The polynomial coefficients a_i and b_i can be retrieved using the following relations:

$$a_i = \frac{1}{h_i^2}(c_i + c_{i+1}) + \frac{2}{h_i^3}(y_i - y_{i+1}) \tag{4.40}$$

$$b_i = \frac{3}{h_i^2}(y_{i+1} - y_i) - \frac{1}{h_i}(c_{i+1} + 2c_i) \tag{4.41}$$

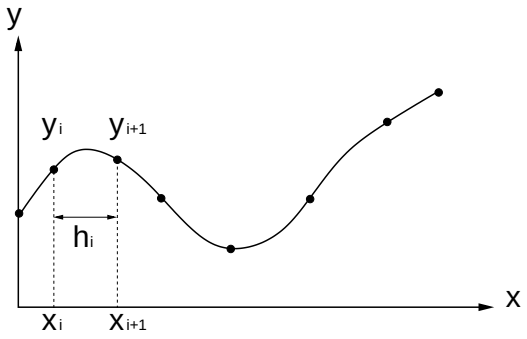

Figure 4.18: Sketch of a cubic spline interpolation.

To enhance the accuracy of the force fit we have described the derivative of the interaction potential V_2, and not the potential itself, through the cubic spline interpolation:

$$\frac{\partial V_2(r)}{\partial r} = f(r; \{x_i, y_i\}) \tag{4.42}$$

The parameters defining the spline function are now the ordinates of the curves, $\{y_i\}$. According to the Levenberg-Marquardt procedure, the derivatives of the force with respect to the parameters have to be calculated:

$$\frac{\partial^2 V_2(r)}{\partial r \partial y_i} = \frac{\partial f(r;\{x_i,y_i\})}{\partial y_i}. \tag{4.43}$$

To achieve this, one needs to solve the system of equations obtained by differentiating the matrix relation (4.36):

$$\frac{\partial\left(\mathbf{TD}\cdot\mathbf{C}\right)}{\partial y_i} = \frac{\partial \mathbf{G}}{\partial y_i} \tag{4.44}$$

$$\mathbf{TD}\cdot\frac{\partial \mathbf{C}}{\partial y_i} = \frac{\partial \mathbf{G}}{\partial y_i}, \qquad \text{as} \qquad \frac{\partial \mathbf{TD}}{\partial y_i} = 0, \tag{4.45}$$

where

$$\frac{\partial g_{i-1}}{\partial y_i} = \frac{3}{h_{i-1}^2}, \quad \frac{\partial g_i}{\partial y_i} = 3\left(\frac{1}{h_{i-1}^2} - \frac{1}{h_i^2}\right), \quad \frac{\partial g_{i+1}}{\partial y_i} = -\frac{3}{h_i^2} \tag{4.46}$$

4.4.2 Results

The spline method requires various input data: The distance and the interatomic force corresponding to the pair of species considered at that distance. Considering different sets of fixed distances the fitting procedure finds the optimal values of the forces. The potential has been fitted using 21 configurations taken from an NVT *ab initio* simulation at 3600K using 78 atoms. Different attempts have been made in order to evaluate the optimal repartition of the fixed interatomic distances required for the fit. Step lengths of 0.2 ± 0.1 Å have been considered[8]. Indeed smaller step lengths were detrimental to the smoothness of the potential (small fluctuations were observed) whereas large length steps could miss some shouldering of the potential. A polynomial repulsive interaction has been added to the spline potential so as to avoid particle fusion, see also section (2.2.4.1). The interatomic forces given by the spline procedure are presented in Figs. 4.19 and 4.20. Two different potentials have been considered. As it can be seen in Fig. 4.19 the Si-Si interatomic force represented in green exhibits shouldering. This potential will be referred as the Spline 1 potential. Another potential fitted on the same grid points using some constraints (using some fixed points [9]) in order to soften the irregular outline of the Spline 1 potential has been proposed. This second potential is referred as Spline 2, see Fig. 4.20. Some attempts have been made for proposing potentials having an extended length scale but these potential were not satisfactory as they were described by non monotonic functions.

[8] The following grids of point have been used: For O-O interactions $\{1.8, 2.0, 2.2, 2.5, 2.7, 2.9, 3.1, 3.3\}$, for the Si-O interactions $\{1.2, 1.3, 1.4, 1.6, 1.8, 2.0, 2.2, 2.6, 2.8, 3., 3.1, \}$, for the Si-Si interactions $\{2.0, 2.2, 2.4, 2.6, 2.8, 3.0, 3.2, 3.4\}$

[9] At 2.7Å the spline function corresponding to the Si-O force has been set equal to 0.125 eV.Å^{-1}. The spline function corresponding to the Si-Si interactions has been taken from another spline fit.

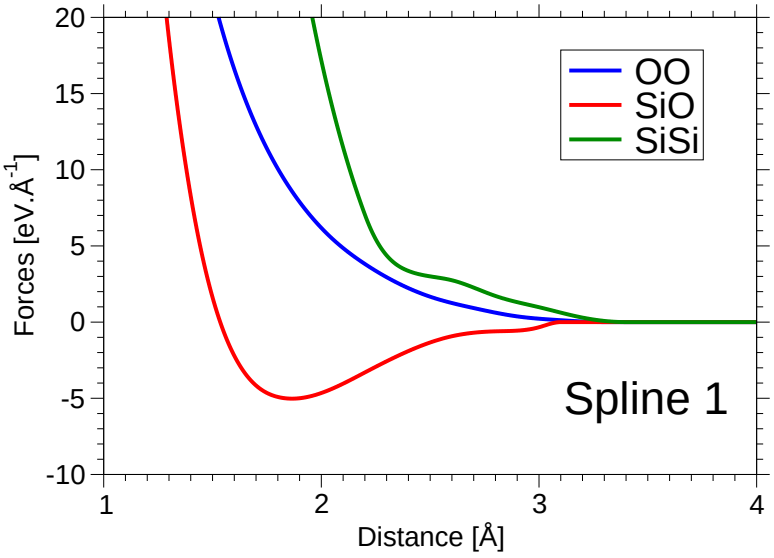

Figure 4.19: The force fitted spline ansatz.

Some NVT simulations have been carried out on 78 atoms samples at 3600K to check the validity of this approach. The angular and the pair correlation functions given by the splines potentials have been calculated for this purpose and are presented in Figs. 4.21 and Figs. 4.22. The pair correlation functions are in good agreement with the *ab initio* ones. Unfortunately, the angular distribution functions are poorly described by the spline potentials, the heights and positions of the peaks do not match to the CPMD simulations. One can note a strong shouldering in the $\widehat{\text{SiOSi}}$ angular distribution function which corresponds to an excess of edge-sharing tetrahedra already pinpointed in section (4.2.0.2). Some additional simulations have been made using a 600 atoms sample at 3600K using the Spline 1 potential and the corresponding pair correlation functions are compared to the *ab initio* ones in Fig. 4.23. This time, the simulation made on a bigger sample are in strong disagreement with the reference data: The peaks heights and positions are not properly reproduced, especially for the Si-Si pair correlation function. These strong disagreements can be explained by the very short range of the spline potentials. For this reason no further attempts have been made using this class of potential.

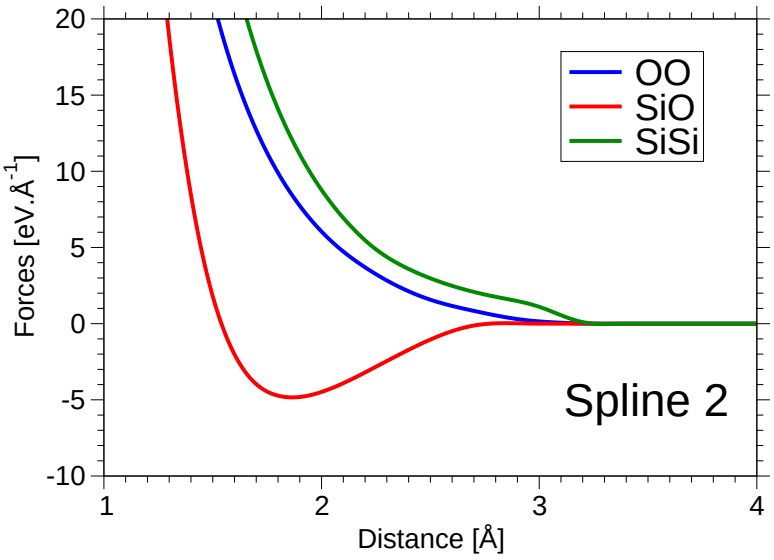

Figure 4.20: The force fitted spline ansatz using constrained sets of points.

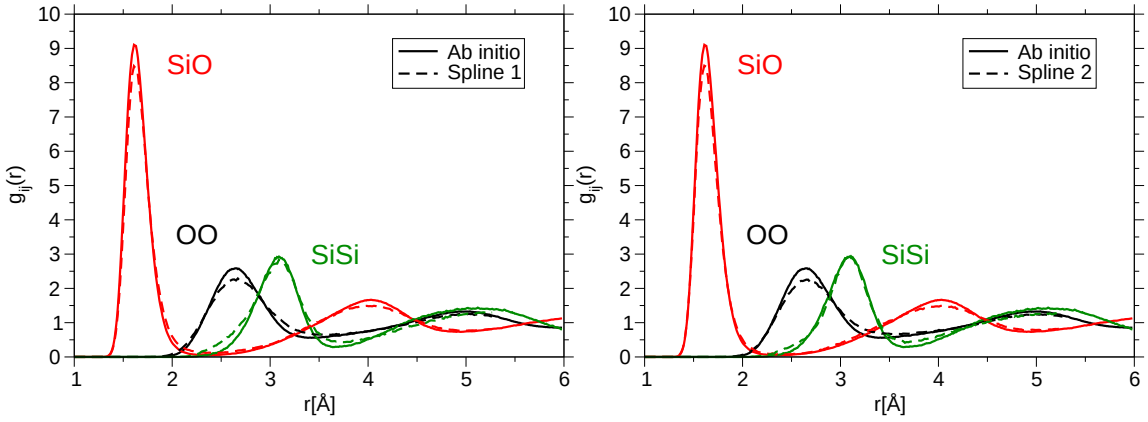

Figure 4.21: Left panel: Pair correlation functions of silica calculated using the Spline 1 potential (dashed line) compared to the pair correlations given using the CPMD simulation (solid line). Right panel: Pair correlation functions of silica calculated using the Spline 2 potential (dashed line) compared to the pair correlations given using the CPMD simulation (solid line).

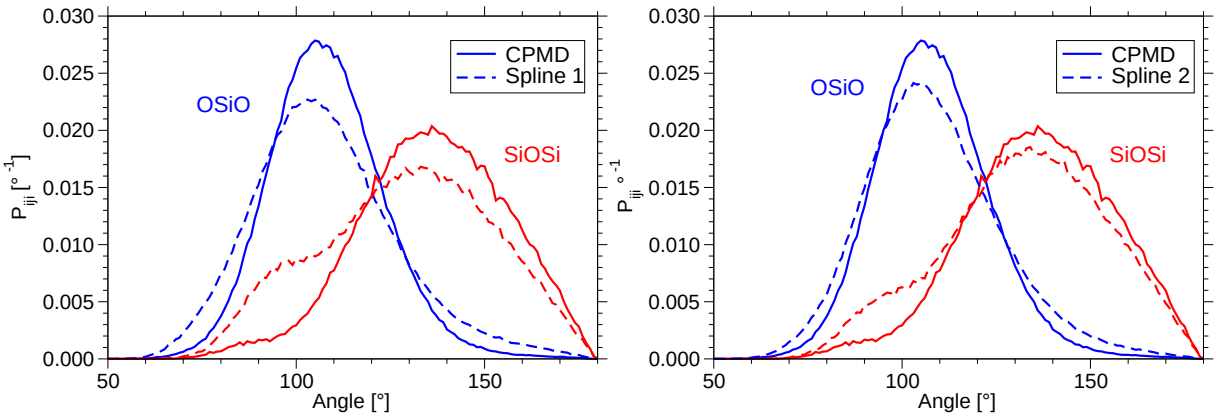

Figure 4.22: Left panel: Angular distribution functions of silica calculated using the Spline 1 potential (dashed line) compared to the angular distributions given using the CPMD simulation (solid line). Right panel: Angular distribution functions of silica calculated using the Spline 2 potential (dashed line) compared to the angular distributions given using the CPMD simulation (solid line)

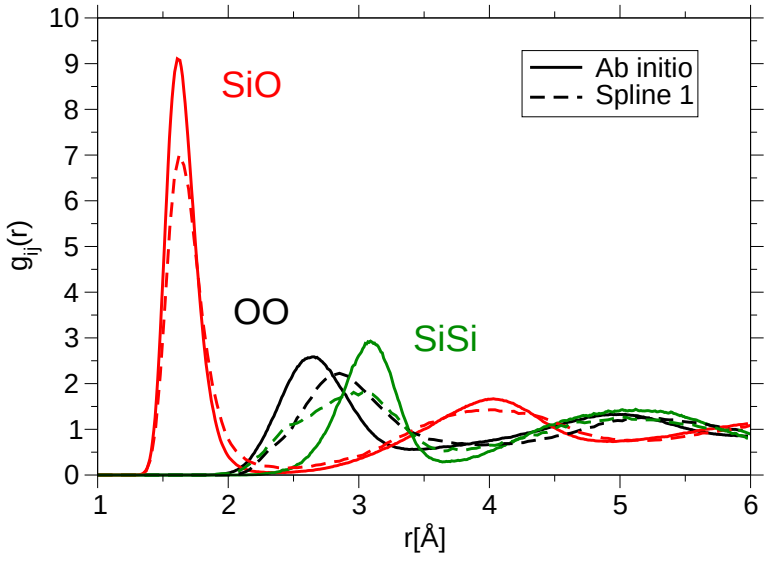

Figure 4.23: Pair correlation functions of silica calculated using the Spline 1 potential (dashed line) on a 600 atom sample compared to the pair correlations given using the CPMD simulation (solid line).

Chapter 5

Screening potential

Pauling [114, 115] classified the Si-O bonding in silicates as being 50% covalent and 50% ionic. For this reason almost all the potentials available in the literature describe silicates using both covalent (short range) and Coulomb (long range) terms. The electrostatic energy is expressed as a conditionally convergent sum which can, *e.g.*, be computed by means of the Ewald method (see section (2.2.4.2)). The calculation of the long range term is time consuming. For a three-dimensional N particle system with periodic boundary conditions in all three spatial directions, the computational load for Ewald method scales like $\mathcal{O}(N^{3/2})$. Whereas the energy corresponding to the short range interaction computed using a "Verlet list" scales like $\mathcal{O}(N)$. Some methods and algorithms have been proposed to reduce the computational cost such as the particle-particle and particle-mesh methods [36, 71] for which the scaling is proportional to $\mathcal{O}(N \log N)$ [53], unfortunately these methods are based on complex algorithms and are only suited for very big systems. In addition to this, the calculation of some features such as elastic constants or shear viscosity via Green-Kubo relation are more complicated and less efficient when Ewald sums have to be considered [28]. For all these reasons, a reliable finite range pair potential to simulate silica is highly desirable. In this chapter we assume that due to screening effects the long-range Coulomb interactions in typical ionic systems can be truncated. According to this assumption we have parameterized a short range Coulomb-like potential and compared the results obtained using this potential to the ones extracted from simulations made using Ewald summation.

5.1 Fitting procedure

Introduction Almost all the previous methods proposed to avoid the time consuming Ewald summation are build upon physical considerations [34, 37, 56, 71, 89, 158, 159]. In this work we have adopted a different point of view. Thus we tried to check whether the long range interactions could be mimicked accurately using an effective potential. The force-matching approach followed in this section is similar to the one presented in chapter 4. A given analytical form for the Coulomb interactions is assumed, thereafter this potential is fitted so as to reproduce classical forces computed using Ewald summations corresponding to the liquid phase of silica. This new potential is used in molecular dynamics simulations and the results are compared to the original data used for the fitting in order to check its accuracy.

5.1.1 Practical considerations

Analytical form The analytical form retained is similar to the one firstly proposed by H. Yukawa in the 30's. This potential is mainly used for the description of the interactions in colloidal systems. In these systems the effective electric field surrounding charged particles is screened by the ions and counter-ions present in the solvent and the effective electrostatic interactions $\phi(r_{ij})$ for a pair of atom $\{ij\}$ separated by a distance r_{ij} with charges q_i and q_j respectively can be expressed as [124]:

$$\phi(r_{ij}) = D_{ij}\frac{1}{4\pi\epsilon_0}\frac{q_i q_j}{r_{ij}}\exp\left(-r_{ij}/\Delta_{ij}\right). \tag{5.1}$$

Here D_{ij} mimics the relative permittivity of the material and Δ_{ij} represents a typical screening length. This potential is short ranged and reproduces the behavior of Coulomb's forces for short and intermediate ranges. It is worthwhile to mention that systems involving Yukawa interaction should be considered with some special care in the case where the interactions cannot be neglected if the screening length of the system is larger than the simulation cell parameters ($\Delta_{ij} > L_{\text{box}}/2$). Then it is necessary to introduce a specific summation method similar to the Ewald summation [125]. Nevertheless, in such cases it is not recommendable to substitute the Yukawa potential by a Coulomb's one as the Ewald method corresponding to the Yukawa potential is even more time consuming than the Ewald summation used for Coulomb's interactions.

The Yukawa potential, presented in Eq. (5.1) is a short range potential, which can be cut off at distance r_{cut} and regularized using the following function (see Sec. 2.2.4.1):

$$G_{r_{\text{cut}}}(r_{ij}) = \exp\left(-\frac{\gamma^2}{\left(r_{ij}-r_{\text{cut}}\right)^2}\right). \tag{5.2}$$

In order to minimize the influence of the cutoff function, see Eq. 5.2, for the description of both forces and their derivatives we applied the smoothing function to the first derivative of the potential presented in Eq. (5.1) and not to the potential itself as it is usually reported in the literature. This method has been retained as it enhances the accuracy of the description of the forces.

Thus, the screened pair potential $V_2^{\text{Yuk.}}(r)$ we have used for the MD simulations is:

$$V_2^{\text{Yuk.}}(r_{ij}) = \int_{r_{\text{cut}}}^{r_{ij}} \frac{d\phi(r)}{dr} G_{r_{\text{cut}}} dr. \tag{5.3}$$

$$\frac{dV_2^{\text{Yuk.}}(r_{ij})}{dr_{ij}} = \frac{dV_2^{\text{Yuk.}}(r_{ij})}{dr_{ij}} G_{\text{cut}}(r_{ij}). \tag{5.4}$$

This method is convenient as it is also computationally less expansive. Indeed the forces are expressed as a single term, see Eq. (5.4) whereas the derivative of a potential $\psi(r)$ smoothed directly by the smoothing function $G_{r_{\text{cut}}}(r)$, $\psi(r) = \phi(r)G_{r_{\text{cut}}}(r)$, would lead to the calculation of one additional term:

$$\frac{d\psi(r_{ij})}{dr_{ij}} = \frac{d\phi(r_{ij})}{dr_{ij}} G_{\text{cut}}(r_{ij}) + \phi(r_{ij}) \frac{dG_{\text{cut}}(r_{ij})}{dr_{ij}}. \tag{5.5}$$

Nevertheless, some calculations have been made using the potential $\phi(r_{ij})$ and the comparison between the simulations made using the potential $V_2^{\text{Yuk.}}$, $\phi(r_{ij})$ and the original simulations of J. Horbach [74, 75] are presented in section (5.1.2). The truncation method presented in Eq. (5.1) will be referenced as the "*force smoothing method*", whereas the truncation method presented in section (2.2.4.1) will be referenced as the "*potential smoothing method*".

The typical screening distance of the smoothing function $G_{\text{cut}}(r)$ is given by the parameters γ. In this work a value of 2 Å has be retained to ensure a smooth decrease of the potential. The electrostatic energy described by Eq. (5.3) has not anymore a simple analytical expression. One has to compute the potential using an integration method (the Simpson's method in our case [118]) and then store it onto a grid. The length step retained for the integration has been set equal to 10^{-4} Å [1].

Fitting parameters: The following definition of the merit function has been used for the fit:

$$\chi^2(\{\mathbf{F}\}) = \left\langle \frac{1}{3N} \sum_{i=1}^{N} \frac{1}{\sigma_i^2} \left| \mathbf{F}_i^{\text{BKS}} - \mathbf{F}_i^{\text{Yuk.}} \right|^2 \right\rangle \tag{5.6}$$

$$\sigma_i = \sqrt{\langle (\mathbf{F}_i^{\text{BKS}})^2 \rangle - \langle \mathbf{F}_i^{\text{BKS}} \rangle^2}. \tag{5.7}$$

The fits have been performed using the Levenberg Marquardt algorithm, see section 4.1.1. The configuration database needed for these fits has been taken from previous NVE simulations of liquid silica carried out by Horbach [74]. We have not considered any *ab initio* calculations as our aim was to reproduce by means of a Yukawa ansatz the effects of the long ranged Coulomb terms without changing the covalent/short ranged contributions. This task is not doable using CPMD as due to the complexity of the *ab*

[1] The distance range for which the interactions have been precomputed start from 0.5Å up to 10Å, this represents 95000 points representing a total of 3.9 Megabytes.

initio ansatz it is not possible to disentangle the different physical contributions of the *ab initio* forces (long ranged/short-ranged).

These samples are made of 8016 particles contained in a 48.37 Å cubic box corresponding to a density of 2.37 g/cm^3. As the BKS potential shows a diverging behavior for very short distances, quadratic terms mimicking strong repulsive interactions have been considered by Vollmayr *et al.* [153] and Horbach and Kob [75] in their simulation, see also section (2.2.4.1). To quantify the dependence of the parameters with respect to the temperature, fits have been made for the whole set of temperatures investigated by Horbach. The original potential parameters (cutoffs, smoothing factors, *etc*) have been used for the computation of the Born-Mayer forces ($A_{ij}\exp(b_{ij}r_{ij}) - c_{ij}/r_{ij}^6$, see also section 4.1.1). Different sets of atomic configurations and the corresponding forces (short and long range terms) are used as an input for the fitting procedure. We have also taken into account the contribution of the repulsive interactions to the overall forces since at high temperatures ($T > 5200$K) this distance range is also probed by the particles. The occurrence and the influence of these repulsive terms on the fitting results were supposed to be physically irrelevant since the quadratic terms have been set up arbitrarily. Nevertheless attempts made without taking explicitely these repulsive terms into account were leading to significant bumps in the temperature dependence of the D_Y, Δ and χ for high temperatures.

5.1.2 Results

Some attempts have been made to fit the Yukawa potential in a unconstrained way where different parameters $\{D_{ij},\ \Delta_{ij}\}$ were assigned for the different kinds of pairs (O-O, Si-O, and Si-Si). These tries did not give rise to satisfactory results as they were leading to mechanically unstable structures characterized by a negative pressure (typically $\simeq -20$ GPa). Indeed, the addition of extra degrees of freedom with a view to lowering χ^2 were made at the expense of the charge neutrality constraint. These results illustrate that the fitting criterion should be cautiously handled, as an attempt to lower the χ^2 may be in disagreement with the physics of the system. To get rid of this neutrality issue a single set of parameters ($D_{ij} = D_Y$, $\Delta_{ij} = \Delta$) valid for all the pairs has been retained. Two kinds of fits have been carried out. Firstly we have investigated different cutoffs for a given temperature. Afterwards, we have used different sets of configurations corresponding to different temperatures using a fixed cutoff to check the influence of the temperature.

Potential/force cutoff Fits have been carried out using a 10Å cutoff for the two different potential ansatz described in the previous section (5.1.1). The forces computed using the smoothing potential approach exhibit a strong unphysical shoulders, see Fig. 5.1. This observation is consistent with the value of the χ^2 (for a 10Å cutoff $\chi^2 = 0.002494$). Indeed, χ^2 is two times larger for the smoothed-potential $\phi(r)$ defined in Eq. (5.5), than the value obtained for the force cut potential $V_2^{\text{Yuk.}}(r)$ defined in Eq. (5.3).

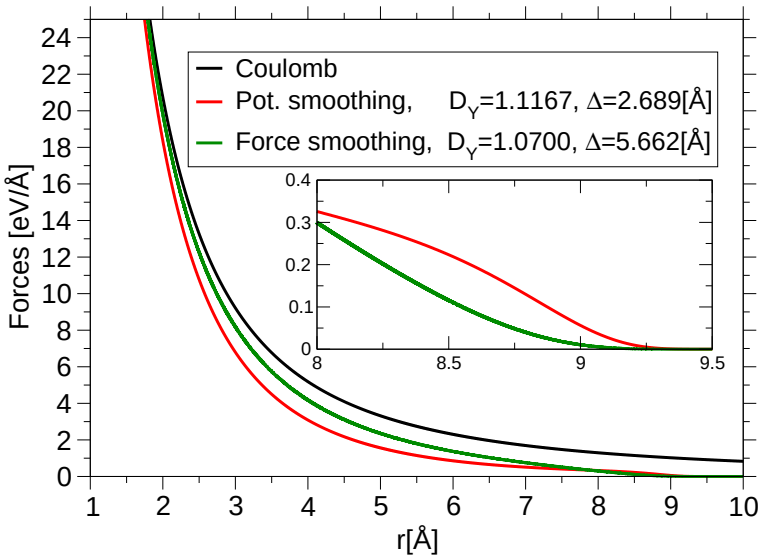

Figure 5.1: Force between a pair of silicon particles as a functions of the interparticle distance for different potentials: The Coulomb potential, the Yukawa potential using a potential smoothing function and the Yukawa potential using a force smoothing function. The fits have been made with a 10Å cutoff using configurations extracted from simulations made at 3760K. In the inset is represented the second derivatives of the potential.

Subsequently molecular dynamics simulations have been made using these two potential ansatz. The static properties have been compared to the original data of J. Horbach [75] used for the fit. For this purpose we have represented in Fig. 5.2 the function $\Delta g_{\mathrm{SiSi}}(r)$ corresponding to the difference between the original Si-Si pair correlation function of Horbach [75] and the simulations made using the force-fitted potential. The function $\Delta g_{\mathrm{SiSi}}(r)$ is defined as:

$$\Delta g_{\mathrm{SiSi}}(r) = g_{\mathrm{SiSi}}^{\mathrm{Ewald}}(r) - g_{\mathrm{SiSi}}^{\mathrm{Yuk.}}(r). \tag{5.8}$$

The differences are significantly larger for the potential smoothing method in agreement with our previous results regarding to the values of the χ^2. Due to the better results given by this method in following part of this chapter we will refer solely to the force smoothing approach.

Cutoff dependence The χ^2 and the couple of fitted parameters $\{D_Y, \Delta\}$ are respectively displayed in Fig. 5.3, 5.4 and 5.5. For large cutting distance r_{cut}, see Eqs. (2.40) and (5.3), one expects to converge to the Coulomb potential, $\{D_Y, \Delta\} \to \{1, \infty\}$ which is consistent with the results presented in Figs. 5.4 and 5.5. It is worthwhile to note that the values of the χ^2 plotted in Fig. 5.3 are very low compared to the values obtained using the force fitted potential obtained from *ab initio* simulations, see Table 4.3. From this statement we can assert that the Coulomb components of the BKS forces are accurately described by our Yukawa ansatz.

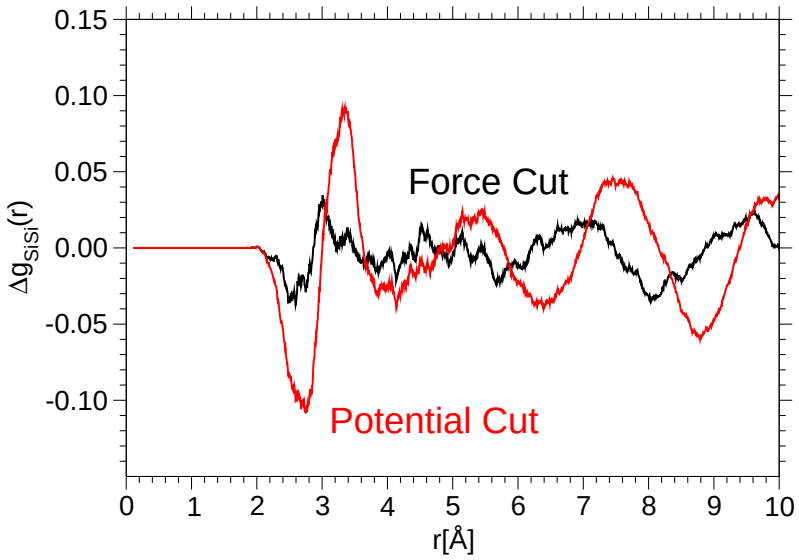

Figure 5.2: The differences between the partial Si-Si pair correlation function corresponding to the BKS and to the Yukawa potential (potential cut + force cut), the simulation have been realized at 6100K.

The plot corresponding to the Δ parameter shows the strongest dependence with respect to the cutoff, $\Delta(r_{\text{cut}})$. Consequently, this parameter has been retained for the interpretation of the connection between the pair distribution functions and the cutoff used for the fits. In Fig. 5.5 one can clearly distinguish two extrema of $\Delta(r_{\text{cut}})$ at 6.1 Å and 6.7 Å. The maximum at 6.1 Å is connected to the maximum of the Si-O pair correlation function represented in Fig. (5.6). For such distances, half of the Si-O pairs are not taken into account, the electro-neutrality is not ensured, the screening can hardly be effective. The extremum at 6.7Å is a minimum of $\Delta(r_{\text{cut}})$, for this distance all the partial pair correlation functions are close to one. Recalling the definition of the pair correlation function this means that all the ions involved within this cutoff make a whole neutral ensemble[2], and then the screening is more effective. Beyond 6.7Å, the screening length parameter shows a monotonic decrease, but the slope of the curves can still be interpreted by means of the partial pair correlation functions. The effect occurring for 6.7Å is still observed for 7.9Å and 9.01Å, but this time, they have to be linked to the minimum of the derivative of $\Delta(r_{\text{cut}})$. For 7.3Å, Δ is rapidly increasing and this corresponds to the heterogeneous environment shown by the partial pair correlation functions, with maxima for $g_{\text{SiSi}}(r)$ and $g_{\text{OO}}(r)$ and a minimum for the $g_{\text{SiO}}(r)$.

Temperature/cutoff dependence Even if the variations of D_Y and Δ over the whole temperature range are gentle, see Figs. 5.7 and 5.8, the surrounding environment still plays an important role on the parameters. An increasing value of the cutoff used

[2]The charge surrounding a silicon atom $Q_{Si}(r)$ contained in a layer of thickness dr and of radius r is given by $Q_{Si}(r) = (q_{Si}g_{SiSi}(r) + 2q_O g_{SiO}(r))4\pi r^2$, if $g_{SiSi}(r) = g_{SiO}(r) \simeq 1$, $Q_{Si}(r) \simeq 0$.

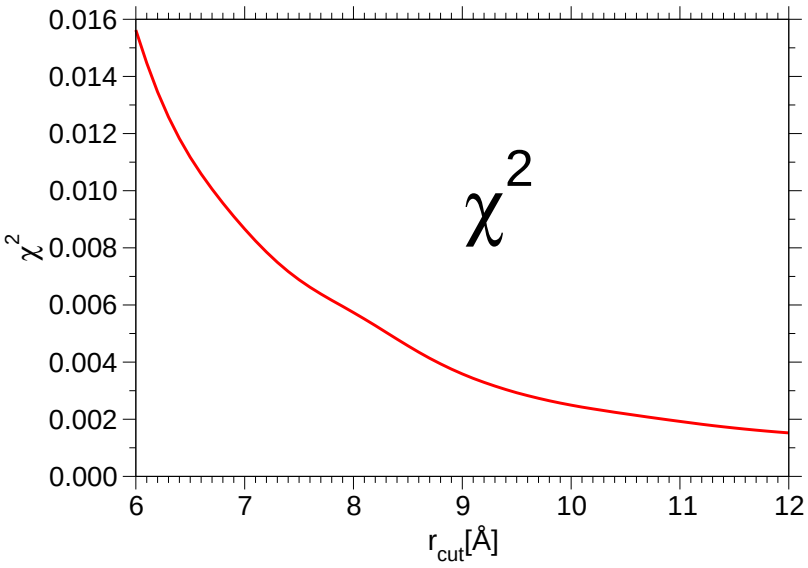

Figure 5.3: χ^2 dependence with respect to the cutting distance. The input configurations for the fits have been taken from a molecular dynamics simulation on a 8016 particles model of liquid silica computed using the BKS potential at 3580K.

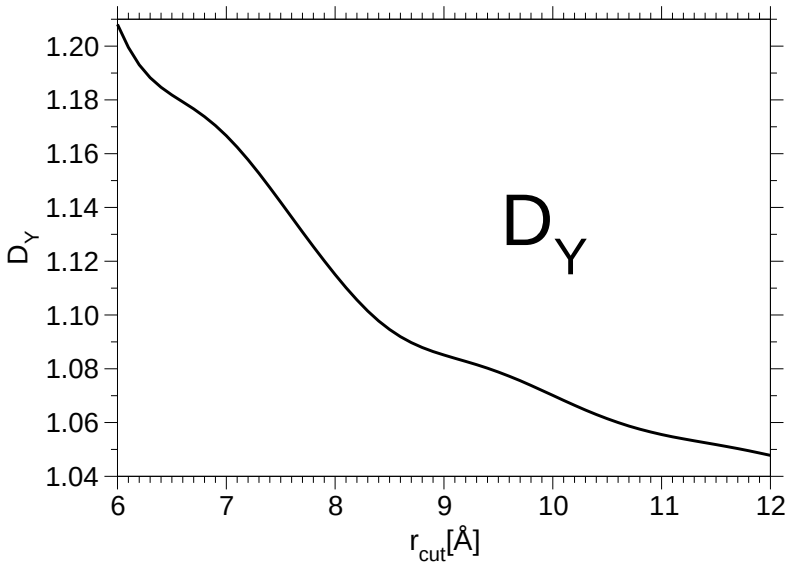

Figure 5.4: Cutoff dependence of the prefactor D_Y.

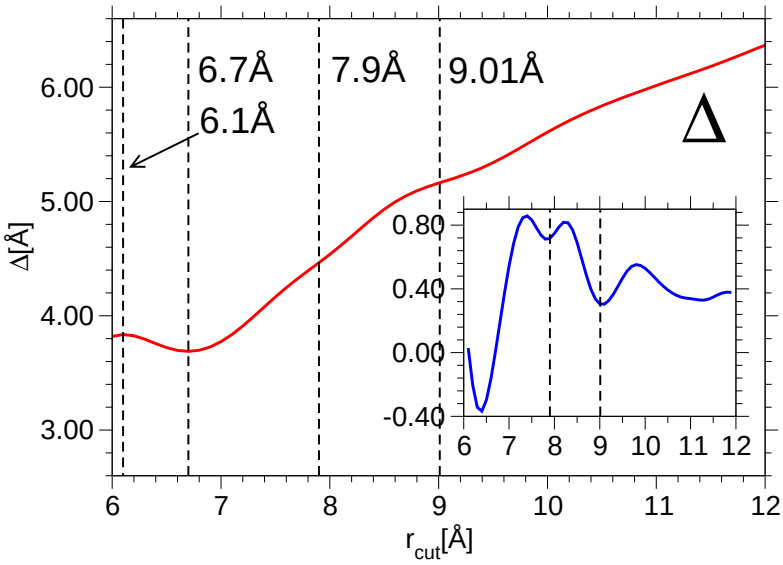

Figure 5.5: Cutoff dependence of the Δ factor. In the inset it is represented the derivative $d\Delta/dr_{cut}$. The configurations used for this fit have been extracted form a T=3580K simulation.

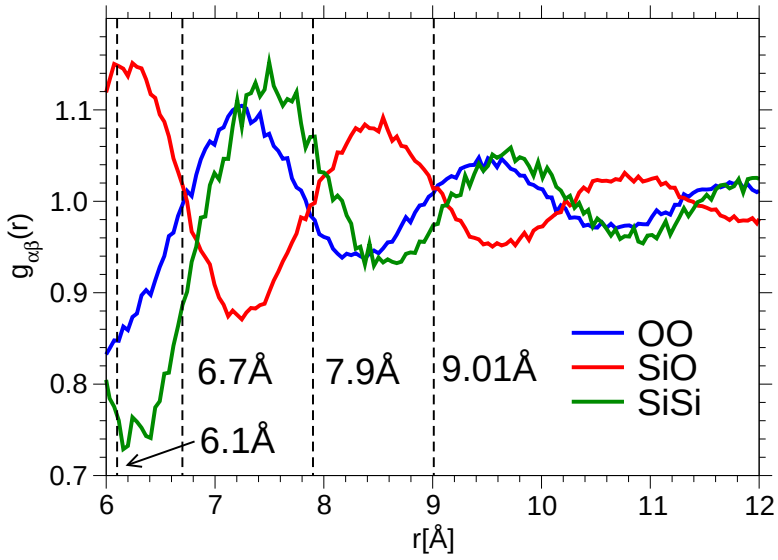

Figure 5.6: Pair correlation functions corresponding the molecular dynamics simulations made at T=3580K [75].

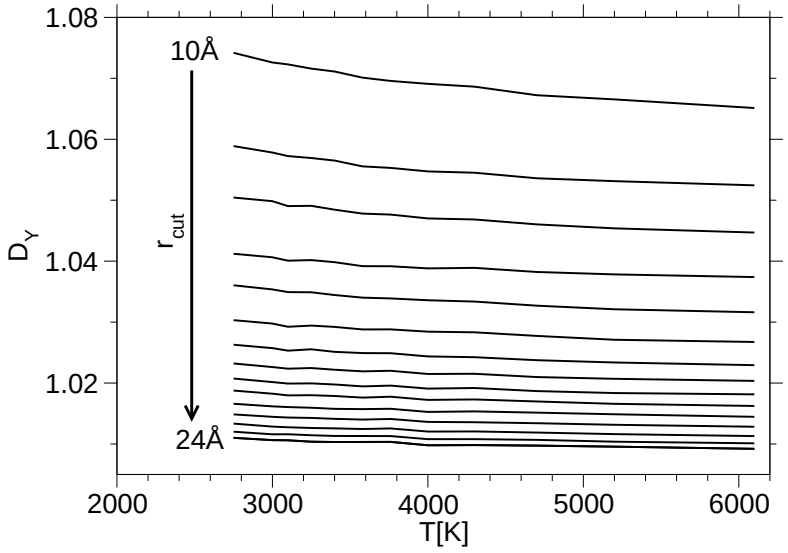

Figure 5.7: The temperature dependence of the prefactor D_Y for different cutoffs $r_{\text{cut}} \in \{10, 11, 12, 13, 14, 15, 16, 17, 18, 19, 20, 21, 22, 23, 24\}$.

for the fitting comes with a softening of the temperature dependence of the $\{D_Y, \Delta\}$ parameters. These results were expected as for large cutoffs r_{cut} the corresponding values of D_Y and Δ converge to $\{1, \infty\}$ as the Coulomb potential does not depend on the temperature.

Physically, the value of Δ obtained using the minimization procedure results from a compromise. On the one hand, a large screening length Δ should be used to recover a "bare" Coulomb potential. On the other hand, the introduction of a finite distance cutoff r_{cut} produces large errors due to incorrect charge balance [158]. In the present scheme this is compensated by screening more strongly the Coulomb interaction by using a smaller screening length Δ. Thus the results of Fig. 5.8 indicate that charge neutrality is best satisfied, for a fixed cutoff value r_{cut}, if the temperature is high, so that a larger screening length Δ can be used at high temperatures. This suggest that charges are screened on a smaller lengthscale when temperature is high, that is when the system is more disordered.

5.2 Liquid silica

Simulations have been carried out to check the reliability of the Yukawa potential. As we aim at comparing quantitatively the Yukawa potential to the BKS one, simulations have been done using the same physical conditions (temperatures, density) and parameters for the smoothing function for the short range potential as proposed by Horbach [75] and presented in section (2.2.4.1). The samples investigated were made of 1002 atoms, the time step $\delta t = 0.16$ fs, the density ρ was the one previously retained by Horbach and Kob [75] $\rho = 2.37$ g.cm^{-3}, the simulation time as well as the temperature

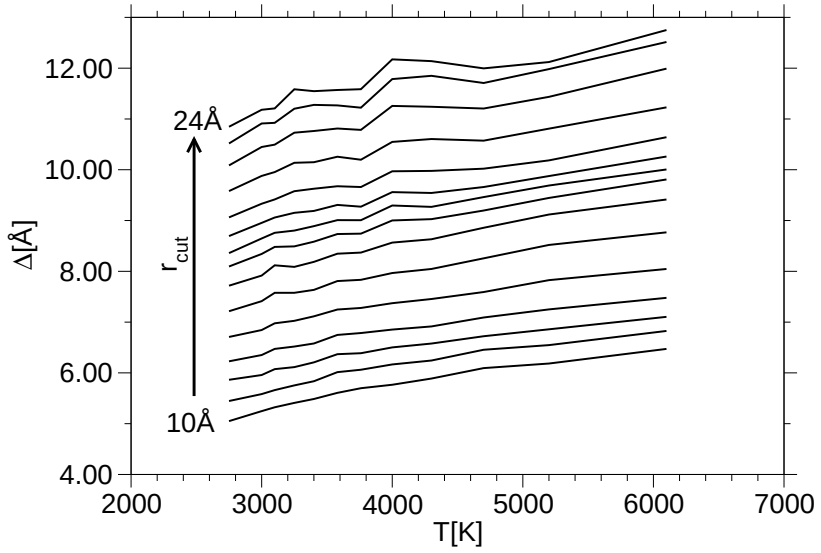

Figure 5.8: The temperature dependence of the screening length Δ for different cutoffs $r_{\text{cut}} \in \{10, 11, 12, 13, 14, 15, 16, 17, 18, 19, 20, 21, 22, 23, 24\}$.

are also taken in agreement with Ref. [75].

Parameter sets As stated in the previous section the Yukawa parameters D_Y and Δ show a slight temperature dependence. Therefore simulations have been carried out using different sets of parameters obtained from fits of data at 3250K, 6100K as well as the ones "averaged" (arithmetic mean) over the whole temperature range to check their influence on the static features of the system, see Table 5.1. The corresponding results are plotted in Figs. 5.9 and 5.10. The partial pair correlation functions and structure factor calculated for the three different potentials are all very similar, the corresponding pressures have also been calculated and similar results have been also found ($\simeq 1.13$ GPa). Consequently, the choice of the parameters set is not so crucial regarding static features. The dependence of the dynamical features has been investigated too, see Fig. 5.11. The mean squared displacement of silicon and oxygen appear to depend only slightly on the parameters set considered. If not explicitely mentioned all the simulations presented in the next section have been performed using the "averaged" parameters.

The effects of the potential range have also been investigated. Following the previous methodology, fits have been made for different cutoff r_{cut} (6 Å, 8 Å and 10 Å) and thereafter their arithmetic averages over the temperatures investigated for the fits have been considered for simulations. The results of these simulations are shown in Fig. 5.12. As it can be seen, the cutoff has a significant impact on the physics of the system. The pair correlation function for the Si-Si term is strongly affected as some peaks are out-of-phase for large distances. Furthermore, the systems simulated using the 6 Å and 8 Å cutoff potentials are more diffusive than the 10 Å one, see Fig. 5.13. This underlines the sensitivity of the system with respect to the potential range.

For the simulations presented in this text we opted for a $r_{cut} = 10$ Å potential as the parameters D_Y and Δ show only a weaker dependence with respect to the cutting distance beyond this limit, see Fig. 5.4.

Temperature[K]	D_Y	Δ[Å]
3250	1.072	5.405
6100	1.062	6.452
arithmetic mean	1.070	5.650

Cutoff[Å]	D_Y	Δ[Å]
6	1.208	3.876
8	1.114	4.608
10	1.070	5.650

Table 5.1: Left table: Sets of parameters given for 10Å fits at 3250K, 6100K, and averaged over the whole temperature range previously studied by J. Horbach [75]. Right table: Thermal averages of the parameters for different cutoffs.

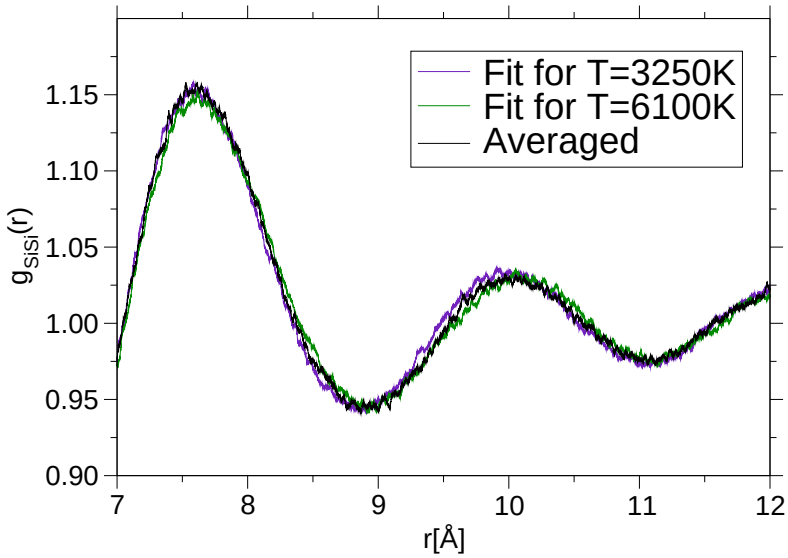

Figure 5.9: The Si-Si partial pair correlation functions computed at 3250K using the Yukawa potential for three different sets of parameters $\{D_Y, \Delta\}$ corresponding to the different temperatures given in Table 5.1. The value used for $r_{\rm cut}$ was set to 10 Å.

5.2.1 Static properties: Comparison to the BKS model

The main structural features have been computed and compared to the corresponding BKS data on 8016 atoms systems, *i.e.* the pair correlation functions, the angle distribution functions and static structure factors.

Pair correlation functions The Si-Si pair correlation function is the most sensitive to changes made on Coulomb potential as the Si-Si interaction consists only in an electrostatic term. However the statements made here are also valid of the O-O and

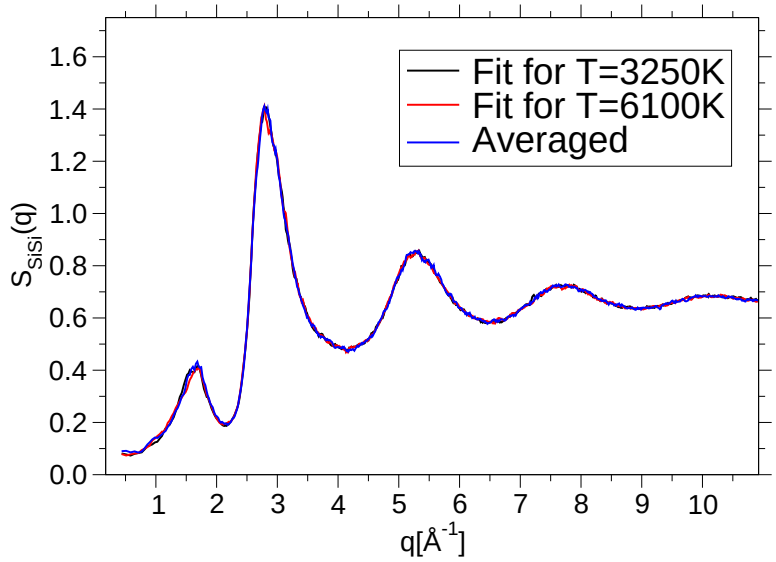

Figure 5.10: The Si-Si structure factor computed at 3250K using the Yukawa potential for three different sets of parameters $\{D_Y, \Delta\}$ corresponding to the different temperatures given in Table 5.1. The value used for r_{cut} was set to 10 Å.

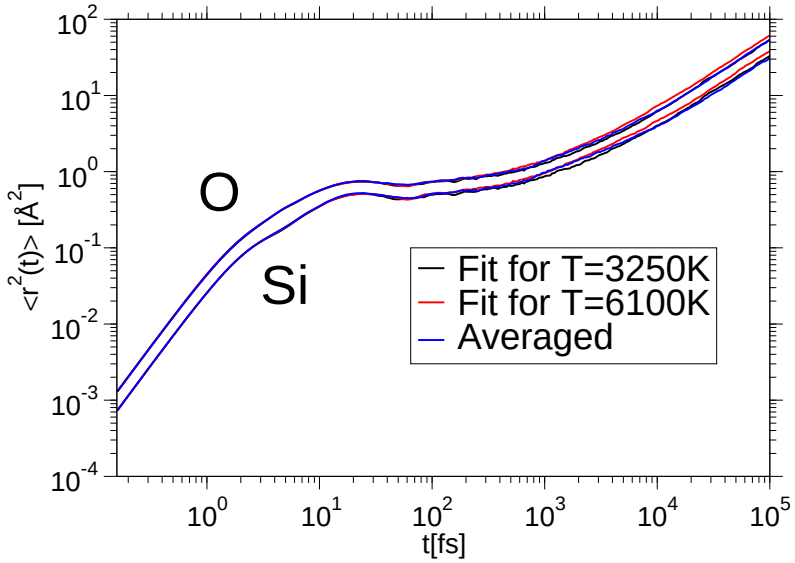

Figure 5.11: Time dependence of the mean squared displacements of silicon and oxygen atoms at 3250K using the Yukawa potential for three different sets of parameters $\{D_Y, \Delta\}$ corresponding to the different temperatures given in Table 5.1. The value used for r_{cut} was set to 10 Å.

Si-O pairs. In Fig. 5.14 the pair correlation functions are presented for three different temperatures (3000K, 4000K and 6100K). For short distance (< 6.3Å) no differences can be detected between the pair correlation functions computed using the Yukawa

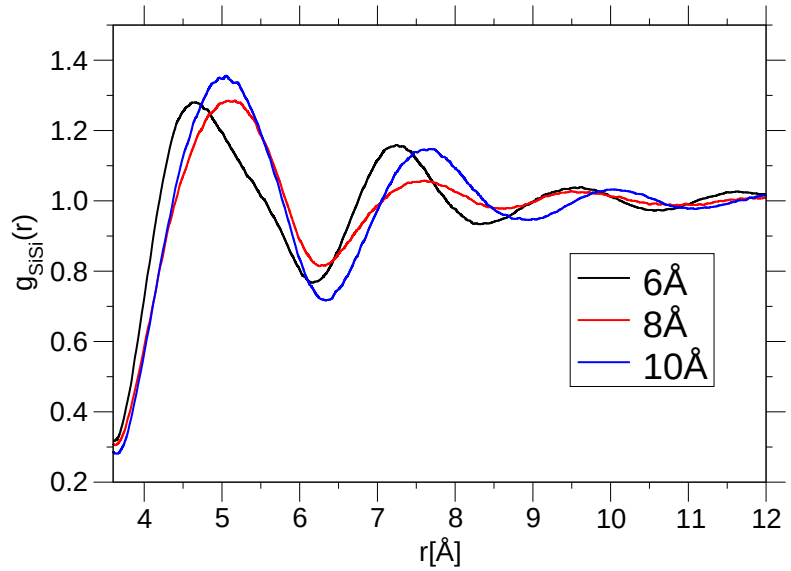

Figure 5.12: The partial Si-Si pair correlation functions at $T = 3250$K computed using the three different cutoffs r_{cut} given in Table 5.1.

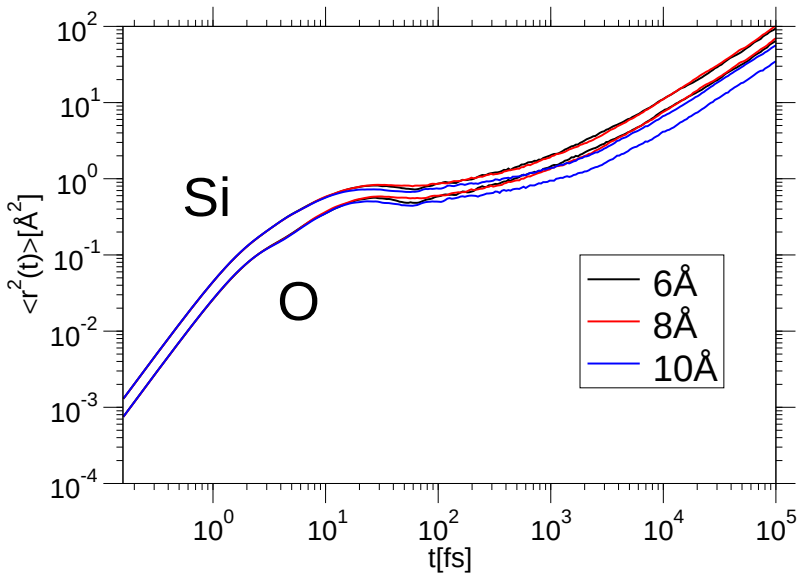

Figure 5.13: The mean squared displacements at $T = 3250$K computed using the three different cutoffs r_{cut} given in Table 5.1.

potential and the ones obtained with Ewald summation. Beyond the second neighbor shell (> 6.3Å) the peaks positions are shifted, and these shifts increase with increasing distance. Moreover slight discrepancies can be noticed regarding the heights of the peaks. However, compared to the crude adjustments made to the Coulomb potential one can consider that the Yukawa results are in reasonable agreement with the

simulations made using the Ewald summation.

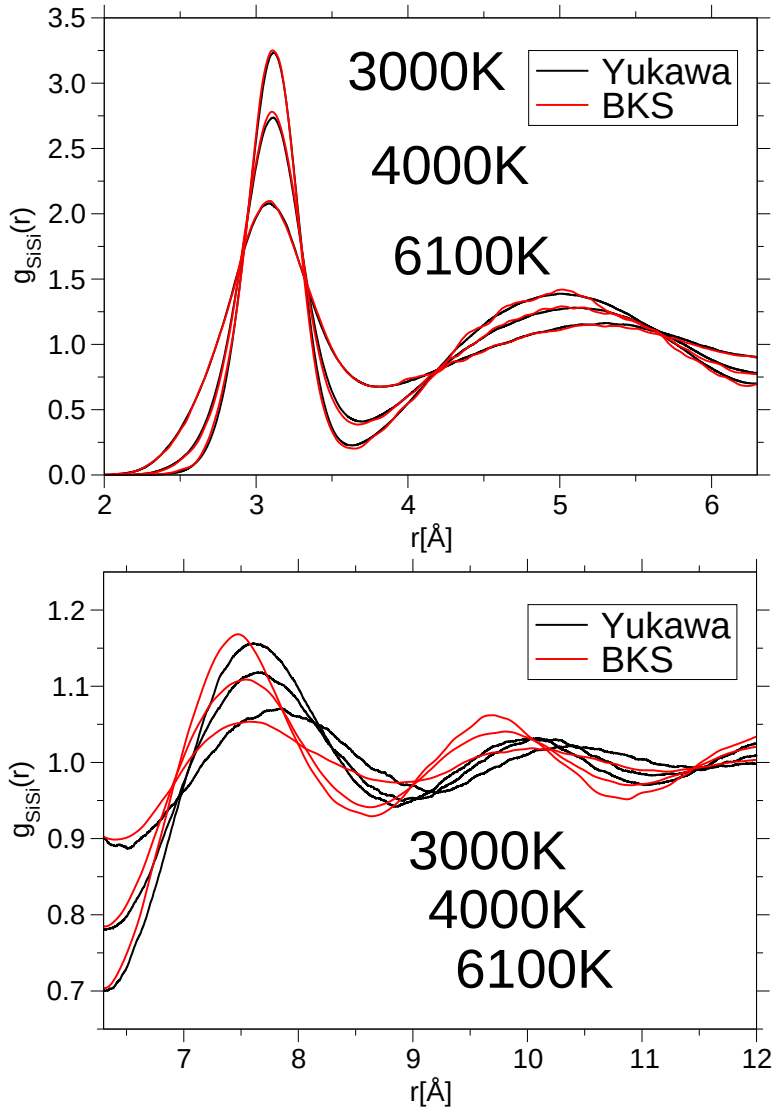

Figure 5.14: Si-Si pair correlation function computed using a 10Å cutoff (black lines) and compared to the corresponding BKS data (red lines) for 3000K, 4000K and 6100K.

Static Structure Factors Using the definitions given in section (2.4.1) we have computed the partial structure factors $S_{\alpha\beta}(q)$ and plotted it in Fig. 5.15.For large wavevectors ($q > 3.5\text{Å}^{-1}$) the Yukawa potential correctly reproduces the Ewald data. This is not surprising as we already know from the preceding paragraph that the Yukawa potential reproduces with a good accuracy the local structure. The peak at 1.6 Å^{-1} corresponds to the so-called first sharp diffraction peak (FSDP). This peak accounts for the local chemical ordering of tetrahedron-like structures. Its position is connected to the distance between neighboring tetrahedra. This feature is properly reproduced

by the Yukawa potential. In contrast to this the peak heights and positions at 2.7Å^{-1} are underestimated.

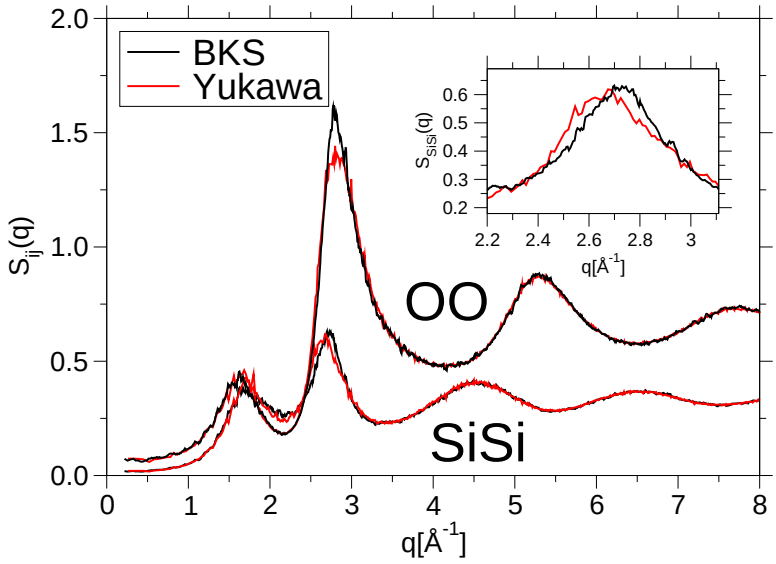

Figure 5.15: Partial structure factors for 3000K. The inset focuses on the Si-Si peak at 2.7 Å^{-1}.

Angular distribution functions The local geometry characterized by the angular distribution functions has already been discussed in section 3.4.2. These quantities have been computed and compared for three different temperatures, see Figs. 5.16 and 5.17. The Yukawa simulations show a very good agreement with the corresponding Ewald ones. Such probability distributions involve triplets of bonded atoms separated by a maximum distance of 4.7Å[3]. This is again consistent with our previous statement that the screened potential only shows small discrepancies for large distances keeping the local structure unmodified.

5.2.2 Dynamic properties: Comparison to the BKS model

Mean squared displacement The relevance of this quantity for the investigation of dynamic properties of the system has already been discussed in one of the previous chapter, see section (3.4.3). The time dependence for these quantities is shown in Figs. 5.18 and 5.19. Three main regimes can be distinguished at low temperatures: The short time scales are characterized by a ballistic motion of the particles[4]. Thus, the MSD is proportional to t^2. Intermediate time scales are characterized by the β-relaxation process [13]. A plateau-like region is present and this plateau becomes more pronounced with decreasing temperature. This regime is due to the cage effect. The

[3]Defined equal to two times the minimum of the first peak of $g_{SiO}(r)$ located at 2.35Å

[4]$\mathbf{r}(t) \simeq \mathbf{r}(0) + \dot{\mathbf{r}}t$

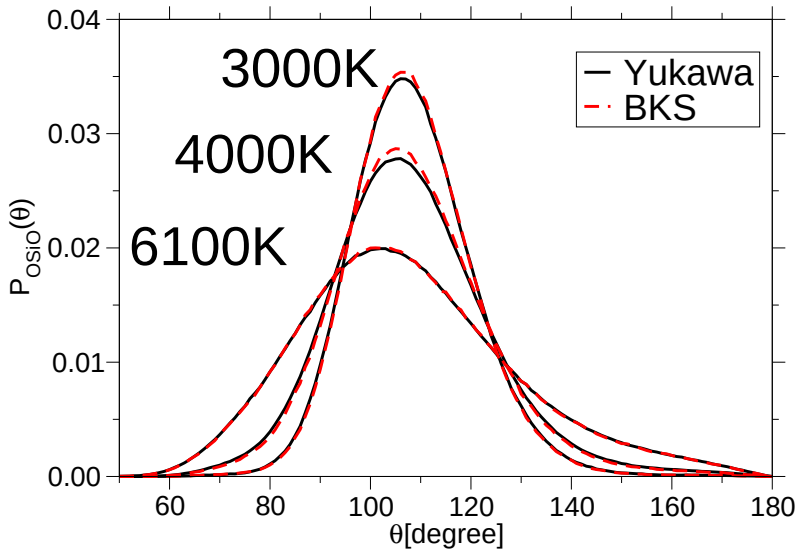

Figure 5.16: $\widehat{\mathrm{OSiO}}$ angle distributions for three temperatures corresponding to the BKS and Yukawa force-fields.

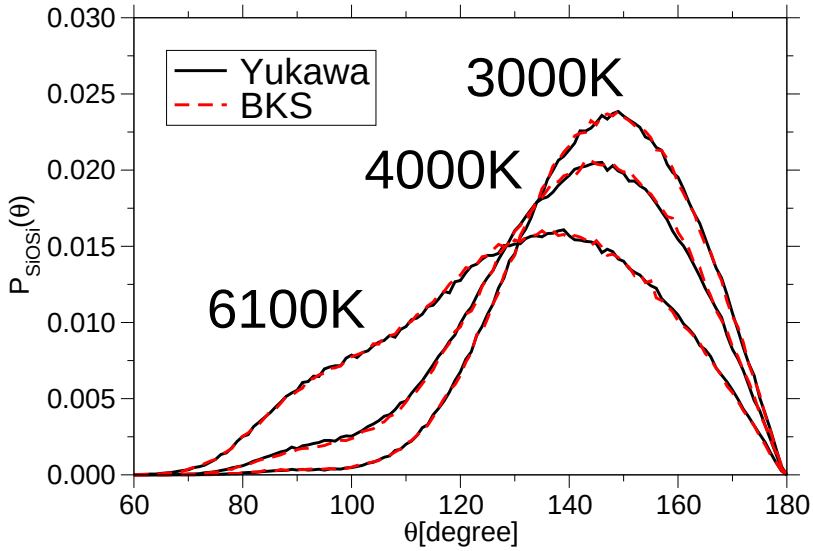

Figure 5.17: $\widehat{\mathrm{SiOSi}}$ angle distributions for three temperatures corresponding to the BKS and Yukawa force-fields.

particle is trapped by its surrounding neighbors. At long times, the particle exhibits a diffusive motion and thus the MSD shows a linear time dependence, according to the Einstein relation.

For high temperatures, no discrepancies can be noted between the Yukawa and the BKS data. However, for low temperatures, the Yukawa dynamics is more diffusive than the BKS ones. The diffusion constants for silicon and oxygen D_α have been represented in Fig. 5.20 as an Arrhenius plot. Whereas at the highest temperature, $T = 6100$K

Yukawa and Ewald methods yield the same values for D_α within the statistical accuracy, at lower temperatures the Yukawa values are about a factor of 2 higher that the "exact" Ewald values. From both methods similar activation energies (similar slopes) are found for the temperature dependence of D_α in the low-temperature regime.

It is worthwhile to notice that the shouldering in the MSD usually observed for the BKS at 0.2 ps is still present in the simulation with Yukawa, see Figs. 5.18 and 5.19. This peak [3] is related to the so-called Boson peak which is a vibrational feature for low frequency whose precise origin is still a matter of debate, see Courtens *et al.* [32].

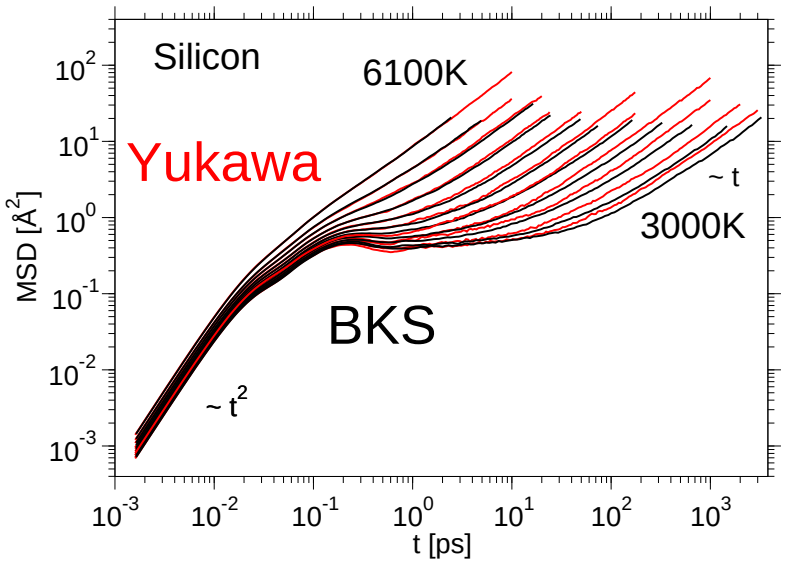

Figure 5.18: Time dependence of the mean squared displacement of silicon atoms for the BKS and the Yukawa potential.

Vibrational density of states Using the description given in section (3.2.1), we have calculated the vibrational density of states (VDOS) by means of the velocity auto-correlation function. For this purpose ten independent samples equilibrated at 3000K have been quenched to 300K using a infinite quench rate[5]. The samples have then been annealed for 1 ns. Thereafter the VDOS has been extracted and averaged from NVE runs made over runs of 20 ps.

Within the harmonic approximation (*i.e.* small atomic displacements from their equilibrium positions) the displacements of an atom j from its equilibrium positions $\mathbf{u}_j(t)$ at time t can be decomposed in contributions of normal modes of frequency w_ν:

$$\mathbf{u}_j(t) = \sum_\nu \frac{A_\nu}{\sqrt{N m_j}} \exp(-\imath w_\nu) \mathbf{e}_{j,\nu} \tag{5.9}$$

[5]The temperature has not been progressively lowered, but instantaneously.

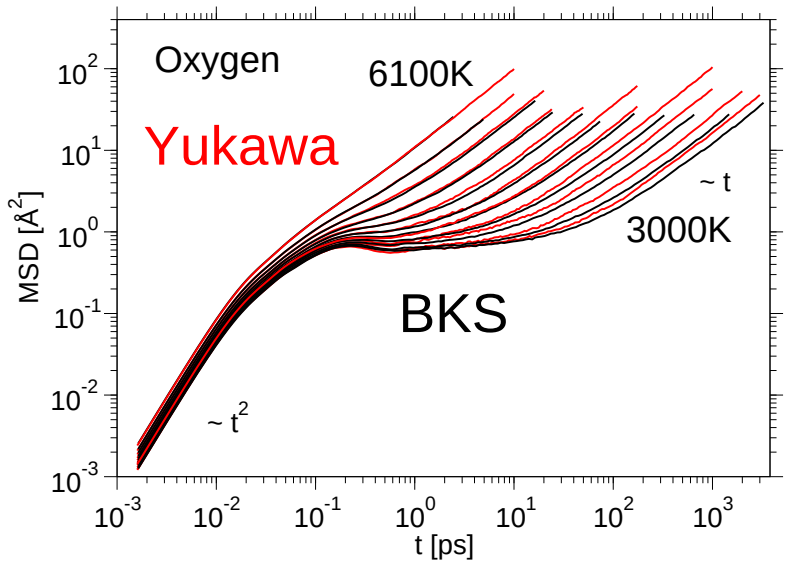

Figure 5.19: Time dependence of the mean squared displacement of oxygen atoms for the BKS and the Yukawa potential.

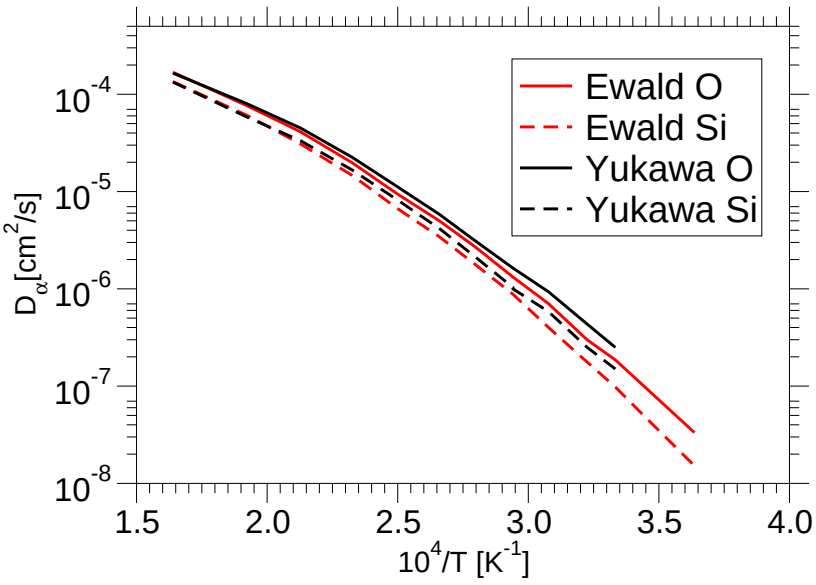

Figure 5.20: Arrhenius plots of the self-diffusion constants for Ewald and Yukawa methods.

The prefactor A_ν is connected to the amplitude of the displacements and N represents the number of atoms considered and m_j is the mass of the particle j considered. The vectors $\mathbf{e}_{j,\nu}$ are called the displacement vectors, they depend on the particle considered j and also on the vibrational mode ν. The displacement vectors are all orthonormal:

$$\sum_j |\mathbf{e}_{j,\nu}|^2 = 1, \quad \text{and} \quad \sum_j \mathbf{e}_{j,\mu} \cdot \mathbf{e}_{j,\nu} = \delta_{\mu,\nu}. \tag{5.10}$$

The velocity of the j-th atom in a harmonic system can be derived form Eq. 5.9:

$$\dot{\mathbf{u}}_j(t) = \frac{-\imath}{\sqrt{Nm_j}} \sum_\nu A_\nu w_\nu \exp(-\imath w_\nu t)\mathbf{e}_{j,\nu}. \tag{5.11}$$

According to this definition the kinetic $\langle K_\nu \rangle$ and the potential energy $\langle V_\nu \rangle$ ($\langle K_\nu \rangle = \langle V_\nu \rangle$ within the harmonic approximation) can be expressed as follows:

$$\langle K_\nu \rangle = \frac{A_\nu^2 w_\nu^2}{2N} \tag{5.12}$$

Thus, the overall energy of the system $\langle E_\nu \rangle$ is:

$$\langle E_\nu \rangle = \frac{A_\nu^2 w_\nu^2}{N}. \tag{5.13}$$

This mean energy can also be expressed using the Bose-Einstein statistic:

$$\langle E_\nu \rangle = \hbar w_\nu \left[\frac{1}{2} + n(\nu) \right] \tag{5.14}$$

$$n(\nu) = \left[\exp(\hbar w_\nu / k_B T) - 1 \right]^{-1}. \tag{5.15}$$

In the classical limit ($\hbar w / k_B T \ll 1$) the occupation number $n(\nu)$ reduces to:

$$n(\nu) + \frac{1}{2} \simeq \frac{k_B T}{\hbar w}, \tag{5.16}$$

the total energy of the system is given by the following expression:

$$\langle E_\nu \rangle = \frac{A_\nu^2 w_\nu^2}{N} = k_B T \tag{5.17}$$

Thus the mass weighted velocity autocorrelator is:

$$\sum_j m_j \langle \dot{\mathbf{u}}_j(t) \cdot \dot{\mathbf{u}}_j(0) \rangle = \sum_\nu \left\langle \frac{w_\nu^2 A_\nu^2}{N} \exp(-\imath w_\nu t) \right\rangle \tag{5.18}$$

$$= \sum_\nu \frac{w_\nu^2 A_\nu^2}{N} \langle \exp(-\imath w_\nu t) \rangle \tag{5.19}$$

$$= \sum_\nu \frac{w_\nu^2 A_\nu^2}{N} \cos(w_\nu t) \tag{5.20}$$

$$= k_B T \sum_\nu \cos(w_\nu t). \tag{5.21}$$

The Fourier transform $g(w)$ of Eq. 5.21 is:

$$g(w) = \int_0^\infty \frac{1}{k_B T} \sum_j m_j \langle \dot{\mathbf{u}}_j(t) \cdot \dot{\mathbf{u}}_j(0) \rangle \exp(-\imath w t) dt \tag{5.22}$$

$$= \int_0^\infty \sum_\nu \cos(w_\nu t)\exp(-\imath w t)dt \tag{5.23}$$

$$\propto \sum_\nu \delta(w - w_\nu) \tag{5.24}$$

The function $g(w)$ is a sum over the frequencies of the normal modes w_ν of $\delta(w - w_\nu)$ functions.

Fortunately the density of states of a correlation function can be obtained without calculating the correlation function by using the Wiener-Khintchine theorem [40]. The density of state $g(w_\nu)$ can be expressed:

$$g(w) = \frac{1}{\mathcal{N}}\left[\sum_i \int m_i \dot{\mathbf{u}}_i(t)\exp(-\imath w t)dt\right]^2. \tag{5.25}$$

Where $\mathcal{N}$ is a normalization constant.

The results shown in Fig. 5.21 are in very good agreement compared to the BKS ones. The small discrepancies in the peak heights are most likely due to some cooling rate effects as reported by Vollmayr and coworkers [153]. The VDOS corresponding to the low frequency domain is accurately reproduced. The vibrational modes accounting for the low frequency domain correspond to delocalized motions of particles correlated over long distances. This results should be viewed as an encouraging clue that the short range Yukawa ansatz is able to describe the low frequency domain of the VDOS.

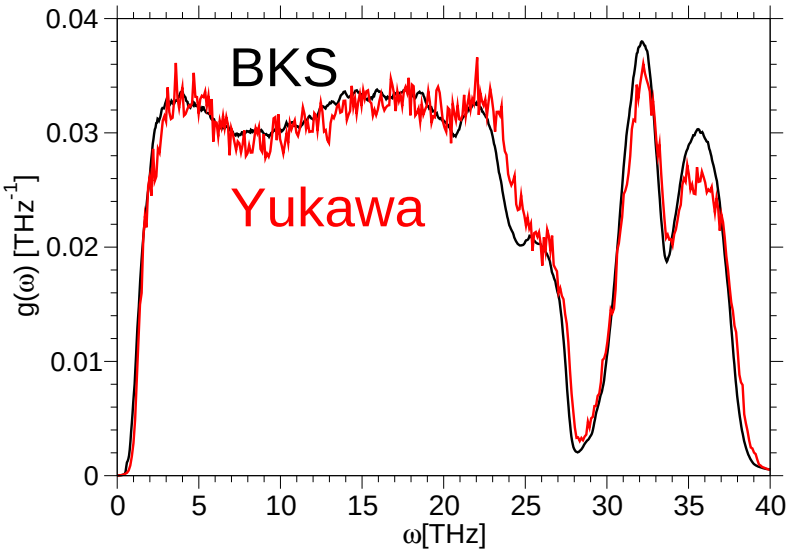

Figure 5.21: Vibrational density of state computed via the velocity-velocity autocorrelation function. The results computed using the Yukawa potential have been averaged over ten independent simulations (1002 atoms) at 300K. The BKS plots have been calculated using two different samples made of 8016 particles.

5.2.3 Thermodynamical properties: Pressure

Experimentally it has been observed that amorphous silica shows a maximum in the temperature dependence of the density at 1820K, [24]. This density anomaly is qualitatively reproduced by the BKS although overestimated ($\simeq$ 4700K). For the purpose of comparison our simulations have been carried out within the NVE ensemble and as a consequence the density is constant during the simulation. However the density anomaly is also reflected by the pressure dependence of the system with respect to the temperature. For the different temperatures investigated we have computed the corresponding pressure according to the virial theorem (see Appendix A) and plotted in Fig. 5.22. Even if the Yukawa potential systematically overestimates the average pressure by 0.2 GPa, the overall temperature dependence of the pressure is preserved although shifted. The temperature corresponding to the minimum of the pressure in this range is kept constant. The temperature at which the pressure remains constant for the low temperature domain is slightly underestimated by the Yukawa potential, also, the height of the plateau is overestimated.

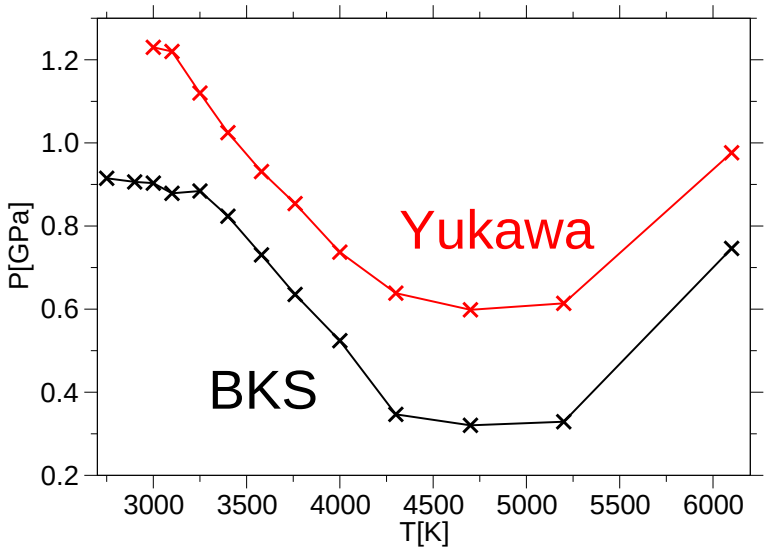

Figure 5.22: Pressure as a function of the temperature. The black crosses represent the pressure obtained with the BKS potential using Ewald summation. The red crosses represent the pressure obtained using the Yukawa potential.

5.3 Crystalline structure

In this chapter we have assumed that the electrostatic interactions can be screened for amorphous system. This hypothesis may not hold anymore when considering crystalline structures. In section (5.1.2) we stated that the introduction of a finite distance cutoff r_{cut} produces large errors in the description of the effective interactions applied on a given atom due to incorrect charge balance [158]. If the system is disordered,

the charge neutrality is best satisfied and the screening length is small. In contrast to this when considering crystalline phases (ordered phases) the charge neutrality may not be fullfiled and the Yukawa ansatz could be in total disagreement with the results obtained using the Ewald method. This section will investigate some properties of the Yukawa potential related to α-quartz. These results are compared to the BKS ones.

5.3.1 Equilibrium geometry

The equilibrium geometry of a 243 atoms sample is computed by relaxing the atomic coordinates in order to minimize the forces using a simple steepest descent algorithm, see section 4.1.1. During the minimization procedure, the properties of the space group symmetry, see Table 5.2 have to be preserved [20]. This constraint reduces the number of degrees of freedom, as only four fractional coordinates $\{u, x, y, z\}$ are necessary to define the inner cell structure of α-quartz. The atomic positions $\{u, x, y, z\}$ of atoms $\kappa = 1$ and $\kappa = 4$, see Table 5.2, have been modified according to the forces, and the rest of the atomic coordinates have been updated according to the space group symmetry. The presence of residual constraints on the system is checked by computing all the effectives atomic forces. The stability of the structure has been checked using the Hessian matrix[6] of the system.

No attempts have been made to optimize the cell parameters, as we already know from our preceding simulations on liquid silica that the pressure is overestimated (+0.2 GPa). This shift of the internal pressure would affect the lattice parameters as the lattice cell would naturally tend to increase. The short range part of the potential used in this minimization was truncated at 10 Å cutoff and regularized by an exponential function. This cuttoff distance has been chosen as for the BKS potential it is giving the exact lattice properties originally predicted by van Beest *et al.* [9].

Equivalent position	Species	κ	(x_1,x_2,x_3)
3a	Si	1	$(u, 0, 0)$
		2	$(0, u, \frac{2}{3})$
		3	$(\overline{u}, \overline{u}, \frac{1}{3})$
6c	O	4	(x, y, z)
		5	$(y, x, \frac{2}{3} - z)$
		6	$(\overline{y}, x - y, z + \frac{2}{3})$
		7	$(\overline{x}, y - x, \frac{1}{3} - z)$
		8	$(y - x, \overline{x}, z + \frac{1}{3})$
		9	$(x - y, \overline{y}, \overline{z})$

Table 5.2: Asymmetric unit coordinates according to the $P3_121$ space group.

[6]The Hessian matrix is the matrix of the second derivatives of energy with respect to the coordinates. If a system lie in a local minimum the small variations of the atomic positions can be described by convex quadratic terms ($(H)_{ii} \geq 0$)

Asymmetric Coordinates	BKS	Yukawa	Error(%)
u	0.465	0.458	1.55
x	0.427	0.428	-0.28
y	0.272	0.278	-2.42
z	0.208	0.210	-0.95

Table 5.3: Comparison of the force fields for α-quartz.

The structure thus obtained is stable according to the eigenvalues of the Hessian. The geometry optimization leads to the results shown in Table 5.3. The structure given by the BKS potential is comparable to the one given using the Yukawa potential.

5.3.2 Vibrational density of states

The vibrational density of state (VDOS) $g(\nu)$ gives informations about the relative number of normal modes $g(\nu)d\nu$ having a frequency in the range ν and $\nu + d\nu$. This quantity can be measured by neutron scattering experiment [26, 44, 141, 157]. Moreover this technique can give access to more precise informations such as phonon dispersion curves. Numerically these quantities can be computed within the harmonic approximation, assuming that atoms make only small displacements around their equilibrium positions ($\frac{\partial V(\mathbf{r})}{\partial \mathbf{r}_{i,\alpha}} = 0$). Consequently the dynamics of the system can be described by second order contributions.

t w_ν.

The density of states of BKS and Yukawa potential are compared in Fig. 5.23. The spectra overlap almost perfectly, and only slight discrepancies in the peak positions are noticeable in the high frequency domain. The peak heights are also in good agreement. It is whortwhile noting that the low frequencies domain is not affected at all by cutting off the long range interactions.

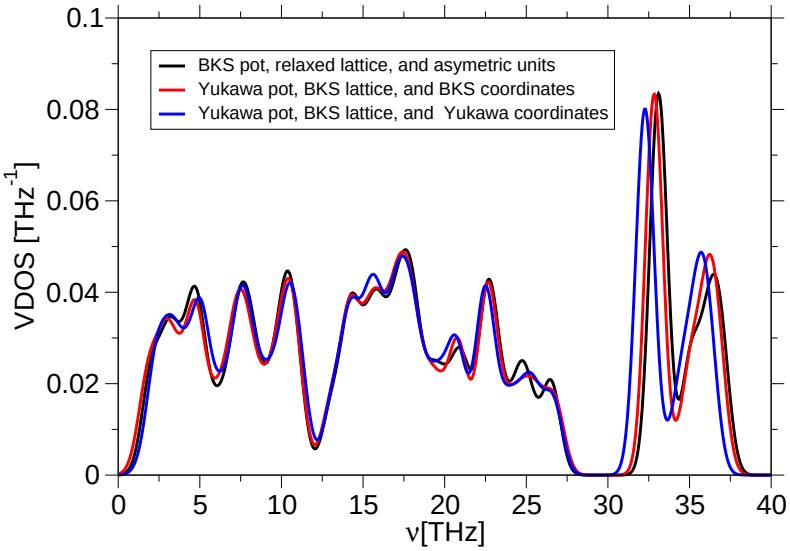

Figure 5.23: Vibrational density of states for α-quartz. Three different kinds of computations have been carried out on the α-quartz: In black, the VDOS as given by the BKS potential, in red the VDOS of the Yukawa potential using the BKS geometric parameters, in blue the density of Yukawa potential using the relaxed coordinates given in Table 5.3.

Chapter 6

Structural fitting procedure

The preceding fitting attempts made using the fitting to the *ab initio* forces have not been considered satisfactory as they were leading to an inaccurate description of the structure of silica. The structure has been considered *a posteriori* for validating the force-fitted potential, whereas it could have been directly considered into the fit. This proposition have already been discussed in the previous works of Lyubartsev and Laaksonen [95] and Soper [135] by means of reverse Monte Carlo (RMC) simulation. Lyubartsev and Laaksonen tried to reproduce the effective potential between the ions in aqueous NaCl solutions. To this end, they used the ion-ion radial distribution functions computed from molecular dynamics simulations. Soper also used the similar approach in order to propose an effective potential for water. The structural features can be expressed as a function of the parameters of the potential considered at the expense of strong approximations [63], for this reason the parameter space has been probed by these authors [95, 135] via a random walk in search for set of optimal parameters that is consistent with structural data. This algorithm is not fully satisfactory as the stochastic RMC approach is not a fast and accurate optimization method. In this chapter we will present the fast converging approach followed to take explicitely into account the structure given using the first-principles approach.

6.1 Fitting procedure

In chapter 4 we showed that fitting a pair potential ansatz for silica does not work as the structure of silica is not properly described. In this chapter we will propose a new criterion (χ^2) based on the structure given by the *ab initio* simulations.

We aim at taking explicitely into account some characteristic functions related to the structure. In view of the nature of the data considered any optimization algorithms based on the gradient method can hardly be performed. Indeed structural features[1] cannot be expressed in a simple analytical way as a function of the potential parameters. As a consequence the gradients corresponding to these structural quantities, necessary for any efficient minimization procedure (see section 4.1.1), cannot be derived analytically. In some previous works, [95, 135] this difficulty has been circumvented by means of stochastic reverse Monte-Carlo procedures at the expense of both convergence speed and accuracy of the results. In this work, we opted for the more direct approach by computing explicitely the derivatives of the pair correlation functions The fitting method retained for this purpose is the Levenberg-Marquardt algorithm, already discussed in section (4.1.1).

6.1.1 Practical considerations

Fitting criterion We assume a Born-Mayer Coulomb form for the interatomic potential, see Eq. (1.1).The structural merit function (χ^2) chosen for the fits is analog to the force merit function, see Eq. (4.14) of chapter 4. The forces in Eq. (4.14) have been replaced by the partial pair correlation. We chose the following definition for χ^2 for the fits:

$$\chi^2_{g(r)} = \sum_{\ell=0}^{\frac{L_{\rm Box}}{2\Delta}} \chi^2_{g(r)}(\ell) \tag{6.1}$$

$$= \sum_{\ell=0}^{\frac{L_{\rm Box}}{2\Delta}} \left[\frac{g^{\rm CPMD}_{\alpha\beta}(\Delta\ell) - g^{\rm BM}_{\alpha\beta}(\Delta\ell; \{q_i, A_{ij}, b_{ij}, c_{ij}\})}{\sigma^{\rm CPMD}_{g(r)}} \right]^2, \tag{6.2}$$

where $\{q_i, A_{ij}, b_{ij}, c_{ij}\}$ stand for the Coulomb and Born-Mayer parameters. The simulation cell is cubic and the typical box length is $L_{\rm box}$. The distances are discretized by means of the length step Δ.

- The $g^{\rm CPMD}_{\alpha\beta}(\ell\Delta)$ correspond to the partial pair correlation functions ($\alpha, \beta \in \{\mathrm{Si}, \mathrm{O}\}$) at distance $r_\ell = \ell\Delta$ computed using CPMD;

- The $g^{\rm BM}_{\alpha\beta}(\ell\Delta)$ correspond to the partial pair correlation functions ($\alpha, \beta \in \{\mathrm{Si}, \mathrm{O}\}$) at distance $r_\ell = \ell\Delta$ computed using the classical Born-Mayer potential;

[1] The structural quantities are given via thermal averages, see also section (2.2). This means that they can only be computed over a whole NVT run.

- $\sigma_{g(r)}^{\mathrm{CPMD}}$ correspond to the standard deviation of the *ab initio* partial pair correlation function, in this context we assumed that $\sigma_{g(r)}^{\mathrm{CPMD}}$ do not depend on the distance;

An example of the calculation of $\chi^2_{g(r)}$, using the constrained force fitted potential defined in Table 4.3, is given in Figs. 6.1, 6.2 and 6.3. The heights of the peaks of the pair correlation functions decreases to 1 for increasing distance, see section (2.4.1), and as a consequence the differences between the partial pair correlation functions corresponding to the CPMD calculation and to the classical trajectory vanish, by design, for large distances, $\lim_{\ell\to\infty}\chi^2_{g(r)}(\ell)=0$. The magnitudes of the discretized contributions $(\chi^2_{g(r)}(\ell))$ to the overall $\chi^2_{g(r)}$ decrease for increasing distances. Consequently fitting made using the $\chi^2_{g(r)}$ will describe more accurately the local structure characterized by high peaks compared to the intermediate and long range structure. In order to counterbalance this effect and thus to emphasize the sensitiveness of the fits on the intermediate and long range scale some other χ^2 have been considered:

$$\chi^2_{rg(r)} = \sum_{\ell=0}^{\frac{L_{\mathrm{Box}}}{2\Delta}} \chi^2_{rg(r)}(\ell) \tag{6.3}$$

$$= \sum_{\ell=0}^{\frac{L_{\mathrm{Box}}}{2\Delta}} \left[\frac{(\Delta\ell)g^{\mathrm{CPMD}}_{\alpha\beta}(\Delta\ell) - (\Delta\ell)g^{\mathrm{BM}}_{\alpha\beta}(\Delta\ell;\{q_i,A_{ij},b_{ij},c_{ij}\})}{\sigma^{\mathrm{CPMD}}_{rg(r)}}\right]^2 \tag{6.4}$$

$$\chi^2_{4\pi r^2 g(r)} = \sum_{\ell=0}^{\frac{L_{\mathrm{Box}}}{2\Delta}} \chi^2_{4\pi r^2 g(r)}(\ell) \tag{6.5}$$

$$= \sum_{\ell=0}^{\frac{L_{\mathrm{Box}}}{2\Delta}} \left[\frac{4\pi(\Delta\ell)^2 g^{\mathrm{CPMD}}_{\alpha\beta}(\Delta\ell) - 4\pi(\Delta\ell)^2 g^{\mathrm{BM}}_{\alpha\beta}(\Delta\ell;\{q_i,A_{ij},b_{ij},c_{ij}\})}{\sigma^{\mathrm{CPMD}}_{4\pi r^2 g(r)}}\right]^2 \tag{6.6}$$

In the following, we will refer to the definitions given by Eqs. (6.2), (6.4), and (6.6) as $g(r)$, $rg(r)$ and $4\pi r^2 g(r)$ criterion, respectively. The different standard deviations are all considered equivalent $\sigma^{\mathrm{CPMD}}_{g(r)} = \sigma^{\mathrm{CPMD}}_{rg(r)} = \sigma^{\mathrm{CPMD}}_{4\pi r^2 g(r)} = 1$. The choice accounting for these different definitions can be understood from the following example: Supposing that the classical pair correlation function $g(r_l)^{\mathrm{BM}}$ differs from the *ab initio* one $g(r_l)^{\mathrm{CPMD}}$ by a quantity ε at a distance r_l, $g(r_l)^{\mathrm{BM}} + \varepsilon = g(r_l)^{\mathrm{CPMD}}$.

- If $r_l = \Delta\ell > 1/\sqrt{4\pi}$ Å, then:

$$\chi^2_{g(r)}(\ell) = \varepsilon^2 < \chi^2_{rg(r)}(\ell) = (\Delta\ell\varepsilon)^2 < \chi^2_{4\pi rg(r)}(\ell) = (4\pi(\Delta\ell)^2\varepsilon)^2 \tag{6.7}$$

- If $r_l = \Delta\ell < 1/\sqrt{4\pi}$ Å, then:

$$\chi^2_{4\pi rg(r)}(\ell) = (4\pi(\Delta\ell)^2\varepsilon)^2 < \chi^2_{rg(r)}(\ell) = (\Delta\ell\varepsilon)^2 < \chi^2_{g(r)}(\ell) = \varepsilon^2. \tag{6.8}$$

These different χ^2 are also explicitely described on Figs. (6.4) and (6.5).

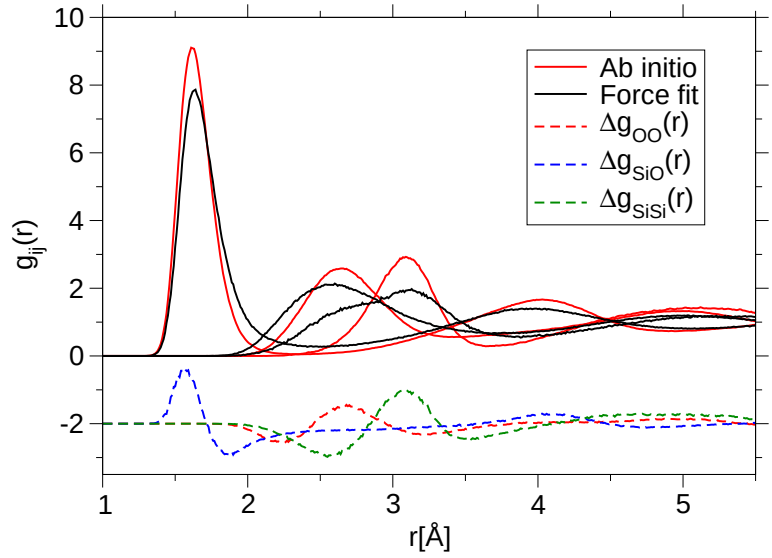

Figure 6.1: The partial pair correlation functions corresponding to the *ab initio* simulations (in red) and to the classical simulation made using a force fitted potential (black). Both simulations have been carried out at 3600K. 114 particles have been considered for the *ab initio* simulation whereas a 1152 atoms sample have been used for the classical simulations. For clarity the differences in between the black and the red curves have been shifted downward by 2.

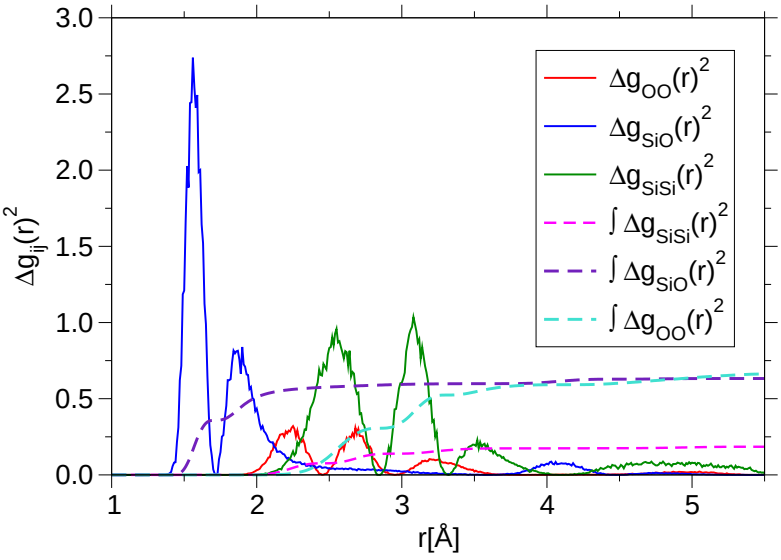

Figure 6.2: The squared differences in between partial pair correlation functions (solid line), and their corresponding integral form (dashed line).

Derivative calculation As the dependence of $g_{\alpha\beta}(r)$ with respect to the potential parameter has no simple analytical expression, the derivatives necessary for the cal-

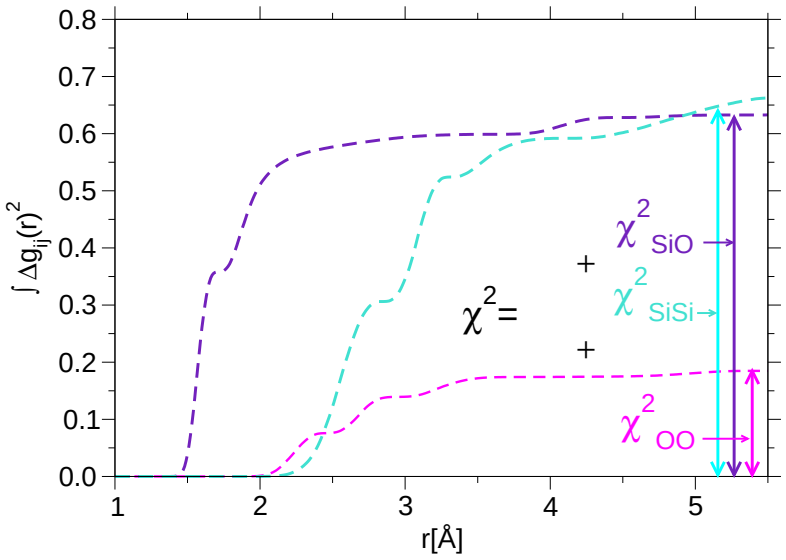

Figure 6.3: The χ^2 defined for the structural fitting procedure accounts for the sum of the integral of the squared difference of the partial pair correlation functions.

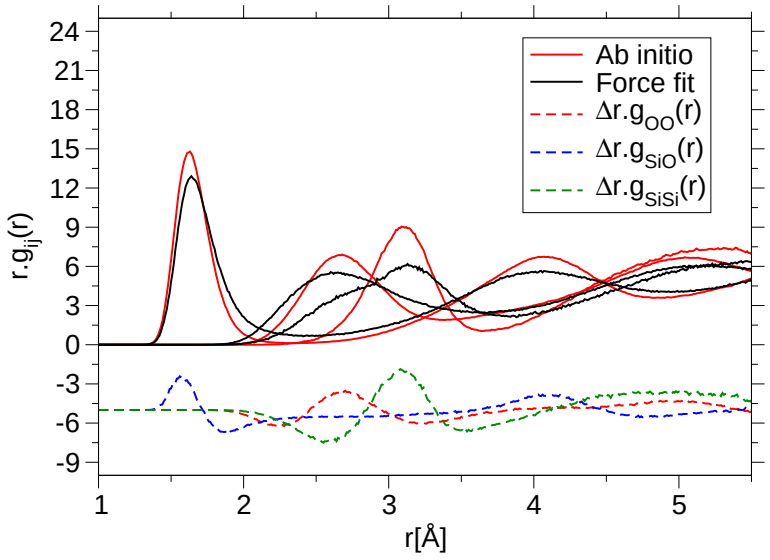

Figure 6.4: The plots representing $rg_{ij}(r)$ and $\Delta\left[rg_{ij}(r)\right]$.

culation of both gradient and Hessian matrix have been computed numerically. We proceed here by finite centered differences ε_{ζ_i}:

$$\frac{\partial g_{\alpha\beta}(r_\ell;\{\zeta\})}{\partial \zeta_i} = \lim_{\varepsilon_{\zeta_i}\to 0} \frac{g_{\alpha\beta}(r_\ell;\{\ldots,\zeta_i+\varepsilon_{\zeta_i},\ldots\}) - g_{\alpha\beta}(r_\ell;\{\ldots,\zeta_i-\varepsilon_{\zeta_i},\ldots\})}{2\epsilon_i}. \quad (6.9)$$

The variable ζ_i stands for one of the parameters of the Born-Mayer potential, $\zeta_i \in \{q_{Si}, A_{ij}, b_{ij}, c_{ij}\}$. For this purpose, NVT simulations have to be carried out. The sys-

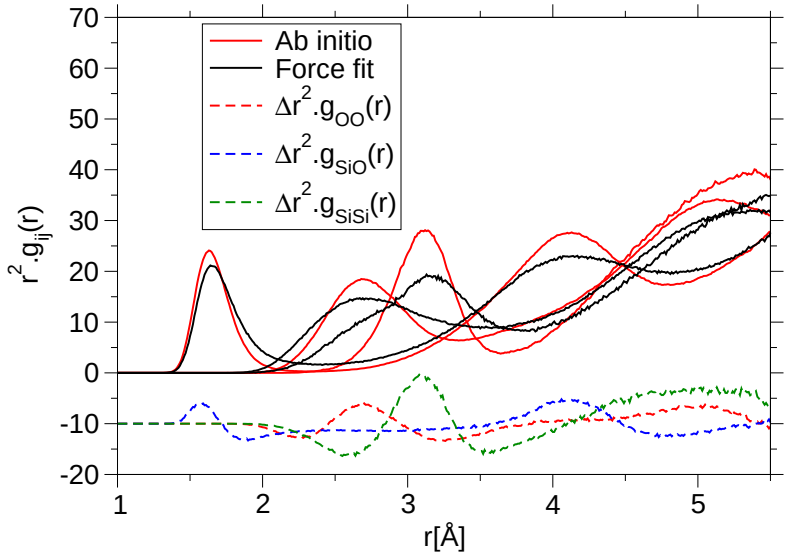

Figure 6.5: The $r^2 g_{ij}(r)$ and $\Delta\left[r^2 g_{ij}(r)\right]$ plots. The classical simulations have been made in the NVT ensemble on a 1152 atoms sample at 3600K. The *ab initio* simulations are already described on chapter (3.4.1).

tem under consideration consists of 1152 atoms in a cubic box using periodic boundary conditions. The density was set to 2.2 g/cm^3 corresponding to a box length L_{box} = 25.904 Å). The simulations last for 10 ps, this time range has been retained in agreement with the previous simulations of Horbach [74]. Changes in the potential which occur at each optimization step lead to significant increase of the temperature. To circumvent any energy conservation and stability problems, see also section (2.2.1), a time step of 1 fs has been retained for the simulations. The changes in the potential lead also to other side effects: As already stated in section (2.2.4.1) the Born-Mayer form has some drawbacks due to the presence of dispersive term ($\propto 1/r^6$) that may lead to diverging behavior for very short distances. To avoid these effects some artificial repulsive interactions effective[2] at very small distances have been added to the potential:

$$V_{\text{rep.}} = \frac{D_{ij}}{r_{ij}^{24}}. \tag{6.10}$$

The repulsive parameters are presented in Table 6.1. However it is worthwhile to note that these repulsive potentials may gives spurious local minima in the potential energy shape. These repulsive terms are efficient providing that the changes in the initial parameter sets are small. To get rid of relaxations effects due to changes in the potential occurring at the beginning of each simulation the first fifth of the trajectory is not taken into account for the calculation of the χ^2.

[2]The quadratic term previously used in the simulations of Vollmayr *et al.* [153] and Horbach and Kob [75] cannot be applied in this context. The repulsive quadratic terms they proposed suppose that one knows the position of the local maximum of the Si-O interaction term for example. However during a fitting process this maximum is not necessarily defined.

Pair	D_{ij} [eV.Å^{24}]
O-O	112.916259141
Si-O	29.272378219
Si-Si	3423204.14631

Table 6.1: Numerical values of the repulsive parameters required for the stability of the simulations, the repulsive potential is outlined on Eq. (6.10).

The parameters present in the Born-Mayer terms are not all equivalent (magnitude, prefactor/exponent), changes of some given parameters affect more the structural and dynamical features of the system considered. As a consequence different steps ε_{ζ_i} have to be defined for the different parameters of the potential. It is wortwhile to note that for averaging reasons (noise in the $g_{\alpha\beta}(r)$) the values also depend on the simulation length. The values of ε_{ζ_i} are somewhat chosen *ad hoc*. The guess ε_{ζ_i} has been set proportional to the BKS parameters for the O-O and Si-O term[3], the parameters corresponding to the Si-Si interaction have been chosen equal to the previous results given by the force-matching procedure. Underestimated values of ε_{ζ_i} may lead to variations in the $g_{\alpha\beta}(r)$ below their statistical errors, thus giving spurious results. In contrast to this, overestimated values might miss some fine details of the local structure and can also be detrimental to the accuracy of the convergence of the parameters. The final values retained are summarized in Table 6.2.

To check the stability of the procedure we have proceeded to preliminary tests on an oversimplified case. For these tests we wanted to reproduce the liquid structure given by the BKS potential. The guess parameters used for this purpose were obtained by making arbitrary changes on the BKS ones[4]. However the results were striking as the optimized set was different from what we expected, although the structures were similar. Numerically it appears that there is not an unique relationship between the site-site pair potential and the site-site pair correlation function[5]. Taking this into consideration, one has to carefully define the guess parameters. Different starting sets of parameters can lead to different local minima of the χ^2. In this work, the initial sets of parameters considered are the force fitted ones which in spite of a poor description of the structure give a good description of the forces ($\chi^2_{\text{Force}} \simeq 0.18$).

6.1.2 Fitting

Similar to the approach followed in section (4.2.0.1) we have realized two kinds of fits. In the first set of optimization the Si-Si terms have been constrained to zero whereas in the second sets we allowed an overall relaxation of the parameters. The

[3]The proportionnality factor has been chosen among the following list: $\{0.001, 0.002, 0.005, 0.010, 0.020, 0.050, 0.100\}$

[4]The test has been carried out using the folowing values $\{q_{\text{Si}} = 2.8, A_{\text{OO}} = 2600.77300, b_{\text{OO}} = 2.76, c_{\text{OO}} = 100.0, A_{\text{SiO}} = 12000.7572, b_{\text{SiO}} = 4.87318, c_{\text{SiO}} = 75.0\}$

[5]This is not true anymore when one adopts a pure mathematical point of view [47].

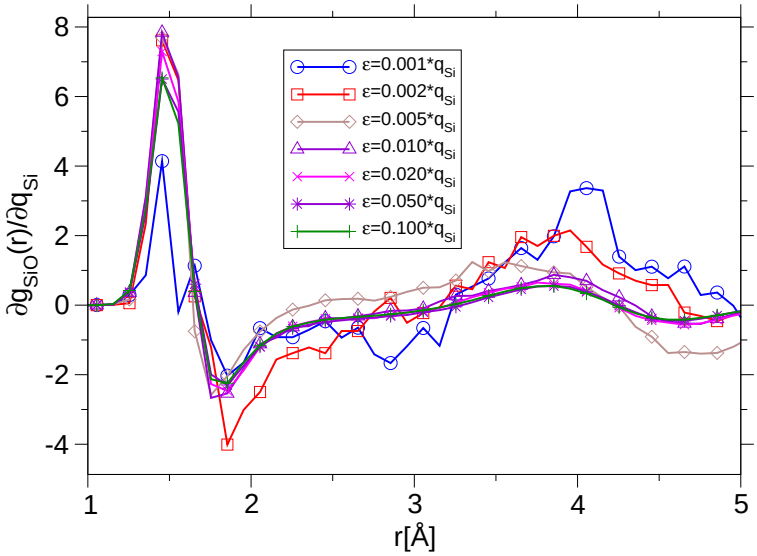

Figure 6.6: Derivatives of the Si-O pair correlation function with respect to the Coulomb charge for different distances ($r_\ell = \Delta\ell$, $\ell \in [0; \text{Ł}_{\text{Box}}/2\Delta]$). Different infinitesimal step $\varepsilon_{q_{\text{Si}}}$ have been defined to test the convergence of the results. The parameter set used for the dynamics have been defined in Table 6.2, the step for the discretization of the $g(r)$ is $\Delta = 0.02$Å.

Parameters	Value	ε_{min}	ε_{av}	ε_{max}
q_{Si} [C]	2.4	0.05	0.075	0.1
A_{OO} [eV]	1388.773	70.	105.	140.
b_{OO} [Å^{-1}]	2.76	0.03	0.085	0.14
c_{OO} [eV.Å^6]	175.	8.75	13.125	17.5
A_{SiO} [eV]	18003.7572	180.	540.	900.
b_{SiO} [Å^{-1}]	4.87318	0.01	0.03	0.05
c_{SiO} [eV.Å^6]	133.5381	1.5	4.1	6.7
A_{SiSi} [eV]	3976.776	200.	300.	400.
b_{SiSi} [Å^{-1}]	2.7943	0.014	0.03	0.056
c_{SiSi} [eV.Å^6]	882.59	44.13	66.	88.26

Table 6.2: Parameters values and their corresponding ε_{ζ_i} step. Three values are given here corresponding to the lower limit, to the upper one, and to the average value used for the fit. The O-O and Si-O parameters are the BKS parameters, the Si-Si parameters are the ones given by the force fitting procedure.

results are compiled in Tables 6.3, 6.4 and 6.5. The comparison between the partial contributions of the $rg(r)_{\text{unconst.}}$ potential and the BKS are given in Fig. 6.26. The most satisfying set of parameters is the one given using the $g(r)$ and the $rg(r)$ criteria in their unconstrained form (reliable angular distribution functions and pair correlation

functions). The corresponding structural quantities are displayed in Figs. 6.7, 6.8, 6.9 and 6.10.

Some attempts have been realized to check whether the output parameter sets resulting from the structural fitting procedure could be reinjected into the input of the force fitting procedure. Unfortunately, the optimized parameters given by the force fitting procedure were reconverging to their preceding values, these results are shown in Table 6.6. It is interesting to note that the force criterion[6] χ^2_{force} is not drastically affected. On the contrary, forces are still in better agreement than compared to the BKS potential. Furthermore, it appears that the structural fitting criterion, see Eq. (6.2), emphasizing the optimization of the local structure affects less the description of the forces whereas the long range $4\pi r^2 g(r)$ criterion leads to significant discrepancies with respect to the forces.

Parameters	$g(r)_{\text{const.}}$	$g(r)_{\text{unconst.}}$
q_{Si} [C]	1.932431	1.820380
A_{OO} [eV]	608.524841	723.064941
b_{OO} [Å^{-1}]	2.630410	2.649810
c_{OO} [eV.Å^6]	16.564278	46.315239
A_{SiO} [eV]	25525.568359	27694.904297
b_{SiO} [Å^{-1}]	5.164890	5.190189
c_{SiO} [eV.Å^6]	135.081451	145.668900
A_{SiSi} [eV]	-	3161.797607
b_{SiSi} [Å^{-1}]	-	2.877782
c_{SiSi} [eV.Å^6]	-	582.533447

Table 6.3: Force-field parameters given using the $g(r)$ fitting criterion.

Parameters	$rg(r)_{\text{const.}}$	$rg(r)_{\text{unconst.}}$
q_{Si} [C]	1.983317	1.910418
A_{OO} [eV]	753.638245	659.595398
b_{OO} [Å^{-1}]	2.731122	2.590066
c_{OO} [eV.Å^6]	13.243844	26.836679
A_{SiO} [eV]	23867.341797	27029.419922
b_{SiO} [Å^{-1}]	5.153327	5.158606
c_{SiO} [eV.Å^6]	127.584831	148.099091
A_{SiSi} [eV]	-	3150.462646
b_{SiSi} [Å^{-1}]	-	2.851451
c_{SiSi} [eV.Å^6]	-	626.751953

Table 6.4: Force-field parameters given using the $rg(r)$ fitting criterion.

[6] See definition in Eq. (4.14).

Parameters	$4\pi r^2 g(r)_{\text{const.}}$	$4\pi r^2 g(r)_{\text{unconst.}}$
q_{Si} [C]	2.011609	1.934870
A_{OO} [eV]	669.314575	913.573547
b_{OO} [Å^{-1}]	2.675462	2.661725
c_{OO} [eV.Å^6]	-15.721647	56.550533
A_{SiO} [eV]	25654.265625	26934.230469
b_{SiO} [Å^{-1}]	5.216061	5.182786
c_{SiO} [eV.Å^6]	128.086639	144.906982
A_{SiSi} [eV]	-	2057.579102
b_{SiSi} [Å^{-1}]	-	2.789539
c_{SiSi} [eV.Å^6]	-	526.447327

Table 6.5: Force-field parameters given using the $r^2 g(r)$ fitting criterion.

Criterion	Constraints	Initial χ^2_{force}	Final χ^2_{force}
$g(r)$	constr.	0.45	0.18
	unconstr.	0.40	0.17
$rg(r)$	constr.	0.55	0.18
	unconstr.	0.54	0.17
$4\pi r^2 g(r)$	constr.	0.79	0.18
	unconstr.	0.74	0.17

Table 6.6: Shown on this table, the χ^2 obtained from the force as defined in Eq. (4.14), the starting parameters are the ones presented in the above Tables 6.3, 6.4, and 6.5. The χ^2 values are given before and after the optimization process.

6.2 Liquid silica

6.2.1 Pair correlation functions

In this chapter, the pair correlation functions have been regarded as a fitting observable. Consequently, the agreement with respect to the *ab initio* data is rather good, see Figs. 6.11-6.16. The height and the position of the first peaks are generally well described. The $g(r)$ potential is the most accurate in this distance range. Nonetheless, the $rg(r)$ potential gives reliable results for the Si-Si pair. Regarding to the BKS potential, it appears that it systematically underestimates the position of the first peaks, whereas the second peak height and position are even more accurately described than compared to the fitted potentials, see Figs. (6.13) and (6.15).

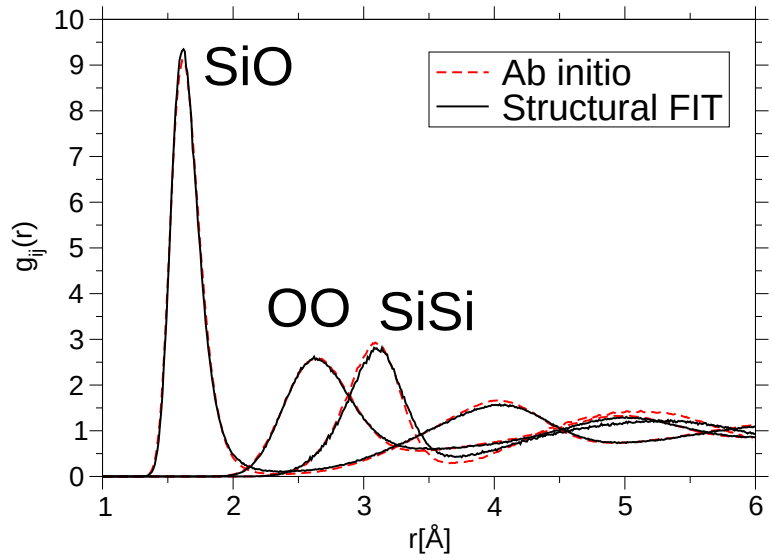

Figure 6.7: Compared on this figure the classical (solid), given by the $g(r)_{\text{unconst.}}$ criterion, and the *ab initio* (dashed) pair correlation functions.

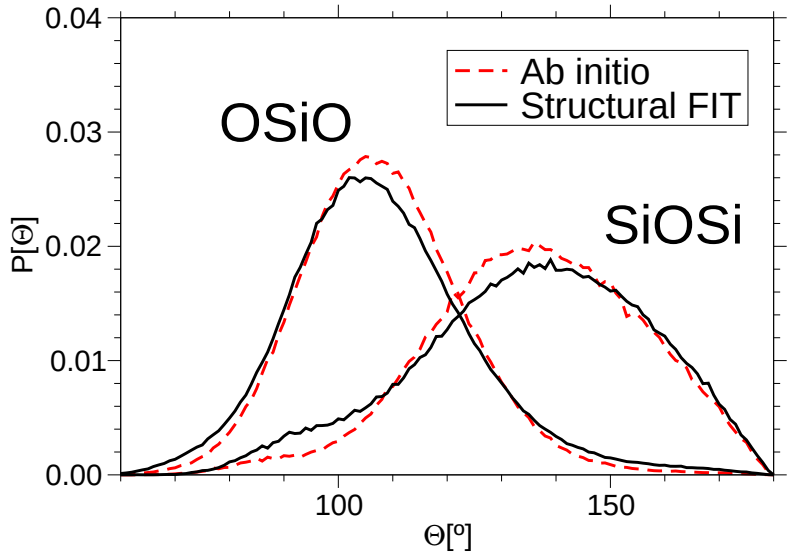

Figure 6.8: Compared on this figure the classical (solid), given by the $g(r)_{\text{unconst.}}$ criterion, and the *ab initio* (dashed) angular distribution functions.

6.2.2 Angular distribution functions

The comparison of the angular distribution functions to the *ab initio* data are presented in Figs. 6.17 and 6.18. The case of the BKS force field is quite instructive. As already mentioned the radial distribution functions are quite well described and even the $\widehat{\text{OSiO}}$ angular distribution function is in good agreement with the CPMD data. Nonetheless,

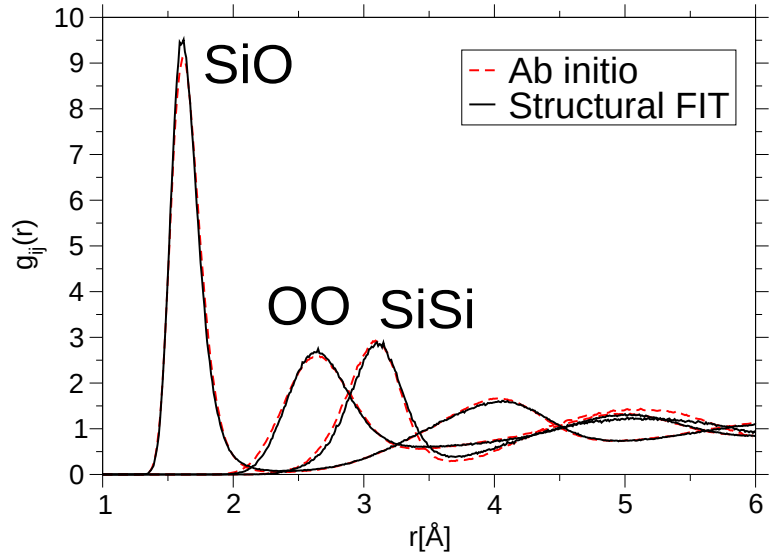

Figure 6.9: Compared on this figure the classical (solid), given by the $rg(r)_{\text{unconst.}}$ criterion, and the *ab initio* (dashed) pair correlation functions.

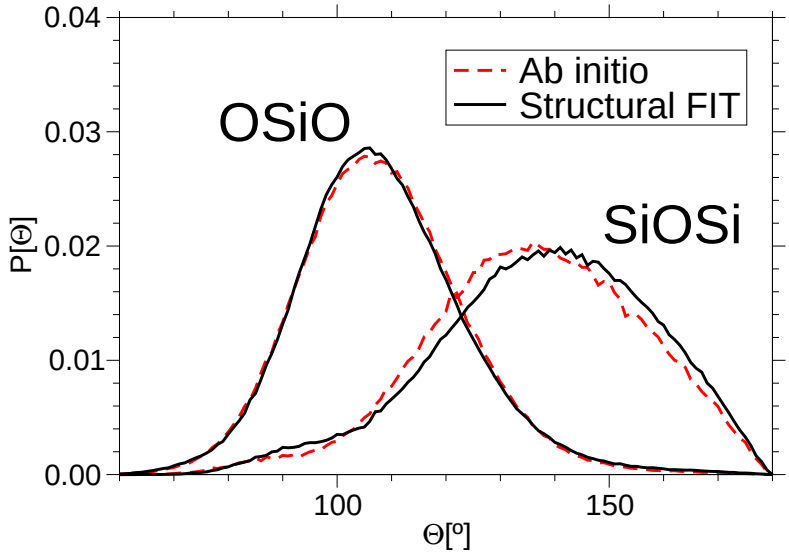

Figure 6.10: Compared on this figure the classical (solid), given by the $rg(r)_{\text{unconst.}}$ criterion, and the *ab initio* (dashed) angular distribution functions.

the $\widehat{\text{SiOSi}}$ plot exhibits differences when compared to the *ab initio* data. The very good prediction of the structural potentials are somehow surprising, especially for the intertetrahedral angles. The shapes, the positions and the heights of the peaks are in good agreement with the *ab initio* data. From this point, we will only consider the unconstrained $rg(r)$ potential in the following sections because of its ability in reproducing the structure of liquid silica.

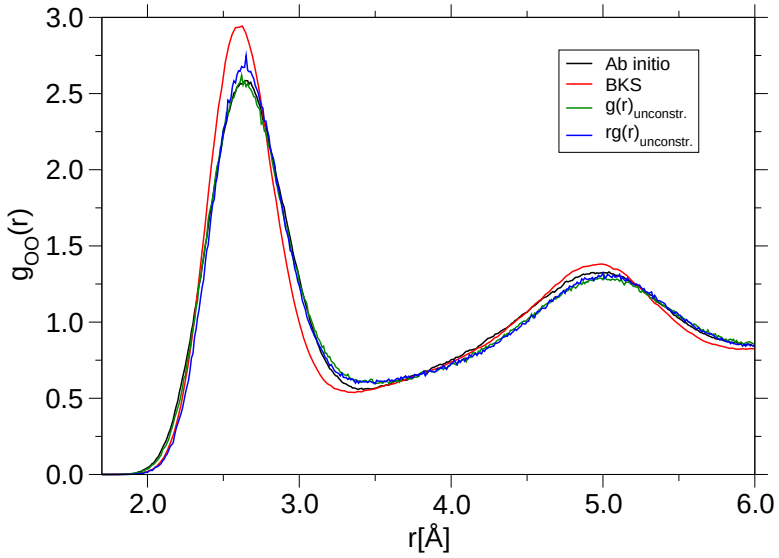

Figure 6.11: The O-O radial distribution functions for different methods and potentials at $T = 3600$K.

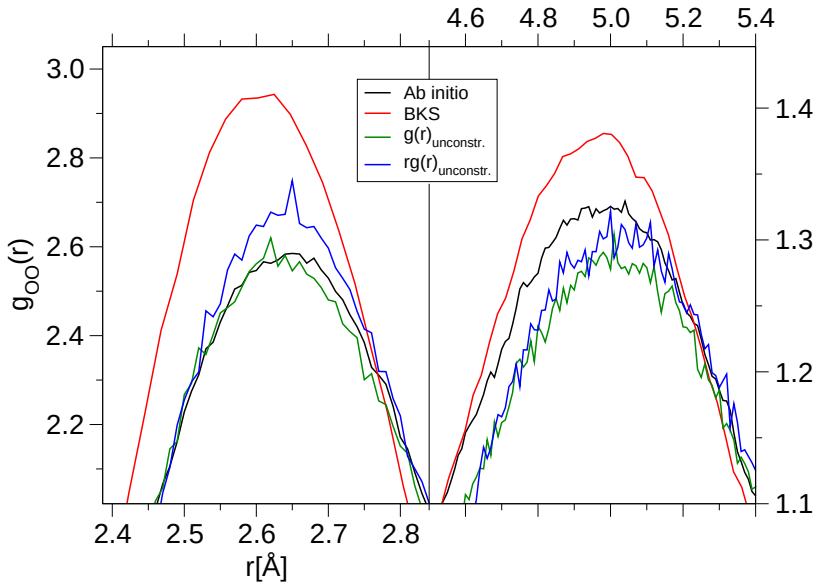

Figure 6.12: An expanded view of the first and second peaks of the O-O radial distribution functions for different methods and potentials.

6.2.3 Structure factors

The neutron scattering function (NSF) defined in section 2.4.1 has been calculated for the simulation realized using the $rg(r)_{unconstr.}$ potential and compared to the previous results of Horbach and Kob [75] and also to the experiments of Susman *et al.* [142], see Fig. (6.19). The sample considered for the calculation of this quantity has been taken

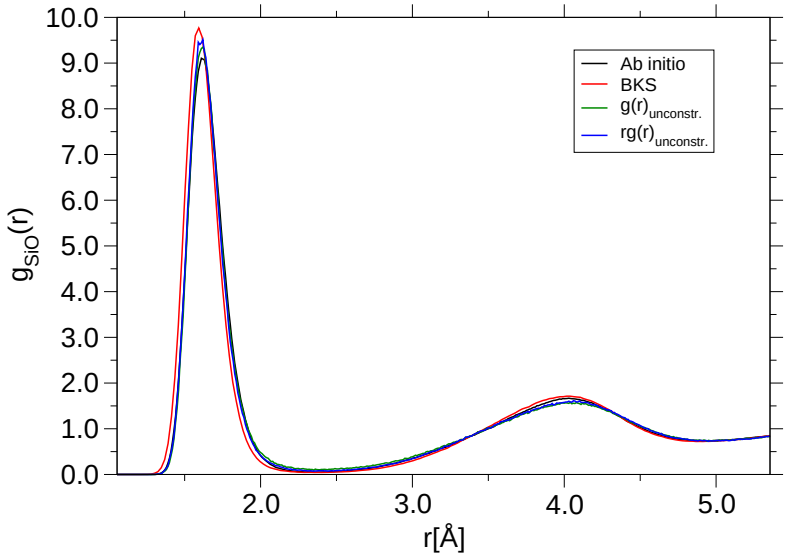

Figure 6.13: The Si-O radial distribution functions for different methods and potentials.

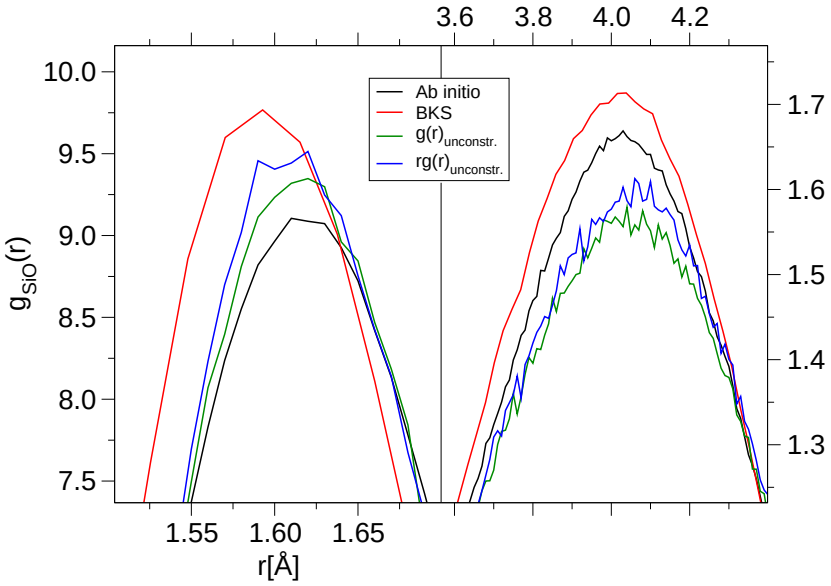

Figure 6.14: An expanded view of the first and second peaks of the Si-O radial distribution functions for different methods and potentials.

from sixteen independent simulations properly thermalized at 2440K and quenched to 300 K. The $rg(r)_{unconstr.}$ gives results that are very similar to the BKS, the minima at 2.2 $Å^{-1}$ and 6.4 $Å^{-1}$ are still underestimated by our potential when compared to the experimental data. The position and the height of the peaks above 2.2 $Å^{-1}$ is in good agreement with the experiments. However the position and the height of the first sharp diffraction peak (FSDF) is better reproduced (slightly shifted on the left) by the

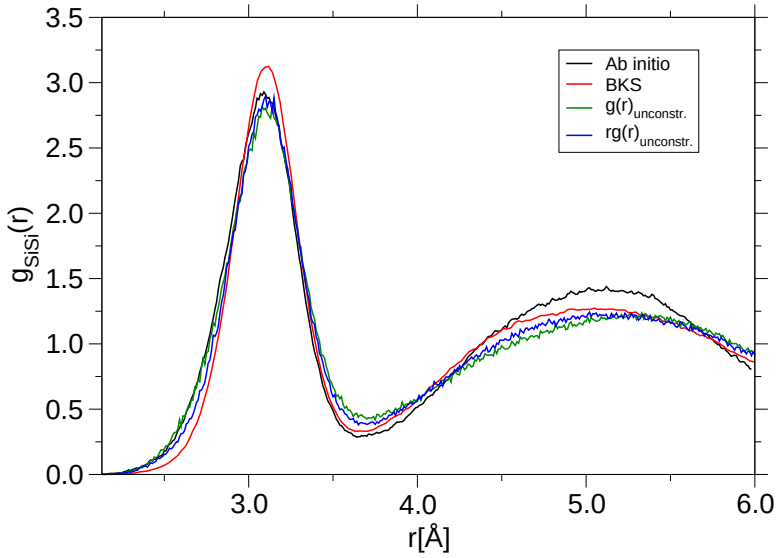

Figure 6.15: The Si-Si radial distribution functions for different methods and potentials.

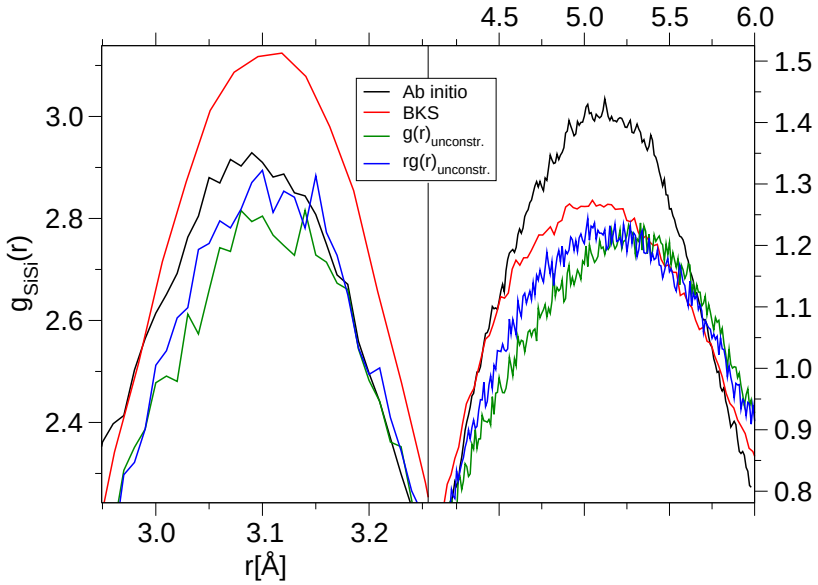

Figure 6.16: An expanded view of the first and second peaks of the Si-Si radial distribution functions for different methods and potentials.

$rg(r)_{unconstr.}$ potential in comparison to the BKS potential.

6.2.4 Pressure

As the density anomaly is a rather peculiar feature of silica, we have tested to what extent our $rg(r)$ potential was able to reproduce it. For this purpose we varied the

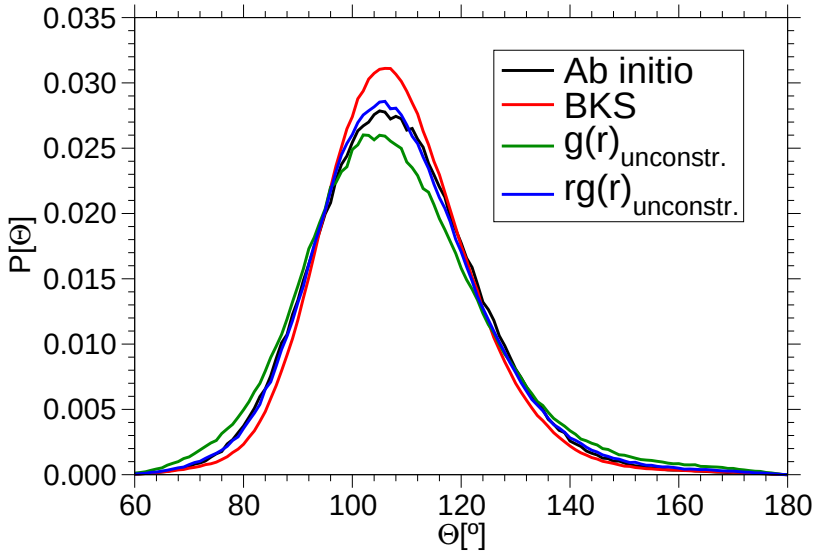

Figure 6.17: The $\widehat{\mathrm{OSiO}}$ distribution function for different methods and potentials.

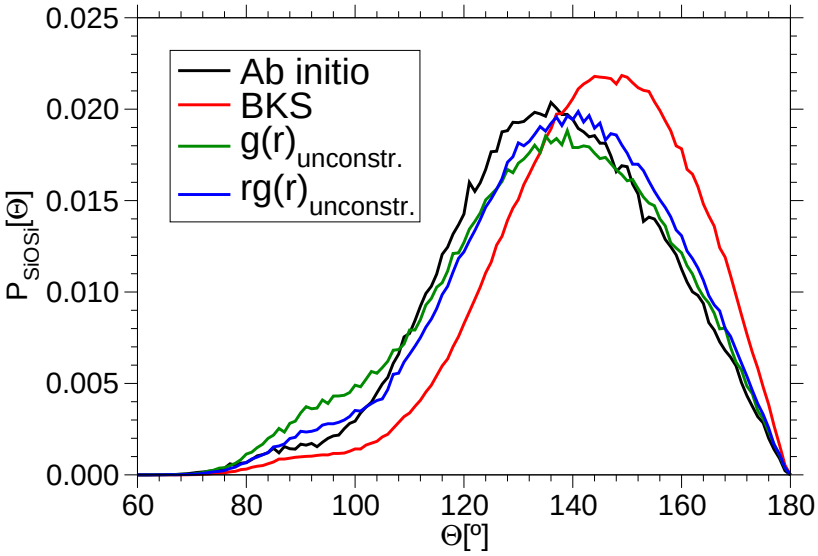

Figure 6.18: The $\widehat{\mathrm{SiOSi}}$ distribution function for different methods and potentials.

short range cutoff to check its influence on the pressure profile, and thereafter to set the equilibrium density of the system for a given temperature range. The temperature dependence of the pressure is presented in Fig. 6.20. We see that the pressure is mainly shifted towards lower values as the cutoff is increased. This profile is satisfactory as the system exhibits only a slight temperature dependence. We have opted for a 6.5Å cutoff that appears to be compatible with the mechanical stability of the system ($p > 0$). However, the data are incomplete as it was not possible to investigate quantitatively temperatures below $T = 2440$K, due to CPU time limitation. In the

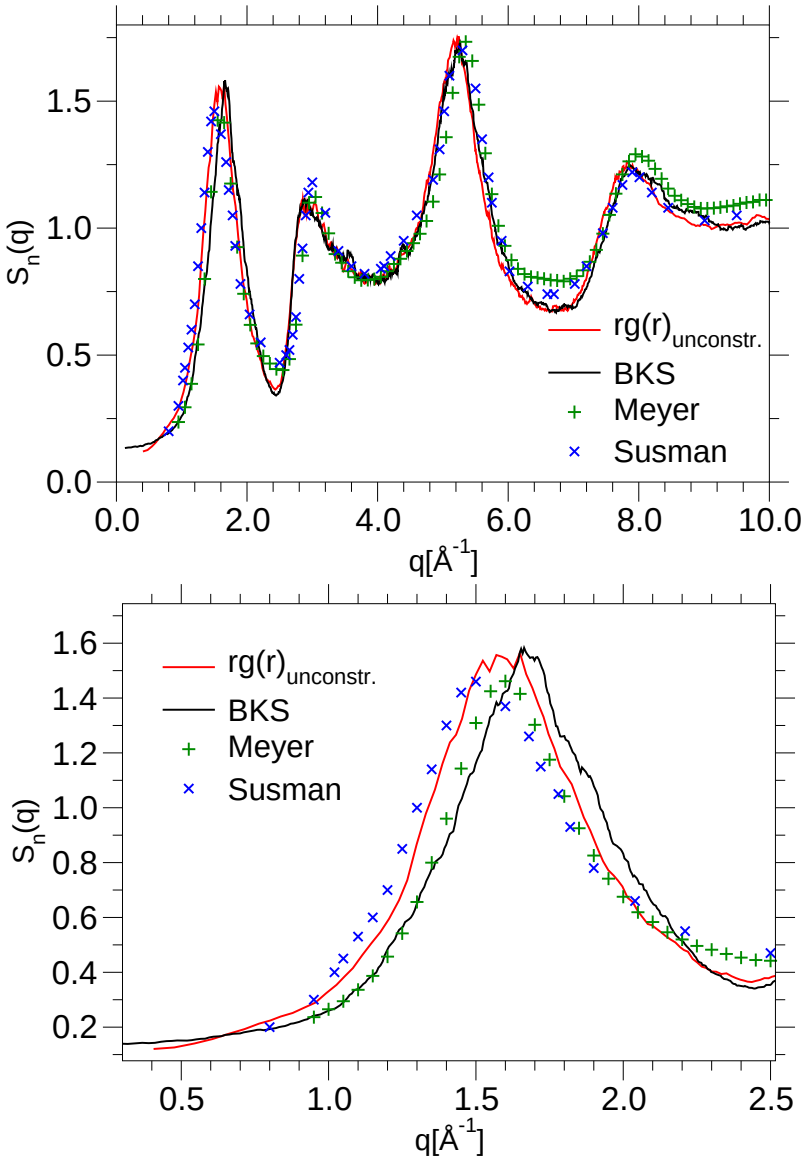

Figure 6.19: Comparison of the neutron scattering functions of different potentials to experiment: The BKS potential (in black) from Ref. [75], the $rg(r)_{unconstr.}$ potential (in red) and the experimental neutron scattering functions from Meyer *et al.* [106] (green crosses) and the one from Susman *et al.* [142] (blue crosses).

low temperature domain the pressure does not depend on the temperature, moreover if a the new potential is able to predict a negative thermal expansion (characterized by a minimum in $p(T)$) this would occur below $T = 3000$K *i.e.* closer to the experiment compared to the BKS[7]. These results have to be envisaged as encouraging clues that the potential describes liquid silica quite reasonably.

[7]The minimum in the temperature dependence of the pressure for the BKS potential corresponds to $T = 4500K$

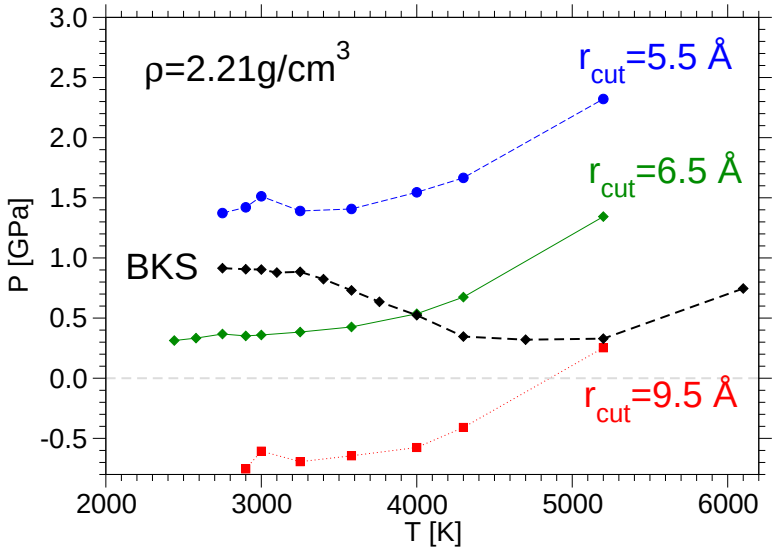

Figure 6.20: Temperature dependence of the pressure given by the $rg(r)_{\text{unconst.}}$ force field. The different curves correspond to different cutting distances r_{cut}. The BKS simulations have been carried out using 8016 atoms samples while the $rg(r)$ simulations have been realized on samples with 1152 atoms.

6.3 Dynamic properties

6.3.1 Vibrational density of states

The vibrational density of states has also been investigated to check whether the potential is able to properly reproduce the *ab initio* results. For this purpose, sixteen independent runs properly thermalized at 2440K have been considered and quenched down to 300K using an infinite quench rate. Here a 6.5 Å cutoff has been retained whereas in the preceding sections a 5.5 Å cutoff has been chosen. The density of states has been extracted using the Fourier transform of the velocity autocorrelation function, see section 5.2.2. The results have been compared to the ones of Horbach [74] and to the ones given in Ref. [12], see Fig. 6.21. From this direct comparison one can observe that the typical double peak pattern for the high frequency domain is predicted by both BKS and $rg(r)$ force fields. Regarding BKS, this feature is clearly well described and somewhat overestimated, but one has to keep in mind that these features have been directly taken into account for the fitting of the potential. Indeed, van Beest and coworkers [9] have used the stretching (T_d) and the bending (D_{2h}) modes to adjust the O-O and the Si-O terms. These modes are directly involved in this double peak structure. In contrast our $rg(r)$ potential has only been fitted on the structure starting from an optimized force fitted set of parameters. Moreover the shape of the double peaks structure, as described by our $rg(r)$ potential, can be improved by further investigations at lower temperatures. Indeed some cooling rate effects [153] may account for the lack of precision in the description of this part of the spectrum. Another distinction

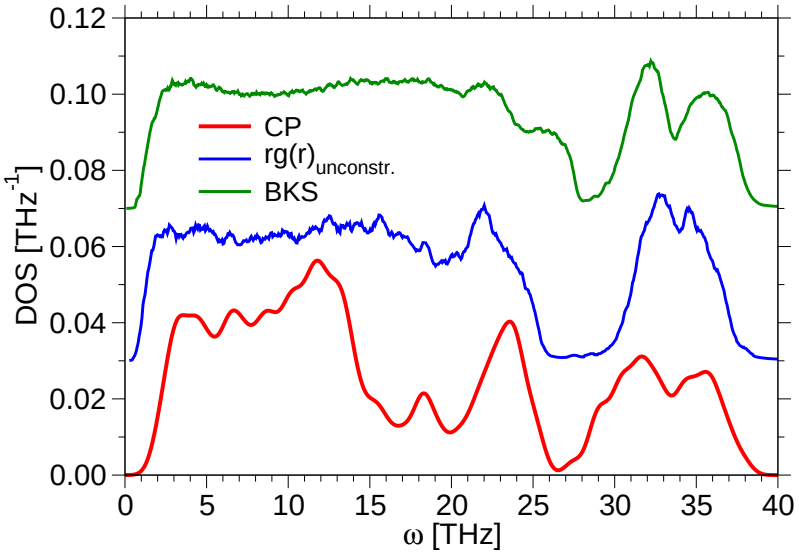

Figure 6.21: Vibrational density of states for vitreous silica. The curves corresponding to the $rg(r)$ and BKS potentials have been computed using the velocity autocorrelation function at 300K on samples containing 1152 and 8016 atoms, respectively. The *ab initio* data have been computed at 0K using the dynamic matrix on a 78 atoms samples. For clarity the curves for the $rg(r)$ and BKS force fields have been shifted upward by 0.03 and by 0.07, respectively.

can be made in between the two classical potentials in that the BKS clearly exhibits a spurious shouldering at 26 THz whereas our potential shows only a single peak in this frequency range at 21.8 THz, slightly underestimated when compared to the 23.7 THz given by CPMD. These results connected to the high frequency domain should be considered as encouraging. Regarding the rest of the curves the results shown by the BKS and the $rg(r)$ potential are similar. However, some deeper investigations are necessary, especially in the range going from 16 THz to 27 THz, to check whether our potential leads to more precise results [12].

6.3.2 Diffusion

Calculations have been carried out to investigate the diffusive dynamics described by our force-field. The mean squared displacements and the Arrhenius plot of the diffusion constants[8] are represented in Figs. 6.22, 6.23 and 6.24. The BKS gives a dynamics which is less diffusive than the one described by our potential: The diffusion constants differ by a factor three in the low temperature domain ($T \simeq 2440$ K). The temperature dependence of the diffusion constant can be reliably well described by an Arrhenius fit for the low temperature domain ($T \leq 3000$ K). This Arrhenius dependence is consis-

[8] In an Arrhenius plot the diffusion constant are represented as a function of the inverse temperature $D = A\exp(-E_A/k_BT)$.

tent with the experimental sighting for strong glass former such SiO_2. The activation energies are 4.51 eV and 4.97 eV for oxygen and silicon respectively[9]. These values are close compared to the ones given for the BKS potential provided by Horbach *et al.* [75], 4.66 eV and 5.18 eV for oxygen and silicon, respectively. These numbers compare well with the ones determined in experiments at significantly lower temperatures, 4.7 eV for oxygen [107] and 6 eV for silicon [23]. However according to Hemmati and Angell [5] some special care needs to be taken when considering these quantities since activation energies as well as diffusion constants depend much more sensitively on the potential than structural quantities.

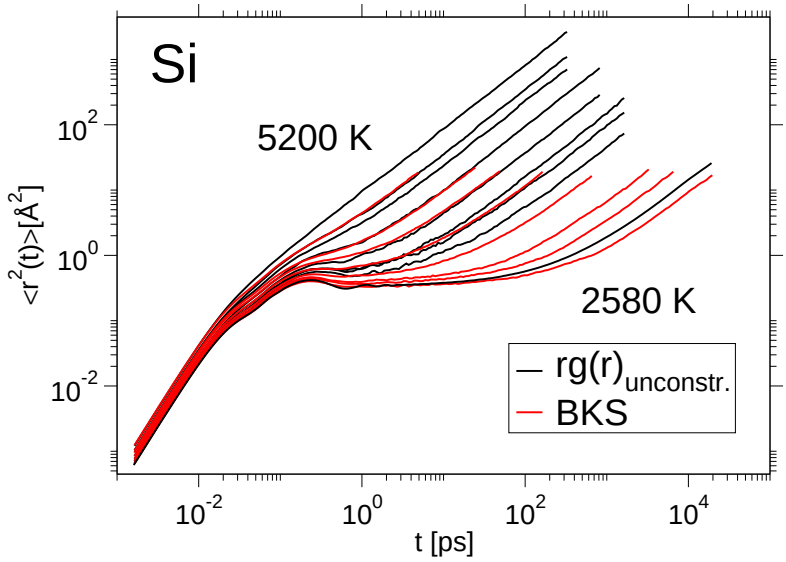

Figure 6.22: In black: Time dependence of the mean squared displacement of Si atoms for $rg(r)_{\text{unconst.}}$ potential for different temperatures (2580 K, 2750 K, 2900 K, 3000 K, 3250 K, 3580 K, 4000 K, 4300 K and 5200 K). The cutoff used for the short range terms was 6.5Å. The system under consideration was made of 1152 atoms. In red: Time dependence of the MSD of the BKS potential for (2750 K, 2900 K, 3000 K, 3250 K, 3580 K, 4000 K, 4300 K and 5200 K) the system under consideration was made of 8016 atoms, see Ref. [75].

6.4 Crystalline structure

In this section we compare the lattice energy minimization of quartz using the new potentials $g(r)$, $rg(r)$ and the BKS. Here we aim at testing the transferability of our potential on a very different phase of silica: α-quartz. As we have not implemented the calculation of the elastic constants in our codes we have used the version 3.0.1 of the

[9]The results of the fits give: $D_{\text{Si}} = 110.2665\exp(-4.97/k_BT)$ cm^2.s^{-1}, and $D_{\text{O}} = 27.9104\exp(-4.51/k_BT)$ cm^2.s^{-1}.

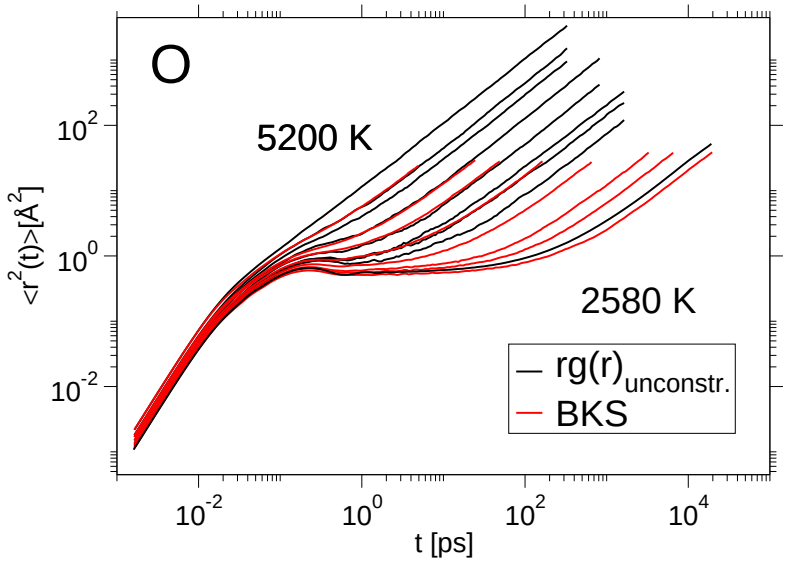

Figure 6.23: Time dependence of the mean squared displacement of the $rg(r)_{\text{unconst.}}$ potential for different temperatures (2580 K, 2750 K, 2900 K, 3000 K, 3250 K, 3580 K, 4000 K, 4300 K and 5200 K). The cutoff used for the short range terms was 6.5Å. The system under consideration was made of 1152 atoms. In red: Time dependence of the MSD of the BKS potential for (2750 K, 2900 K, 3000 K, 3250 K, 3580 K, 4000 K, 4300 K and 5200 K) the system under consideration was made of 8016 atoms, see Ref. [75].

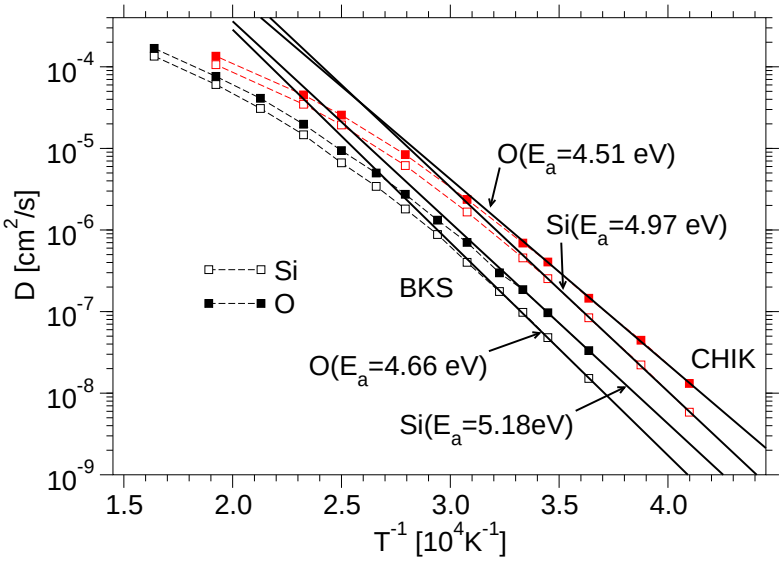

Figure 6.24: Arrhenius plot of the diffusion constants as determined from our simulation using the $rg(r)_{\text{unconst.}}$ potential (circles) compared to the diffusion constants from [75] (squares). The lines corresponds to the fitted Arrhenius fits to the data for low temperatures (2580 K, 2750 K, 2900 K, 3000 K).

GULP[10] code developed by Gale and coworkers [54]. The optimizations have been done on a primitive α-quartz cell[11] made of nine atoms, the distance defined for the potential truncation has been set to 10 Å according to the value already defined in section 5.3.1. Note that the repulsive interactions mentioned in section 6.1.1 have not been required in this case. The lattice energy minimizations are summarized in Table 6.7 and their corresponding elastic constants are given in Table 6.8. As already mentioned, the BKS has been fitted so as to perfectly reproduce the asymmetric coordinates and the elastic constants of α-quartz. As a consequence, most of the predicted results match almost perfectly. Nonetheless, it is striking to note that the $g(r)$-potential is in close agreement to the experimental data, even as precise as the BKS when dealing with the x and y asymmetric coordinates. Regarding the $rg(r)$-potential, the lattice optimization yields to fairly good results even if one can deplore the misleading description of the z asymmetric coordinate.

The elastic constants have also been checked. These quantities are quite sensitive to the force field as they are defined via the second derivatives of the potential energy U with respect to the components of the strain (see appendix A.2.1):

$$C_{ij} = \frac{1}{V}\left(\frac{\partial^2 U}{\partial\varepsilon_i \partial\varepsilon_j}\right) \tag{6.11}$$

thereby describing the mechanical hardness of the material with respect to deformation. The BKS has been fitted so as to explicitely reproduce these constants too, though forces are not properly described, see section 4.2.0.2. Furthermore it is interesting to mention that these constants at $T = 0$ K correspond very closely to the experimental data at $T = 300$ K while the agreement is less good for the $T = 300$ K simulations[12], see also Fig. 6.25 [109]. Somehow the BKS results should be regarded as fitting artefacts as the underlying microscopic interactions accounting for the elastic constants are not properly described[13]. Regarding the new force-fields, one can see that the $g(r)$-potential is in disagreement with experiments (C_{ij} for $i \neq j$). In contrast to this, the $rg(r)$-force field gives quite reliable results.

[10] http://www.ivec.org/GULP/

[11] See Table 5.2 for details related to the space group properties.

[12] The experimental values change slightly with temperature [103], by about ±2 GPa.

[13] The second derivatives of the energy $\propto C_{ij}$ are properly described whereas the forces are not in agreement with the *ab initio* simulation, see chapter 4.

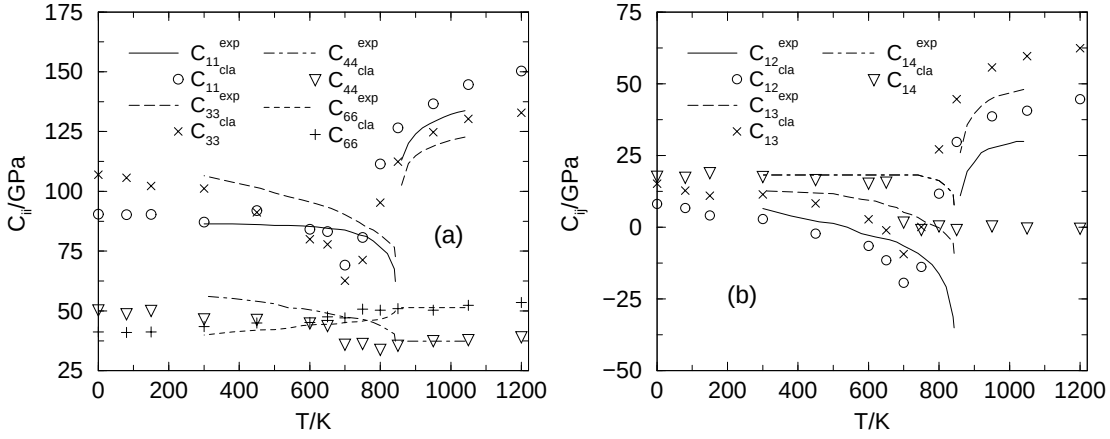

Figure 6.25: Elastic constants of α-quartz as a function of temperature. Solid lines show experimental data from Carpenter *et al.* [27]. Symbols show simulation results of Ref. [109] using the BKS potential. The transition temperature from the α-quartz to the β-quartz form is $T_{\text{trans.}}^{\text{BKS}} = 740 \pm 5\text{K}$ whereas the experimental transition temperature is $T_{\text{trans.}}^{\text{Exp.}} = 846\text{K}$.

Parameters	Exp. [154]	BKS		$g(r)_{\text{unconst.}}$		$rg(r)_{\text{unconst.}}$	
		value	error %	value	error %	value	error %
V [Å^3]	112.933	115.201	2.01	113.179	-1.76	121.677	7.74
a [Å]	4.91239	4.940922	0.58	4.910	-0.61	5.04502	2.69
b [Å]	4.91239	4.940922	0.58	4.910	-0.61	5.04502	2.69
c [Å]	5.40385	5.448928	0.83	5.412	-0.55	5.52019	2.15
u	0.4701	0.4648	1.13	0.4589	2.38	0.4731	0.64
x	0.4139	0.4268	3.12	0.4201	1.49	0.4268	3.12
y	0.2674	0.2715	1.53	0.2802	4.78	0.2597	2.87
z	0.2144	0.2085	2.75	0.2167	1.07	0.2012	6.16

Table 6.7: Prediction of α-quartz structure, compared with experiment. The asymmetric coordinates are defined in Table 5.2.

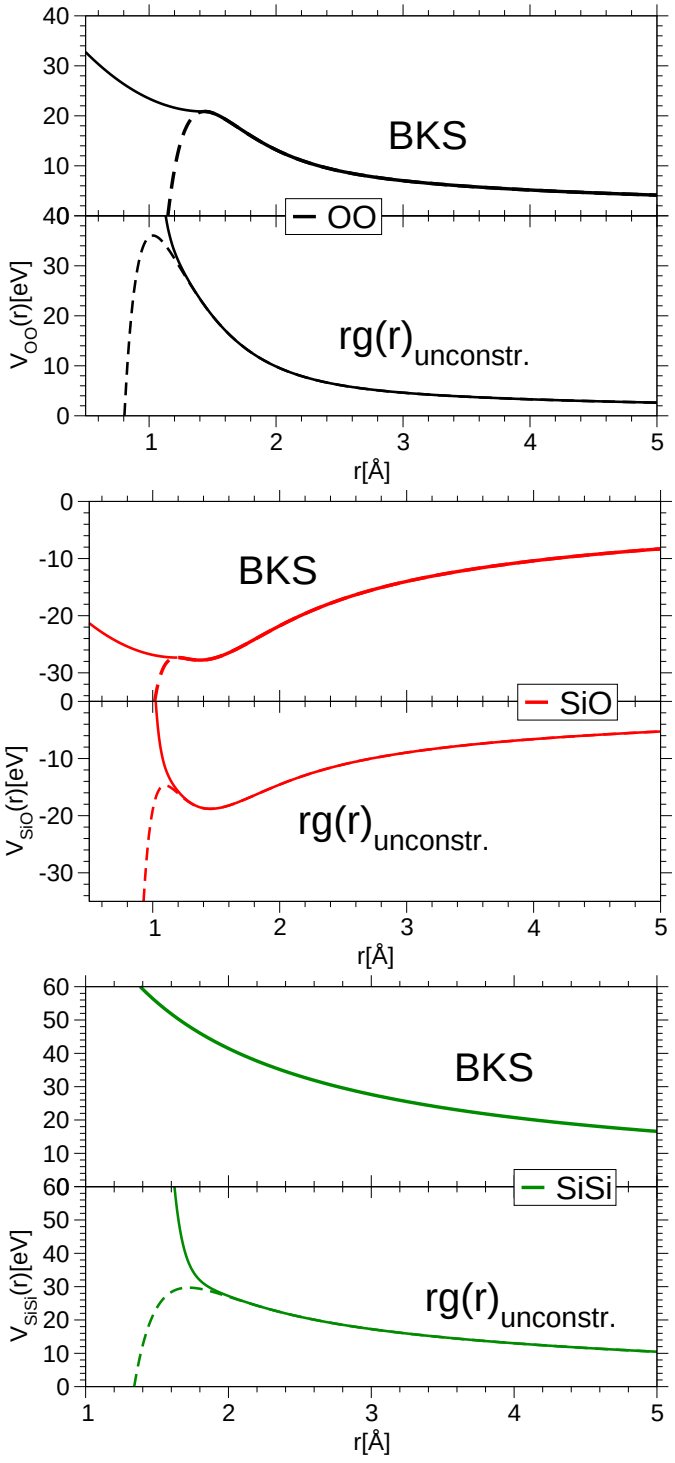

Figure 6.26: Represented on these figures the comparisons between the $rg(r)_{unconstr.}$ potential and the BKS one. In dashed lines are represented the diverging behavior for short ranges induced by the dispersion term of the Born-Mayer ansatz. In solid lines are represented the potentials and their added repulsive contributions used in the molecular dynamics simulations.

Elastic Constant [GPa]	Exp. [103]	BKS		$g(r)_{\text{unconst.}}$		$rg(r)_{\text{unconst.}}$	
		value	error %	value	error %	value	error %
C_{11}	86.8	90.6	4.19	78.0	-10.74	91.9	5.87
C_{33}	105.8	107.0	1.13	111.8	0.89	91.3	-13.42
C_{44}	58.2	50.2	-13.74	43.2	-1.53	46.8	-19.41
C_{66}	39.9	41.2	3.26	30.4	-23.81	42.6	6.76
C_{12}	7.0	8.1	15.71	17.2	145.71	6.6	-5.71
C_{13}	19.1	15.2	20.41	25.6	34.03	18.3	-3.14
C_{14}	-18.0	-17.6	2.22	-9.6	46.66	-14.5	20.00

Table 6.8: Elastic constants for α-quartz calculated at 0K for different force fields, the experimental results are given at room temperature ($T = 298$K).

Discussion and Conclusions

In this work, different approaches for the development of classical force-fields for amorphous silica are investigated. These approaches are based on first-principles calculations. The main goal has been to find a simple and efficient model potential that is well-suited for large scale molecular dynamics computer simulations. In most of previous works, potentials are fitted using peculiar methods, by mixing experimental and theoretical data or by using highly complex analytical expression for the potential. For these reasons potential fitting is mostly considered as an art. In the scope of this thesis we aimed at clarifying the methodology in order to propose a rational way of fitting potentials suited for pure oxides but applicable also on mixed oxides and to more complex systems.

This work can be divided into four parts. Molten silica samples have first been generated and simulated by means of Car-Parrinello molecular dynamics (CPMD). In CPMD, the electronic degrees of freedom are taken into account explicitely by a density functional theory and thus this method can be classified as an *ab initio* method. Some inherent shortcomings connected to this approach have been underlined in the scope of this work. Far from being the panacea the *ab initio* simulations have shown a poor ability to reproduce crucial features such as pressure and thus mechanical stability, for molten silica characterized by a strong negative pressure of -6.9 GPa. Some dynamical features such as the diffusivity have also been found in disagreement when compared to experiments. However, despite all these limitations, the crystalline phases were accurately predicted and most of the structural features connected to the molten phase were also consistent with experiments.

According to the fitting scheme proposed by Ercolessi and Adams the *ab initio* database only composed of configurations and forces have been considered at first. In spite of strong improvements in the description of the forces when compared to the BKS potential (χ^2_{Force} improved by a factor 7.6) our potentials turned out to lead to unphysical results. To overcome these limitations we have taken into account additional observables in the fitting procedure such as stress tensor without success. Even the addition of extra degrees of freedom into the potential formulation, through the use of spline functions to enhance the flexibility of our potential were not satisfying at all. These results were consistent with precedent observations made on liquid germania [64] and embedded atom models of gold [58].

In the end the potentials developed using the force matching procedure turned out to be inaccurate as they were not able to reproduce properly the structural properties of silica. However, at first stage these properties should be envisaged as being the most

crucial one so as to discriminate different classical potentials, as many features such as the vibrational density of states or diffusion constants can not be interpreted and connected to experiments without any proper description of the structure.

The failure of the spline approach highlighted the issue of the interactions range in silica. Most of the time, rigid ion potentials are computed by means of Ewald summation. In this work, we have investigated whether this complicated integration scheme for the Coulomb interaction is compulsory and to which extent one is able to mimic it through the force matching procedure using a Yukawa ansatz. The results were in semi-quantitative agreement, as larger cutoff should be used to yield to better results [28]. Nonetheless, features such as static properties, vibrational density of states or temperature dependence of the pressure were very comparable to ones given by means of Ewald summation.

In the forth part of this work we have developed a structural matching procedure with three different criteria using the *ab initio* partial pair correlation functions. The initial guess parameters used for this procedure were the ones resulting from the force matching procedure. The sets of potentials so obtained turned out to be in very good agreement with the structure, as required by the optimization scheme, but they were also found to be able to accurately describe the forces.

We carried out microcanonical and canonical simulations to investigate the thermodynamical properties of our potential. The temperature dependence of the pressure which is a very peculiar feature of silica appears to be qualitatively described although complementary simulations at low temperature need to be envisaged.

The vibrational density of states is in fairly good agreement with experiment especially in the high frequency domain. The very characteristic double peak feature in the range starting from 30 THz to 38 THz should no longer be considered as an enforced result connected to the data considered for the fit as at this time our potential has not been fitted using explicitely normal modes of vibrations contrarily to the BKS.

Surprisingly the properties of crystalline phases as predicted by our potential were found to be in very good agreement with experiments. The asymmetric coordinates, the cell parameters and second order quantity such as elastic constants were quantitatively well reproduced. These encouraging preliminary results underline the transferable nature of our potential although it has solely been fitted considering the liquid phase.

In this thesis we have mainly demonstrated that the accuracy of the model potentials are not necessarily gained by increasing its complexity. This work is evidently a methodological one as we developed a rational way of extracting simple classical force-fields based only upon *ab initio* calculations. The main perspectives is now to develop the same kind of potentials for other oxides like germania, or to develop potential suited for mixtures of SiO_2 with alkali ions. Regarding the present potential some deeper investigations are still required so as to check all its thermodynamical features in the low temperature ranges for example.

Appendix A

Stress tensor

A.1 Virial theorem

In molecular dynamics simulations the pressure can be defined via the virial theorem. In this section we present the general consideration leading to the definition of pressure used in molecular dynamics simulation for pairwise additive interactions. Considering a N particle system contained in a cubic box of volume $V = L^3$. The virial $\mathcal{V}$ is defined [63]:

$$\mathcal{V} = \sum_{i=1}^{N} \mathbf{r}_i \cdot \mathbf{F}_i \tag{A.1}$$

where $\mathbf{r}_i$ stands for the position of a particle i and $\mathbf{F}_i$ is the force applied on this particle. The virial theorem makes the connection between the potential and the kinetic energy $\langle T \rangle$:

$$2 \langle T \rangle = - \sum_{k=1}^{N} \langle \mathbf{F}_k \cdot \mathbf{r}_k \rangle . \tag{A.2}$$

A.1.1 Demonstration

General considerations It is possible to make a connection between the virial and the kinetic energy of the system. For this purpose one has to consider the second derivative of the squared position of a particle with respect to time:

$$(\ddot{\mathbf{r}}_i^2) = 2\dot{\mathbf{r}}_i^2 + 2\mathbf{r}_i \cdot \ddot{\mathbf{r}}_i. \tag{A.3}$$

By multiplying the above expression by m_i, the mass of particle i and by calculating the sum over all the particles we have:

$$\sum_{i=1}^{N} m_i(\ddot{\mathbf{r}}_i^2) = 2 \sum_{i=1}^{N} \left(m_i \dot{\mathbf{r}}_i^2 + \mathbf{r}_i \cdot m_i \ddot{\mathbf{r}}_i \right) . \tag{A.4}$$

The second member of Eq. (A.4) can be simplified using the Newton's second law:

$$\sum_{i=1}^{N} m_i(\ddot{\mathbf{r}_i^2}) = 2\sum_{i=1}^{N}\left(m_i\dot{\mathbf{r}}_i^2 + \mathbf{r}_i\cdot\mathbf{F}_i\right) \tag{A.5}$$

This equation can be simplified by considering the ensemble average $\langle\cdot\rangle$ of the macroscopic quantity $\sum_{i=1}^{N} m_i(\ddot{\mathbf{r}_i^2})$ which is equal to zero for any system at equilibrium:

$$0 = \left\langle 2\sum_{i=1}^{N}\left(m_i\dot{\mathbf{r}}_i^2 + \mathbf{r}_i\cdot\mathbf{F}_i\right)\right\rangle \tag{A.6}$$

$$\left\langle\sum_{i=1}^{N}\mathbf{r}_i\cdot\mathbf{F}_i\right\rangle = \left\langle\sum_{i=1}^{N} m_i\dot{\mathbf{r}}_i^2\right\rangle \tag{A.7}$$

$$\langle\mathcal{V}\rangle = 2\langle T\rangle . \tag{A.8}$$

here we have used the usual definition of the kinetic energy for a system made of N particles, $E_{kin.} = \frac{1}{2}\sum_{i=1}^{N} m_i\mathbf{v}_i^2$.

The forces applied on the system have two origins:

- The intermolecular contribution to the forces applied on a particle i by the other particles j referred to $\mathbf{F}_i^{int.}$;
- The external interactions between the particles i and the walls of the box referred to $\mathbf{F}_i^{ext.}$.

According to these definitions we can split the virial in two contributions:

$$\mathcal{V} = \mathcal{V}_{int.} + \mathcal{V}_{ext.} \tag{A.9}$$

$$\mathcal{V} = \sum_{i=1}^{N}\mathbf{r}_i\cdot\mathbf{F}_i^{int.} + \sum_{i=1}^{N}\mathbf{r}_i\cdot\mathbf{F}_i^{ext.}. \tag{A.10}$$

Each of these contributions are developed in the two following sections.

Internal contribution If we consider the expression of the quantity $\mathcal{V}_{int.}$ for a system described by pair interactions we can rewrite the internal contribution of the virial as:

$$\mathcal{V}_{int.} = \sum_{i=1}^{N}\mathbf{r}_i\cdot\mathbf{F}_i^{int.} \tag{A.11}$$

$$= -\sum_{i=1}^{N}\mathbf{r}_i\cdot\sum_{j\neq i}\nabla_i V_2(\mathbf{r}_{ij}) \tag{A.12}$$

$$= \sum_{i=1}^{N}\mathbf{r}_i\cdot\sum_{j\neq i}\mathbf{F}_{ij} \tag{A.13}$$

(A.14)

Newton's third equation states that:

$$\mathbf{F}_{ij} = -\mathbf{F}_{ji}. \tag{A.15}$$

Using this relation we can simplify the expression given by Eq. (A.13):

$$\begin{aligned}
\mathcal{V}_{int.} &= \sum_{i=1}^{N}\sum_{j\neq i}\mathbf{r}_i\cdot\mathbf{F}_{ij} && \text{(A.16)}\\
&= \sum_{i=1}^{N}\sum_{j<i}\mathbf{r}_i\cdot\mathbf{F}_{ij}+\mathbf{r}_j\cdot\mathbf{F}_{ji} && \text{(A.17)}\\
&= \sum_{i=1}^{N}\sum_{j<i}\mathbf{r}_i\cdot\mathbf{F}_{ij}-\mathbf{r}_j\cdot\mathbf{F}_{ij} && \text{(A.18)}\\
&= -\sum_{i=1}^{N}\sum_{j<i}\mathbf{r}_{ij}\cdot\mathbf{F}_{ij}. && \text{(A.19)}
\end{aligned}$$

External contribution The molecules of the gas interact with the confining box when they collide with the walls. So as to simplify the calculation of the external contribution of forces to the virial we can define the origin of our system at one corner of the box as illustrated in Fig. A.1. The force applied by the box to the particles are normal to the side of the walls. So the contributions of the sides $\{adeh\}$, $\{defc\}$ and $\{abcd\}$ to the external forces since the scalar product $\mathbf{r}\cdot\mathbf{F}^{ext.}$ is zero:

$$\mathcal{V}_{ext.} = \underbrace{\sum_{i=1}^{N}\mathbf{r}_i\cdot\left(\mathbf{F}^{ext.}_{i,\{adeh\}}+\mathbf{F}^{ext.}_{i,\{defc\}}+\mathbf{F}^{ext.}_{i,\{abcd\}}\right)}_{0}+\sum_{i=1}^{N}\mathbf{r}_i\cdot\left(\mathbf{F}^{ext.}_{i,\{ehgf\}}+\mathbf{F}^{ext.}_{i,\{abgh\}}+\mathbf{F}^{ext.}_{i,\{bcfg\}}\right). \tag{A.20}$$

The remaining three contributions can be calculated easily as illustrated in Fig. A.2, as the scalar product $\mathbf{r}_i\cdot\mathbf{F}^{ext.}_{i,\{bcfg\}}$ can be expressed as:

$$\mathbf{r}_i\cdot\mathbf{F}^{ext.}_{i,\{bcfg\}} = -L\mathbf{F}^{ext.}_{i,\{bcfg\}}. \tag{A.21}$$

According to the usual definition of the pressure:

$$P = \frac{\left\langle\sum_{i=1}^{N}F_i^{ext.}\right\rangle}{L^2}, \qquad \text{or} \qquad PV = \left\langle\sum_{i=1}^{N}F_i^{ext.}\right\rangle L \tag{A.22}$$

we can express the external contributions of each side of the box to the virial as:

$$\langle\mathcal{V}_{ext.}\rangle = -3PV \tag{A.23}$$

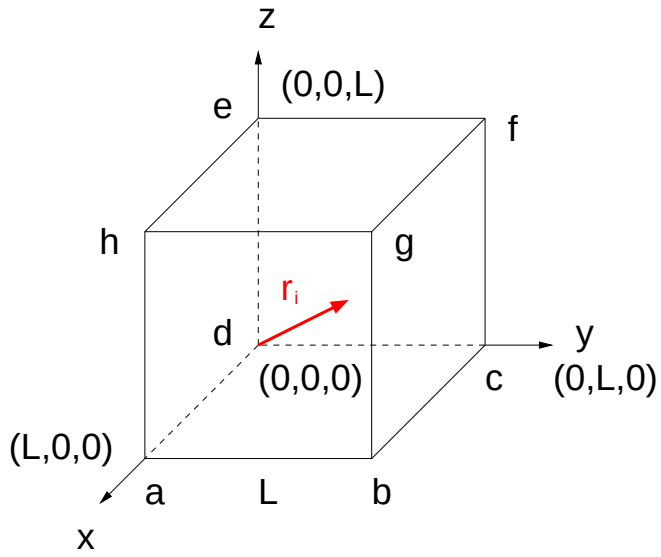

Figure A.1: Sketch representing a cubic box. The corners are named by letters $\{a, b, c, d, e, f, g, h\}$, the origin of the system coordinates is located at the corner $\{d\}$, the x-, y- and z- axis of the Cartesian system are joined to the lines (da) (dc) (de) of the box.

Equation of state The kinetic energy of the system and the temperature can be connected according to the equipartition theorem:

$$\langle E_{kin.} \rangle = \frac{3}{2} N k_B T. \tag{A.24}$$

If one injects the results of Eqs. (A.9), (A.23), (A.24) in Eq. (A.8) one finds:

$$\frac{3}{2} N k_B T = \frac{3}{2} PV - \left\langle \frac{1}{2} \sum_{i<j}^{N} \mathbf{r}_{ij} \cdot \mathbf{F}_{ij} \right\rangle \tag{A.25}$$

$$\text{or} \qquad P = \frac{N k_B T}{V} + \frac{1}{3V} \left\langle \sum_{i<j}^{N} \mathbf{r}_{ij} \cdot \mathbf{F}_{ij} \right\rangle \tag{A.26}$$

which is the general equation of state for a gas described by pairwise additive interactions. As we will see in section A.2, the second term of Eq. (A.26) can be connected to the stress tensor.

A.2 General expression

In some more complex cases where the interatomic interactions are described by N-body potentials the pressure can be calculated using the stress tensor. The stress tensor components Π_{uv}, $(u, v) \in \{1, 2, 3\}$ are defined by the sum of two contributions:

- A kinetic contribution $\Pi_{uv}^{kin.}$;

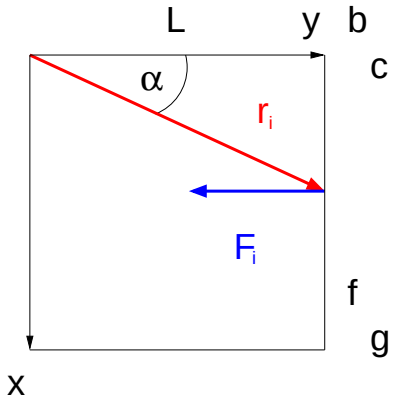

Figure A.2: Sketch representing the contribution to the virial of the interactions of the wall $\{bcfg\}$. The external force $\mathbf{F}^{ext.}_{i,\{bcfg\}}$ is perpendicular to the wall.

- The partial derivative of the potential energy with respect to the strain components, $\Pi^{pot.}_{uv}$.

$$\Pi_{uv} = \Pi^{kin.}_{uv} + \Pi^{pot.}_{uv} \tag{A.27}$$

These contributions will now be calculated.

A.2.1 General definitions

The strain tensor is used to define a slight homogeneous deformation of a crystal cell[1]. The lattice parameters can be summarize using the matrix formalism:

$$\underline{\underline{h}} = \begin{pmatrix} a_1 & b_1 & c_1 \\ a_2 & b_2 & c_2 \\ a_3 & b_3 & c_3 \end{pmatrix}, \tag{A.28}$$

where a_1, a_2, a_3 stand for the component of the lattice vector $\mathbf{a}$. The Voigt strain tensor [20] is defined as:

$$\underline{\underline{\varepsilon}} = \begin{vmatrix} 1+\varepsilon_{11} & \frac{1}{2}\varepsilon_{12} & \frac{1}{2}\varepsilon_{13} \\ \frac{1}{2}\varepsilon_{21} & 1+\varepsilon_{22} & \frac{1}{2}\varepsilon_{23} \\ \frac{1}{2}\varepsilon_{31} & \frac{1}{2}\varepsilon_{32} & 1+\varepsilon_{33} \end{vmatrix}. \tag{A.29}$$

The subscripts can be redefined giving:

$$\varepsilon_{11} = \varepsilon_1,\ \varepsilon_{22} := \varepsilon_2,\ \varepsilon_{33} := \varepsilon_3,$$

$$\varepsilon_{12} = \varepsilon_{21} := \varepsilon_6,\ \varepsilon_{13} = \varepsilon_{31} := \varepsilon_5,\ \varepsilon_{23} = \varepsilon_{32} := \varepsilon_4.$$

[1]The concepts and notations introduced in this section are not only valid for crystals but also in continuum mechanics.

A.2.2 Kinetic contribution

The kinetic contribution to the stress tensor is simply defined by:

$$\Pi_{uv}^{\text{kin.}} = \sum_{i=1}^{N} m_i \mathbf{v}_i^u \mathbf{v}_i^v. \tag{A.30}$$

If one considers the trace of this tensor we can recognize the first term of the left part of equation A.26:

$$\begin{aligned} \text{Tr}\left(\Pi_{uv}^{\text{kin.}}\right) &= \sum_{u\in\{x,y,z\}} \sum_{i=1}^{N} m_i \mathbf{v}_i^u \mathbf{v}_i^u && \text{(A.31)} \\ &= \sum_{i=1}^{N} m_i \mathbf{v}_i^2 && \text{(A.32)} \\ &= 2T && \text{(A.33)} \end{aligned}$$

A.2.3 Potential contribution

Direct space contribution The derivative of the total potential energy of a pair potential, see equation (A.34), with respect to the strain can be straightforwardly calculated:

$$\begin{aligned} V_2 &= \sum_{i<j} V_2(r_{ij}) && \text{(A.34)} \\ \frac{\partial V_2}{\partial \varepsilon_{\alpha\beta}} &= \sum_{i<j} \frac{\partial V_2(r_{ij})}{\partial \varepsilon_{\alpha\beta}} && \text{(A.35)} \\ &= \sum_{i<j} \frac{\partial V_2(r_{ij})}{\partial r_{ij}} \frac{\partial r_{ij}}{\partial r_{ij}^2} \frac{\partial r_{ij}^2}{\partial \varepsilon_{\alpha\beta}}. && \text{(A.36)} \end{aligned}$$

The squared interatomic distance r_{ij}^2 can be easily expressed using the tensorial notation :

$$\begin{aligned} r_{ij}^2 &= \mathbf{r}_{ij} \cdot \mathbf{r}_{ij} && \text{(A.37)} \\ &= \underline{\underline{h}}\mathbf{X}_{ij} \cdot \underline{\underline{h}}\mathbf{X}_{ij} && \text{(A.38)} \\ &= \mathbf{X}_{ij}^{\dagger} \underline{\underline{h}}^{\dagger} \underline{\underline{h}} \mathbf{X}_{ij}, && \text{(A.39)} \end{aligned}$$

where $\mathbf{X}_{ij}$ stands for the reduced coordinates of the $\mathbf{r}_{ij}$: $\mathbf{r}_{ij} = \underline{\underline{h}}\mathbf{X}_{ij}$. If a small deformation is applied to the cell of the system by means of the strain tensor the new distances r'_{ij} can the be expressed by the following expression:

$$r_{ij}^{2'} = \mathbf{r}'_{ij} \cdot \mathbf{r}'_{ij} \tag{A.40}$$

$$= \underline{\underline{h}}'\mathbf{X}_{ij} \cdot \underline{\underline{h}}'\mathbf{X}_{ij} \tag{A.41}$$
$$= \underline{\underline{\varepsilon h}}\mathbf{X}_{ij} \cdot \underline{\underline{\varepsilon h}}\mathbf{X}_{ij} \tag{A.42}$$
$$= \mathbf{X}_{ij}^{\dagger}\underline{\underline{h}}^{\dagger}\left(\underline{\underline{\varepsilon}}^{\dagger}\underline{\underline{\varepsilon}}\right)\underline{\underline{h}}\mathbf{X}_{ij} \tag{A.43}$$
$$= \mathbf{r}_{ij}^{\dagger}\left(\underline{\underline{\varepsilon}}^{\dagger}\underline{\underline{\varepsilon}}\right)\mathbf{r}_{ij}. \tag{A.44}$$

Here $\underline{\underline{h}}'$ stands for the new deformed cell. The strain tensor is symmetric by definition as a consequence the derivative of the components of the strain tensor can be straightforwardly calculated:

$$\frac{\partial r_{ij}^{2'}}{\partial \varepsilon_{\alpha\beta}} = \mathbf{r}_{ij}^{\dagger}\frac{\partial\left(\underline{\underline{\varepsilon}}^{\dagger}\underline{\underline{\varepsilon}}\right)}{\partial \varepsilon_{\alpha\beta}}\mathbf{r}_{ij} \tag{A.45}$$
$$\frac{\partial\left(\underline{\underline{\varepsilon}}^{\dagger}\underline{\underline{\varepsilon}}\right)}{\partial \varepsilon_{\alpha\beta}} = \frac{\partial\left(\underline{\underline{\varepsilon}}^{2}\right)}{\partial \varepsilon_{\alpha\beta}} = 2\cdot\begin{vmatrix} \delta_{1\alpha,1\beta} & \frac{1}{2}\delta_{1\alpha,2\beta} & \frac{1}{2}\delta_{1\alpha,3\beta} \\ \frac{1}{2}\delta_{2\alpha,1\beta} & \delta_{2\alpha,2\beta} & \frac{1}{2}\delta_{2\alpha,3\beta} \\ \frac{1}{2}\delta_{3\alpha,1\beta} & \frac{1}{2}\delta_{3\alpha,2\beta} & \delta_{3\alpha,3\beta} \end{vmatrix}. \tag{A.46}$$

using equation (A.36) and (A.46) the expression of the strain tensor components are given by:

$$\frac{\partial V_2}{\partial \varepsilon_1} = \sum_{i<j}\frac{\partial V_2(r_{ij})}{\partial \varepsilon_i} \tag{A.47}$$
$$= \sum_{i<j}\frac{\partial V_2(r_{ij})}{\partial r_{ij}}\frac{\mathbf{r}_{ij,x}\mathbf{r}_{ij,x}}{r_{ij}} \tag{A.48}$$
$$\frac{\partial V_2}{\partial \varepsilon_2} = \sum_{i<j}\frac{\partial V_2(r_{ij})}{\partial r_{ij}}\frac{\mathbf{r}_{ij,y}\mathbf{r}_{ij,y}}{r_{ij}} \tag{A.49}$$
$$\frac{\partial V_2}{\partial \varepsilon_3} = \sum_{i<j}\frac{\partial V_2(r_{ij})}{\partial r_{ij}}\frac{\mathbf{r}_{ij,z}\mathbf{r}_{ij,z}}{r_{ij}} \tag{A.50}$$
$$\frac{\partial V_2}{\partial \varepsilon_4} = \frac{1}{2}\sum_{i<j}\frac{\partial V_2(r_{ij})}{\partial r_{ij}}\frac{\mathbf{r}_{ij,y}\mathbf{r}_{ij,z}}{r_{ij}} \tag{A.51}$$
$$\frac{\partial V_2}{\partial \varepsilon_5} = \frac{1}{2}\sum_{i<j}\frac{\partial V_2(r_{ij})}{\partial r_{ij}}\frac{\mathbf{r}_{ij,x}\mathbf{r}_{ij,z}}{r_{ij}} \tag{A.52}$$
$$\frac{\partial V_2}{\partial \varepsilon_6} = \frac{1}{2}\sum_{i<j}\frac{\partial V_2(r_{ij})}{\partial r_{ij}}\frac{\mathbf{r}_{ij,x}\mathbf{r}_{ij,y}}{r_{ij}} \tag{A.53}$$

Reciprocal space contribution The previous equations (A.47-A.53) holds for the direct space term of the potential. In some case one needs to express the stress tensor of interactions expressed in the reciprocal space, *i.e.* for the Ewald summation, which can be computed using the same methodology. The first step consists in calculating the derivative of a slightly modified reciprocal vector $\mathbf{k}'$,

$$\frac{\partial k^{2'}}{\partial \varepsilon_{\alpha\beta}} = \mathbf{k}^{\dagger}\frac{\partial\left(\underline{\underline{\varepsilon}}^{\dagger}\underline{\underline{\varepsilon}}\right)^{-1}}{\partial \varepsilon_{\alpha\beta}}\mathbf{k}. \tag{A.54}$$

As the derivative of the inverse of a matrix $\underline{\underline{A}}$ can be expressed as

$$\frac{\partial \underline{\underline{A}}^{-1}}{\partial x} = -\underline{\underline{A}}^{-1}\frac{\partial \underline{\underline{A}}}{\partial x}\underline{\underline{A}}^{-1} \tag{A.55}$$

by injecting the results of A.55 into A.54 one obtains:

$$\frac{\partial k^{2'}}{\partial \varepsilon_{\alpha\beta}} = -\mathbf{k}^{\dagger}\left(\underline{\underline{\varepsilon}}^{\dagger}\underline{\underline{\varepsilon}}\right)^{-1}\frac{\partial\left(\underline{\underline{\varepsilon}}^{\dagger}\underline{\underline{\varepsilon}}\right)}{\partial \varepsilon_{\alpha\beta}}\left(\underline{\underline{\varepsilon}}^{\dagger}\underline{\underline{\varepsilon}}\right)^{-1}\mathbf{k}. \tag{A.56}$$

Now, if we consider an infinitely small perturbation, we have:

$$\frac{\partial k^{2}}{\partial \varepsilon_{\alpha\beta}} = -\mathbf{k}^{\dagger}\frac{\partial\left(\underline{\underline{\varepsilon}}^{\dagger}\underline{\underline{\varepsilon}}\right)}{\partial \varepsilon_{\alpha\beta}}\mathbf{k} \quad \text{as} \quad \left(\underline{\underline{\varepsilon}}^{\dagger}\underline{\underline{\varepsilon}}\right)^{-1} \simeq \underline{\underline{1}}. \tag{A.57}$$

The derivative of the volume Ω can also be straightforwardly calculated:

$$\Omega' = |\underline{\underline{\varepsilon h}}| \tag{A.58}$$

$$\Omega' = |\underline{\underline{\varepsilon}}||\underline{\underline{h}}| \tag{A.59}$$

$$\frac{\partial \Omega'}{\partial \varepsilon_{\alpha\beta}} = \frac{\partial|\underline{\underline{\varepsilon}}|}{\partial \varepsilon_{\alpha\beta}}|\underline{\underline{h}}| \tag{A.60}$$

$$\frac{\partial|\underline{\underline{\varepsilon}}|}{\partial \varepsilon_{\alpha\beta}} = \frac{\partial\left[(1+\varepsilon_{11})(1+\varepsilon_{22})(1+\varepsilon_{33})+\theta(\varepsilon^2)\right]}{\partial \varepsilon_{\alpha\beta}}. \tag{A.61}$$

The zeroth order term in ε gives:

$$\frac{\partial \Omega}{\partial \varepsilon_{\alpha\beta}} = \delta_{\alpha\beta}\Omega \tag{A.62}$$

It is whortwhile to note that the "forces" applied on the cell can be connected to the stress tensor through the following identity:

$$\Pi^{pot.}_{uv} = -\frac{1}{\Omega}\sum_{s}\frac{\partial E_{\text{total}}}{\partial \mathbf{h}_{us}}\mathbf{h}^{\dagger}_{sv}. \tag{A.63}$$

Ewald summation When substituting equation (A.53), (A.57) and (A.62) in the Ewald summation (2.64) one obtains the general expression of the stress tensor for a system of interacting point charges [99]:

$$\Omega\Pi^{pot.}_{\alpha\beta} = -\frac{\partial V_2}{\partial \varepsilon_{\alpha\beta}} \tag{A.64}$$

$$= \frac{1}{2}\sum_{i\neq j}\frac{q_i q_j}{r_{ij}^2}\left[\frac{\operatorname{erfc}(\sqrt{\alpha}r_{ij})}{r_{ij}} + 2\sqrt{\frac{\alpha}{\pi}}\exp\left(-\alpha r_{ij}^2\right)\right] r_{ij,\alpha}r_{ij,\beta} \tag{A.65}$$

$$+2\frac{\pi}{\Omega}\sum_{\mathbf{k}\neq 0}\frac{\exp(-k^2/4\alpha)}{k^2}\left[\delta_{\alpha\beta} - 2\frac{1+k^2/4\alpha}{k^2}k_\alpha k_\beta\right]\sum_{i,j}\exp\left[i\mathbf{k}\cdot(\mathbf{r}_i-\mathbf{r}_j)\right]$$

Using the above equation and the relations expressed in Eqs. (A.27) and (A.30) one can calculate the contributions of the long range interactions to the stress tensor.

Bibliography

[1] M. P. Allen and D. J. Tidesley, *Computer Simulation of Liquids* (Oxford Science Publication 1987).

[2] H. C. Andersen, J. Chem. Phys. **72**, 2384 (1980).

[3] C. A. Angel, P. H. Poole, and J. Shao, Nuovo Cimento D **16**, 993 (1994).

[4] M. J. Annen, M. E. Davis, J. B. Higgins, and J .L. Schlenker, J. Chem. Soc., Chem. Commun. 1175 (1991).

[5] M. Hemmati and C. A. Angell, *Physics Meets Mineralogy* (Cambridge University Press, Cambridge, 2000).

[6] G. B. Bachelet, D. R. Hamann, and M. Schlüter, Phys. Rev. B **26**, 4199 (1982).

[7] F. Bacon, A. A. Hasapis, and J. W. Wholley, Phys. Chem. Glass 1 **90**, (1960).

[8] T. F. W. Barth, Am. J. Sci. **23**, 350 (1932).

[9] B. W. H. van Beest, G. J. Kramer, and R. A. van Santen, Phys. Rev. Lett. **64**, 1955 (1990).

[10] M. Benoit, S. Ispas, P. Jund, and R. Jullien, Euro. Phys. J. B **13**, 631 (2000).

[11] M. Benoit, S. Ispas, and M. E. Tuckerman, Phys. Rev. B **64**, 224205 (2001).

[12] M. Benoit and W. Kob, Europhys. Lett. **60**, 269 (2002).

[13] K. Binder and W. Kob, *Glassy Materials and Disordered Solids*, (World Scientific, Singapore, 2005).

[14] N. Bingelli, N. Troullier, J. L. Martins, and J. R. Chelikowsky, Phys. Rev. B **44**, 4771 (1991).

[15] F. Bloch, Z. Physik **52**, 555 (1928).

[16] S. Blonski and S. H. Garofalini, J. Am. Ceram. Soc. **80**, 1997 (1997).

[17] K. de Boer, A. P. J. Jansen, and R. A. van Santen, Chem. Phys. Lett. **223**, 46 (1994).

[18] K. de Boer, A. P. J. Jansen, and R. A. van Santen, Phys. Rev. B **52**, 12579 (1995).

[19] K. de Boer, A. P. J. Jansen, R. A. van Santen, G. W. Watson, and S. C. Parker, Phys. Rev. B **54**, 826 (1996).

[20] M. Born and K. Huang, *Dynamical Theory of Crystal Lattices* (Oxford University Press, New York, 1954).

[21] M. Born and J. R. Oppenheimer, Ann. Physik **84**, 457 (1927).

[22] M. Born and J. E. Mayer, Z. Phys. **75**, 1 (1932).

[23] G. Brébec, R. Seguin, C. Sella, J. Bevenot, and J. C. Martin, Acta Metall. **28**, 327 (1980).

[24] R. Brückner, J. Non-Cryst. Solids **5**, 123 (1970).

[25] R. Car and M. Parrinello, Phys. Rev. Lett. **55**, 2471 (1985).

[26] J. M. Carpenter and D. L. Price, Phys. Rev. Lett. **54**, 441 (1985).

[27] M. A. Carpenter, E. K. H. Salje, A. Graeme-Barber, B. Wruck, M. T. Dove, and K. S. Knight, Am. Miner. **83**, 2 (1998).

[28] A. Carré,

[29] D. Chandler, *Introduction to Modern Statistical Mechanics* (Oxford University Press, New York, 1987).

[30] J. R. Chelikowsky, H. E. King, and J. Glinnemann, Phys. Rev. B **41**, 10866 (1990).

[31] J. R. Chelikowsky and M. Schlüter, Phys. Rev. B **15**, 4020 (1977).

[32] E. Courtens, M. Foret, B. Hehlen, and R. Vacher, Solid State Commun. **117**, 187 (2001).

[33] `CPMD`, Copyright IBM Corp 1990-2006, Copyright MPI für Festkörperforschung Stuttgart 1997-2001.

[34] T. Darden, D. York, and L. Pedersen, J. Chem. Phys. **98**, 10089 (1993).

[35] E. Demiralp, T. Cagin, and W. A. Goddard III, Phys. Rev. Lett. **82**, 1708 (1999).

[36] M. Deserno and C. Holm, J. Chem. Phys. **109**, 7678 (1998); J. Chem. Phys. **109**, 7694 (1998).

[37] H. Q. Ding, N. Karasawa, and W. Goddard, J. Chem. Phys. **97**, 4309, (1992).

[38] P. A. M. Dirac, Proc. Roy. Soc. London Ser. A, 117 (1928).

[39] P. A. M. Dirac, Proc. Roy. Soc. London Ser. A, 118 (1928).

[40] M. T. Dove, *Introduction to Lattice Dynamics* (Cambridge University Press, Cambridge, 1993).

[41] L. Duffrène and J. Kieffer, J. Phys. Chem. Solids **59**, 1025 (1998).

[42] B. Diu, C. Guthmann, D. Lederer, and B. Roulet, *Physique statistique* (Hermann, Paris, 1989).

[43] A. C. T. van Duin, S. Dasgupta, F. Lorant, and W. A. Goddard III, J. Phys. Chem. A **105**, 9396 (2001).

[44] P. A. Egelstaff, *Thermal Neutron Scattering* (Academic, London, 1965).

[45] P. Ehrenfest, Zeitschrift für Physik A Hadrons and Nuclei, **45**, 455 (1927).

[46] F. Ercolessi, and J. B. Adams, Europhys. Lett. **26**, 583 (1994).

[47] R. A. Evans, Mol. Sim. **4**, 409 (1990).

[48] H. M. Evjen, Phys. Rev. **39**, 675 (1932).

[49] P. P. Ewald, Ann. Phys. **64**, 253 (1921).

[50] B. P. Feuston and S. H. Garofalini, J. Chem. Phys. **89**, 5818 (1988).

[51] E. Flikkema and S. T. Bromley, Chem. Phys. Lett. **378**, 622 (2003).

[52] V. Fock, Z. Phys. **61**, 126 (1930).

[53] D. Frenkel and B. Smit, *Understanding Molecular Simulation: From Algorithms to Applications* (Academic Press, London, 2002).

[54] J. D. Gale and A. L. Rohl, Mol. Simul. **29**, 291 (2003).

[55] S. Goedecker, M. Teter, and J. Hutter, Phys. Rev. B **54**, 1703 (1996).

[56] L. Greengard and V. Rokhlin, J. Comp. Phys. **73**, 325 (1987).

[57] D. I. Grimley, A. C. Wright, and R. N. Sinclair, J. Non-Cryst. Solids **119**, 49 (1990).

[58] G. Grochola, S. P. Russo, and I. K. Snook, J. Chem. Phys. **123**, 204719 (2005).

[59] J. Grunthaner, Mater. Sci. Rep. **1**, 65 (1986).

[60] Y. Guissani and B. Guillot, J. Chem. Phys. **104**, 7633 (1996).

[61] D. R. Hamann, M. Schlter, and C. Chiang, Phys. Rev. Lett. **43**, 1494 (1979).

[62] D. R. Hamann, Phys. Rev. Lett. **76**, 660 (1996).

[63] J. P. Hansen and I. R. McDonald. *Theory of Simple Liquids* (Academic Press, London, 1990).

[64] M. Hawlitzky, *Klassische un ab initio Molekulardynamik-Untersuchungen zu Germaniumdioxidshmelzen* (Ph. D. Thesis, Mainz, 2006).

[65] P. J. Heaney, C. T. Prewitt, and G. V. Gibbs, *Silica, Physical Behavior, Geochemistry and Materials Applications*, Reviews in Mineralogy **29**, 1 (1994).

[66] M. Hemmati and C. A. Angell, J. Non-Cryst. Solids **217**, 236 (1997).

[67] D. Herzbach, *Comparison of model potentials for molecular dynamics simulation of crystalline silica*. Thesis, Johannes Gutenberg-University Mainz (2004).

[68] D. Herzbach, K. Binder, and M. H. Müser, J. Chem. Phys. **123**, 124711 (2005).

[69] F. J. Himpsel, Surf. Sci. **168**, 764 (1986).

[70] V. V. Hoang, Eur. Phys. J. B **54**, 291 (2006).

[71] R. W. Hockney and J. W. Eastwood, *Computer Simulations Using Particles*, (McGraw-Hill, New York, 1981).

[72] P. Hohenberg and W. Kohn, Phys. Rev. B **136**, 864 (1964).

[73] W. G. Hoover, Phys. Rev. A **31**, 1695 (1985).

[74] J. Horbach *Molekulardynamiksimulationen zum glasübergang von Silikatschmelzen* (Ph. D. Thesis, Mainz, 1998).

[75] J. Horbach and W. Kob, Phys. Rev. B **60**, 3169 (1999).

[76] L. Huang, J. Kieffer, J. Chem. Phys. **118**, 1487 (2003).

[77] S. Izvekov, M. Parrinello, C. J. Burnham, and G. A. Voth, J. Chem. Phys. **120**, 10896 (2004).

[78] R. A. Jackson and C. R. A. Catlow, Mol. Simul. **1**, 107 (1988).

[79] R. A. Jackson and C. R. A. Catlow, Mol. Simul. **1**, 207 (1988).

[80] A. Kerrache, V. Teboul, and A. Monteil, Chem. Phys. **321**, 69 (2006).

[81] K. Kihara, Euro. J. Mineral. **2**, 63 (1990).

[82] C. Kittel, *Introduction to Solid State Physic* (Dunod, Paris, 1998).

[83] C. Klein and C. S. Hurlbut Jr, *Manual of Mineralogy, 21st ed.* (John Wiley and Sons, New York, 1985).

[84] W. Kohn and L. J. Sham, Phys. Rev. A **140**, 1133 (1965).

[85] G. J. Kramer, N. P. Farragher, B. W. H. van Beest, and R. A. van Santen, Phys. Rev. B **43**, 5068 (1991).

[86] T. Kumagai, S. Izumi, S. Hara, and S. Sakai, *The international Conference on Computational Methods*, December 15-17 (2004) Singapore.

[87] A. Laio, S. Bernard, G. L. Chiarotti, S. Scandolo, and E. Tosatti, Science **287**, 1027 (2000).

[88] A. C. Lasaga and G. V. Gibbs, Phys. Chem. Minerals **14**, 107 (1987).

[89] F. S. Lee and A. Warshel, J. Chem. Phys. **97**, 3100 (1992).

[90] C. Leforestier, J. Chem. Phys. **68**, 4406 (1978).

[91] C. Levelut, A. Faivre, R. Le Parc, B. Champagnon, J.-L Hazemann, and J.-P Simon, Phys. Rev. B **72**, 224201 (2005).

[92] Y. Liang, C. R. Miranda, and S. Scandolo, Phys. Rev. B **75**, 24205 (2007).

[93] F. Liu, S. H. Garofalini, R. D. King-Smith, and D. Vanderbilt, Phys. Rev. Lett. **70**, 2750 (1993).

[94] F. L. Liu, S. H. Garofalini, D. K. Smith, and D. Vanderbilt, Phys. Rev. B **49**, 12528 (1994).

[95] A. P. Lyubartsev and A. Laaksonen, Phys. Rev. E **52**, 3730 (1995).

[96] G. J. Martyna, M. L. Klein, and M. E. Tuckerman, J. Chem. Phys. **97**, 2635 (1992).

[97] G. J. Martyna, M. E. Tuckerman, D. J. Tobias, and M. L. Klein, Mol. Phys. **87**, 1117 (1996).

[98] R. M. Martins, *Electronic Structure: Basic Theory and Practical Methods* (Cambridge University Press, Cambridge, 2004).

[99] D. Marx and J. Hutter, *Ab initio dynamics: Theory and Implementation*, Jülich, NIC Series, Vol. 1.

[100] M. Matsui and T. Matsumoto, Acta Cryst. B, **41**, 377 (1985).

[101] M. Matsui, M. Akaogi, and T. Matsumoto, Phys. Chem. Minerals **14**, 101 (1987).

[102] P. F. McMillan, B. T. Poe, P. Gillet, and B. Reynard, Geochim. Comsochim. Acta **58**, 3653 (1994).

[103] H. J. McSkimin, P. Andreatch, and R. N. Thurston, J. Appl. Phys. **36**, 1624 (1965).

[104] Q. Mei, C. J. Benmore, and J. K. R. Weber, Phys. Rev. Lett. **98**, 57802 (2007).

[105] S. Merlino, Eur. J. Miner. **2**, 809 (1990).

[106] A. Meyer, private communication.

[107] J. C. Mikkelsen, Appl. Phys. Lett. **45**, 1187 (1984).

[108] R. L. Mozzi and B. E. Warren, J. Appl. Cryst. **2**, 164 (1969).

[109] M. H. Müser and K. Binder, Phys. Chem. Min. **28**, 746 (2001).

[110] K. D. Nielson, A. C. T. van Duin, J. Oxgaard, W. Q. Deng, and W. A. Goddard III, J. Phys. Chem. A **109**, 493 (2005).

[111] W. Nieuwenkamp, Z. Kristallogr. **96**, 454 (1937).

[112] S. Nosé, J. Chem. Phys. **81**, 511 (1984).

[113] G. Pastore, E. Smargiassi, and F. Buda, Phys. Rev. A **44**, 6334 (1991).

[114] L. Pauling, *The Nature of the Chemical Bond* (Cornell University Press, New York, 1960).

[115] L. Pauling, Am. Mineral **65**, 321 (1980).

[116] D. R. Peacor, Z. Kristallogr. **138**, 274 (1973).

[117] M. Pöhlmann, M. Benoit, and W. Kob, Phys. Rev. B **70**, 184209 (2004).

[118] W. H. Press, S. A. Teukolsky, W. T. Vetterling, and B. P. Flannery, *Numerical Recipes in C The Art of Scientific Computing, Second Edition* (Cambridge University Press, Cambridge, 1992).

[119] P. Pulay, Molec. Phys. **17**, 197 (1969).

[120] P. Pulay, Adv. Chem. Phys. **69**, 241 (1987).

[121] D. C. Rapaport, *The art of Molecular Dynamics Simulation* (Cambridge University Press, Cambridge, 1995).

[122] S. M. Rigden, T. J. Ahrens, and E. M. Stolper, Science **226**, 1071 (1984).

[123] G. Roma, Y. Limoges, and S. Baroni, Phys. Rev. Lett. **86**, 4564 (2001).

[124] W. B. Russel, D. A. Saville, and W. R. Schowalter, *Colloidal Dispersions* (Cambridge University Press, Cambridge, 1989).

[125] G. Salin and J. M. Caillol, J. Chem. Phys. **113**, 10459 (2000).

[126] J. Sarnthein, A. Pasquarello, and R. Car, Phys. Rev. Lett. **74**, 4682 (1995).

[127] J. Sarnthein, A. Pasquarello, and R. Car, Phys. Rev. B **52**, 12690 (1995).

[128] J. Sarnthein, A. Pasquarello, and R. Car, Phys. Rev. Lett. **5**, 4682 (1995).

[129] S. Scandolo, private communicaton.

[130] M. J. Sanders, M. Leslie, and C. R. A. Catlow, J. Chem. Soc., Chem. Commun. 1271 (1984).

[131] V. F. Sears, Neutron News **3**, 26 (1992).

[132] S. M. Shnurre, J. Grobner, and R. Schmid-Fretzer, J. Non-Cryst. Solids **336**, 1, (2004).

[133] K. P. Schröder, J. Sauer, M. Leslie, C. R. A. Catlow, and J. M. Thomas, Chem. Phys. Lett. **188**, 320 (1992).

[134] L. Stixrude and M. S. T. Bukowinski, Phys. Rev. B, **44** 2523 (1991).

[135] A. K. Soper, Chem. Phys. **202**, 295 (1996).

[136] T. F. Soules, J. Chem. Phys., **71**, 4570 (1979).

[137] M. Sprik, J. Phys. Chem. **95**, 2283 (1991).

[138] F. H. Stillinger and T. A. Weber, Phys. Rev. B **31**, 5262 (1985).

[139] A. Strachan, E. M. Kober, A. C. T. van Duin, J. Oxgaard, and W. A. Goddard III, J. Chem. Phys. **122**, 54502 (2005).

[140] A. Strachan, A. C. T. van Duin, D. Chakraborty, S. Dasgupta, and W. A. Goddard III, Phys. Rev. Lett. **91**, 98301 (2003).

[141] D. Strauch and B. Dorner, J. Phys.: Condens. Matter **5**, 6149 (1993).

[142] S. Susman, K. J. Volin, D. G. Montague, and D. L. Price, Phys. Rev. B **43**, 11076 (1991).

[143] A. Szabo and N. S. Ostlund, *Modern Quantum Chemistry: Introduction to Advanced Electronic Structure Theory* (Dover Publication, New York, 1989).

[144] P. Tangney and S. Scandolo, J. Chem. Phys. **117**, 8898 (2002).

[145] P. Tangney, *Improving molecular-dynamics simulations of simple ionic systems*, Scuola Internazionale Superiore di Studi Avanzati (SISSA) Trieste, 2002.

[146] S. N. Taraskin and S. R. Elliott, Phys. Rev. B **55**, 117 (1997).

[147] S. N. Taraskin and S. R. Elliot, Phys. Rev. B **56** 8605 (1997).

[148] N. Trouiller and J. L. Martins, Phys. Rev. B **43**, 1993 (1991).

[149] S. Tsuneyuki, M. Tsukada, H. Aoki, and Y. Matsui, Phys. Rev. Lett. **61**, 869 (1988).

[150] M. G. Tucker, D. A. Keen, and M. T. Dove, Mineral. Mag. **65**, 489 (2001).

[151] M. E. Tuckerman and M. Parrinello, J. Chem. Phys. **101**, 1302 (1994).

[152] P. Vashishta, R. K. Kalia, J. P. Rino, and I. Ebbsjö, Phys. Rev. B **41**, 12197 (1990).

[153] K. Vollmayr, W. Kob, and K. Binder, Phys. Rev. B **54**, 15808 (1996).

[154] G. Will, M. Bellotto, W. Parrish, and M. Hart, J. Appl. Cryst. **21**, 182 (1988).

[155] M. Wilson, P. A. Madden, J. Phys.: Condens. Matter **5**, 2687 (1993).

[156] M. Wilson, P. A. Madden, M. Hemmati, and C. A. Angell, Phys. Rev. Lett. **77**, 4023 (1996).

[157] A. Wischnewski, U. Buchenau, and A. J. Dianoux, Phys. Rev. B **57**, 2663 (1998).

[158] D. Wolf, Phys. Rev. Lett. **68**, 3315 (1992).

[159] D. Wolf, P. Keblinski, S. R. Phillpot, and J. Eggebrecht, J. Chem. Phys. **110**, 8254 (1999).

[160] L. V. Woodcock, C. A. Angell, and P. Cheeseman, J. Chem. Phys. **65**, 1565 (1976).

[161] A. F. Wright and A. J. Leadbetter, Philos. Mag. **31**, 1391 (1975).

[162] R. W. G. Wyckoff, Am. J. Sci. **9**, 448 (1925).

[163] R. W. G. Wyckoff, Z. Kristallogr. **62**, 189 (1925).

[164] R. W. G. Wyckoff, *Crystal Structures* (Interscience, New York, 1965).

[165] Y. Xu and W. Y. Ching, Phys. Rev. B **44**, 11048 (1991).

[166] Z. Yan, Eur. J. Phys. **21**, 625 (2000).

[167] V. P Zakaznova-Herzog, H. W. Nesbitt, G. M. Bancroft, J. S. Tse, X. Gao and W. Skinner, Phys. Rev. B **72**, 205113 (2005).